Tune-out measurement in lukewarm lithium with phase-patterned atom interferometry

by

Eric Allen Copenhaver

A dissertation submitted in partial satisfaction of the

requirements for the degree of

Doctor of Philosophy

in

Physics

in the

Graduate Division

of the

University of California, Berkeley

Committee in charge:

Associate Professor Holger Müller, Chair
Professor Dan M. Stamper-Kurn
Professor Kristie A. Boering

Summer 2019

Tune-out measurement in lukewarm lithium with phase-patterned atom interferometry

Abstract

Tune-out measurement in lukewarm lithium with phase-patterned atom interferometry

by

Eric Allen Copenhaver

Doctor of Philosophy in Physics

University of California, Berkeley

Associate Professor Holger Müller, Chair

Atom interferometry deploys atoms as sensors, delivering precision measurements that span the gamut of physics. Laser-cooled samples simplify uniform detection strategies and allow meticulous control over degrees of freedom and systematic effects. Advanced cooling and interferometry techniques do apply readily to a few atomic species, but they leave behind a large class of species otherwise suited for precision sensing. This thesis describes atom interferometry with a sample of lukewarm ^{7}Li, near the Doppler temperature. High thermal speeds demand rapid atom optics and complicate detection. We nevertheless develop interferometer techniques that considerably relax cooling requirements, including a recoil-sensitive scheme capable of measuring the fine-structure constant that takes advantage of ^{7}Li's low mass. We also establish a phase-patterning protocol to inscribe and sense spatially-varying phases with matter-wave interferometers whose sample sizes exceed the arm separation. Phase patterning forms the basis of the first precision measurement of ^{7}Li's red tune-out wavelength, the wavelength where AC Stark shifts from the D-line transitions cancel and the polarizability vanishes. Our measurement registers a 3-σ tension with *ab initio* atomic theory regarding the tensor-shifted tune-out wavelength and a 2-σ tension regarding the size of the tensor shift, but agrees with theory regarding the scalar tune-out wavelength. These results motivate further work on lithium's polarizability, enable direct measurements of hyperpolarizability, and empower an assortment of future applications of phase patterning in matter-wave interferometry.

To Jackie
and future generations

Contents

List of Figures

List of Tables

Acknowledgments

It wasn't that long ago that science never entered my thoughts. It took an entire freshman undergrad year dedicated to jazz guitar and an inaugural year studying Philosophy to acquire a taste for Physics. En route to this dissertation, so many folks lent helping hands to pull me up and push me along.

The first thanks go to Alex Modon for making a "pact" with me to take Physics for our general science requirement, arguably the most difficult option on the table. He totally bailed. But it set me on course nevertheless and that seed has somehow now blossomed into this dissertation, so I suppose I'll forgive a lifelong friend.

My first Physics courses with Prof. Jutta Luettmer-Strathmann grabbed my attention as quickly as Allen Stone's vocals. She took a bright-eyed kid into her research group, taught me how to code, how to think, inculcated me into academia, and sprang me into formative summer research opportunities at Vanderbilt and Michigan. I am so thankful to Dr. Jutta, Prof. Shane Hutson, and Prof. Jennifer Ogilvie for giving me the early resources to thrive in research. For my summer at Michigan, I am also so thankful to have benefitted from the fantastic mentorship of Daniel Wilcox.

After an accelerated undergrad in Physics, I delightedly earned a spot at Berkeley. The friends I made throughout my time there helped guide me through some of the toughest obstacles in my career; for that, I'll be forever grateful to Fabio Sanches, Alejandro Ruiz, Sam Kohn, Mariel Goddu, and Thomas Mittiga[1].

My first summer at Berkeley was the one that inexorably oriented me towards shooting laser at atoms. Prof. Dan Stamper-Kurn's rigor and poetic passion was infectious and I am so thankful to him for hosting me and giving me occasion to quiet down the motion of my first cold atoms. I also first met Ed Marti that summer. Ed has since been everything from brilliant and pedagogical to nurturing. His strong mentorship continued even into the final stages of some subtle points in this dissertation and I thank him deeply for the role he's played in my career.

Prof. Holger Müller and his group were also cooling atoms next door, so I asked to meet and talk about his work. We hit it off immediately over a beer and he gave me a paid slot in his research group there on the spot. Wow. Holger had built a group with a strong culture and brawny experimental chops. It was such a powerful influence to be surrounded by great people with great ideas: Brian Estey, Matt Jaffe, Philipp Hasligner, Vicky Xu, Richard Parker, Xuejian Wu, Osip Schwartz, Sara Campbell, Zack Pagel, and everyone in the Müller group. They helped me with my circuits, my lasers, my analysis, my ideas, and my software. I am grateful to each one of them. I am especially grateful for Kayleigh Cassella who was the one who welcomed into the lab and her project, showed me how to run an experiment, and helped navigate new directions on the world's only cold lithium interferometer. We surmounted some peculiar obstacles like a ruddy vacuum leak and a ransomware attack to accomplish the best science we could.

[1]Even though he unremorsefully shamed me in the gym. I mean, who the heck does 40 pull ups in a row?

I am deeply appreciative of Holger himself. After only several weeks in the group, I was giving a tour to some impressionable undergrads and told them how long I had been "working for Holger..." when he interrupted, "No! Eric works *with* me." Holger treated me like valuable colleague capable of contributing from day one, well before I felt like I had earned it. I came to grad school to learn how to ask valuable scientific questions and pursue answers to them and Holger provided a fun and safe space to do exactly that. Through this PhD, I picked up some of Holger's zeal for fundamental physics, some of his technical prodissertationwess, and a good friend.[2]

I also appreciate a whole cast of people who helped behind the scenes of the science. My mom always believed in me no matter what path I chose and my dad always believed I'd eventually choose the right path. My brother Drew piqued my interest in physics at an early age, though my interest slumbered for many years. My parents in law – Helen and Jerry Slack – have been warm, supportive, and cultivating through it all. My brother in law – John Slack – has made me a better and stronger scientist in all aspects of life.

Ultimately, my deepest gratitude goes to my best friend – $\alpha\gamma\acute{\alpha}\pi\eta\ \mu o\upsilon$ – Jackie. We've been at each other's sides since before my journey in physics really began. She braved the changes that diving into science often brings about in a person and she grew with me. She never gave up on me. She talked when I needed to talk and distracted me when I didn't have the stomach to. She found the courage to smile when I couldn't requite and shone brilliantly on what were many of my darkest times. There was even that time she tried to bring the home to the lab – we hatched a plan to watch Netflix while I babysat the tune-out data campaign around the clock – only to be surprised by Xuejian and a gaggle of Chinese visitors in the market for a lab tour at 9 pm on a Friday.[3] Thank you, Jackie, for everything you have done and everything you are. We finally made it together.

[2]There were also a few priceless memories like how exuberantly he lopped off the barrel of a camera with a hacksaw and that time he chortled as he tested a power supply by connecting the terminals of a power supply with a resistor (a.k.a. a wire) and watched the insulation smolder.

[3]He and the visitors seemed completely unfazed by Jackie's presence, despite the fact that she had set up camp atop a green blanket on the floor in front of a tool chest. She didn't even get up.

Chapter 1

Motivation

1.1 Atomic antennae

Atoms are like little antennas. Charges within an atom shift in response to electric fields, like charge carriers in an antenna responding to radio waves transmitting sound from Angus Young or Jad Abumrad. A field shoves positive charges one direction and negative charges the other. The perturbation on the relative positions of the charges sets up an electric dipole. Should the field strike a resonant chord, the atom will likely undergo a quantum transition. When tuned to a different beat, the atomic dipole will dance along – either in step or out, depending on the frequency.

The dipole that light inspires in an atom serves two broad uses: as a handle that experimentalists leverage to manipulate atomic states and as a sensor that witnesses the local field.

As a handle, resonant transitions can pump an entire ensemble into a pure internal electronic state and steer the atoms' motion through momentum transfer. These capabilities allow preparing atoms a mere fraction of a degree above absolute zero temperature. Further control of the momentum thereafter can assemble superpositions of trajectories that yield quantum interference between the paths of the atomic matter waves. So-called atom interferometry has matured into an accomplished tool in precision metrology, capable of searching

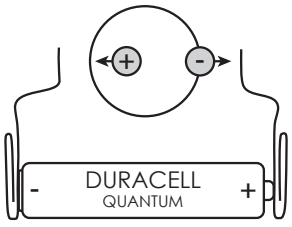

Figure 1.1: Polarizing an atom at home. A pair of paper clips attached to the terminals of a battery generate an electric field. That DC field exerts opposite forces on an atom between the clips. Not drawn to scale.

for low-energy signatures of exotic physics.

As a sensor, atomic dipoles are capable of heralding the local electric field environment. For example, a single atom can even tune in to radio signals [1].[1] The off-resonant response of the dipole also happens to fall within the purview of modern calculations. Combining fundamental quantum mechanics and electrodynamics, *ab initio* atomic theory delivers predictions at a precision that is measurable by experiments. Peculiarities in the dipole response therefore present an opportunity for measurements to stringently test atomic theory.

This dissertation will make full use of the atomic dipole response, both to engineer quantum states and to sense fields in a test of atomic theory.

1.2 Polarizing lithium

The magnitude of an atomic dipole's response to a field is called its polarizability. Polarizability is ubiquitous, appearing across atomic physics as a useful handle in optical dipole traps [2, 3] and as a pesky nuisance through blackbody radiation shifts [4, 5, 6]. One might expect that the charges should oscillate irrespective of frequency, that the polarizability should always be nonzero. After all, atoms are always composed of electric charges and those charges must obey the direction of electric fields. But atoms do not respond to every frequency. Particular frequencies of light – an oscillating electric field – inspire no response[2]. That is called a tune-out wavelength, where the polarizability vanishes altogether. This dissertation is largely dedicated to precisely measuring one particular tune-out wavelength for one particular atom.

Tune-out wavelengths are something of an ironic probe of polarizability, namely because the polarizability there is known exactly; it is precisely zero. Pinpointing exactly where the polarizability is zero, however, requires both theorists and experimentalists to develop a mastery of their respective domains. Comparing experimental [7] and theoretical results [8, 9, 10, 11] for the tune-out wavelength of helium – a small and simple atom like lithium – has inspired a rich and ongoing dialogue that incorporates deep physics.

Lithium, a unique species, can serve as a particularly powerful probe of atomic polarizability. Its three electrons are more than enough to keep theorists occupied, but difficult enough that lithium is the final frontier for many *ab initio* theoretical techniques. At the same time, its single valence electron exhibits a hydrogen-like energy structure that lends itself to the experimental prowess developed for alkali atoms. Lithium is one of a few systems where experiment and theory meet one another with such exactitude. The theory of lithium's polarizability [12, 13, 14, 15, 16] ultimately depends even on relativistic and quantum-electrodynamic effects [17, 18, 19, 20, 21, 22, 23].

Atom interferometers have measured the static polarizability of Li [24], as well as K, Rb, and Cs [25]. Groups have also measured tune-out wavelengths recently for K [26, 27], Rb

[1] Only the most polarizable kind of atoms, Rydberg atoms, should be chosen for radio detection.

[2] As we will see in Sec. 2.2.8, there is an instantaneous response, but the time-averaged dipole response vanishes.

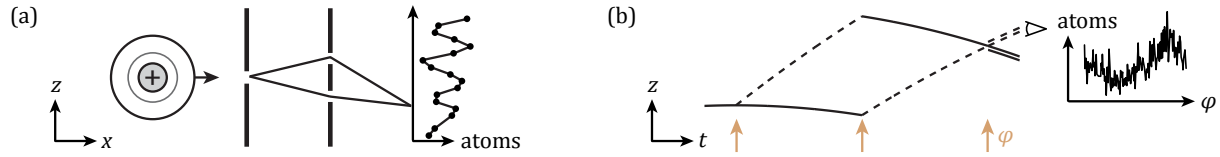

Figure 1.2: The first atom interferometers. In each of two 1991 experiments, the matter-wave behavior of atoms produced interference fringes for the first time. (a) Carnal and Mlynek built a Young's double-slit interferometer for metastable helium (He*) [34] atoms can travel along two paths in space to reach each final position at the detector. (b) Kasevich and Chu built a light-pulse sodium atom interferometer along a single spatial dimension [35].

[28, 29, 30, 31], and Dy [32], but no one has attempted a tune-out measurement for Li prior to this dissertation.

We should be wary of donning Li's rose-colored glasses too blindly. Lithium can be a thorny little atom to work with: assaulting viewports that cap its chambers, resisting standard laser-driven manipulations that other atoms readily yield to, and traveling with higher speeds than heavier species at a given temperature.

Here, we have adopted the circumstance as an opportunity to learn how to cope with higher temperatures in atom interferometers. Though the sample's temperature is a mere fraction above absolute zero, well below 1 mK, it is lukewarm by cold-atom standards.[3] This dissertation demonstrates how to perform interferometry with lukewarm samples in multiple geometries, as well as how to interpret the signals. In spite of the expansive obstacles, we achieve the first measurement of tune-out wavelength in Li. Ours also happens to be the tune-out measurement with the finest wavelength precision ever recorded, around 2 fm.[4]

Since interferometry is the method we employ to measure lithium's tune-out wavelength, we briefly introduce and justify it now.

1.3 Interferometry

Atoms are like little waves. This proposition dates back to Louis de Broglie's 1924 PhD dissertation proffering that atomic momentum p bears a relationship to a wavelength λ in analogy to the relation that holds for light waves: $\lambda = h/p$, where h is Planck's constant.

[3] We are committed to referring to our sample's temperature as "lukewarm" as a result of the work reporting interferometry at room temperature [33].

[4] While this statement is true, it should not be received with as much fanfare as it might appear to deserve. Each atom has a unique set of parameters that determine how sensitively the polarizability varies with wavelength. Lithium is endowed with a much more highly-sloped polarizability than other species, so it may come as no surprise that our wavelength precision finds no precedent from measurements in other species. Lithium, of course, presents particular challenges as a direct result of that sensitivity, but we nevertheless abstain from advertising that this is the most precise measurement to date because measurement precisions across species are more-or-less incommensurate.

Waves exhibit a few distinct phenomena – including delocalization and interference – that can be employed to delocalize a wave's path along multiple trajectories and build metrological tools called interferometers. Paths that enclose an area are sensitive to rotation in a ring laser gyroscope [36], as the recombination beam splitter recedes from one light path and pursues the other. Interferometers that measure the path difference along perpendicular paths can sense gravitational waves [37].[5] Even a mere pair of photons can show interference effects, demonstrable in Hong-Ou-Mandel interference [38]. Displaying interference only requires that the constituents behave as waves and that there exist "optics", or methods to manipulate the waves' trajectories. If atoms behave like waves, they too should interfere.

In May of 1991, Carnal and Mlynek were the first to detect atomic interference with helium, constructing a double-slit experiment with transmission gratings [39] for atoms with wavelengths at the 1-Å scale [34]. Atoms could travel along one of two trajectories to reach the final detector at each position. The phase difference between the paths determines the interference condition, producing atoms to be detected for constructive interference and a deficit of atoms for destructive interference (Fig. 1.2(a)). The double-slit experiment offers atoms two trajectories that separate in two spatial dimensions. Kasevich and Chu imagined an interferometer in which pulses of laser light would resonantly kick an atom along a single dimension. Similar atom-light diffraction had already shown promise in the Pritchard group [40, 41]. In order to stay within the pulsing beam, the atoms would have to enter the interferometer at low velocity. Chu had recently demonstrated techniques to cool [42] and trap [43] sodium atoms, also using lasers. Not two months after Carnal and Mlynek, Kasevich and Chu demonstrated the first light-pulse atom interferometer [35]. The phase of the laser beam that kicks the atoms imprints itself onto the matter wave, so they scanned the phase of the laser and detected interference fringes in the atoms appearing in one of the two output states (Fig. 1.2(b)). In both experiments, the matter wave travels along a superposition of trajectories.[6] Waves, after all, are delocalized entities, so atoms' capacity to "be in two places at once" should come as little surprise.[7]

Since 1991, atom interferometers have flourished as precision instruments. Atom interferometers can compete with laser interferometers in measuring rotation [52, 53, 54] and are

[5] I envied my parents' generation as a kid. They saw humans first travel to the moon and anticipated new Led Zeppelin albums hot off the press. Many feats during my graduate career have ameliorated much of that jealousy. One is the detection of gravitational waves in 2016. In other news, SpaceX first recovered all three Falcon Heavy first-stage boosters in 2019 and Jacob Collier is melting faces on the regular.

[6] The term "atom interferometer" usually refers to an interferometer whose arms spatially separate [44]. Plenty of experiments exploit quantum interference phenomena of matter waves that travel along different trajectories in Hilbert space, from atomic clocks to momentum-space interferometers in lattices [45].

[7] Superposition may seem surreal to many at first glance, but it is a generic feature of waves. My interest in quantum foundations follows next, at the measurement problem [46]. Even if the quantum state is a delocalized wave, measurements routinely record localized outcomes. Collapse theories that describe why a measurement device records a single outcome might be of most interest to experimentalists, since they are subject to experimental constraint. Ghirardi, Rimini, and Weber devised the first collapse theory [47] and Sir Roger Penrose champions that superpositions of massive objects generate an instability in spacetime that must collapse to one state [48]. Experiments to test collapse theories are under development [49, 50] and even Stanford's atom interferometer has weighed in [51].

also under development as gravitational wave sensors [55, 56, 57]. Even Hong-Ou-Mandel interference of pairs of atoms was recently demonstrated [58]. Atom interferometers have some strong advantages over light interferometers since atoms interact gravitationally and electromagnetically, perhaps as well as with fields yet to be discovered. While the arms' difference in interactions may be small, atom interferometers translate them into measurable phase shifts by integrating the frequency difference over the interrogation time. Light-pulse atom interferometers [59] have precisely measured gravity and inertial forces [52, 60, 61, 62, 63, 6, 64], gravity gradients [61, 65, 66, 67, 68], Newton's gravitational constant G [69, 70, 71], the fine-structure constant α_{fsc} [72, 73, 74], and a Rb tune-out wavelength [28, 29]; they have tested Einstein's equivalence principle [75, 76, 77, 78, 79, 80, 81], Lorentz invariance [82], severely constrained a dark energy model [83, 84], and have shown promising progress toward improving these measurements with quantum entanglement [85, 86, 87]. The prevailing spirit of precision measurement is to search for signs of new physics and atom interferometers are surely worth their weight in that vein.

Almost without exception [76, 88, 89], atom interferometers sum the signal in the output ports to improve the signal-to-noise ratio. Interferometers are capable of sensing spatially-varying signals in principle, but this summation averages out such signals. While one technique prints a phase gradient onto the output [88], it only facilitates readout of the average phase of the ensemble.

In this dissertation, we devise and demonstrate a new method for reading out metrologically relevant spatial variations of the interferometer phase. The phase we measure results from the coherent interaction of atoms with a laser beam. The signal source imprints a spatially-varying phase gradient onto an atom interferometer that we use in a precision measurement of a tune-out wavelength, the first tune-out measurement performed in ^{7}Li. The measurement result is intriguing, in 3-σ tension with *ab initio* atomic theory. En route to the tepid tune-out measurement, we also develop a tool kit of methods for interfering lukewarm samples whose outputs cannot be individually detected, including one relevant for recoil-sensitive interferometers that measure the fine-structure constant.

1.4 Organization of this dissertation

This dissertation primarily addresses three demographics: graduate students who want to learn about atom interferometry, researchers interested in understanding or using phase patterning, and folks endeavoring to work with lithium or lukewarm samples.

Chapter 2 describes the theoretical tools necessary to become a practitioner of atom interferometry. Many of the derivations I provide may be found elsewhere, but I present my own treatments with the strategies or motivation that I wish I would have seen as an early-year graduate student. It begins with a thorough introduction to two-level systems. The methods and results for two-level systems apply pervasively for quantum systems with three and more levels, so the intuition we develop for two-level systems is a powerful skill for atomic physicists. We see the polarizability, or AC Stark shift, for two level systems

both with and without dissipation – results that extend intuitively to many-level systems like atoms with a little care. Three levels reduce to two in stimulated Raman transitions. We also explore hyperpolarizability, essentially the only effect we consider that cannot be recycled from a two-level treatment. The atomic physics culminates in the debut of the ^{7}Li atom and its peculiarities. From there, a primer on the theory of atom interferometry introduces readers to practical considerations regarding different geometries, their signals, and their contrast.

Chapter 3 orients the audience to our apparatus, details our techniques, and catalogs particular vagaries of our machine that may or may not be useful to other readers. Readers who need to operate that specific experiment may find this chapter particularly useful, though they should recognize that the litany is incomplete.

Chapter 4 introduces our first interferometry results, the world's first cold-atom interferometer with lithium. Lithium's low mass and high recoil frequency bestow an advantage in recoil-sensitive interferometry, but the high thermal velocity spread complicates driving and detecting the interferometer.

Chapter 5 explicates our precision measurement of ^{7}Li's red tune-out wavelength for $|2S_{1/2}, F = 2, m_F = 0\rangle$ with $\sigma^{\pm}$ polarization, as well as the phase-patterning technique we develop to that end. We thoroughly study the systematics we considered in the measurement. The tension with theory inevitably invites a critical evaluation of our methods, so we endeavor to provide as much detail as might be useful.

Chapter 6 dreams of a future with liberal application of phase patterning and cold lithium atom interferometers. In particular, we concoct a scheme to draw out ^{7}Li's hyperpolarizability from a similar method to the tune-out measurement; motivate a tune-out measurement near 323 nm and consider using ^{6}Li; we imagine other applications of phase patterning in a few arenas; we share some routes to improving our apparatus with extended interrogation times; and we end with a path towards atom interferometers that have very long interrogation times, supported by a harmonic trap. No plan is fully conceived, but each should contain enough information to pique interest in pursuing this future work.

Chapter 2

Theoretical tools

This dissertation relies in many ways on the interaction of atoms with electric fields, both as a handle for engineering quantum states and as a probe of atomic structure. In this chapter, we will assemble the minimal theoretical understanding of that interaction that is required to experimentally manipulate the quantum states.

We use the theory to develop a satisfactory conceptual and intuitive model for the interplay between the field and atom. Building a satisfactory model for the atom-light interaction requires that we study familiar derivations like the Lorentz oscillator, the semiclassical two-level system – which produces the AC Stark shift (with and without dissipation) and the Optical Bloch Equations – and three-level systems like that required to understand stimulated Raman transitions. These familiar checkpoints will lead this dissertation to develop somewhat new approaches for a few phenomena, including the hyperpolarizability of two- and three-level systems and a conceptual picture for the behavior of the atomic dipole driven by the oscillating electric field of passing light. The latter presents an intriguing conundrum regarding how an illuminated atom can have no dipole energy, yet still sport the non-zero dipole moment implicated by single-photon scattering.

We will also develop some tools of practical interest to experimentalists, particularly those working with ^{7}Li and atom interferometers. Table 2.2 collects some of the ubiquitous atomic parameters of ^{7}Li and its interaction with light. For atom interferometers, standard approaches yield the phase difference, while we will also see a novel matrix formulation of quantum amplitudes for modeling the contrast of different interferometer geometries.

Before we begin, let a primer set the mood for detailing atom-light interactions.

Atoms are composite particles, comprising a positively-charged nucleus and negatively-charged electrons. An electric field $\vec{E}$ influences the dynamics of the system of charges and polarizes it, forcing electrons in one direction and the nucleus in the other direction. That is, the field induces a dipole moment $\vec{d}$. The dipole moment is proportional to the field, with the proportionality constant given by the polarizability α:

$$\vec{d} \approx \alpha \vec{E}. \tag{2.1}$$

Figure 2.1: The Lorentz model treats an electron as harmonically bound to the nucleus. This diagram evokes a lithium atom, with two $1S$ core electrons in light gray and a valence electron in the $2S$ state, bound to the nucleus by a spring.

The total energy of the dipole in the field is given by integrating $dU = -\vec{d} \cdot d\vec{E}$,

$$U \approx -\frac{1}{2}\alpha E_0^2, \tag{2.2}$$

assuming the dipole moment is induced parallel to the field and that the field has magnitude E_0. An oscillating electric field, or light, induces an oscillating dipole moment. The details of this dipole interaction forms the basis for many concepts in this dissertation, from the beam splitters that construct the atom interferometers to the tune-out wavelength measured herein.

2.1 Lorentz oscillator

Let us begin with a fully classical treatment of atoms and their response to electric fields, Lorentz oscillator model. While it is simplistic, it faithfully reproduces the response in the far-detuned regime and establishes some basic intuition for the physics of the atom-field interaction.

We know that electrons are bound to atomic nuclei in quantized orbits that are stable to small perturbations. The Lorentz oscillator model treats that stability by regarding the electrons as bound by a spring to the nucleus. If an electron ventures too far away or too close to the nucleus, a restoring force encourages it back towards the stable orbit (albeit with some damping γ).

Consider an electron with charge e a distance x away from the nucleus, bound by a spring with natural frequency ω_0 and damped at a rate γ[1]. Driven at a frequency ω by a field with amplitude E_0, the equation of motion is

$$m\ddot{x} + m\gamma\dot{x} + m\omega_0^2 x = -eE_0 e^{-i\omega t}, \tag{2.3}$$

where the mass m is most properly the reduced mass of the system. To solve for the dynamics, we assume a periodic response that follows the driving field, $x = Ae^{-i\omega t}$. Inserting this ansatz

[1]This damping rate can be shown to equal the spontaneous emission rate by comparison to Einstein's rate equation model. Lithium's D-lines have $\gamma \sim 2\pi\times 5.87$ MHz, which is considerably smaller than most detunings we consider.

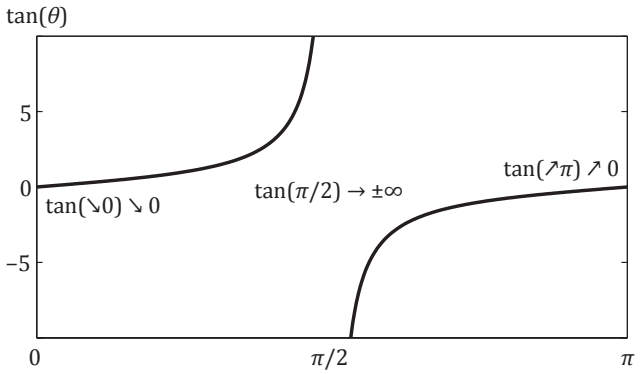

Figure 2.2: The phase offset θ between the Lorentz oscillator and the driving force depends on the frequency ratio $\tan(\theta) = \gamma\omega/(\omega_0^2 - \omega^2)$.

into the equation of motion yields

$$A = \frac{-e/m}{\omega_0^2 - \omega^2 - i\gamma\omega} E_0. \tag{2.4}$$

The dipole moment is the product of the charge and the separation we just calculated $\vec{d} = e\vec{x} = \alpha\vec{E}$[2]. The polarizability is therefore

$$\alpha = \frac{e^2/m}{\omega_0^2 - \omega^2 - i\gamma\omega} = \left(\frac{e^2}{m}\right) \frac{\omega_0^2 - \omega^2 + i\gamma\omega}{(\omega_0^2 - \omega^2)^2 + \gamma^2\omega^2}. \tag{2.5}$$

The polarizability is a complex number. At a given frequency ω, the imaginary part of the polarizability adds a phase offset between the oscillator response x and the drive. The complex angle θ of α describes this phase offset and requires just a bit of geometry in the complex plane.

$$\tan(\theta) = \frac{\gamma\omega}{\omega_0^2 - \omega^2}. \tag{2.6}$$

The limiting cases highlighted in Fig. 2.2 provide some strong intuition for the response of the oscillator. When $\omega \ll \omega_0$, the ratio on the right-hand side of Eq. (2.6) approaches 0 from above, implying that the offset phase is approximately 0. The oscillator's response is therefore in phase with the drive for large red detunings. When $\omega \gg \omega_0$, the ratio takes on small but negative values that approach 0 from below, implying that the offset phase approaches π. The oscillator responds to the drive 180° out of phase for large blue detunings.

The Lorentz oscillator model provides even more intuition than fits within the scope of this introduction. One may use it to derive expressions for the line width of a transition, the saturation intensity, and more [90]. For now, the main takeaway should be that the atom

[2]Of course, the lithium atom boasts a nuclear charge of $+3e$, but the two core electrons predominantly screen two of the nuclear charges from the valence electron that implicitly interests us. Such details are of little concern to us anyway, as we merely play with this toy model for some intuition.

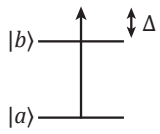

Figure 2.3: A system with two levels $|a\rangle$ and $|b\rangle$ at energies $\hbar\omega_a$ and $\hbar\omega_b$ is subjected to a driving force with detuning $\Delta = \omega - (\omega_b - \omega_a)$.

acts like an oscillator that responds in-phase with a red-detuned drive and out-of-phase with a blue-detuned drive.

As a preview of coming attractions, consider a system sporting three levels. For three levels, there are two transitions from the ground state to each of the two excited states. Imagine a drive tuned to a frequency between the two transition frequencies. The drive is blue-detuned from the lower-frequency transition and red-detuned from the higher-frequency transition. The interaction with the drive comprises the interaction with each transition so the total polarizability is just the sum of the polarizabilities from each transition. The lower transition contributes oscillations largely out of phase with the drive while the upper transition contributes oscillations largely in phase. Those oscillations superpose and cancel at some a particular frequency. That is the essence of a tune-out wavelength, the frequency at which the polarizability exactly vanishes due to an interference between response modes.

2.2 Two-level systems

The Lorentz oscillator is a fully classical treatment of an atomic system that is quantum and should be treated as quantum. Treating an atom semi-classically – a quantum two-level system driven by a classical light field – accesses much of the rich quantum dynamics used throughout modern atomic physics. While we will assume the form of the field to be classical, we will occasionally reason using the quantized energy and momentum of the photons in the field.[3]

Interferometers generate multiple trajectories so that differences in phase accrued along the trajectories can be made measurable. Separating the trajectories requires imparting some momentum to the atom. The original atom interferometer [34], as well as some contemporary experiments [92, 24, 25], accomplished the momentum transfer by shooting high-speed atom beams at microfabricated gratings. The gratings act similarly to light gratings, generating constructive matter-wave interference at quantized output angles that satisfy the Bragg condition [44, 93].

Light with a well-defined wave number k offers an alternative method to transfer momentum. We must understand the dynamics of how light interacts with an atom in order to use a light pulse to transfer momentum. Patiently solving the dynamics of the two-level system provides powerful insights that are applicable throughout this dissertation. More

[3] A fully quantum treatment, for example in Ref. [91], defends those results.

complicated multi-level systems cede a plethora of shortcuts to physicists with a careful understanding of the two-level model.

2.2.1 Semi-classical treatment

Let us perform the semi-classical treatment here. The classical light field is simply an electric field oscillating along a polarization direction $\hat{\epsilon}$. The phase of the field may be offset by a spatiotemporal laser phase $\phi_L = \vec{k}\cdot\vec{z} - \omega t_0$ at position $\vec{z}$ with wave vector $\vec{k}$ and time t_0. By time t, the phase advances beyond ϕ_L at a fixed position by an amount $\omega\tau$, where $\tau = t - t_0$.

$$\vec{E} = E_0 \cos(\omega\tau + \phi_L)\hat{\epsilon}. \tag{2.7}$$

The field acts on a two-level system with a ground state $|a\rangle$ and an excited state $|b\rangle$. The electric field induces a dipole $\vec{d}$ in the composite charged particle. The interaction of the induced dipole with the field that induces it specifies the energy as

$$\hat{V} = -\hat{\vec{d}}\cdot\vec{E}. \tag{2.8}$$

This interaction is only the lowest-order term in a larger multipole expansion. By regarding it alone, we have made the electric dipole approximation (specifying to $E1$ transitions). Quadrupole ($E2$), octupole ($E3$), etc. transitions are the results of the higher-order terms.

Each state has an associated time-dependent quantum amplitude c_a and c_b. The state vector $|\psi\rangle = \begin{pmatrix} c_a \\ c_b \end{pmatrix}$ follows the dynamics of the Schrödinger equation under the influence of the Hamiltonian $\hat{H}$:

$$i\hbar\frac{d}{d\tau}|\psi\rangle = \hat{H}(\tau)|\psi\rangle. \tag{2.9}$$

where $\hbar$ is the reduced Planck constant.

2.2.2 Temporal evolution of eigenstates

It is worth appreciating a feature of Eq. (2.9), a feature true even beyond two-level systems. If the state $|\psi\rangle$ happens to be an eigenstate of the Hamiltonian, then the Hamiltonian leaves $|\psi\rangle$ untouched and returns the energy eigenvalue. For these atomic eigenstates, the Schrödinger equation implies that the temporal derivative of the state $|s\rangle = |a(b)\rangle$ is the state itself with a multiplier $-i\omega_s$. The solution is simply $\exp(-i\omega_s t)$. The corresponding operator describing temporal evolution over a small time $d\tau$ must be

$$\hat{U}(\tau, d\tau) = e^{-i\hat{H}(\tau)d\tau/\hbar} \tag{2.10}$$

The operator expands to $1 - i\hat{H}(\tau)d\tau/\hbar$, the second term acts on the state to return the energy, and re-exponentiating the result returns $\exp(-i\omega_s d\tau)$. Sequential application of these

infinitesimal temporal evolutions results in a product of phase factors whose exponents sum to the factor we expected

$$\hat{U}(\tau) = e^{-i\hat{H}\tau/\hbar}, \tag{2.11}$$

where we assume that the structure of the Hamiltonian is independent of time.[4] In App. A, we employ this evolution for a simpler treatment of a subset of interferometer phases that avoids a more complicated treatment with the action.

2.2.3 The Hamiltonian

Having established the form for the field we will use, we can derive the Hamiltonian for the semi-classical system. The Hamiltonian that describes the state dynamics includes a both the atomic Hamiltonian with the states' energies, as well as the interaction with the light field.

The matrix elements of the interaction in Eq. (2.8) are constrained by parity. The induced dipole operator looks like $\hat{\vec{d}} \sim -e\hat{\vec{r}}$, where $\hat{\vec{r}}$ is the separation of the electron from the nucleus that we set at the origin. Consider the parity operator $\hat{\Pi}$, which flips the sign of spatial coordinates. Applying the parity operator to a state returns the parity eigenvalue of the state, $\Pi = +1$ for spatially symmetric (even parity) states or $\Pi = -1$ for states that flip sign under spatial inversion (odd parity). The parity of an atomic orbit is connected to the famous parity relation for spherical harmonics ($\hat{\Pi} Y_l^m = (-1)^l Y_l^m$) and is +1 for atomic S states ($l = 0$) and -1 for P states ($l = 1$). Regardless of which state the atom is in, $\hat{\Pi}|a(b)\rangle = \Pi_{a(b)}|a(b)\rangle$ and $\Pi_{a(b)}^2 = 1$. That allows us to equate $-e\langle a(b)|\,\hat{\vec{r}}\,|a(b)\rangle = -e\Pi_{a(b)}^2\langle a(b)|\hat{\Pi}^\dagger\,\hat{\vec{r}}\,\hat{\Pi}|a(b)\rangle$. Those parity operators could also transform the separation operator, $\hat{\Pi}^\dagger\,\hat{\vec{r}}\,\hat{\Pi} = -\hat{\vec{r}}$. Doing so leads us to the conclusion that this matrix element equals its opposite, $-e\langle a(b)|\,\hat{\vec{r}}\,|a(b)\rangle = e\langle a(b)|\,\hat{\vec{r}}\,|a(b)\rangle$, which is true only if these diagonal matrix elements are 0. The diagonal matrix elements for the full Hamiltonian therefore only include the energies of the atomic states and contain no influence from the interaction.

The off-diagonal matrix elements of the interaction are allowed to be non-zero. We assume that the field induces an atomic dipole parallel to the polarization, $\hat{\vec{d}} \cdot \hat{\epsilon} = \hat{d}$.

$$\langle b|\hat{V}|a\rangle = -\langle b|\hat{d}|a\rangle E_0 \tag{2.12}$$

We can express this energy as the product of Planck's constant and a frequency. We define the Rabi frequency Ω as the rate associated with the coupling between $|a\rangle$ and $|b\rangle$:

$$\Omega \equiv -\frac{1}{\hbar} d_{ba} E_0, \tag{2.13}$$

where we define the dipole matrix element $d_{ba} = \langle b|\hat{d}|a\rangle = d_{ab}^*$.

[4] When the Hamiltonian changes over time, it becomes more complicated. If the state adiabatically evolves into eigenstates of the changing Hamiltonian, then a different energy is returned each $d\tau$ when expanding the exponential. If the Hamiltonian changes too rapidly for the state to follow, that is unfortunate.

The full Hamiltonian is[5]

$$\hat{H} = \hbar \begin{pmatrix} 0 & \Omega \cos(\phi_L - \omega\tau) \\ \Omega^* \cos(\phi_L - \omega\tau) & \omega_b \end{pmatrix}. \tag{2.14}$$

The explicit time dependence in the Hamiltonian makes finding solutions to the Schrödinger equation annoying. Some clever manipulation transforms away the time dependence. First, we rewrite the cosines as a sum of counter-rotating exponentials.

$$i\dot{c}_a = \frac{\Omega}{2}(e^{i\omega\tau - i\phi_L} + e^{-i\omega\tau + i\phi_L})c_b, \tag{2.15}$$

$$\begin{aligned} i\dot{c}_b &= \frac{\Omega^*}{2}(e^{i\omega\tau - i\phi_L} + e^{-i\omega\tau + i\phi_L})c_a + \omega_b c_b \\ i(\dot{c}_b + i\omega_b c_b) &= \frac{\Omega^*}{2}(e^{i\omega\tau - i\phi_L} + e^{-i\omega\tau + i\phi_L})c_a \end{aligned} \tag{2.16}$$

The left-hand side of Eq. (2.16) looks almost like it behaves as the derivative of a complex exponential, albeit without the exponential factor. Multiplying both sides by $e^{i\omega_b\tau}$ makes the equation more convenient.

$$i(e^{i\omega_b\tau}\dot{c}_b + i\omega_b e^{i\omega_b\tau}c_b) = \frac{\Omega^*}{2}(e^{i(\omega+\omega_b)\tau - i\phi_L} + e^{-i\Delta\tau + i\phi_L})c_a,$$

where the detuning is the difference between the laser frequency and transition frequency

$$\Delta \equiv \omega - (\omega_b - \omega_a). \tag{2.17}$$

Having referenced energies to ω_a, we have $\Delta = \omega - \omega_b$. The left-hand side now fully motivates the change of variable

$$\tilde{c}_b \equiv e^{i\omega_b\tau}c_b, \tag{2.18}$$

for which $\dot{\tilde{c}}_b = e^{i\omega_b\tau}\dot{c}_b + i\omega_b e^{i\omega_b\tau}c_b$. The equations of motion with this transformed variable become

$$i\dot{c}_a = \frac{\Omega}{2}(e^{i\Delta\tau - i\phi_L} + e^{-i(\omega+\omega_b)\tau + i\phi_L})\tilde{c}_b, \tag{2.19}$$

$$i\dot{\tilde{c}}_b = \frac{\Omega^*}{2}(e^{i(\omega+\omega_b)\tau - i\phi_L} + e^{-i\Delta\tau + i\phi_L})c_a. \tag{2.20}$$

Atomic dipole transition frequencies are in the hundreds of THz. The phase factor involving the sum of frequencies drives dynamics on inaccessible time scales that effectively

[5]This may appear at first to be a strange choice of sign. The motivation for doing so is to remain consistent with describing the laser phase as $\phi_L = \vec{k}\cdot\vec{z} - \omega t_0$, which advanced in time with the same sign as $-\omega\tau$ up to the moment of the interaction.

average out. Neglecting those terms constitutes the rotating wave approximation (RWA)[6].

$$ie^{-i\Delta\tau}\dot{c}_a = \frac{\Omega}{2}e^{-i\phi_L}\tilde{c}_b, \tag{2.21}$$

$$i\dot{\tilde{c}}_b = \frac{\Omega^*}{2}e^{i\phi_L}e^{-i\Delta\tau}c_a. \tag{2.22}$$

The time dependence is not fully extinguished, but one more change of variables appears promising:

$$\tilde{c}_a \equiv e^{-i\Delta\tau}c_a, \tag{2.23}$$

for which $\dot{\tilde{c}}_a = e^{-i\Delta\tau}\dot{c}_a - i\Delta e^{-i\Delta\tau}c_a$. The fully transformed equations have no more explicit time dependence.

$$i\dot{\tilde{c}}_a = \frac{\Omega}{2}e^{-i\phi_L}\tilde{c}_b + \Delta\tilde{c}_a, \tag{2.24}$$

$$i\dot{\tilde{c}}_b = \frac{\Omega^*}{2}e^{i\phi_L}\tilde{c}_a. \tag{2.25}$$

Written in the form of the Schrödinger equation, we see the ubiquitous rotating-frame Hamiltonian for a two-level system under the RWA.

$$i\begin{pmatrix}\dot{\tilde{c}}_a\\ \dot{\tilde{c}}_b\end{pmatrix} = \begin{pmatrix}\Delta & e^{-i\phi_L}\Omega/2\\ e^{i\phi_L}\Omega^*/2 & 0\end{pmatrix}\begin{pmatrix}\tilde{c}_a\\ \tilde{c}_b\end{pmatrix} \tag{2.26}$$

Guess the Hamiltonian with dressed states

There is a shortcut for expediently guessing the rotating-frame Hamiltonian in Eq. (2.26). The trick utilizes the dressed-state basis. The driven two-level system includes both the atomic system with states $|a\rangle$ and $|b\rangle$, as well as the light field. The energy of the full system is the energy of the atomic state and the field. Consider the two lowest energy states: $|+\rangle$ with an atom in $|a\rangle$ plus one photon and $|-\rangle$ with an atom in $|b\rangle$ with no photon. We can move the reference energy as we please, so we choose to subtract out the upper state energy $\hbar\omega_b$. The newly referenced energies become

$$U_+ = \hbar\omega_a + \hbar\omega \quad \rightarrow \quad \tilde{U}_+ = \hbar(\omega - (\omega_b - \omega_a)) = \hbar\Delta, \tag{2.27}$$

$$U_- = \hbar\omega_b \quad \rightarrow \quad \tilde{U}_- = 0. \tag{2.28}$$

These are precisely the diagonal entries in the Hamiltonian. Employing this trick later will aid in reasoning towards the Hamiltonian for a three-level system in a rotating frame.

[6] There is a physical manifestation of the terms that the RWA neglects, called the Bloch-Siegart shift. The effect looks like an AC Stark shift $\hbar\Omega^2/4\Delta$, with a more highly suppressed denominator, $\hbar\Omega^2/4(\omega+\omega_b)$ [90].

The amplitudes

We now seek solutions for the amplitudes. Differentiating Eq. (2.25) with respect to time and inserting Eq. (2.24) in the ensuing appearance of $\dot{\tilde{c}}_a$ leads to

$$i\ddot{\tilde{c}}_b = \frac{\Omega^*}{2}e^{i\phi_L}\left(-i\left(\frac{\Omega}{2}e^{-i\phi_L}\tilde{c}_b + \Delta\tilde{c}_a\right)\right). \tag{2.29}$$

Eq. (2.25) donates a substitution for $\tilde{c}_a$.

$$i\ddot{\tilde{c}}_b = \frac{\Omega^*}{2}e^{i\phi_L}\left(-i\left(\frac{\Omega}{2}e^{-i\phi_L}\tilde{c}_b + i\frac{2\Delta}{\Omega^*}e^{-i\phi_L}\dot{\tilde{c}}_b\right)\right). \tag{2.30}$$

$$\ddot{\tilde{c}}_b + i\Delta\dot{\tilde{c}}_b + \frac{|\Omega|^2}{4}\tilde{c}_b = 0. \tag{2.31}$$

The vanishing sum of consecutive derivatives suggests an exponential solution $\tilde{c}_b = Be^{if\tau}$. Then, $f^2 + \Delta f - |\Omega|^2/4 = 0$ and the two solutions are $f_\pm = \left(-\Delta \pm \sqrt{|\Omega|^2 + \Delta^2}\right)/2$. The general solution is a sum of the two independent solutions $\tilde{c}_b = B_-e^{if_-\tau} + B_+e^{if_+\tau}$. We will define the generalized Rabi frequency

$$\Omega' \equiv \sqrt{|\Omega|^2 + \Delta^2} \tag{2.32}$$

so that

$$\tilde{c}_b = e^{-i\Delta\tau/2}(B_-e^{-i\Omega'\tau/2} + B_+e^{i\Omega'\tau/2}). \tag{2.33}$$

Initial state $|a\rangle$

With the general solution in hand, consider the dynamics for an atom initially in $|a\rangle$. That is, $c_a(\tau = 0) = 1$ and $c_b(\tau = 0) = 0$. This respects the normalization that must be satisfied at all times $|c_a|^2 + |c_b|^2 = 1$. At $\tau = 0$, $c_b = \tilde{c}_b = 0 = B_- + B_+$, so we define $B \equiv B_- = -B_+$. At time τ,

$$\tilde{c}_b = -e^{-i\Delta\tau/2}B\left(e^{i\Omega'\tau/2} - e^{-i\Omega'\tau/2}\right) = -e^{-i\Delta\tau/2}2B\sin(\Omega'\tau/2) \tag{2.34}$$

Differentiating this and substituting into Eq. (2.25) yields

$$-i2B\left(-i\frac{\Delta}{2}e^{-i\Delta\tau/2}\sin(\Omega'\tau/2) - e^{-i\Delta\tau/2}\frac{\Omega'}{2}\cos(\Omega'\tau/2)\right) = \frac{\Omega^*}{2}e^{i\phi_L}\tilde{c}_a, \tag{2.35}$$

which, upon inserting $\tau = 0$, implies

$$B = ie^{i\phi_L}\frac{\Omega^*}{2\Omega'}. \tag{2.36}$$

The amplitude transferred from $|a\rangle$ to $|b\rangle$ is therefore

$$c_b = -ie^{-i\omega_b\tau}e^{-i\Delta\tau/2}e^{i\phi_L}\frac{\Omega^*}{\Omega'}\sin(\Omega'\tau/2) \tag{2.37}$$

We can insert this solution into Eq. (2.25) and solve for c_a.

$$c_a = e^{i\Delta\tau/2}\left(\cos(\Omega'\tau/2) - i\frac{\Delta}{\Omega'}\sin(\Omega'\tau/2)\right) \tag{2.38}$$

Initial state $|b\rangle$

A similar procedure produces the amplitudes if the atom begins in $|b\rangle$. Differentiating Eq. (2.24) and inserting Eq. (2.25) into the resulting appearance of $\dot{\tilde{c}}_b$ gives

$$\ddot{\tilde{c}}_a + i\Delta\dot{\tilde{c}}_a + \frac{|\Omega|^2}{4}\tilde{c}_a = 0. \tag{2.39}$$

This is again solved by the general solution $\tilde{c}_a = B'_- e^{if_-\tau} + B'_+ e^{if_+\tau}$. Since at $\tau = 0$, $\tilde{c}_a = c_a = 0$, we see that $B' \equiv B'_- = -B'_+$ and $\tilde{c}_a = -e^{-i\Delta\tau/2} 2B' \sin(\Omega'\tau/2)$. We differentiate that solution as before, but now substitute Eq. (2.24) and solve for B' using $\tau = 0$, at which $\tilde{c}_a = 0$ and $\tilde{c}_b = 1$. The result is

$$B' = ie^{-i\phi_L}\frac{\Omega}{2\Omega'}. \tag{2.40}$$

The amplitude for transferring from $|b\rangle$ to $|a\rangle$ is

$$c_a = -ie^{i\Delta\tau/2}e^{-i\phi_L}\frac{\Omega}{\Omega'}\sin(\Omega'\tau/2). \tag{2.41}$$

We insert this result into Eq. (2.24) and solve for c_b, the amplitude for starting and staying in $|b\rangle$,

$$c_b = e^{-i\omega_b\tau}e^{-i\Delta\tau/2}\left(\cos(\Omega'\tau/2) + i\frac{\Delta}{\Omega'}\sin(\Omega'\tau/2)\right). \tag{2.42}$$

2.2.4 Coherent dynamics: Rabi oscillations

The complex amplitudes we have just derived provide important insight into the dynamics of the system. Their norm gives the probability for finding the system in each state (Born's rule). For an atom initially in the ground state, the atom oscillates between the ground and excited state. The probability of transferring an atom from $|a\rangle$ to $|b\rangle$ follows from Eq. (2.37).

$$|c_b|^2 = \frac{|\Omega|^2}{\Omega'^2}\sin^2(\Omega'\tau/2). \tag{2.43}$$

The system starting in state $|a\rangle$ oscillates between the two levels at a frequency of Ω' (Fig. 2.4, left). When the system is in $|a\rangle$, illuminating the system longer increases the chance that the drive stimulates the system to absorb the light. Once the system is in $|b\rangle$, longer illumination increases the chance of stimulated emission. These cycles of stimulated absorption from $|a\rangle$ to $|b\rangle$ and subsequent stimulated emission from $|b\rangle$ back to $|a\rangle$ are called Rabi oscillations.

One may also look at the spectral characteristics of the population transfer (Fig. 2.4 left). When the drive frequency matches the system's resonance, a pulse duration chosen to satisfy $\Omega\tau = \pi$ maximizes the transfer probability. For the same pulse time, non-zero detunings produce less response.

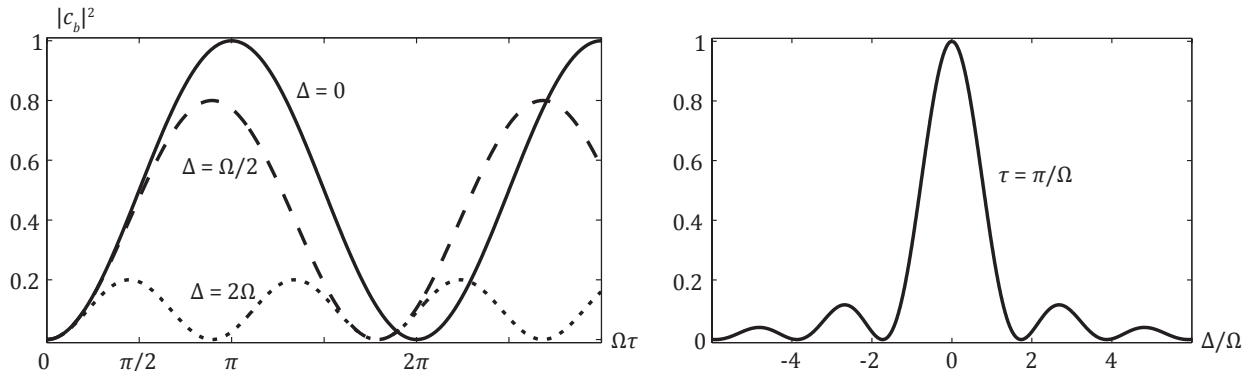

Figure 2.4: Left: A two-level system starting in $|a\rangle$ oscillates into $|b\rangle$ and back at a freqeuncy $\Omega' = \sqrt{\Omega^2 + \Delta^2}$. The frequency and maximum amplitude of the oscillations depend on the detuning from resonance. Right: The response to a particular pulse duration (here a π pulse on resonance) varies with detuning. The suppressed response for nonzero detuning can be partially compensated by choosing a longer pulse length.

2.2.5 Atom optics: beam splitters and mirrors

The population dynamics above offer a handle we can use to manipulate the quantum state of an atom. Critically, we must also recognize that light carries momentum, $\hbar k$ per photon to be precise. Momentum must be conserved in the interaction, so if the atom is stimulated to absorb a photon, the atom must also absorb its momentum. That is, the atom must recoil at a speed v_r,

$$v_r = \hbar k/m. \tag{2.44}$$

The coupled states are more appropriately labeled by both their internal energy state and their momentum. For an atom initially moving at speed v_0 along the light's propagation direction, the light field couples

$$|a, mv_0\rangle \leftrightarrow |b, mv_0 + \hbar k\rangle. \tag{2.45}$$

This can be explicitly shown by quantizing the electromagnetic field and approaching the two-level system from a fully quantum perspective [91]. Atom interferometers employ this momentum transfer to manipulate the path of atoms, impelling one state to recoil away from the other in space and time.

Tuning the interaction time τ manipulates the system into superpositions of the two states at will. Two particular operations are germane to interferometers: beam splitters and mirrors. These are named in analogy to the optical components in light interferometers that manipulate the path of the beam. The beam splitter mixes each input path into a combination of two output paths. The mirror takes one input path and outputs an alternative path.

The operators that describe these atom optics are special cases of the amplitudes in Eqs. (2.37), (2.38), (2.41), and (2.42). We define these operators for conditions idealized in two

ways. First, the interaction time τ evidently introduces a phase to the amplitudes. We assume, however, that the interaction only requires an infinitesimally short time to occur, at least compared to the rate at which the phase accrues on the amplitude ($\omega_b \tau \to 0$). Even if the phase this neglects is non-zero, it will only contribute a constant phase offset as long as the pulse duration remains stable across iterations of the experiment. It is possible to treat the pulse as one with finite duration and solve for the phase offset it produces in an interferometer [94], but that phase offset is inconsequential for the work presented here.[7] Second, we assume that the interaction is on resonance, $\Delta = 0$. The factor $\sin(\Omega'\tau/2)$ is $1/\sqrt{2}$ when the pulse area

$$\Omega\tau_{\pi/2} \equiv \pi/2, \tag{2.46}$$

called a "$\pi/2$ pulse" or "beam splitter" $\hat{S}$. Alternatively, $\sin(\Omega'\tau/2)$ is 1 when the pulse area

$$\Omega\tau_{\pi} \equiv \pi, \tag{2.47}$$

called a "π pulse" or "mirror" $\hat{M}$. The operators that act on the state $|\psi\rangle$ are

$$\hat{S}(\phi_L) = \frac{1}{\sqrt{2}} \begin{pmatrix} 1 & -ie^{-i\phi_L} \\ -ie^{i\phi_L} & 1 \end{pmatrix}, \tag{2.48}$$

$$\hat{M}(\phi_L) = \begin{pmatrix} 0 & -ie^{-i\phi_L} \\ -ie^{i\phi_L} & 0 \end{pmatrix}. \tag{2.49}$$

It may also be useful to define the operator more generally for readers interested in accounting for different atoms' behavior in an ensemble as in Fig. 2.9, using Eqs. (2.37), (2.38), (2.41), and (2.42).

Both beam splitters (Eq. (2.48)) and mirrors (Eq. (2.49)) evidently imprint the initial phase of the light field ϕ_L onto the amplitude of the quantum state. Depending on whether the system transitions from $|a\rangle \to |b\rangle$ or $|b\rangle \to |a\rangle$, the sign with which the phase imprints onto the state is opposite. Accounting for this phase is crucial in atom interferometry. The phases of the laser that drive the atom optics inform the total phase shift the interferometer records.

2.2.6 AC Stark shift

A final and crucial consequence of the Hamiltonian in Eq. (2.26) is that it shifts the energy levels of the system. It has off-diagonal components, implying that the basis states we chose are not eigenstates. Diagonalizing the Hamiltonian delivers the energies of the eigenstates Λ, which allow us to calculate the matter-wave phase by simply evolving those eigenstates in time as in App. A.

$$\begin{vmatrix} \Delta - \Lambda & e^{i\phi_L}\Omega/2 \\ e^{-i\phi_L}\Omega^*/2 & -\Lambda \end{vmatrix} = (\Delta - \Lambda)(-\Lambda) - |\Omega|^2/4 = 0, \tag{2.50}$$

[7] Unless it is unstable, either through a pulse duration that changes from shot to shot, or from instability in Δ.

for which the eigenenergies become

$$\hbar\Lambda_{\pm} = \frac{\hbar\Delta}{2} \pm \frac{\hbar\sqrt{\Delta^2 + |\Omega|^2}}{2}. \tag{2.51}$$

Atomic physicists frequently work in a far-detuned regime where $|\Delta| \gg |\Omega|$. There, we can approximate the root with an expansion $\sqrt{\Delta^2 + |\Omega|^2} = \Delta\sqrt{1 + |\Omega|^2/\Delta^2} \approx \Delta(1 + (1/2)|\Omega|^2/\Delta^2 + ...)$. Inserting this approximate result into the eigenenergies above and ignoring the offset $\hbar\Delta$ of the ground state, we find that the ground state is shifted by an energy called the AC Stark shift

$$\Delta U_{AC} = \hbar\frac{|\Omega|^2}{4\Delta}. \tag{2.52}$$

Recall that the Rabi frequency Ω is proportional to the magnitude of the light's electric field. The AC Stark shift is therefore proportional to the intensity of the light. Furthermore, the shift follows the sign of the detuning. The AC Stark shift is stabilizing (i.e. produces negative energy shifts) at negative detunings for which the photon energy is lower than the transition energy. Gradients in intensity produce gradients in the AC Stark shift, so focused laser beams detuned far below the transition form attract atoms into the lowest energy state where the intensity is highest. This constitutes an optical dipole trap (ODT) [2], sometimes called a far off-resonant trap (FORT) [3].

Stated more generally, Ω is proportional to the strength of the coupling between the two levels. While the coupling strength varies with the intensity, it is also proportional to the strength of the dipole transition d_{ab}. That dipole matrix element depends on the geometry of the two atomic states being coupled, a contribution quantified in part by Clebsch-Gordan coefficients. The dependence of the AC Stark shift on Clebsch-Gordan coefficients will be critical for computing atomic polarizabilities beyond the two-level model.

2.2.7 Dissipation

The AC Stark shift as written in Eq. (2.52) diverges for small Δ, which we must somehow reconcile on the grounds that it is clearly unphysical. The finite-energy field and atom surely do not interact to produce a new infinite-energy system, so the model must neglect relevant physics near resonance. One candidate is damping, which was included in the Lorentz model. The excited states of the atom that concern us typically decay rather quickly, in a time $\tau_\gamma = 1/\gamma \sim 30$ ns. We have not accounted for this source of dissipation since our consideration of the Lorentz oscillator model, so we include it here. We argue for how to include this decay phenomenologically, starting with the observation that an atom in the excited state $|b\rangle$ decays at a rate γ. After a time t, the probability that the atom remains in $|b\rangle$ must fall as $|c_b|^2 \propto e^{-\gamma t}$. The bare state amplitude evloves as the exponential $e^{-i\omega_b t}$. If the energy term in the exponent had contained an imaginary component $-i\gamma/2$, then the amplitude's evolution would follow $e^{-i(\omega_b - i\gamma/2)t} = e^{-i\omega_b t}e^{-\gamma t/2}$. Upon squaring such an amplitude, we would have $|c_b|^2 \propto e^{-\gamma t}$. Thus, an imaginary component to the state energy

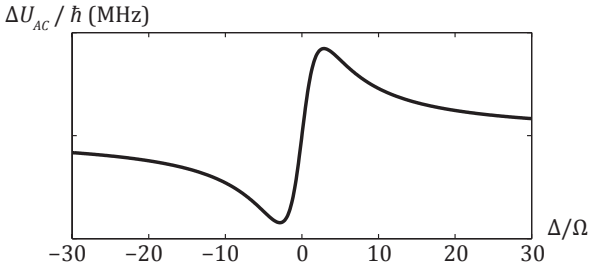

Figure 2.5: Two-level AC Stark shift with damping. The AC Stark shift for a two-level system no longer diverges close to resonance upon accounting for damping. The shift here is shown for $\Omega = 1$ MHz and $\gamma = 6$ MHz and has extrema of approximately ± 0.042 MHz.

produces the decay we seek to describe.[8] In the rotating frame, we can account for disippation by modifying the Hamiltonian

$$\hat{\tilde{H}} \to \hbar \begin{pmatrix} \Delta & e^{i\phi_L}\Omega/2 \\ e^{-i\phi_L}\Omega^*/2 & -i\gamma/2 \end{pmatrix} \tag{2.53}$$

Now we obtain eigenfrequencies,

$$\Lambda_\pm = \frac{\Delta - i\gamma/2}{2} \pm \frac{\sqrt{(\Delta - i\gamma/2)^2 + |\Omega|^2 + i2\Delta\gamma}}{2} = \frac{\Delta - i\gamma/2}{2} \pm \frac{\sqrt{(\Delta + i\gamma/2)^2 + |\Omega|^2}}{2}. \tag{2.54}$$

The AC Stark shift is the shift referenced to the state energy at zero field. The first term is therefore irrelevant and we study the second term, subtracting its zero-field value at $|\Omega|^2 \to 0$.

$$\Delta U_{AC} = \hbar \,\mathrm{Re}\left[\frac{1}{2}\sqrt{(\Delta + i\gamma/2)^2 + |\Omega|^2} - \frac{1}{2}(\Delta + i\gamma/2)\right]. \tag{2.55}$$

Only the real part of the expression describes the observable energy shift, which is not readily identifiable because of the root. To discern the real part, we set $\sqrt{(\Delta + i\gamma/2)^2 + |\Omega|^2} = a + ib$ and solve for a. Squaring both sides and equating the real components gives $a^2 - b^2 = \Delta^2 - \gamma^2/4 + |\Omega|^2$, while equating the imaginary components gives $b = \gamma\Delta/2a$. Inserting b into the previous condition gives a quadratic equation for (a^2) whose roots are

$$a^2 = \frac{1}{2}(\Delta^2 - \gamma^2/4 + |\Omega|^2) \pm \frac{1}{2}\sqrt{(\Delta^2 - \gamma^2/4 + |\Omega|^2)^2 + \gamma^2\Delta^2}. \tag{2.56}$$

Here, we choose only the $+$ root because the $-$ root gives an imaginary a and that would be counterproductive. Alongside the real part $\Delta/2$ of the second term in Eq. (2.55), taking the square root of a^2 presents another sign choice. That sign we choose differently depending on the sign of Δ. The positive root is appropriate when $\Delta > 0$, but the energy shift diverges for $\Delta < 0$ due to the $\Delta/2$ term. Multiplying by the sign of Δ skirts the issue.

$$\Delta U_{AC} = \frac{\hbar}{\sqrt{8}}\left(\frac{\Delta}{|\Delta|}\right)\sqrt{(\Delta^2 - \gamma^2/4 + |\Omega|^2) + \sqrt{(\Delta^2 - \gamma^2/4 + |\Omega|^2)^2 + \gamma^2\Delta^2}} - \frac{\Delta}{2} \tag{2.57}$$

[8] This reasoning extends into the rotating frame.

The form of Eq. (2.57) is regrettably opaque. Fig. 2.5 illustrates the behavior around resonance, which no longer diverges like Eq. (2.52).

Notably, the behavior is only substantially different near resonance. For detunings much larger than the line width, it is sufficient to employ Eq. (2.52).

2.2.8 Dipole oscillations and Optical Bloch Equations

We first attempted to establish an intuitive understanding of how the atomic dipole responds to the optical drive by studying the Lorentz oscillator model. That model did include dissipation, albeit in a fully classical system. In the previous section, we developed the capability to include dissipation in a quantum model. A quantum model with dissipation should produce more accurate results for the dipole's behavior compared to the classical Lorentz oscillator.

What we seek here is the quantum expectation value of the dipole moment of the atomic state $|\psi\rangle$:

$$\langle d\rangle = \langle\psi|\hat{d}|\psi\rangle = (\langle b|c_b^* + \langle a|c_a^*)\hat{d}(c_a|a\rangle + c_b|b\rangle) = c_b^* c_a d_{ba} + c_a^* c_b d_{ba}^*. \tag{2.58}$$

Solving for the dynamics of the dipole's expectation value will lead us to the Optical Bloch Equations. Note that Eq. (2.38) for c_a and Eq. (2.37) for c_b are obsolete here because the route to those solutions did not include damping.

The appearance of $c_b^* c_a$ and $c_a^* c_b$ inspires a pursuit of the dynamics of the density operator, which is constructed from such terms.

$$\rho = |\psi\rangle\langle\psi| = \begin{pmatrix} c_a \\ c_b \end{pmatrix}\begin{pmatrix} c_a^* & c_b^* \end{pmatrix} = \begin{pmatrix} |c_a|^2 & c_a c_b^* \\ c_b c_a^* & |c_b|^2 \end{pmatrix} \equiv \begin{pmatrix} \rho_{aa} & \rho_{ab} \\ \rho_{ba} & \rho_{bb} \end{pmatrix}. \tag{2.59}$$

Assuming the dipole matrix element is real $d_{ab} = d_{ba}$ (and $\Omega = \Omega^*$) and stepping into the rotating frame with the previous definitions in Eq. (2.18) and (2.23),

$$\langle d\rangle = d_{ab}(c_b^* c_a + c_a^* c_b) = d_{ab}(\tilde{c}_b^* \tilde{c}_a e^{i\omega\tau} + \tilde{c}_a^* \tilde{c}_b e^{-i\omega\tau}) \tag{2.60}$$

The density matrix elements may also be written in the rotating frame as $\tilde{\rho}_{ab} = \tilde{c}_a \tilde{c}_b^*$ and $\tilde{\rho}_{ba} = \tilde{c}_b \tilde{c}_a^*$.

$$\begin{aligned} \langle d\rangle &= d_{ab}(\tilde{\rho}_{ab} e^{i\omega\tau} + \tilde{\rho}_{ba} e^{-i\omega\tau}) \\ &= d_{ab}(\tilde{\rho}_{ab}(\cos(\omega\tau) + i\sin(\omega\tau)) + \tilde{\rho}_{ba}(\cos(\omega\tau) - i\sin(\omega\tau))) \\ &= d_{ab}((\tilde{\rho}_{ab} + \tilde{\rho}_{ba})\cos(\omega\tau) + i(\tilde{\rho}_{ab} - \tilde{\rho}_{ba})\sin(\omega\tau)) \\ &= d_{ab}(u\cos(\omega\tau) - v\sin(\omega\tau)), \end{aligned} \tag{2.61}$$

where we have defined u to be the response of the dipole in phase with the field

$$u \equiv \tilde{\rho}_{ab} + \tilde{\rho}_{ba}. \tag{2.62}$$

The quantity v is the magnitude with which the dipole responds 90° in advance of the field, that is proportionally to the $-\sin(\omega\tau)$ instead of $\cos(\omega\tau)$.[9]

$$v \equiv -i(\tilde{\rho}_{ab} - \tilde{\rho}_{ba}). \tag{2.63}$$

Note that we have set $\phi_L = 0$ for simplicity.[10] Another quantity of interest would be the atomic populations. The variable w quantifies this, as $+1$ when the system is in $|a\rangle$ and -1 when the system is in $|b\rangle$,

$$w \equiv \rho_{aa} - \rho_{bb} = \tilde{\rho}_{aa} - \tilde{\rho}_{bb}. \tag{2.64}$$

Just as the temporal derivatives of the amplitudes must obey the Schrödinger equation, so must the temporal derivatives of the density matrix elements and their linear combinations.

$$\dot{u} = \dot{\tilde{\rho}}_{ab} + \dot{\tilde{\rho}}_{ba} = \dot{\tilde{c}}_a\tilde{c}_b^* + \tilde{c}_a\dot{\tilde{c}}_b^* + \dot{\tilde{c}}_b\tilde{c}_a^* + \tilde{c}_b\dot{\tilde{c}}_a^*. \tag{2.65}$$

We first address $\dot{\tilde{\rho}}_{ab}$,

$$\dot{\tilde{\rho}}_{ab} = \dot{\tilde{c}}_a\tilde{c}_b^* + \tilde{c}_a\dot{\tilde{c}}_b^*. \tag{2.66}$$

Substituting $\dot{\tilde{c}}_a$ from Eq. (2.24) and for $\dot{\tilde{c}}_b^*$ from (2.25),

$$\begin{aligned}\dot{\tilde{\rho}}_{ab} &= \left(-i\frac{\Omega}{2}\tilde{c}_b - i\Delta\tilde{c}_a\right)\tilde{c}_b^* + \tilde{c}_a\left(i\frac{\Omega}{2}\tilde{c}_a^*\right) \\ &= i\Omega w/2 - i\Delta\tilde{\rho}_{ab}\end{aligned} \tag{2.67}$$

Inserting Eq. (2.67) into Eq. (2.65) and recognizing $\dot{\tilde{\rho}}_{ba} = \dot{\tilde{\rho}}_{ab}^*$, we find

$$\dot{u} = \dot{\tilde{\rho}}_{ab} + \dot{\tilde{\rho}}_{ba} = i\Omega w/2 - i\Delta\tilde{\rho}_{ab} - i\Omega w/2 + i\Delta\tilde{\rho}_{ba} = \Delta v \tag{2.68}$$

Similarly,

$$\dot{v} = -i(\dot{\tilde{\rho}}_{ab} - \dot{\tilde{\rho}}_{ba}) = -i\left(i\Omega w/2 - i\Delta\tilde{\rho}_{ab} - (-i\Omega w/2 + i\Delta\tilde{\rho}_{ba})\right) = \Omega w - \Delta u. \tag{2.69}$$

The dynamics of the populations

$$\dot{w} = \dot{\tilde{\rho}}_{aa} - \dot{\tilde{\rho}}_{bb} \tag{2.70}$$

must also respect the normalization condition $\tilde{\rho}_{aa} + \tilde{\rho}_{bb} = 1$, so $\dot{\tilde{\rho}}_{aa} + \dot{\tilde{\rho}}_{bb} = 0$ and $\dot{\tilde{\rho}}_{aa} = -\dot{\tilde{\rho}}_{bb}$. Therfore, $\dot{w} = 2\dot{\tilde{\rho}}_{aa} = 2(\dot{\tilde{c}}_a\tilde{c}_a^* + \tilde{c}_a\dot{\tilde{c}}_a^*)$. Using Eq. (2.24) for $\dot{\tilde{c}}_a$ and $\dot{\tilde{c}}_a^*$,

$$\dot{w} = 2\left(\left(-i\frac{\Omega}{2}\tilde{c}_b - i\Delta\tilde{c}_a\right)\tilde{c}_a^* + \tilde{c}_a\left(i\frac{\Omega}{2}\tilde{c}_b^* + i\Delta\tilde{c}_a^*\right)\right) = -\Omega v \tag{2.71}$$

[9] Consequently, $u < 0$ implies a component of the response 180° out of phase with the field, while $v < 0$ describes a response that lags the field by 90°.

[10] The main incentive for including ϕ_L in the first place was to conclude that the laser phase is imprinted on the matter wave during the interferometer. We are no longer concerned with the matter-wave phase and only study the state dynamics in this section, with the consequence of dissipation in mind.

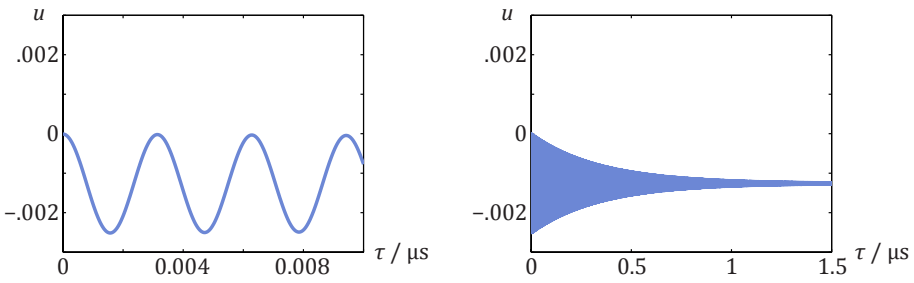

Figure 2.6: Two-level system dipole response. The in-phase component u of the atomic dipole for a system with 2000-MHz detuning from a transition with 7.62-mW/cm^2 saturation intensity and 5.87-MHz linewidth.

The dynamics of u, v, and w are the same as those that describe a spin in a magnetic field, originally developed for studying nuclear magnetic resonance. We can view our two-level quantum system as a spin on the "Bloch sphere". The Bloch vector points up for an atom in the ground state $|a\rangle$ and down for an atom in the excited state $|b\rangle$. On the equator, the atom is in an equal superposition of $|a\rangle$ and $|b\rangle$. The spin precesses around a "laser vector" – analogous to a magnetic field – whose z component gives the detuning and the equatorial component describes the phase and strength of the drive.

These equations have yet to reference damping. As before, phenomenological arguments guide its inclusion. The state $|b\rangle$ decays as $|c_b|^2 = \rho_{bb} \propto e^{-\gamma\tau}$. That is, there is a decay term proportional to the population in that state, $-\gamma\rho_{bb}$ that should accompany the rate $\dot{\rho}_{bb}$, $\dot{\rho}_{bb} \to \dot{\rho}_{bb} - \gamma\rho_{bb}$. In terms of $\dot{w} = \dot{\rho}_{aa} - \dot{\rho}_{bb} = -2\dot{\rho}_{bb}$,

$$\dot{w} \to -2(\dot{\rho}_{bb} - \gamma\rho_{bb}) \tag{2.72}$$

$$= -2\dot{\rho}_{bb} + 2\gamma\frac{1}{2}(1-w) \tag{2.73}$$

$$= \dot{w} - \gamma(w-1). \tag{2.74}$$

So $\dot{w}$ evidently earns an additional $-\gamma(1-w)$. The decay of the Bloch vector from $|b\rangle \to |a\rangle$ sends the z component from -1 to +1, a difference of 2. The coherent components u and v decay to a value of 0 when the atomic stat is purely $|a\rangle$, from a maximum absolute value of 1. So the u and v components decay half the amount in the same time as w. That is, their decay rate is half that of w. Collecting all these decays and adding them in, we arrived at the optical Bloch equations with the effect of damping.

$$\dot{u} = \Delta v - \frac{\gamma}{2}u, \tag{2.75}$$

$$\dot{v} = \Omega w - \Delta u - \frac{\gamma}{2}v, \tag{2.76}$$

$$\dot{w} = -\Omega v - \gamma(w-1). \tag{2.77}$$

The equations above are difficult to solve analytically. Numerically integrating the differential equations with a simple Euler method[11] provides powerful enough insight into the behavior of the dipole. We simulate the dipole's response for a 5.87-MHz linewidth, detuned 2000 MHz blue of a transition with 7.62-mW/cm^2 saturation intensity and plot the results in Fig. 2.6. The in-phase response u oscillates on short timescales (in a frame that rotates at the laser frequency). On long timescales approaching the decay time, the oscillations damp and the in-phase component settles to a nonzero value. The nonzero value of the atomic dipole multiplies the electric field to produce a nonzero energy. That energy is the AC Stark shift.

Steady-state solution

The dissipation damps the coherent oscillations in the driven system, so it eventually reaches a steady state at long times, when all the time derivatives in Eqs. (2.75), (2.76), and (2.77) are 0. Then there are three equations and three unknowns that admit an algebraic solution

$$\begin{pmatrix} u \\ v \\ w \end{pmatrix} = \frac{1}{\Delta^2 + |\Omega|^2/2 + \gamma^2/4} \begin{pmatrix} \Omega\Delta \\ \Omega\gamma/2 \\ \Delta^2 + \gamma^2/4 \end{pmatrix} \tag{2.78}$$

Perhaps the most salient result from the steady-state solution is the excited state population

$$\rho_{bb} = \frac{1-w}{2} = \frac{1}{2}\frac{\Omega^2/2}{\Delta^2 + \Omega^2/2 + \gamma^2/4}. \tag{2.79}$$

Even as the Rabi frequency increases with drive intensity ($\Omega^2 \propto E_0^2 \propto I$), the excited state population saturates and asymptotes at a level of 1/2. It is helpful to define the intensity I relative a resonant ($\Delta = 0$) saturation intensity $I_{sat,ab}$ that parameterizes the transition strength. It is the intensity that excites half of that maximum population in the steady state, where $\rho_{bb} = 1/4$. There, $\rho_{bb} = 1/(2 + \gamma^2/\Omega^2) = 1/4$, so $\Omega^2 = \gamma^2/2$ when $I = I_{sat}$. For general intensity, we write

$$\Omega^2 = \frac{\gamma^2}{2}\frac{I}{I_{sat,ab}}. \tag{2.80}$$

The intensity I is related to the electric field via

$$I = \frac{1}{2}c\varepsilon_0 E_0^2, \tag{2.81}$$

so the saturation intensity must be related to the dipole matrix element by

$$I_{sat,ab} = \frac{c\varepsilon_0\gamma^2\hbar^2}{4d_{ab}^2}, \tag{2.82}$$

[11] We verify that the response does not depend on the time-step size. Also, do not forget the minus sign that lives in the Rabi frequency definition; without it, the signs flip inappropriately in the response.

via the definition of the Rabi frequency in Eq. (2.13). The Rabi frequency depends on intensity, which may vary with a laser beam's profile. The peak intensity for a Gaussian beam occurs at the center where it can be shown that

$$I_p = \frac{2P}{\pi w_x w_z}. \tag{2.83}$$

The saturation intensity scales as $\propto 1/d_{ab}^2$. Saturation intensities for atomic systems are generally stated for fine-structure transitions. For hyperfine transitions, the saturation intensity should be modified to reflect the Clebsch-Gordan coupling coefficient of the transition.

Scattering, cooling, and trapping

The scattering rate is the excitation rate at which atoms leave $|a\rangle$ for $|b\rangle$, a rate of critical importance to experimentalists trying to perform experiments before the universe (or a PhD program) expires. The system must respect normalization at all times $1 = \rho_{aa} + \rho_{bb}$, so $\dot{\rho}_{aa} = -\dot{\rho}_{bb}$. The population of $|b\rangle$ still decays at a rate $-\gamma\rho_{bb}$, so the rate $\dot{\rho}_{aa} = \gamma\rho_{bb}$. Inserting the solution for ρ_{bb} from Eq. (2.79) and multiplying by γ,

$$r_{sc} = \frac{\gamma}{2}\frac{\Omega^2/2}{\Delta^2 + \Omega^2/2 + \gamma^2/4}. \tag{2.84}$$

The scattering rate depends on the detuning from resonance Δ. This detuning may be modified by a Doppler shift for an atom moving towards or away from a beam. An "optical molasses" [42] illuminates atoms along opposing directions detuned to the red of the transition. Only when the atom moves towards one of the beams will it see the beam Doppler shifted to the blue closer to resonance and absorb photons and their momenta opposing the motion of the atom. The range over which we may manipulate the absorption through the Doppler shift is limited by the width of the resonance. That restriction limits the minimum temperature achievable by an optical molasses to the Doppler temperature

$$\mathcal{T}_D = \frac{\hbar\gamma}{2k_B}, \tag{2.85}$$

with k_B being the Boltzmann constant.

While an optical molasses lowers the speeds of atoms, it does not trap them. A magneto-optical trap (MOT) [43] adds a magnetic field gradient into an optical molasses. On top of the preference for scattering photons opposing an atom's momentum, the spatially-varying magnetic field also introduces a spatial dependence to the force. That allows an atomic sample cooled by optical molasses to be spatially trapped, as well. The MOT is essentially an optical molasses with added spatial confinement. Still relying on the Doppler effect, it too is limited to the Doppler temperature.

2.2.9 Polarizability

The dipole's energy in the field follows the polarizability, the coefficient of the dipole energy term proportional to E_0^2 – up to a factor -1/2 (see Eq. (2.2)). The AC Stark shift produces an energy term proportional to E_0^2 with polarizability far from resonance

$$\alpha = -\frac{d_{ab}^2}{2\hbar\Delta} = \frac{1}{8}\frac{c\varepsilon_0\hbar\gamma^2}{\Delta I_{sat,ab}}. \tag{2.86}$$

To treat systems closer to resonance, one may consider expanding Eq. (2.57).

Eq. (2.86) deserves two main points of emphasis. First, the polarizability and the AC Stark shift have opposite sign. This can be a useful fact for experimentalists attempting to interface with theorists. Second, it depends on the squared dipole matrix element. Any vagaries in the coupling strength will enter there, for example through Clebsch-Gordan coefficients.

Note that the atomic unit of polarizability in SI units is [16]

$$1 \text{ a.u.} = 1.6487 \times 10^{-41} \text{ C}^2\text{s}^2/\text{kg}. \tag{2.87}$$

2.2.10 Hyperpolarizability

We have thus far described the AC Stark shift is the energy perturbation due to the interaction between the two-level system and the drive, but that is not the full story. The dipole energy of an atom is more truly a Taylor series expansion in the electric field. The treatment of the AC Stark shift thus far has neglected the next term. If we include it, we find the hyperpolarizability β.

$$\Delta U_{AC} = -\frac{1}{2}\alpha E_0^2 - \frac{1}{24}\beta E_0^4 + ... \tag{2.88}$$

A term proportional to the fourth order in the electric field, or proportional to the square of the optical intensity, arises as a result of the hyperpolarizability. Expanding Eq. (2.51) to the next order reveals such a term $\propto |\Omega|^4 \propto E_0^4$. The square root expands as $\Delta\sqrt{1+|\Omega|^2/\Delta^2} \approx \Delta(1+(1/2)|\Omega|^2/\Delta^2 - (1/8)|\Omega|^4/\Delta^4 + ...)$. Equating the final term to the hyperpolarizability term,

$$-\frac{1}{24}\beta E_0^4 = -\frac{1}{8}\hbar\frac{|\Omega|^4}{\Delta^3} = -\frac{1}{8}\frac{d_{ab}^4 E_0^4}{\hbar^3\Delta^3}, \tag{2.89}$$

we find the hyperpolarizability of the two-level system to be

$$\beta = \frac{3d_{ab}^4}{\hbar^3\Delta^3} = \frac{3}{256}\frac{c^2\varepsilon_0^2\hbar\gamma_{ab}^4}{\Delta^3 I_{sat,ab}^2}. \tag{2.90}$$

The utility of this formula is limited in this dissertation. We derive it simply identify the origin of the hyperpolarizability, a response of the atomic dipole moment that is nonlinear in the electric field, and to volunteer that it is a feature even of two-level systems.

Note that the atomic unit of hyperpolarizability in SI units is [95]

$$1 \text{ a.u.} = 6.23538 \times 10^{-65} \text{ C}^4\text{m}^4/\text{J}^3. \tag{2.91}$$

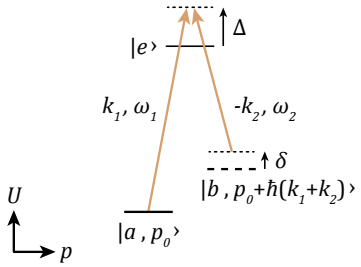

Figure 2.7: Stimulated Raman transition level diagram. The arrows represent two laser fields, whose wave vector and frequency are labeled. They couple two hyperfine ground states at different momenta.

2.3 Three-level systems

We have treated atoms as two-level systems thus far. The treatment is insightful and produces many useful results, but atoms are not two-level systems. We can deepen our understanding of atomic dynamics by carefully extending our theoretical techniques for two-level systems to three-level systems. Three-level systems are ubiquitous in this dissertation, from the atom optics we use (stiulated Raman transitions) to the very foundation of the tune-out wavelength. Treating three-level systems thoroughly here will pay dividends.

2.3.1 Stimulated Raman transitions

We begin our treatment of three-level systems by elucidating the dynamics of stimulated Raman transitions. Note that atom interferometers need to generate superpositions between only two levels, not three; one might consider driving an atom into a superposition of two electronic states, a ground and excited state. In the alkali atoms, however, the excited electronic states decay rapidly in ∼30 ns [96], so this strategy severely limits the maximum interrogation time. We should note that long-lived states excited by such single-photon transitions do present an exciting opportunity for interferometry on narrow-linewidth transitions like those in Sr [97, 65, 57, 56]. The alkalis, on the other hand, demand a different strategy.

For the alkali metals' superposed atomic states to be long-lived, we can choose to superpose two hyperfine states in the ground electronic state, here $|2S_{1/2}\rangle$.[12] Their lifetimes are a suitable $\lesssim$1 eternity. Interferometers require momentum transfer to generate separated spacetime trajectories, but coupling the hyperfine states directly with a microwave would not transfer an appreciable momentum[13]. Optical photons impart significantly more momentum, so we couple the hyperfine ground states via photons through an excited electronic state that we will try not to populate. We will consider all those three levels here.

[12] The spectroscopic notation references the quantum numbers nL_J. The $2S+1$ superscript that often precedes this notation is unnecessary for the alkali valence states we work with, since it is always 2.

[13] They couple via $M1$ magnetic dipole transitions, but not through a relatively stronger $E1$ electric dipole transition because they have the same parity.

Consider Fig. 2.7 that describes an atom in state $|a\rangle$ with another hyperfine state $|b\rangle$ available and an excited electronic state $|e\rangle$ coupled to both $|a\rangle$ and $|b\rangle$ by an electric dipole transition. Light of frequency ω_1 couples $|a\rangle$ and $|e\rangle$ with Rabi frequency Ω_1, while light of frequency ω_2 couples $|b\rangle$ and $|e\rangle$ with Rabi frequency Ω_2. The two-photon detuning from resonance is the difference between the splitting of the laser frequencies and the splitting between $|a\rangle$ and $|b\rangle$,

$$\delta \equiv (\omega_1 - \omega_2) - (\omega_b - \omega_a). \tag{2.92}$$

Fig. 2.7 is a useful guide for writing the single-photon detuning as

$$\Delta = \omega_1 - \omega_e = \omega_2 - (\omega_e - (\omega_b + \delta)) \tag{2.93}$$

so that $\Delta - \delta = \omega_2 - (\omega_e - \omega_b)$.

We can employ the strategy in Section 2.2.3 to catalogue the energies of the photon-dressed atomic states. There are three states to consider. First is the condition we will consider the initial condition $|\check{+}\rangle$, when the atom is in $|a\rangle$ and a photon of frequency ω_1 is present. Then in the intermediate state $|\check{e}\rangle$, the atom absorbs the photon ω_1 so there are no photons present and and the atom is in $|e\rangle$. Finally in $|\check{-}\rangle$, the atom emits a photon of frequency ω_2 and falls into $|b\rangle$. We move into a rotating frame by subtracting $\omega_2 + \omega_b$ from each state.

$$U_{\check{+}} = \hbar\omega_a + \hbar\omega_1 \quad \rightarrow \quad \tilde{U}_{\check{+}} = \hbar\left((\omega_1 - \omega_2) - (\omega_b - \omega_a)\right) = \hbar\delta, \tag{2.94}$$

$$U_{\check{e}} = \hbar\omega_e \quad \rightarrow \quad \tilde{U}_{\check{e}} = -\hbar\left(\omega_2 - (\omega_e - \omega_b)\right) = \hbar(\delta - \Delta), \tag{2.95}$$

$$U_{\check{-}} = \hbar\omega_2 + \hbar\omega_b \quad \rightarrow \quad \tilde{U}_{\check{-}} = 0. \tag{2.96}$$

From these, we can immediately write down the Hamiltonian in a rotating frame.

$$i\hbar\frac{d}{d\tau}|\psi\rangle = i\hbar\begin{pmatrix}\dot{\tilde{c}}_a\\ \dot{\tilde{c}}_b\\ \dot{\tilde{c}}_e\end{pmatrix} = \hbar\begin{pmatrix}\delta & 0 & e^{-i\phi_{L(1)}}\Omega_1/2\\ 0 & 0 & e^{-i\phi_{L(2)}}\Omega_2/2\\ e^{i\phi_{L(1)}}\Omega_1^*/2 & e^{i\phi_{L(2)}}\Omega_2^*/2 & \delta - \Delta\end{pmatrix}\begin{pmatrix}\tilde{c}_a\\ \tilde{c}_b\\ \tilde{c}_e\end{pmatrix}, \tag{2.97}$$

where each laser oscillator has its own laser phase $\phi_{L(i)} = \vec{k}_i \cdot \vec{z} - \omega_i t_0$.

As one could guess from the diagonal entries in the Hamiltonian, this particular rotating frame is one with rotating amplitudes defined by

$$\tilde{c}_a \equiv e^{-i\delta\tau}c_a, \tag{2.98}$$

$$\tilde{c}_b \equiv e^{i\omega_b\tau}c_b, \tag{2.99}$$

$$\tilde{c}_e \equiv e^{i(\Delta-\delta+\omega_e)\tau}c_e, \tag{2.100}$$

given that we define the null energy as $\omega_a = 0$.

Adiabatic elimination

An approximation called adiabatic elimination facilitates solving the coupled equations of Eq. (2.97). Many experimental authors describe adiabatic elimination as the assumption that $|e\rangle$ remains unpopulated. That is not a particularly accurate description of the procedure in general,[14] so here we will follow the theorists of [98] (though we will assume that Ω_1 and Ω_2 are real for simplicity). The equation for $\tilde{c}_e$ is

$$\dot{\tilde{c}}_e + i(\delta - \Delta)\tilde{c}_e = -\frac{i}{2}(e^{i\phi_{L(1)}}\Omega_1\tilde{c}_a + e^{i\phi_{L(2)}}\Omega_2\tilde{c}_b). \tag{2.101}$$

An "integrating factor" from introductory integral calculus solves this equation.

$$\tilde{c}_e = \frac{\int_0^\tau \exp\left(\int_0^{t'} i(\delta-\Delta)dt''\right)\left(-i/2(e^{i\phi_{L(1)}}\Omega_1\tilde{c}_a + e^{i\phi_{L(2)}}\Omega_2\tilde{c}_b)\right)dt'}{\exp\left(\int_0^\tau i(\delta-\Delta)dt'\right)} \tag{2.102}$$

$$= \frac{\int_0^\tau \exp\left(i(\delta-\Delta)t'\right)\left(-i/2(e^{i\phi_{L(1)}}\Omega_1\tilde{c}_a + e^{i\phi_{L(2)}}\Omega_2\tilde{c}_b)\right)dt'}{\exp\left(i(\delta-\Delta)\tau\right)} \tag{2.103}$$

$$= -\frac{i}{2}(e^{i\phi_{L(1)}}\Omega_1\tilde{c}_a + e^{i\phi_{L(2)}}\Omega_2\tilde{c}_b)\frac{\int_0^\tau \exp\left(i(\delta-\Delta)t'\right)dt'}{\exp\left(i(\delta-\Delta)\tau\right)}. \tag{2.104}$$

Adiabatic elimination consists in assuming that the dynamics of $\tilde{c}_a$ and $\tilde{c}_b$ are far slower than the rapidly evolving exponential $e^{i(\delta-\Delta)t'}$, so those terms can be treated as constants with respect to the integral over t'. The final factor integrates to

$$\left(\frac{1}{\exp\left(i(\delta-\Delta)\tau\right)}\right)\frac{\exp\left(i(\delta-\Delta)\tau\right)-1}{i(\delta-\Delta)} = \frac{1-\exp\left(-i(\delta-\Delta)\tau\right)}{i(\delta-\Delta)} \approx \frac{1}{i(\delta-\Delta)}. \tag{2.105}$$

The approximation above is a freedom afforded by adiabatic elimination, since the exponential term oscillates rapidly and averages out of the dynamics of interest. Adiabatic elimination is fundamentally an assumption about timescales, not about populations as is commonly reported. Finally, we assume that the frequencies are tuned far closer to two-photon resonance than either is to single-photon resonance, $|\delta| \ll |\Delta|$,

$$\tilde{c}_e = \frac{1}{2\Delta}(e^{i\phi_{L(1)}}\Omega_1\tilde{c}_a + e^{i\phi_{L(2)}}\Omega_2\tilde{c}_b). \tag{2.106}$$

Inserting this expression into the differential equations for $\tilde{c}_a$ and $\tilde{c}_b$, we find a two-level system

$$i\begin{pmatrix}\dot{\tilde{c}}_a\\ \dot{\tilde{c}}_b\end{pmatrix} = \begin{pmatrix}\delta + \frac{\Omega_1^2}{4\Delta} & e^{-i(\phi_{L(1)}-\phi_{L(2)})}\frac{\Omega_1\Omega_2}{2\Delta}/2\\ e^{i(\phi_{L(1)}-i\phi_{L(2)})}\frac{\Omega_1\Omega_2}{2\Delta}/2 & \frac{\Omega_2^2}{4\Delta}\end{pmatrix}\begin{pmatrix}\tilde{c}_a\\ \tilde{c}_b\end{pmatrix}. \tag{2.107}$$

[14] It is true for the particular case where no amplitude starts in the excited state, which is admittedly the case of interest. We take the opportunity to dive into the pedantry anyway.

These dynamics look just like the two-level system dynamics in Eq. (2.26), with the single-photon AC Stark shifts built in, the role of the detuning played by the two-photon detuning δ and the role of the Rabi frequency played by the two-photon Rabi frequency

$$\check{\Omega} \equiv \frac{\Omega_1 \Omega_2}{2\Delta}. \tag{2.108}$$

All the results from solving the two-level system's dynamics carry over. For example, Rabi flopping between the two levels occurs at the generalized two-photon Rabi frequency

$$\check{\Omega}' \equiv \sqrt{\delta^2 + \Omega_1^2 \Omega_2^2 / 4\Delta^2}. \tag{2.109}$$

Momentum transfer and resonance

The photon momenta k_1 and k_2 in Fig. 2.7 are opposite. This counter-propagating configuration imparts two photons' momenta to the atom along the same direction. An atom in $|a\rangle$ absorbs a photon with energy $\hbar\omega_1$ and its momentum $\hbar\vec{k}_1$, then emits a photon losing energy $\hbar\omega_2$ and its momentum $\hbar\vec{k}_2$. The full momentum kick is $\hbar(\vec{k}_1 - \vec{k}_2)$, with magnitude $\hbar(k_1 + k_2)$ because the photons propagate in opposite directions.

This transition must conserve both energy and momentum. Suppose the atom has initial momentum $p_0 = mv_0$ and final momentum $p_f = mv_f$. A photon before the transition contributes momentum $\hbar k_1$ to the total initial momentum and a different photon contributes momentum $-\hbar k_2$ to the final momentum. The momentum is conserved, so $mv_0 + \hbar k_1 = mv_f - \hbar k_2$ and $v_f = v_0 + \hbar(k_1 + k_2)/m$. The transition also conserves total energy on resonance, so $\hbar\omega_1 + \hbar\omega_a + mv_0^2/2 = \hbar\omega_2 + \hbar\omega_b + mv_f^2/2$. The photon frequencies are experimentally tunable, so we use the momentum conservation condition for v_f to solve for the laser frequency difference $\omega_1 - \omega_2$ that satisfies resonance.

$$\omega_1 - \omega_2 = \left(\omega_b + \frac{\Omega_2^2}{4\Delta} - \omega_a - \frac{\Omega_1^2}{4\Delta}\right) + \frac{\hbar(k_1 + k_2)^2}{2m} + (k_1 + k_2)v_0. \tag{2.110}$$

The laser frequency difference should not only match the ground-state hyperfine splitting (including AC Stark shifts for maximum transfer efficiency), but must also account for the recoil energy and the Doppler shift. Because the beams propagate along opposite directions, the Doppler shifts an atom sees add. An atom moving to the right sees ω_1 Doppler shifted to the red and ω_2 Doppler shifted to the blue. Those conspire to contribute with the same sign to the two-photon detuning. Any nonzero center-of-mass velocity of a sample $\langle v_0 \rangle \neq 0$ shifts the ensemble's Raman resonance to meet the Doppler shfit $(k_1 + k_2)\langle v_0 \rangle$.[15]

The difference between the Raman beams is in the microwave domain, while each is in the optical domain. Therefore, we can regard the wave numbers as effectively equivalent from the perspective of their momentum transfer

$$k \equiv \frac{|k_1| + |k_2|}{2} \approx |k_1| \approx |k_2|. \tag{2.111}$$

[15] We note this here because we will see later that our sample does launch at a velocity $\langle v_0 \rangle \sim 1$ m/s along the Raman beam axis.

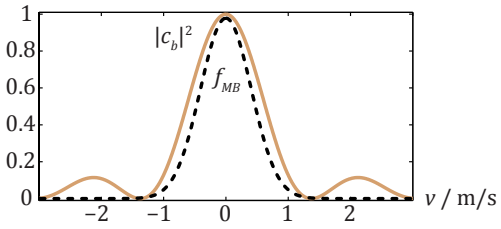

Figure 2.8: Raman response compared to thermal Doppler bandwidth. The temperature of the sample with 7-amu mass is 140 μK and the two-photon Rabi frequency shown here is 1.65 MHz for a π pulse time of 300 ns. These parameters are chosen to match the experiment in this dissertation.

Doppler broadening

We have yet to consider the effect of atoms' velocity along the direction of the Raman beams. Those velocities produce significant Doppler shifts that might push excessive velocities out of resonance. Atoms in a thermal distribution occupy a speed (along one dimension) with probability density described by the Maxwell-Boltzmann distribution

$$f_{MB}(v) = \sqrt{\frac{m}{2\pi k_B \mathcal{T}}} \exp\left(-mv^2/2k_B\mathcal{T}\right), \tag{2.112}$$

where $\mathcal{T}$ is the temperature, m is the atomic mass, and k_B is the Boltzmann constant. This is a gaussian distribution with a standard deviation

$$\sigma_v = \sqrt{\frac{k_B\mathcal{T}}{m}} \tag{2.113}$$

that sets the scale of thermal speeds. An atom with a velocity sees Doppler shifts on each of the Raman beams, so a thermal speed can readily push an atom out of resonance with the Raman transition. This is what is meant by the velocity selectivity of counter-propagating Raman transitions, analyzed in Ref. [99].

To efficiently drive Raman transitions for a whole sample, the bandwidth of the Raman pulse must rival or exceed the Doppler-broadened bandwidth of the sample. The two-photon response of an atom undergoing a stimulated Raman transition from $|a\rangle$ to $|b\rangle$ is

$$|c_b|^2 = \frac{\check{\Omega}^2}{\check{\Omega}'^2}\sin^2(\check{\Omega}'^2\tau/2) = \frac{\Omega_1^2\Omega_2^2/4\Delta^2}{\Omega_1^2\Omega_2^2/4\Delta^2+\delta^2}\sin^2\left(\sqrt{\Omega_1^2\Omega_2^2/4\Delta^2+\delta^2}\tau/2\right). \tag{2.114}$$

We let the two-photon detuning equal the Doppler shift $\delta = (k_1+k_2)v$ and plot the response to a π pulse against the Maxwell-Boltzmann distribution in Fig. 2.8 (the spectral response follows Fig. 2.4). To drive an efficient pulse, the pulse response must have bandwidth equal to or larger than the thermal distribution. To drive efficient Raman transitions in this work, we generate a high Rabi frequency by using substantial optical power concentrated in a relatively small intensity waist, achieving $\pi/2$ pulse times around 160 ns.

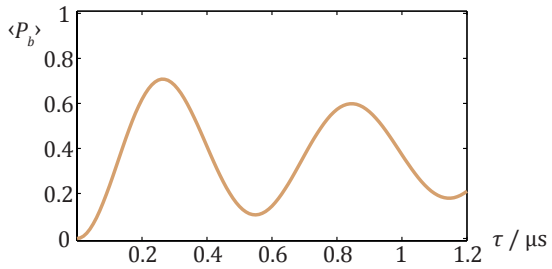

Figure 2.9: Raman pulse thermal dephasing. The temperature of the sample with 7-amu mass is 140 μK and the two-photon Rabi frequency shown here is 1.65 MHz for a π pulse time of 300 ns. These parameters are chosen to match the experiment in this dissertation.

The Doppler bandwidth of the sample is $4k\sigma_v$. One factor of 2 comes from the two, counter-propagating Raman beams and another factor of 2 helps describe the full width of the distribution from $-\sigma_v$ to $+\sigma_v$. At 140 μK, 7 amu, and 671-nm wavelength, our sample has a Doppler width about $2\pi \times 2.4$ MHz. The 300-ns π pulse has a Fourier-limited bandwidth around $2\pi \times 3.3$ MHz.

The work in [33] presents a more extreme application of this bandwidth criterion. A ^{87}Rb sample at 39°C has a Doppler bandwidth of $2\pi\times900$ GHz. Pulses with a bandwidth $2\pi\times3$ MHz near ours carve out and select particular velocity classes on which to perform an interferometer. Multiple velocity classes may be selected and interfered at one time since the pulse bandwidth is so much finer than the sample's Doppler bandwidth.

Ensemble dephasing

The thermal width of the ensemble sets the bandwidth criterion above. Nevertheless, each atom has a particular velocity from the Maxwell-Boltzmann distribution along the Raman beam axis. Each atom therefore sees different Doppler shifts on the Raman beams and a different $\delta = 2kv$. That means each atom undergoes Rabi oscillations at a different generalized Rabi frequency.[16]

$$\langle P_b \rangle = \frac{1}{\sigma_v\sqrt{2\pi}} \int_{-\infty}^{\infty} \exp(-v^2/2\sigma_v^2) \frac{\check{\Omega}^2}{\check{\Omega}^2 + 4k^2v^2} \sin^2\left(\sqrt{\check{\Omega}^2 + 4k^2v^2}\tau/2\right) dv. \tag{2.115}$$

Fig. 2.9 shows the response of an ensemble. The Rabi oscillations decohere compared to Fig. 2.4 and fail to reach a pulse transfer efficiency of 1. This dephasing is inevitable for thermal samples.

[16] The intensity profile of the Raman beams also introduces an additional inhomogeneity into the generalized Rabi frequency of the sample, but we do not consider that here. To consider that, one would need to multiply the Rabi frequency by a spatially-dependent term like term $\exp(-2z^2/w^2)$ that accounts for the intensity profile and integrate over the spatially-dependent density profile of the sample. This treatment also neglects the Stark shifts. Those add another efficiency-reducing factor in the recoil-sensitive portion of this dissertation, because that project requires tuning away from the Stark-shifted Raman resonance condition.

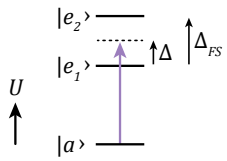

Figure 2.10: Three-level tune out. At some wavelength between the transitions called the tune-out wavelength, the Stark shifts contributed by each transition are equal and opposite, producing a vanishing ground-state polarizability and no AC Stark shift overall.

2.3.2 The tune-out wavelength: polarizability, dipole oscillations, and hyperpolarizability

To understand and predict the tune-out wavelength, we need to modify some details of the system we treated above. In the Raman transition, two ground state levels are each connected to a single excited state via an electric dipole transition. Now consider a single ground state $|a\rangle$ connected to each of two different excited states $|e_1\rangle$ and $|e_2\rangle$ with Rabi frequencies (singe-photon detunings) Ω_1 and Ω_2 (Δ and $\Delta - \Delta_{FS}$), respectively. In a rotating frame and neglecting the laser phases, the evolution follows

$$i\hbar\frac{d}{d\tau}\begin{pmatrix}\tilde{c}_a\\ \tilde{c}_{e1}\\ \tilde{c}_{e2}\end{pmatrix} = \hbar\begin{pmatrix}0 & \Omega_1/2 & \Omega_2/2\\ \Omega_1/2 & -\Delta & 0\\ \Omega_2/2 & 0 & -(\Delta-\Delta_{FS})\end{pmatrix}\begin{pmatrix}\tilde{c}_a\\ \tilde{c}_{e1}\\ \tilde{c}_{e2}\end{pmatrix}, \tag{2.116}$$

where Δ_{FS} (read fine structure) is the splitting between the two excited levels.

Polarizability and the tune-out wavelength

The ground state in the three-level system of Fig. 2.10 receives an AC Stark shift from each of the two transitions coupled. Consider light tuned between the two transitions. The light is detuned blue of the $|a\rangle \to |e_1\rangle$ transition, so that transition contributes a positive AC Stark shift to $|a\rangle$. The detuning is red of the $|a\rangle \to |e_2\rangle$ transition, so it contributes a negative AC Stark shift to $|a\rangle$. At some drive frequency between the two transitions, the AC Stark shifts are equal and opposite. That is called a tune-out wavelength.

Suppose each transition has its own saturation intensity $I_{sat,1}$ and $I_{sat,2}$ and linewidth. If we reference the detuning of the light to the $|a\rangle \to |e_1\rangle$ transition $\Delta_{e1} = \Delta$, then the detuning from the $|a\rangle \to |e_2\rangle$ transition is $\Delta_{e2} = \Delta - \Delta_{FS}$. The total AC Stark shift of the ground state from a light field with intensity I comes from the term proportional to I in the lowest eigenvalue of the Hamiltonian in Eq. (2.116),

$$\Delta U_{AC} = \frac{\hbar\Omega_{e1}^2}{4\Delta_{e1}} + \frac{\hbar\Omega_{e2}^2}{4\Delta_{e2}} = \frac{1}{4\hbar}\left(\frac{d_{e1}^2}{\Delta} + \frac{d_{e2}^2}{\Delta-\Delta_{FS}}\right)E_0^2. \tag{2.117}$$

Written as a polarizability,

$$\alpha = -\frac{2\Delta U_{AC}}{E_0^2} = -\frac{1}{2\hbar}\left(\frac{d_{a,e1}^2}{\Delta} + \frac{d_{a,e2}^2}{\Delta-\Delta_{FS}}\right). \tag{2.118}$$

In terms of saturation intensities and linewidths,

$$\Delta U_{AC} = \frac{\hbar}{8}\left(\frac{\gamma_{e1}^2}{\Delta I_{sat,1}} + \frac{\gamma_{e2}^2}{(\Delta - \Delta_{FS})I_{sat,2}}\right) I. \tag{2.119}$$

Generally, the polarizability of a state is just the sum over the polarizabilities contributed by each of its couplings and their dipole matrix elements. Any modifications to the dipole matrix element, like Clebsch-Gordan coefficients, enter as multipliers on the matrix elements in the sum above.

Tune out occurs when the total shift (or polarizability) is 0, at Δ_{TO}. If we assume that the linewidths are the same (true to 30 ppm in ^{7}Li),

$$\Delta_{TO} = \frac{\Delta_{FS}}{1 + I_{sat,1}/I_{sat,2}} = \frac{\Delta_{FS}}{1 + d_{a,e2}^2/d_{a,e1}^2}. \tag{2.120}$$

The tune-out wavelength depends on the relative strength of the two transitions, but it does not depend on the intensity of the AC Stark-shifting light. This independence of the tune-out wavelength on the light intensity is one factor that makes it a good candidate for precision measurements, since intensity is very difficult to calibrate *in situ*.

Dipole oscillations

Let us ask how the atomic dipole responds to the field when there are two transitions involved. The polarizability treatment above justifies treating each of the two-level systems independently and summing their results. The field drives drives oscillations on each transition at a frequency set by the detuning. We numerically integrate Eqs. (2.75), (2.76), and (2.77) for each of the two two-level systems separately. Fig. 2.11 shows for a general detuning that the superposed dipole oscillations have a nonzero average moment, a nonzero AC Stark shift. At tune out, the dipole oscillates but the oscillations average to a value of zero and the AC Stark shift vanishes. Even though the time-averaged dipole moment (and energy shift) vanishes, that does not mean that the dipole moment vanishes at all times.

The fact that the dipole oscillates among nonzero values even at tune out has an important consequence. The perturbed atomic wave function may have a nonzero overlap onto the excited state wave function at any given time. That overlap allows for single-photon scattering (consider the squared matrix element in Fermi's Golden Rule, for example). While the AC Stark shift vanishes at tune out, scattering does not.

The difference between the coherent and incoherent response (AC Stark shift and scattering, respectively) can be a subtle point. One might naively think that they could solve for γ^2 from the polarizability in Eq. (2.86) and input that into the scattering rate in Eq. (2.84). That would imply that the scattering rate is proportional to the polarizability and that the scattering rate should vanish at tune out when the polarizability vanishes. That implication is untrue, stemming from the fact that those results are derived for a two-level system. Extending two-level system results to three levels clearly demands caution.

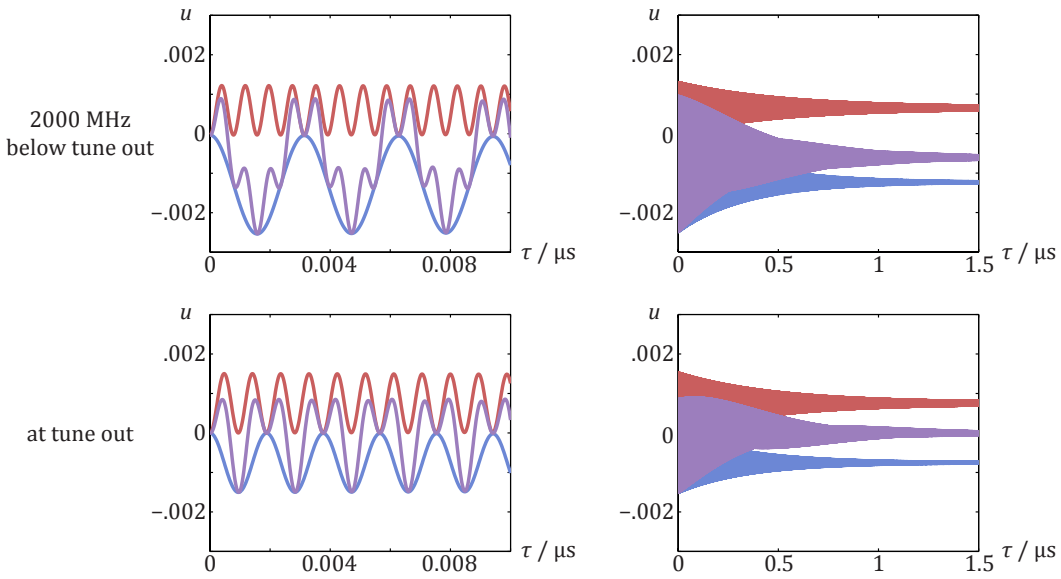

Figure 2.11: Three-level dipole response. The in-phase component u of the atomic dipole oscillates on short timescales and damps to a nonzero value at long timescales. Above: the laser is detuned 2000 MHz (-8000 MHz) from a transition with 5.87-MHz linewidth and 7.62-mW/cm^2 (3.81-mW/cm^2) saturation intensity in blue (red). Purple shows the sum of the dipole responses. Below: the laser is detuned 3333 MHz (-6667 MHz) from a transition with 5.87-MHz linewidth and 7.62-mW/cm^2 (3.81-mW/cm^2) saturation intensity in blue (red). Purple shows the sum of the dipole responses.

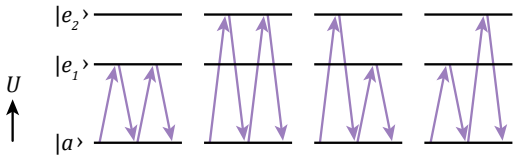

Figure 2.12: Three-level hyperpolarizability interactions. Considering the hyperpolarizability of independent two-level systems reproduces the first two four-photon interaction terms, but fails to account for the cross terms. While two-level behavior describes the polarizability and AC Stark shifts in a three-level model fairly well, treating the hyperpolarizability at tune out requires a three-level model.

Hyperpolarizability and perturbation theory

Even in the two-level system, the AC Stark shift was not the full perturbation. The hyperpolarizability quantifies a part of the response that the polarizability alone does not capture. Before calculating the hyperpolarizability of a three-level system, we should first unravel a critical feature of the hyperpolarizability from perturbation theory. It will illuminate why the hyperpolarizability of two levels does not extend to three.

Quantum mechanical perturbation theory provides the full expression for the dipole en-

ergy. It is the sum over perturbative corrections to all orders due to the perturbative interaction. Here, the perturbative interaction is the dipole interaction $\hat{V} = -\hat{\vec{d}} \cdot \vec{E}$ (an approximation itself). The first-order shift for level $|a\rangle$ in perturbation theory is $\langle a|\hat{V}|a\rangle \equiv V_{a,a}$, which we argued is 0 by a parity argument. In fact, all odd orders in perturbation theory have a factor of $V_{a,a}$, so all odd orders contribute no perturbative shift and we focus only on the even orders.

The second-order correction involves the square of the interaction matrix element between $|a\rangle$ and $|e\rangle$, $|V_{e,a}|^2/(\omega - \omega_e) = \langle a|d|e\rangle\langle e|d|a\rangle E_0^2/\hbar\Delta = \hbar\Omega^2/\Delta$, where we sum over excited states. It is the AC Stark shift for each transition. The fourth-order correction involves summing over interaction matrix elements through different intermediate states, as long as the system starts and ends in the ground state. Consider three excited levels, the maximum number that can be involved in a four-photon process, $|e_1\rangle$, $|e_2\rangle$, and $|e_3\rangle$ labeled by k, m, and n. The fourth-order shift is a sum over terms like [100]

$$\frac{V_{a,n}V_{n,m}V_{m,k}V_{k,a}}{(\omega - \omega_n)\,\omega_m(\omega - \omega_k)} \tag{2.121}$$

and

$$\frac{V_{a,k}^2}{(\omega - \omega_k)}\frac{V_{a,m}^2}{(\omega - \omega_m)^2}. \tag{2.122}$$

Each matrix element represents a single-photon coupling and the order of perturbation theory produces a term of the same order in E_0. The salient point is that the order in perturbation theory corresponds to the number of photons involved in the interaction. The AC Stark shift is a two-photon interaction that describes a photon coupling from ground state up to excited state, then back down. The hyperpolarizability involves four photons: up, down, then up and down again; or up, further up, down some, and all the way down. The two excited states involved in those couplings need not be the same. Of course, in the two-level model, only one excited state exists. In the three-level system, there are two excited levels and the excited state involved in each pair of the four-photon process can be different.

While the two-level model can describe the two effectively-two-level systems between $|a\rangle \leftrightarrow |e_1\rangle$ and $|a\rangle \leftrightarrow |e_2\rangle$, it cannot account for all the proper four-photon couplings. The two-level model reproduces the coupling terms $|a\rangle \to |e_1\rangle \to |a\rangle \to |e_1\rangle \to |a\rangle$ and $|a\rangle \to |e_2\rangle \to |a\rangle \to |e_2\rangle \to |a\rangle$, but only the three-level model can produce the cross-terms $|a\rangle \to |e_1(e_2)\rangle \to |a\rangle \to |e_2(e_1)\rangle \to |a\rangle$.

That has an important physical consequence in the hyperpolarizability of a three-level system. Adding the hyperpolarizabilities for the two two-level systems, $|a\rangle \leftrightarrow |e_1\rangle$ and $|a\rangle \leftrightarrow |e_2\rangle$, produces what would appear to be a very large hyperpolarizability even at tune out. To compute the three-level model's hyperpolarizability, we enlisted Mathematica to solve for the eigenvalues of the Hamiltonian in Eq. (2.116) and extract the term $\propto E_0^4$. The three-level model's hyperpolarizability crosses 0 at precisely the same laser frequency as the polarizability and AC Stark shift.

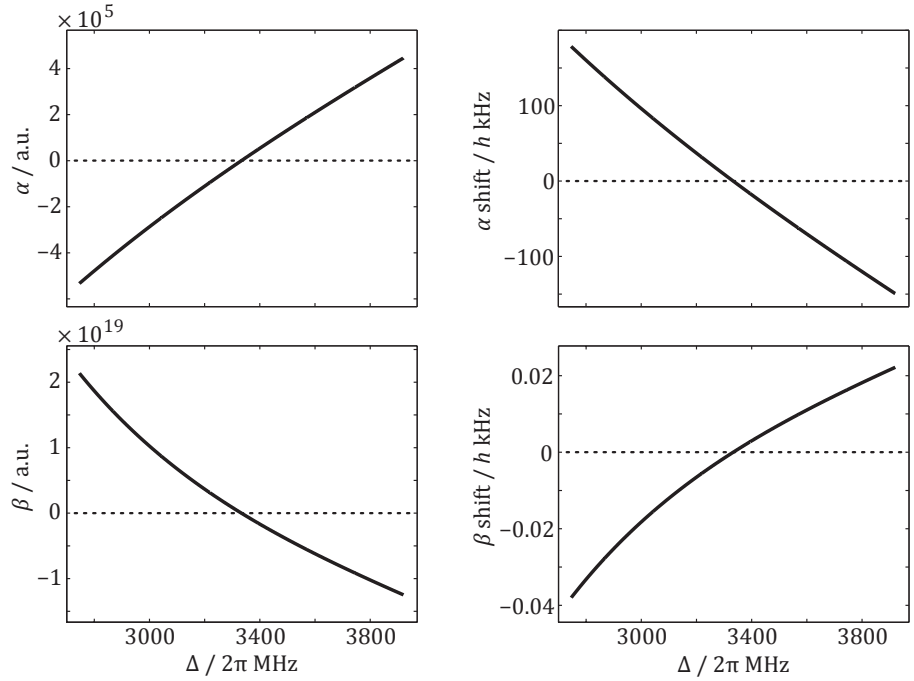

Figure 2.13: Polarizability and hyperpolarizability of a three-level system. All plots are for a system with $\Delta_{FS} = 2\pi \times 10$ GHz, $d_{a,e1} = (\sqrt{1/3})1.988 \times 10^{-29}$ C·m, and $d_{a,e2} = (\sqrt{1/3})2.812 \times 10^{-29}$ C·m. Each parameter is chosen to roughly match ^{7}Li's D-line transitions. The factor of $\sqrt{1/3}$ reflects a Clebsch-Gordan coefficient that mutes the full dipole matrix element, chosen here to reflect our tune-out measurement. The electric field that produces the polarizability and hyperpolarizability shifts on the right is chosen to match the peak field in the tune-out measurement, with 4 mW of optical power and anamorphic beam waists of 0.15 mm and 0.6 mm.

Fig. 2.13 shows the polarizability and hyperpolarizability of a three-level system. We compute each in atomic units, as well as the energy shift each term contributes given specific parameters of the light field relevant to our tune-out measurement. For a three-level system, the hyperpolarizability clearly vanishes at the same wavelength as the tune-out wavelength where the polarizability vanishes. That fact is important for measuring the tune-out wavelength. If the hyperpolarizability was nonzero at tune out, then the total dipole energy where the polarizability vanishes would have an intensity dependence because of the nonzero hyperpolarizability. In other words, the measured value of tune out would depend on intensity. Of course, hyperpolarizability still exerts an important effect away from tune out. A new generation of atomic clocks, optical lattice clocks [101, 102], trap atoms in an optical lattice to increase the possible interrogation time of the clock transition. Since there is no trapping at a tune-out wavelength, the trap light cannot be tuned to a tune-out wavelength and the hyperpolarizability must be nonzero. That introduces a perturbation on the clock transition that needs to be understood [103, 104, 105, 106, 107, 108, 109, 110].

2.4 Many levels

Atoms rarely offer clean, closed two-level or even three-level systems like those we have treated above. There are many levels that deserve consideration. Alkali atoms like lithium have electrons in closed, noble-gas-like cores that screen out the nuclear charge. With a single valence electron beyond, alkalis look much like a hydrogen atom. Hydrogenic states $|nLm_L\rangle$, with principal quantum number n, orbital angular momentum quantum number L and magnetic quantum number m, describe the alkali valence states well to a first approximation. The nuclear potential is a little different due to the increased nuclear charge and electrons in the close core shells. Even still, coupling between the magnetic field generated by the orbital motion of the valence electron and its own magnetic spin split the $|nLm_L\rangle$ states into fine-structure states $|nLJm_J\rangle$. Interaction with the small nuclear magnetic moment further splits the fine structure into a hyperfine structure $|nL_J; F, m_F\rangle$. In this section, we will extend two- and three-level system results to atomic systems with many hyperfine levels.

2.4.1 Clebsch-Gordan coefficients and coupling strengths

The presence of hyperfine and Zeeman sublevel splittings produces a menagerie of allowed transitions that affect coupling rates. To derive the details, it is customary to work in a spherical tensor basis with a basis vector index q that describes the polarization of the coupling. Any vector is a linear combination of three-dimensional basis vectors, for example the dipole moment is $\vec{d} = d_{-1}\hat{e}_{-1} + d_0\hat{e}_0 + d_1\hat{e}_1$. A "$\pi$" transition corresponds to $q = 0$, while (perhaps counterintuitively) $q = \mp 1$ describes a "$\sigma^{\pm}$" transition from m_F to m'_F with

$$m'_F + q = m_F. \tag{2.123}$$

The basis vectors in the spherical tensor basis are linear combinations of Cartesian basis vectors.

$$\hat{e}_{-1} = \hat{\sigma}^+ = \frac{1}{\sqrt{2}}\left(\hat{x} - i\hat{y}\right), \tag{2.124}$$

$$\hat{e}_0 = \hat{\pi} = \hat{z}, \tag{2.125}$$

$$\hat{e}_1 = \hat{\sigma}^- = -\frac{1}{\sqrt{2}}\left(\hat{x} + i\hat{y}\right). \tag{2.126}$$

The Rabi frequencies, AC Stark shifts, etc. all depend on the electric dipole coupling strength from the initial state $|nL_J, F, m_F\rangle$ to a state in question $|n'L'_{J'}, F', m'_F\rangle$. That matrix element is determined in part by geometry and can be written as [111]

$$\langle F, m_F|d_q|F', m'_F\rangle = \langle F||\vec{d}||F'\rangle(-1)^{F'-1+m_F}\sqrt{2F+1}\begin{pmatrix} F' & 1 & F \\ m'_F & q & -m_F \end{pmatrix}, \tag{2.127}$$

with the term in ( ) being a Wigner 3-j symbol. The hyperfine reduced dipole matrix element may be written in terms of a fine-structure reduced dipole matrix element.

$$\langle F||\vec{d}||F'\rangle = \langle J||\vec{d}||J'\rangle(-1)^{F'+J+1+I_n}\sqrt{(2F'+1)(2J+1)}\begin{Bmatrix} J & J' & 1 \\ F' & F & I_n \end{Bmatrix}, \tag{2.128}$$

with the term in { } being a Wigner 6-j symbol and I_n being the nuclear spin.

Taken together, we can write all the factors of Eqs. (2.127) and (2.128) in a coefficient C that depends on the initial J, F, m_F, final J', F', m'_F, and the polarization label q.

$$C(JFm_F; J'F'm'_F; q) = (-1)^{F'+J+1+I_n}\sqrt{(2F+1)(2F'+1)(2J+1)} \times \begin{Bmatrix} J & J' & 1 \\ F' & F & I_n \end{Bmatrix}\begin{pmatrix} F' & 1 & F \\ m'_F & q & -m_F \end{pmatrix}. \tag{2.129}$$

The coupling strength becomes

$$\langle F, m_F|d_q|F', m'_F\rangle = C(JFm_F; J'F'm'_F; q)\langle J||\vec{d}||J'\rangle \equiv C(JFm_F; J'F'm'_F; q)d_{J,J'}. \tag{2.130}$$

The coefficient C is the Clebsch-Gordan coefficient. ^{7}Li has the same structure as ^{87}Rb and shares its Clebsch-Gordan coefficients, so Ref. [111] is a sage lab partner.

Eq. (2.130) illustrates how a Clebsch-Gordan coefficient modifies the coupling strength of a hyperfine transition with respect to the overarching fine-structure transition strength. It is convenient in cold atomic physics because transition strengths are usually quoted in terms of the fine-structure reduced dipole matrix element $d_{JJ'}$. Consider the Rabi frequency for a hyperfine transition $|n_a(L_a)_{J_a}; F, m_F\rangle \to |n_b(L_b)_{J'_b}; F', m'_F\rangle$.

$$\Omega_{ab} = -\frac{1}{\hbar}\langle n_b(L_b)_{J'_b}; F'_b, m'_{F,b}|\hat{\vec{d}}\cdot\vec{E}|n_a(L_a)_{J_a}; F_a, m_{F,a}\rangle. \tag{2.131}$$

We perform the dot product in the spherical tensor basis wherein ϵ_q represent the electric field polarization components.

$$\vec{E} = E_0\sum_q \epsilon_q\hat{e}_q = E_0\left(\epsilon_{-1}\hat{e}_{-1} + \epsilon_0\hat{e}_0 + \epsilon_1\hat{e}_1\right). \tag{2.132}$$

Using the spherical tensor basis admits Clebsch-Gordan coefficients and describe the polarization with spherical tensor components represented by ϵ.

$$\Omega_{ab} = -\frac{E_0}{\hbar}\sum_q \epsilon_q\langle b|\hat{d}_q|a\rangle = -\frac{E_0}{\hbar}\sum_q \epsilon_q C(JFm_F; J'F'm'_F; q)d_{J,J'} \tag{2.133}$$

We may view the Clebsch-Gordan coefficient as modifying the reduced dipole matrix element for the transition. In other words, its square modifies the ratio $\gamma_{ab}^2/I_{sat,ab} \propto d_{J,J'}^2$. The Rabi frequency for a single polarization component may be described in terms of the fine-structure transition's dipole matrix element and a Clebsch-Gordan coefficient, analogous to Eq. (2.80).

$$\Omega_{ab,q} = -\frac{\gamma_{ab}}{\sqrt{2}}\left(\epsilon_q C(JFm_F; J'F'm'_F; q)\right)\sqrt{\frac{I}{I_{sat,ab}}}. \tag{2.134}$$

2.4.2 Raman Rabi frequency and Clebsch-Gordan interference

The presence of many levels modifies the Raman Rabi frequency we previously calculated for the three-level model in a profound way. The two-photon Rabi frequency from Eq. (2.108) involves products of two single-photon (i.e. two-level) Rabi frequencies; that is, it involves products of different Clebsch-Gordan coefficients. This is an important distinction from single-photon transitions where single Clebsch-Gordan coefficients are always squared and lose their sign. Here, it will produce interference effects in Raman Rabi frequencies.

To calculate the Raman Rabi frequency for a single state transitioning to a particular final state, we treat the processes for each polarization as advancing in parallel and add the rates [112]. The label a denotes the initial state $|n_a(L_a)_{J_a}; F_a m_{F,a}\rangle$, the label b denotes the intermediate excited state $|n_b(L_b)_{J_b'}; F_b' m_{F,b}'\rangle$, the label c denotes the final state $|n_c(L_c)_{J_c}; F_c'' m_{F,c}''\rangle$, q denotes the polarization for the first ab transition, and q' denotes the polarization for the second bc transition.

$$\check{\Omega}_{ac} = \sum_{qq',F'm_F',F''m_F''} \frac{\Omega_{ab,q}\Omega_{bc,q'}}{2\Delta_{ab}} \tag{2.135}$$

$$= \sum_{qq',F'm_F',F''m_F''} \frac{\gamma_{ab}\gamma_{bc} I}{4\Delta_{ab}\sqrt{I_{sat,ab} I_{sat,bc}}} \epsilon_{ab,q}\epsilon_{bc,q'} C(JFm_F; J'F'm_F'; q) C(J''F''m_F''; J'F'm_F'; q'). \tag{2.136}$$

We will now consider two polarizations addressing the $|2S_{1/2}, F = 2, m_F = 0\rangle$ state of the ^{7}Li atom with an unresolved $2P_{3/2}$ state and hyperfine structure. We assume that the single-photon detuning is many linewidths, so differences in single-photon detuning between different intermediate $|2P_{3/2}, F'm_F'\rangle$ are negligible.

First consider each of the Raman beams having polarization along $\hat{x} = (\hat{\sigma}^+ - \hat{\sigma}^-)/\sqrt{2}$, so that the polarization components for each are $\epsilon_{\pm 1} = \mp 1/\sqrt{2}$. The $\epsilon_{ab,q}\epsilon_{bc,q'}$ products in the sum are 1, except for when $q = 0$ or $q' = 0$, in which case the product is 0 and the term does not contribute. There are four Raman routes with nonzero Rabi frequency that add to the total two-photon Rabi frequency:

(i) the atom absorbs a σ^+ photon from $|2S_{1/2}, F = 2, m_F = 0\rangle$ to $|2P_{3/2}, F' = 2, m_F' = 1\rangle$ and emits a σ^+ photon to $|2_S1/2, F'' = 1, m_F'' = 0\rangle$,

(ii) absorbs σ^+ to $|2P_{3/2}, F' = 1, m_F' = 1\rangle$ and emits σ^+ to $|2S_{1/2}, F'' = 1, m_F'' = 0\rangle$,

(iii) absorbs σ^- to $|2P_{3/2}, F' = 2, m_F' = -1\rangle$ and emits σ^- to $|2S_{1/2}, F'' = 1, m_F'' = 0\rangle$, and

(iv) absorbs σ^- to $|2P_{3/2}, F' = 1, m_F' = -1\rangle$ and emits σ^- to $|2S_{1/2}, F'' = 1, m_F'' = 0\rangle$.

The products of Clebsch-Gordan coefficients for these routes are $\sqrt{1/8}\left(\sqrt{1/8}\right)$, $\sqrt{1/120}\left(\sqrt{5/24}\right)$, $-\sqrt{1/8}\left(\sqrt{1/8}\right)$, and $\sqrt{1/120}\left(-\sqrt{5/24}\right)$, respectively. Each term has

an equal and opposite partner and the polarization component products all have the same sign, so the sum over these terms is 0. Raman beams with parallel linear polarization do not drive a Raman transition because of destructive interference between different Raman routes.

Now, consider the Raman beams having orthogonal linear polarization, one with $\hat{x} = (\hat{\sigma}^+ - \hat{\sigma}^-)/\sqrt{2}$ and the other with $-\hat{y} = (\hat{\sigma}^+ + \hat{\sigma}^-)/\sqrt{2}$. We refer to this polarization scheme as "lin-⊥-lin". The $\epsilon_q \epsilon_{q'}$ products are 1 for $q = q' = -1$ (terms (i) and (ii) above), but -1 for $q = q' = +1$ (terms (iii) and (iv) above). These factors reverse the opposing signs in the Clebsch-Gordan products, so now the total rates add. To drive Raman transitions $|2S_{1/2}, F = 2, m_F = 0\rangle \rightarrow |2S_{1/2}, F'' = 2, m''_F = 0\rangle$, we therefore use lin-⊥-lin polarization to accommodate interference between Clebsch-Gordan coefficients.

2.4.3 Total polarizability

Calculating the total AC Stark shift for a level $|F, m_F\rangle$ also changes in the presence of many levels. Simpler than the Raman Rabi frequency calculation above, (viewed in one way) it just requires modifying the saturation intensities according to the light polarization and Clebsch-Gordan coefficients then summing over all transitions to hyperfine state $|F', m'_F\rangle$ via transition $|n(L_a)_{J_a}\rangle \rightarrow |n'(L'_b)_{J'_b}\rangle$.

$$\Delta U_{AC} = \frac{\hbar I}{4} \sum_{q,nJn'J',F'm'_F} \frac{\epsilon_q^2 C^2(JFm_F; J'F'm'_F; q)\gamma^2_{nJn'J'}}{\Delta_{nJn'J',Fm_F,F'm'_F} I_{sat,nJn'J'}}, \tag{2.137}$$

where we use the saturation intensity as opposed to an effective saturation intensity. The polarizability in this case is

$$\alpha = -\frac{c\varepsilon_0\hbar}{8} \sum_{q,nJn'J',F'm'_F} \frac{\gamma^2_{nJn'J'}}{\Delta_{nJn'J',Fm_F,F'm'_F} I_{sat,nJn'J'}} \epsilon_q^2 C^2(JFm_F; J'F'm'_F; q). \tag{2.138}$$

The atomic polarizability evidently depends beyond the detuning on the polarization of the coupling light and the hyperfine state and structure.

Experimentalists tend to be comfortable referencing tables of Clebsch-Gordan coefficients or computing them for use in the equations above. Theorists tend to find the dependence on experimental vagaries like light polarization and atomic spin polarization perturbing. They prefer to decompose the polarizability in the spherical tensor basis to terms of increasing tensor rank. In the hyperfine basis [15, 29],

$$\alpha = \alpha^s + \epsilon_C \frac{m_F}{2F} \alpha^v - \epsilon_D \frac{3m_F^2 - F(F+1)}{2F(2F+1)} \alpha^T, \tag{2.139}$$

where the factors $\epsilon_C = |\epsilon_{-1}|^2 - |\epsilon_1|^2$ and $\epsilon_D = 1 - 3|\epsilon_0|^2$ depend on polarization. The scalar (α^s), vector (α^v), and tensor (α^T) contributions to the total polarizability are written in

terms of a tensor-rank-dependent term

$$\alpha^s = \frac{1}{\sqrt{3(2F+1)}}\alpha^{(0)}, \tag{2.140}$$

$$\alpha^v = -\sqrt{\frac{2F}{(F+1)(2F+1)}}\alpha^{(1)}, \tag{2.141}$$

$$\alpha^T = -\sqrt{\frac{2F(2F-1)}{3(F+1)(2F+1)(2F+3)}}\alpha^{(2)}, \tag{2.142}$$

described by

$$\begin{aligned}\alpha^{(K)} = &\frac{1}{\hbar}(-1)^{K+F+1}(2F+1)\sqrt{2K+1} \\ &\sum_{n'J'} d^2_{nJn'J'} \sum_{F'} (-1)^{F'}(2F'+1) \begin{Bmatrix} 1 & K & 1 \\ F & F' & F \end{Bmatrix} \begin{Bmatrix} F & 1 & F' \\ J' & I_n & J \end{Bmatrix}^2 \\ &\mathrm{Re}\left(\frac{1}{\Delta_{nJn'J',Fm_F,F'm'_F} - i\gamma_{nJn'J'}/2} + \frac{1}{\omega + \omega_{nJn'J',Fm_F,F'm'_F} + i\gamma_{nJn'J'}/2}\right).\end{aligned} \tag{2.143}$$

Note that deriving this tensor description of the polarizability does not assume the RWA, while the Clebsch-Gordan approach in Eq. (2.138) does have the RWA built in by our treatment of two-level systems.

The two approaches to describing the polarizability are equivalent up to the RWA[17], so whichever provides the most convenience in each application may be preferred. If one wishes to account for Zeeman shifts, they would enter the detuning $\Delta_{Fm_F,F'm'_F}$ [28]. The theorists' approach does have the advantage of separating terms in a hierarchy of magnitudes. At most frequencies, the scalar polarizability dominates and the vector and tensor terms may be neglected. The scalar polarizability is often sufficient for computing dipole trap potentials tuned far from any resonance, for example. A precision measurement of the tune-out wavelength, however, certainly requires accounting for all the terms.

2.4.4 Total scattering

Eq. (2.84) describes the single-photon scattering rate for a two-level system, which extends very simply to many levels. It contains a squared single-photon Rabi frequency and a squared detuning. In calculating the Raman Rabi rate, products of different Clebsch-Gordan coefficients permitted the entrance of different signs in a sum and allowed for interference and cancellation. In calculating the total polarizability and AC Stark shift above, a sign may

[17] Interested readers could return to the two-level system and skip the RWA in order to derive a more exact expression for two-level systems' polarizability.

enter the detuning and different Stark shifts may cancel. The scattering rate only involves squared Rabi frequencies and squared detunings, so every term is always positive. Scattering rates always add. The total single-photon scattering rate is just the sum over the scattering rates contributed by each two-level transition in the many-level system.

$$r_{sc} = \sum_{q,n'J'F'm'_F} \frac{\gamma_{nJn'J'}}{2} \frac{\Omega^2_{q,nJFm_F,n'J'F'm'_F}/2}{\Delta^2_{q,nJFm_F,n'J'F'm'_F} + \Omega^2_{q,nJFm_F,n'J'F'm'_F}/2 + \gamma^2_{nJn'J'}/4}. \tag{2.144}$$

Written in this way, the Clebsch-Gordan coefficients and polarization components enter the Rabi frequencies, but not the linewidth that appears here as a fine-structure decay rate.

2.5 The ^{7}Li atom

What follows below is an introduction to the peculiarities of the ^{7}Li atom. This section may be considered more germane to the experimental sphere of tools in the next chapter, but consider it an interlude on the way to a description of the experiment.

2.5.1 D-line transitions

Alkali experimentalists often refer to the $|2S_{1/2}\rangle \to |2P_{1/2}\rangle$ and $|2S_{1/2}\rangle \to |2P_{3/2}\rangle$ transitions as the D_1 and D_2 lines, respectively (for historical reasons). Knowing the transition energies and strengths helps in controlling dynamics on the transitions. Fig. 2.14 shows the lowest 3 electronic energy levels of the ^{7}Li atom. Higher transitions to the $3S$ and $3P$ levels can also be useful in cooling and tune-out measurements [113, 114], but we do not consider them here.

The transition strengths determine the Rabi frequency for a given light intensity. The transition strength may be parameterized in a number of ways: the oscillator strength, the transition dipole matrix element, the saturation intensity, the line width. They are all related [90]. The tune-out measurement presented in this dissertation is primarily a measurement of the relative D-line transition strengths, so it is worth some effort to understand their practical application.

A two-level system with levels $|a\rangle$ and $|b\rangle$ decays at a rate set by the dipole matrix element d_{ab}[18]

$$\gamma_{ba} = \frac{\omega^3_{ab} d^2_{ab}}{3\pi\varepsilon_0 \hbar c^3}. \tag{2.145}$$

The ^{7}Li atom is clearly not a two-level system. In principle, the total decay rate is a weighted sum over two-level decay rates for each pair of connected levels. The Wigner-Eckart theorem

[18] The Wigner-Weiskopf derivation of this decay rate is a slick and incredibly illuminating application of quantum mechanics, a must-do for atomic physics students. It assumes that the vacuum modes of the electromagnetic field stimulate emission at a Rabi rate set by the vacuum coupling. Rich results spring forth, including the modification of decay rates in cavities or near surfaces where the mode structure of the electromagnetic field changes in response to the boundary conditions.

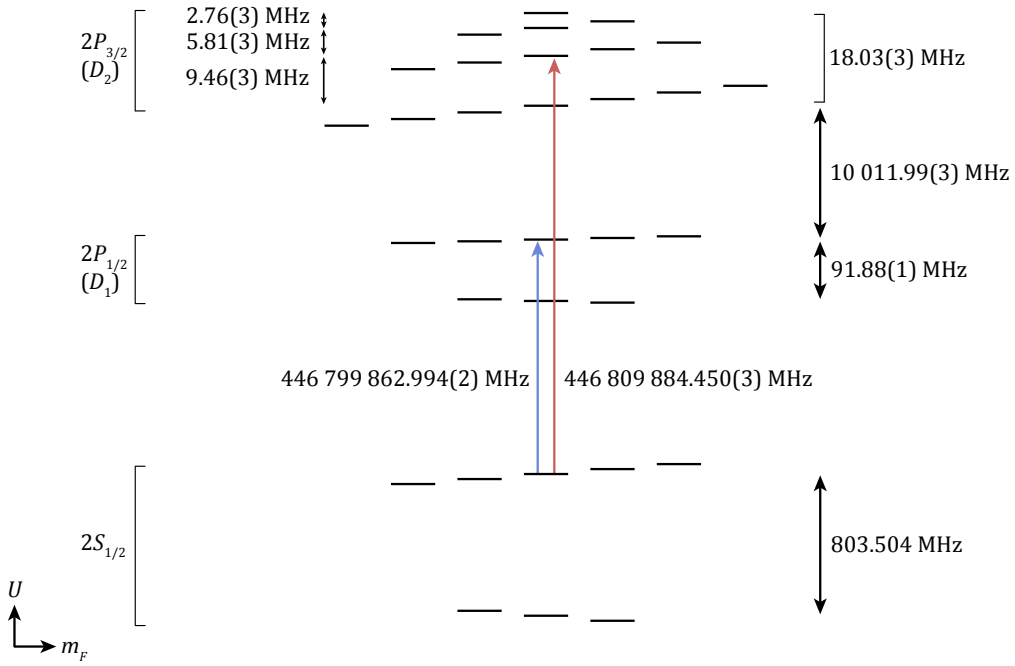

Figure 2.14: ^{7}Li energy levels and transitions. The Zeeman shifts are shown for a positive field and are drawn to scale according to g_F. The splittings between hyperfine levels are not drawn to scale. Experimental transition energies and splittings for $|2S_{1/2}, F = 2\rangle \rightarrow |2P_{1/2}, F' = 2\rangle$ and $|2S_{1/2}, F = 2\rangle \rightarrow |2P_{3/2}, F' = 2\rangle$ are from Ref. [115]. The experimental ground state hyperfine splitting of 803.504 MHz is from Ref. [116]. All frequencies here are given as cycles per time, as opposed to angular frequencies that are in radians per time.

can be used to simplify the sum for an unpolarized sample to a simple degeneracy factor of the upper and lower levels with J_u and J_l, respectively,

$$\sum_{q,F} |\langle F, m'_F + q|d_q|F', m'_F\rangle|^2 = \frac{2J_u + 1}{2J_l + 1} |\langle J_l||d||J_u\rangle|^2. \tag{2.146}$$

In this case, the decay rate is related to the reduced dipole matrix element by

$$\gamma_{ul} = \frac{\omega_{ul}^3}{3\pi\varepsilon_0\hbar c^3} \left(\frac{2J_l + 1}{2J_u + 1}\right) |\langle J_l||d||J_u\rangle|^2. \tag{2.147}$$

The reduced dipole matrix elements are therefore

$$|\langle J_l||d||J_u\rangle|^2 = d_{ul}^2 = \frac{3\hbar\varepsilon_0 c^3}{8\pi^2 f_{ul}^3} \frac{2J_u + 1}{2J_l + 1} \gamma_{ul}, \tag{2.148}$$

where $f_{ul} = \omega_{ul}/2\pi$ is the transition frequency. Clebsch-Gordan coefficients are frequently defined as multipliers of this reduced dipole matrix element [111].

Tread lightly and remain highly vigilant. Theorists tend to absorb a factor of $\sqrt{2J_l+1}$ into $|\langle J_l||d||J_u\rangle|$ [12, 16, 117]. Experimentalists tend not to absorb this factor [111, 90]. We adopt the latter convention for the purposes of this section, but we use the former convention when calculating the full polarizability using Eq. (2.143) in Sec. 5.7.1.

The ^{7}Li D-line transitions have linewidths

$$\gamma_{D2} = 2\pi \times 5.8714 \text{ MHz}, \tag{2.149}$$

$$\gamma_{D1} = 2\pi \times 5.8712 \text{ MHz}, \tag{2.150}$$

that are very nearly equal due to the similarity in the transition frequencies. The lifetime measurements presented in [96] were not even able to distinguish the small difference in lifetimes between $|2P_{1/2}\rangle$ and $|2P_{3/2}\rangle$, arriving at $1/\gamma = 27.102(7)$ ns for both. The reduced dipole matrix elements are [12][19]

$$d_{D2} = 2.812 \times 10^{-29} \text{ C}\cdot\text{m}, \tag{2.151}$$

$$d_{D1} = 1.988 \times 10^{-29} \text{ C}\cdot\text{m}. \tag{2.152}$$

Note that atomic units for dipole moments are related to SI via

$$1 \text{ a.u.} = 8.4783536 \times 10^{-30} \text{ C}\cdot\text{m}. \tag{2.153}$$

In this work, we tend to use spin-polarized atomic samples. The sum over spins in Eq. (2.146) that leads to the degeneracy simplification is no longer particularly helpful. The saturation intensities most convenient for spin-polarized samples are those that specify to a particular hyperfine transition. "The" saturation intensity, is [90]

$$I_{sat,ab} = \frac{c\varepsilon_0\gamma_{ab}^2\hbar^2}{4d_{ab}^2}. \tag{2.154}$$

This definition bears the full strength of the dipole transition. For a spin-polarized sample, however, the transition is suppressed by the Clebsch-Gordan coefficient. By the definition above, the D_1 and D_2 lines have saturation intensities of

$$I_{sat,D1} = 2.54 \text{ mW/cm}^2 \tag{2.155}$$

$$I_{sat,D2} = 1.27 \text{ mW/cm}^2 \tag{2.156}$$

The weaker D_1 transition has a saturation intensity twice that of the D_2 line because it has half the number of states.

The convenience of the relation $\Omega = \gamma\sqrt{I/2I_{sat}}$ may be preserved by building into the saturation intensity the coupling strength as modified by Clebsch-Gordan coefficients. These effective saturation intensities I_{sat}^* depend on the initial state and the polarization of the light.

[19] Reminder: here we have removed the factor of $\sqrt{2J_l+1}$ embedded in the dipole moments reported in that reference.

For the stretched-state MOT cooling transition $|2S_{1/2}, F = 2, m_F = 2\rangle \rightarrow |2P_{3/2}, F' = 3, m'_F = 3\rangle$, the Clebsch-Gordan coefficient is $\sqrt{1/2}$. That suppression factor must multiply the dipole matrix element, so the effective saturation intensity for that transition is twice as large.

$$I^*_{sat,D2,22\rightarrow 33} = 2.54 \text{ mW/cm}^2. \tag{2.157}$$

In this work, we drive Stimulated Raman transitions from $|2S_{1/2}, F = 2, m_F = 0\rangle$ to $|2S_{1/2}, F = 1, m'_F = 0\rangle$ through the $|2P_{3/2}, F' = 1, m'_F = \pm 1\rangle$ and $|2P_{3/2}, F' = 2, m'_F = \pm 1\rangle$ states. Consider the route $|2S_{1/2}, F = 2, m_F = 0\rangle \rightarrow |2P_{3/2}, F' = 1, m_F = 1\rangle \rightarrow |2S_{1/2}, F = 1, m_F = 0\rangle$, which involves stimulated absorption of a σ^+ photon from $F = 2$ and stimulated emission of a σ^+ photon from $F = 1$. The rate contributed by this route involves the product of those Clebsch-Gordan coefficients, weighted by the light amplitude in that polarization, which is $\pm 1/\sqrt{2}$ for our lin-$\perp$-lin polarization scheme that reverses some otherwise destructively interfering signs from the Clebsch-Gordan coefficients. The sum over routes yields a summed product of Clebsch-Gordan coefficients of 1/6, so the saturation intensity relevant to our Raman transitions is six times larger than the 1.27 mW/cm^2 figure.

$$I^*_{sat,\text{Raman}} = 7.62 \text{ mW/cm}^2. \tag{2.158}$$

Using this saturation intensity to calculate the two-photon Rabi frequency for for this work's 30-mW and 15-mW beams with 2.1-mm $1/e^2$ gaussian intensity waist, we arrive at a predicted $\pi/2$ pulse time of 150 ns for peak intensity. We use a 160 ns pulse time, slightly longer likely due to the intensity profile.

We use the D_1 line to optically pump the sample to the $|2S_{1/2}, F = 2, m_F = 0\rangle$. Optically pumping on the π-polarized transition involves different saturation intensities for each initial state, 7.62 (30.48) mW/cm^2 for the $m_F = \pm 2$ (± 1) states. Of course, the π transition for $m_F = 0$ is forbidden so its saturation intensity is infinite. Note, however, that off-resonant excitations to $|2P_{1/2}, F = 1, m_F = 0\rangle$ limit the steady state pumping efficiency.

The tune-out measurement couples $|2S_{1/2}, F = 2, m_F = 0\rangle$ to both $|2P_{1/2}\rangle$ and $|2P_{3/2}\rangle$ with $\sigma^\pm$ polarization. The sum over squared Clebsch-Gordan coefficients to $|2P_{3/2}\rangle$ gives 1/3, as does the sum for $|2P_{1/2}\rangle$. The effective saturation intensities for the tune-out measurement are then

$$I^*_{sat,D2,TO} = 3.81 \text{ mW/cm}^2. \tag{2.159}$$

$$I^*_{sat,D1,TO} = 7.62 \text{ mW/cm}^2. \tag{2.160}$$

These would be the saturation intensities relevant to Eq. (2.120), neglecting any hyperfine structure.

2.5.2 Mass and recoil

The ^{7}Li mass is not exactly the sum of the masses of its 3 protons, 4 neutrons, and 3 electrons, which matters for the magnitude of its photon recoil. The binding energy of the atom reduces the mass by 0.6%. The oscillation frequency of atomic ions in Penning traps

State	F	J	L	S	g_F
$2P_{3/2}$	0	3/2	1	1/2	2/3
$2P_{3/2}$	1	3/2	1	1/2	2/3
$2P_{3/2}$	2	3/2	1	1/2	2/3
$2P_{3/2}$	3	3/2	1	1/2	2/3
$2P_{1/2}$	2	1/2	1	1/2	1/6
$2P_{1/2}$	1	1/2	1	1/2	-1/6
$2S_{1/2}$	2	1/2	0	1/2	1/2
$2S_{1/2}$	1	1/2	0	1/2	-1/2

Table 2.1: ^{7}Li g factors. ^{7}Li has a nuclear spin $I_n = 3/2$.

produce fantastically precise measurements of atomic masses [118]. ^{7}Li's mass is $m_{\mathrm{Li}} = 7.0160034256(45)$ amu [119].

The momentum of a photon with wave number k kicks an atom, inducing a recoil speed

$$v_r = \frac{\hbar k}{m}. \tag{2.161}$$

For a photon tuned to the D_2 line, that recoil speed is $v_r = 8.476552$ cm/s. The formula above falls out readily from applying conservation of momentum. We may also use conservation of energy and assign an energy $\hbar\omega_r$ to the kinetic energy $mv_r^2/2$,

$$\omega_r = \frac{\hbar k^2}{2m}. \tag{2.162}$$

Again, for a photon tuned to the D_2 line, that recoil frequency is $\omega_r = 2\pi \times 63.16715$ kHz.

2.5.3 Zeeman shifts

We place lithium atoms into magnetic fields for trapping and state manipulation. Here, we compute the level shifts due to magnetic fields.

Linear Zeeman shift

The linear Zeeman shift dominates at the low field strengths used in this experiment. The energy shift of a level in a magnetic field B_b is governed by the g factor of the state and the m_F quantum number.

$$\Delta U = \mu_B g_F m_F B_b, \tag{2.163}$$

where μ_B is the Bohr mangeton. Tab. 2.1 tabulates the hyperfine g factors for the lowest three ^{7}Li electronic states. The g factors are [111]

$$g_F \approx g_J \frac{F(F+1) - I_n(I_n+1) + J(J+1)}{2F(F+1)}, \tag{2.164}$$

with

$$g_J \approx 1 + \frac{J(J+1) + S(S+1) - L(L+1)}{2J(J+1)}. \tag{2.165}$$

In the $2S_{1/2}$ ground state, $g_F = \pm 1/2$. Eq. (2.163) gives a linear Zeeman shift in the ^{7}Li ground state of

$$\left(\frac{\Delta f}{\Delta B}\right) = 0.7 \text{ MHz/G}. \tag{2.166}$$

Quadratic Zeeman shift

The ground-state hyperfine splitting is 803.504 MHz. Fig. 3.27 shows microwave transitions between the $2S_{1/2}$, $F = 1$ and 2 levels. The linear Zeeman shifts suggest a field strength of 1.3 G. The $m_F = 0 \rightarrow m'_F = 0$ transition with no linear Zeeman shift is shifted by 8.5 kHz to 803.5125 MHz. The two $m_F = 0$ levels shift in opposite directions, so the quadratic Zeeman shift is half the size of the shift on the transition.

$$\left(\frac{\Delta f}{(\Delta B)^2}\right) \approx 2.5 \text{ kHz/G}^2. \tag{2.167}$$

2.5.4 Clebsch-Gordan coefficients

We saw above how the Clebsch-Gordan coefficients are critical for predicting the dynamics and coupling rates generated by laser fields. They depend on ^{7}Li's quantum numbers, like its nuclear spin of $I_n = 3/2$ and angular momentum structure identical to ^{87}Rb. Its Clebsch-Gordan coefficients are therefore identical to those of ^{87}Rb, which can be found tabulated in [111].

2.5.5 Unresolved D_2 line

Different from most alkali atoms, ^{7}Li's D_2 is unresolved, creating some headaches in handling the atoms. The four levels of the D_2 line are all within 18 MHz of each other, insignificant compared to the 6-MHz linewidth. Addressing any specific hyperfine transition on the D_2 line becomes essentially impossible as other sublevel transitions will not have significantly different detunings and any polarization impurity can drive to the wrong Zeeman sublevel.

The lack of a closed cycling transition brings to the fore an array of complications, including inefficient cooling and detection. Detecting an an atom in a particular hyperfine ground state would benefit from a cycling transition that scatters a bunch of signal photons. Because of the unavoidability of unintended transitions, atoms may excite to unintended states and decay to unintended dark states to never provide another signal photon. Simple Monte-Carlo simulations based on excitation and decay Clebsch-Gordan coefficients suggest that our atoms scatter merely $\sim$2 D_2 photons from $|2S_{1/2}, F = 2\rangle$ before decaying to $|2S_{1/2}, F = 2\rangle$ and going dark. This number proved handy in estimating signal strengths at

Parameter	Value	Reference
ω, $\|2S_{1/2}, F=2\rangle \rightarrow \|2P_{1/2}, F'=2\rangle$	$2\pi \times 446.799862.994(2)$	[115]
ω, $\|2S_{1/2}, F=2\rangle \rightarrow \|2P_{3/2}, F'=2\rangle$	$2\pi \times 446.809884.450(3)$	[115]
$\|2S_{1/2}\rangle$ hyperfine splitting	$2\pi\times$803.5040866(10) MHz	[116]
d_{D1}	1.988×10^{-29} C·m	
d_{D2}	2.812×10^{-29} C·m	
$I_{sat,D1}$	2.54 mW/cm^2	
$I_{sat,D2}$	1.27 mW/cm^2	
γ_{D1}	$2\pi\times$5.8714 MHz	
γ_{D2}	$2\pi\times$5.8712 MHz	
$\mathcal{T}_D$	140 μK	
$\|2S_{1/2}\rangle \rightarrow \|3P_{1/2}\rangle$ wavelength	323.3576 nm	
$\|2S_{1/2}\rangle \rightarrow \|3P_{3/2}\rangle$ wavelength	323.3566 nm	
$\gamma_{3P\rightarrow 2S}$	$2\pi \times 0.1595$ MHz	[120]
$\gamma_{3P\rightarrow 3S}$	$2\pi \times 0.595$ MHz	
γ_{3P}	$2\pi \times 0.754$ MHz	
$d_{2S1/2\rightarrow 3P1/2}$	0.110×10^{-29} C·m	
$d_{2S1/2\rightarrow 3P3/2}$	0.156×10^{-29} C·m	
$I_{sat,2S1/2\rightarrow 3P1/2}$	0.613 mW/cm^2	
$I_{sat,2S1/2\rightarrow 3P3/2}$	0.305 mW/cm^2	
Nuclear spin I_n	3/2	
Mass m_{Li}	7.0160034256(45) amu	[119]
Recoil velocity v_r at 671 nm	8.4761 cm/s	
Recoil frequency ω_r at 671 nm	$2\pi \times 63.160$ kHz	
Linear Zeeman shift	$2\pi\times$700 kHz/G (for $g_F = 1/2$)	
Quadratic Zeeman shift	$2\pi\times$2.5 kHz/G^2 (for $g_F = 1/2$)	Fig. 3.27
Li core (Li$^+$) polarizability α_c	0.1883(20) a.u.=1.596(17)$\times 10^{-30}$ C·m	[16]

Table 2.2: ^{7}Li at a glance. Note that the dipole matrix elements reported here have not absorbed the factor of $\sqrt{2J_l+1}$.

some times during the course of this experiment. It is also relevant for how much repump power is required in the magneto-optical trap, about half that of the cooling light.

2.5.6 The Hylleraas basis

The lithium atom is relatively simple system in theory, with just three electrons and a nucleus. The parameters above should be calculable from theory, however, the complexity underlying those calculations is belied by even lithium's apparent simplicity.

The dynamic interactions between each of the particles make *ab initio* atomic structure calculations challenging in general. The (non-relativistic) Hamiltonian for three-electron Li

in the center-of mass frame, for example, is [18]

$$\hat{H}_0 = -\frac{1}{2\mu}\left(\sum_{i=1}^{3}\nabla_i^2\right) - \frac{1}{m_n}\left(\sum_{i>j\geq 1}^{3}\vec{\nabla}_i\cdot\vec{\nabla}_j\right) + q_n\left(\sum_{i=1}^{3}\frac{q_i}{r_i}\right) + \left(\sum_{i>j\geq 1}^{3}\frac{q_i q_j}{r_{ij}^2}\right). \tag{2.168}$$

where q_n is the nuclear charge, q_i is the charge for electron i, r_i is the distance of electron i to the nucleus, r_{ij} is the distance between electron i and electron j, and $\mu = m_n m_e/(m_n + m_e)$ is the reduced mass for nuclear mass m_n and electron mass m_e.

States of the atom solve Ψ_0 the Schrödinger equation

$$\hat{H}_0\Psi_0(\vec{r}_1,\vec{r}_2,\vec{r}_3) = E_0\Psi_0(\vec{r}_1,\vec{r}_2,\vec{r}_3). \tag{2.169}$$

The Hylleraas functions serve as the basis functions for the state:

$$\phi(\vec{r}_1,\vec{r}_2,\vec{r}_3) = r_1^{j_1}r_2^{j_2}r_3^{j_3}r_{12}^{j_{12}}r_{23}^{j_{23}}r_{31}^{j_{31}}\exp\left(-\alpha' r_1 - \beta' r_2 - \gamma' r_3\right)\mathcal{Y}^{LM_L}_{(l_1l_2)l_{12},l_3}(\hat{r}_1,\hat{r}_2,\hat{r}_3)\chi(1,2,3), \tag{2.170}$$

where a vector-coupled product of spherical harmonics $Y_{l_i,m_i}(\hat{r}_i)$ forms $\mathcal{Y}^{LM_L}_{(l_1l_2)l_{12},l_3}$ with total angular momentum L and projection M_L and $\chi(1,2,3)$ is the three-electron spin-1/2 function. The Hylleraas method is variational, optimizing the parameters to minimize the state energy. It can be applied to calculating polarizability, hyperpolarizability, long-range interatomic interaction coefficients, etc. [18].

The intention for displaying these equations is not to instruct in their usage, but rather to illustrate that simple hydrogenic wave functions underlie the Hylleraas method. Theorists can explicitly account for correlations in atomic electron dynamics by applying a variational approach to Hylleraas basis states. The Hylleraas approach is therefore expected to provide the most accurate computational results, but lithium and its numerous three electrons represent the final frontier for the method [12]. Hylleraas calculations [17, 21, 20, 121, 19, 14, 122] serve as a benchmark for other methods [12, 11, 13]. Validating the other methods against Hylleraas calculations in lithium helps to fortify confidence in applying those methods to heavier atoms.

2.6 Atom interferometers

Now that we know how to manipulate and describe the response of simple atomic systems, we turn to the behavior of atom interferometers. The theoretical machinery this section develops will aid in describing the signals of interferometers and their strength.

All interferometers separate waves along multiple paths. Upon recombination, differences in phase the waves accrue along each path translate into population differences at the output ports. Light interferometers separate light waves. Atom interferometers separate matter waves in the form of atoms.

There is an important distinction between light interferometers and atom interferometers. Photons are allowed to overlap and interfere with each other. Atoms, on the other hand,

suffer collisional interactions with each other, a consequence of their electrically charged constituents. So different atoms cannot be made to interfere with each other. Instead, an atom must interfere with itself.[20] A single atom must itself explore multiple paths that find their way back to one another so that they may interfere. This is the case at least for thermal distributions of atoms, though the notion of different atoms interfering with each other may be more applicable to Bose-Einstein condensates.[21]

In this work, we use light-pulse atom interferometry [59]. Pulses of light manipulate the matter-wave trajectories along one spatial dimension. The trajectories evolve in position as a function of time, generating distinct spacetime trajectories. Here, we investigate how beam splitters and mirrors manipulate the matter waves into producing interference terms. We start by looking at the simplest Ramsey interferometer, then we will look at simplified Mach-Zehnder and Ramsey-Bordé interferometers to establish a framework for computing interferometer output populations and contrasts. Only after will we dig more deeply into precisely how to calculate the interferometers' phases.

2.6.1 Simplified Ramsey interferometer

We begin to establish a framework for treating interferometers by considering the simplest interferometer, the Ramsey interferometer. It consists of a beam splitter, some free-evolution time, and another beam splitter. The first beam splitter $\hat{S}$ splits an initial state

$$|\psi(0)\rangle = \begin{pmatrix} c_a(0) \\ c_b(0) \end{pmatrix} = \begin{pmatrix} 1 \\ 0 \end{pmatrix} \tag{2.171}$$

into an equal superposition

$$\hat{S}(\phi_{L1})|\psi(0)\rangle = \frac{1}{\sqrt{2}} \begin{pmatrix} 1 \\ -ie^{i\phi_{L1}} \end{pmatrix}, \tag{2.172}$$

where ϕ_{L1} is the phase of the laser at this first pulse and we have neglected pulse inefficiencies like detuning. We allow the superposition to freely evolve for some time T. Assuming the atomic states are eigenstates of the Hamiltonian that describes this time evolution, $|a\rangle$ and $|b\rangle$ pick up phases $e^{-i\omega_{a,b}T}$ and we set $\omega_a = 0$.

$$\hat{U}(T)\hat{S}|\psi(0)\rangle = \frac{1}{\sqrt{2}} \begin{pmatrix} 1 \\ -ie^{i(\phi_{L1}-\omega_b T)} \end{pmatrix}. \tag{2.173}$$

After the free evolution, we apply another beam splitter to recombine the arms.

$$\hat{S}(\phi_{L2})\hat{U}(T)\hat{S}(\phi_{L1})|\psi(0)\rangle = \frac{1}{2} \begin{pmatrix} 1 - ie^{i(\phi_{L1}-\phi_{L2}-\omega_b T)} \\ -ie^{i\phi_{L2}} - ie^{i(\phi_{L1}-\omega_b T)} \end{pmatrix}, \tag{2.174}$$

[20] Of course, photons also "interfere with themselves", say when integrating interference patterns over many shots of sending a single photon through a double slit.

[21] Even then, the condensation is a result of indistinguishability. So it still may be inappropriate to look at "different" atoms as interfering with each other.

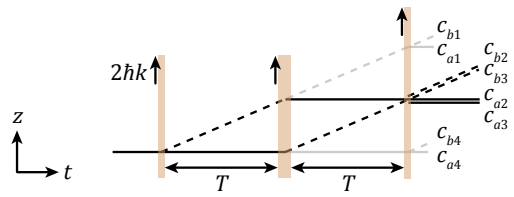

Figure 2.15: A simple Mach-Zehnder interferometer. Each c labels an amplitude in the outputs of the interferometer. Non-interfering outputs appear in light gray.

where ϕ_{L2} is the phase of the laser at the second pulse. Detecting the output into state $|b\rangle$,

$$|c_b|^2 = \frac{1}{4}\left(-ie^{i\phi_{L2}} - ie^{i(\phi_{L1}-\omega_b T)}\right)\left(ie^{-i\phi_{L2}} + ie^{-i(\phi_{L1}-\omega_b T)}\right) \tag{2.175}$$

$$= \frac{1}{4}\left(1+1+e^{i(\phi_{L1}-\phi_{L2}-\omega_b T)} + e^{-i(\phi_{L1}-\phi_{L2}-\omega_b T)}\right) = \frac{1}{2}\left(1+\cos(\Delta\phi)\right), \tag{2.176}$$

where $\Delta\phi = \phi_{L1} - \phi_{L2} - \omega_b T$ collects all the phases from lasers and free evolution. The Ramsey interferometer's phase difference compares the laser oscillator to the quantum system's energy, making it the canonical choice for clocks and spectroscopy. The main motivation here is to demonstrate how an interferometer translates phase differences between arms into population differences that oscillate with $\Delta\phi$.

In the limit of $T \to 0$, the laser oscillator has not had any chance to advance in phase and the free-evolution phase is also 0. The back-to-back $\pi/2$ pulses form a π pulse. For such a vanishing phase difference, $\Delta\phi = 0$, we would expect the population to be fully transferred to the detected state as is true for a π pulse. Indeed, the equation above produces this result.

2.6.2 Simplified Mach-Zehnder interferometer

The simple Ramsey interferometer suffers when using velocity-selective, counter-propagating stimulated Raman transitions. The photon recoil separates the arms of the interferometer and the arms' waves no longer overlap after a short evolution time, producing no observable interference. A π pulse in the center redirects the arms back toward one another, akin to a spin-echo pulse. This is a Mach-Zehnder interferometer, shown in Fig. 2.15. The diagram emphasizes that interfering output ports may have come from either of two inputs. Amplitude in c_{b2} (and c_{a2}) originates from the upper arm of the interferometer in $|a, 0\rangle$ prior to the final beam splitter, while amplitude in c_{b3} (and c_{a3}) originates from the lower arm of the interferometer in $|b, 2\hbar k\rangle$ prior to the final beam splitter.

Fig. 2.15 also emphasizes that there are truly 8 important states after the three-pulse sequence (though only 6 are distinguishable at the output due to interference), not only 2 as we assumed in the Ramsey interferometer. Augmenting the framework to account for all these levels is a bit cumbersome, but can be rewarding. The coupling between states at each pulse is a bit more complicated than merely the coupling between the two hyperfine ground states. One important feature we must demand from the framework is that it distinguishes

the pulse outputs that do interfere from the ones that do not interfere. That would avoid coupling states in the math that are not coupled in the experiment.

Labeling the outputs according to their fate at the end of the interferometer helps to distinguish the state couplings. With 2 outputs from each of 3 pulses, there are 2^3 possible routes through the three-pulse sequence, so that is the number of amplitudes we must track. The state is therefore an 8-row column vector

$$|\psi\rangle = \begin{pmatrix} c_{a1} & c_{b1} & c_{a2} & c_{b2} & c_{a3} & c_{b3} & c_{a4} & c_{b4} \end{pmatrix}^{\mathrm{T}}. \tag{2.177}$$

The initial state is in $|a\rangle$ aimed at output 4, so the initial state is

$$|\psi(0)\rangle = \begin{pmatrix} 0 & 0 & 0 & 0 & 0 & 0 & 1 & 0 \end{pmatrix}^{\mathrm{T}}. \tag{2.178}$$

While this dissertation does not employ any Mach-Zehnder interferometers for science, working through its 8×8 pulse operators provides a blueprint for extending to the four-pulse schemes we use, whose 16×16 pulse operators do not fit on the page.

We will label the pulse operators with the pulse index. The first beam splitter pulse couples output in c_{a4} to output in c_{b1}.

$$\hat{S}_{MZ1}(\phi_{L1}) = \begin{pmatrix} 1 & 0 & 0 & 0 & 0 & 0 & 0 & 0 \\ 0 & 1/\sqrt{2} & 0 & 0 & 0 & 0 & -ie^{i\phi_{L1}}/\sqrt{2} & 0 \\ 0 & 0 & 1 & 0 & 0 & 0 & 0 & 0 \\ 0 & 0 & 0 & 1 & 0 & 0 & 0 & 0 \\ 0 & 0 & 0 & 0 & 1 & 0 & 0 & 0 \\ 0 & 0 & 0 & 0 & 0 & 1 & 0 & 0 \\ 0 & -ie^{-i\phi_{L1}}/\sqrt{2} & 0 & 0 & 0 & 0 & 1/\sqrt{2} & 0 \\ 0 & 0 & 0 & 0 & 0 & 0 & 0 & 1 \end{pmatrix}. \tag{2.179}$$

The mirror pulse in the center drives two couplings. It couples output in c_{a4} to output in c_{b3} and it couples output in c_{b1} to c_{a2}.

$$\hat{M}_{MZ2}(\phi_{L2}) = \begin{pmatrix} 1 & 0 & 0 & 0 & 0 & 0 & 0 & 0 \\ 0 & 0 & -ie^{i\phi_{L2}} & 0 & 0 & 0 & 0 & 0 \\ 0 & -ie^{-i\phi_{L2}} & 0 & 0 & 0 & 0 & 0 & 0 \\ 0 & 0 & 0 & 1 & 0 & 0 & 0 & 0 \\ 0 & 0 & 0 & 0 & 1 & 0 & 0 & 0 \\ 0 & 0 & 0 & 0 & 0 & 0 & -ie^{-i\phi_{L2}} & 0 \\ 0 & 0 & 0 & 0 & 0 & -ie^{i\phi_{L2}} & 0 & 0 \\ 0 & 0 & 0 & 0 & 0 & 0 & 0 & 1 \end{pmatrix}. \tag{2.180}$$

The final beam splitter couples four pairs of states. It couples output in c_{b1} to output in c_{a1}; it couples output in c_{a2} to c_{b2} and vice versa; it couples output in c_{b3} to c_{a3} and vice versa;

and it couples output in c_{a4} to c_{b4}.

$$\hat{S}_{MZ3}(\phi_{L3}) = \frac{1}{\sqrt{2}}\begin{pmatrix} 1 & -ie^{-i\phi_{L3}} & 0 & 0 & 0 & 0 & 0 & 0 \\ -ie^{i\phi_{L3}} & 1 & 0 & 0 & 0 & 0 & 0 & 0 \\ 0 & 0 & 1 & -ie^{-i\phi_{L3}} & 0 & 0 & 0 & 0 \\ 0 & 0 & -ie^{i\phi_{L3}} & 1 & 0 & 0 & 0 & 0 \\ 0 & 0 & 0 & 0 & 1 & -ie^{-i\phi_{L3}} & 0 & 0 \\ 0 & 0 & 0 & 0 & -ie^{i\phi_{L3}} & 1 & 0 & 0 \\ 0 & 0 & 0 & 0 & 0 & 0 & 1 & -ie^{-i\phi_{L3}} \\ 0 & 0 & 0 & 0 & 0 & 0 & -ie^{i\phi_{L3}} & 1 \end{pmatrix}. \tag{2.181}$$

Neglecting the free-evolution phases between pulses, the output of the sequence is

$$\hat{S}_{MZ3}(\phi_{L3})\hat{M}_{MZ2}(\phi_{L2})\hat{S}_{MZ1}(\phi_{L1})|\psi(0)\rangle = \frac{1}{2}\begin{pmatrix} 0 & 0 & -e^{i(\phi_{L1}-\phi_{L2})} & ie^{i(\phi_{L1}-\phi_{L2}+\phi_{L3})} & -e^{i(\phi_{L2}-\phi_{L3})} & -ie^{i\phi_{L2}} & 0 & 0 \end{pmatrix}^{\mathrm{T}}. \tag{2.182}$$

For the simplest case, both the upper arm of the interferometer and the lower arm spend the same amount of time in each state, so the free-evolution phase cancels anyway.[22]

We ultimately detect atoms in $|b\rangle$, but we only want to account for interference between the contributions to $|b\rangle$ that interfere, namely c_{b2} and c_{b3}. So we compute

$$P_{MZb} = |c_{b1}|^2 + |c_{b2} + c_{b3}|^2 + |c_{b4}|^2. \tag{2.183}$$

Given perfect pulse efficiencies, the amplitudes c_{b1} and c_{b4} vanish, but noting the detected output this way helps to calculate amplitudes in four-$\pi/2$-pulse interferometers in which the interferometer necessarily outputs amplitude into non-interfering outputs. The result is

$$P_{MZb} = \frac{1}{2}\left(1 - \cos(\Delta\phi)\right), \tag{2.184}$$

where the phase difference is $\Delta\phi = \phi_{L1} - 2\phi_{L2} + \phi_{L3}$.

In the limit of $T \to 0$, there are back-to-back $\pi/2$-π-$\pi/2$ pulses that together form a 2π pulse. For such a vanishing phase difference, $\Delta\phi = 0$, we would expect the population to be fully transferred back to the initial state and remain undetected. Indeed, the equation above produces this result.

2.6.3 Simplified Ramsey-Bordé interferometer

The Ramsey-Bordé interferometer offers another solution to the Ramsey interferometer's overlap problem. Instead of sending the lower arm toward the upper arm with a mirror

[22] More exotic effects may enter through the free-evolution phases, for example the gravitational redshift integrates to a different result for each arm in vertically oriented interferometers.

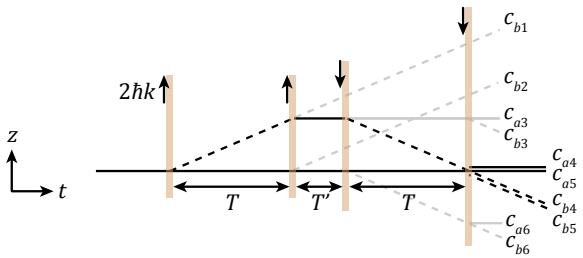

Figure 2.16: A simplified Ramsey-Bordé interferometer. Only the upper arm spends any time with the excess kinetic energy of photon recoil, so this interferometer measures the atomic recoil frequency. Each c labels an amplitude in the outputs of the interferometer. Non-interfering outputs appear in light gray.

pulse, we may first stop the recoiling upper arm and send it backwards to the lower arm. Mirror pulses are not an option for this task despite their efficiency, because the lower arm needs to retain amplitude in the stationary trajectory. Only a $\pi/2$ pulse can produce both amplitude for the upper arm to come to a stop and amplitude for the lower arm to remain stationary. This necessarily shunts amplitude into non-interfering trajectories, reducing the maximum possible contrast of the Ramsey-Bordé to 50%.[23]

There is nevertheless an advantage. Consider the trajectories in Fig. 2.16. Only the upper arm spends time with excess kinetic energy from photon recoil. In the Mach-Zehnder interferometer, that energy cancels out because both the upper arm and the lower arm spend the same amount of time with that extra energy during free evolution. The Ramsey-Bordé interferometer therefore measures the atomic recoil frequency $\omega_r = \hbar k^2/2m$.

The state is begins as a 10-row column vector

$$|\psi\rangle = \begin{pmatrix} c_{b1} & c_{b2} & c_{a3} & c_{b3} & c_{a4} & c_{b4} & c_{a5} & c_{b5} & c_{a6} & c_{b6} \end{pmatrix}^{\mathrm{T}}. \tag{2.185}$$

The initial state is in $|a\rangle$ aimed at output 5, so the initial state is

$$|\psi(0)\rangle = \begin{pmatrix} 0 & 0 & 0 & 0 & 0 & 0 & 1 & 0 & 0 & 0 \end{pmatrix}^{\mathrm{T}}. \tag{2.186}$$

[23] The simple Ramsey-Bordé shown here has a contrast of only 25%. To achieve 50%, the non-resonant outputs of the third and fourth pulses would need to get addressed by the final two pulses to form a conjugate interferometer that contributes another 25% in contrast.

The first pulse couples output in c_{a5} to output in c_{b1}.

$$\hat{S}_{RB1}(\phi_{L1}) = \begin{pmatrix} 1/\sqrt{2} & 0 & 0 & 0 & 0 & 0 & -ie^{i\phi_{L1}}/\sqrt{2} & 0 & 0 & 0 \\ 0 & 1 & 0 & 0 & 0 & 0 & 0 & 0 & 0 & 0 \\ 0 & 0 & 1 & 0 & 0 & 0 & 0 & 0 & 0 & 0 \\ 0 & 0 & 0 & 1 & 0 & 0 & 0 & 0 & 0 & 0 \\ 0 & 0 & 0 & 0 & 1 & 0 & 0 & 0 & 0 & 0 \\ 0 & 0 & 0 & 0 & 0 & 1 & 0 & 0 & 0 & 0 \\ -ie^{-i\phi_{L1}}/\sqrt{2} & 0 & 0 & 0 & 0 & 0 & 1/\sqrt{2} & 0 & 0 & 0 \\ 0 & 0 & 0 & 0 & 0 & 0 & 0 & 1 & 0 & 0 \\ 0 & 0 & 0 & 0 & 0 & 0 & 0 & 0 & 1 & 0 \\ 0 & 0 & 0 & 0 & 0 & 0 & 0 & 0 & 0 & 1 \end{pmatrix}. \tag{2.187}$$

The second pulse couples output in c_{b1} to output in c_{a3} and it couples output in c_{a5} to output in c_{b2}.

$$\hat{S}_{RB2}(\phi_{L2}) = \begin{pmatrix} 1/\sqrt{2} & 0 & -ie^{i\phi_{L2}}/\sqrt{2} & 0 & 0 & 0 & 0 & 0 & 0 & 0 \\ 0 & 1/\sqrt{2} & 0 & 0 & 0 & 0 & -ie^{i\phi_{L2}}/\sqrt{2} & 0 & 0 & 0 \\ -ie^{-i\phi_{L2}}/\sqrt{2} & 0 & 1/\sqrt{2} & 0 & 0 & 0 & 0 & 0 & 0 & 0 \\ 0 & 0 & 0 & 1 & 0 & 0 & 0 & 0 & 0 & 0 \\ 0 & 0 & 0 & 0 & 1 & 0 & 0 & 0 & 0 & 0 \\ 0 & 0 & 0 & 0 & 0 & 1 & 0 & 0 & 0 & 0 \\ 0 & -ie^{-i\phi_{L2}}/\sqrt{2} & 0 & 0 & 0 & 0 & 1/\sqrt{2} & 0 & 0 & 0 \\ 0 & 0 & 0 & 0 & 0 & 0 & 0 & 1 & 0 & 0 \\ 0 & 0 & 0 & 0 & 0 & 0 & 0 & 0 & 1 & 0 \\ 0 & 0 & 0 & 0 & 0 & 0 & 0 & 0 & 0 & 1 \end{pmatrix}. \tag{2.188}$$

The third pulse couples output in c_{a3} to output in c_{b4} and it couples output in c_{a5} to output in c_{b6}. At this point, we consider outputs aimed at c_{b1} and c_{b2} as off-resonant for these reversed Raman beams, so they remain uncoupled for the third and fourth pulses.

$$\hat{S}_{RB3}(\phi_{L3}) = \begin{pmatrix} 1 & 0 & 0 & 0 & 0 & 0 & 0 & 0 & 0 & 0 \\ 0 & 1 & 0 & 0 & 0 & 0 & 0 & 0 & 0 & 0 \\ 0 & 0 & 1/\sqrt{2} & 0 & 0 & -ie^{-i\phi_{L3}}/\sqrt{2} & 0 & 0 & 0 & 0 \\ 0 & 0 & 0 & 1 & 0 & 0 & 0 & 0 & 0 & 0 \\ 0 & 0 & 0 & 0 & 1 & 0 & 0 & 0 & 0 & 0 \\ 0 & 0 & -ie^{i\phi_{L3}}/\sqrt{2} & 0 & 0 & 1/\sqrt{2} & 0 & 0 & 0 & 0 \\ 0 & 0 & 0 & 0 & 0 & 0 & 1/\sqrt{2} & 0 & 0 & -ie^{-i\phi_{L3}}/\sqrt{2} \\ 0 & 0 & 0 & 0 & 0 & 0 & 0 & 1 & 0 & 0 \\ 0 & 0 & 0 & 0 & 0 & 0 & 0 & 0 & 1 & 0 \\ 0 & 0 & 0 & 0 & 0 & 0 & -ie^{i\phi_{L3}}/\sqrt{2} & 0 & 0 & 1/\sqrt{2} \end{pmatrix}. \tag{2.189}$$

The final pulse couples output in c_{a3} to output in c_{b3}, it couples output in c_{a4} to output in c_{b4}, it couples output in c_{a5} to output in c_{b5}, it couples output in c_{a6} to output in c_{b6}.

$$\hat{S}_{RB4}(\phi_{L4}) = \frac{1}{\sqrt{2}}\times$$
$$\begin{pmatrix} \sqrt{2} & 0 & 0 & 0 & 0 & 0 & 0 & 0 & 0 & 0 \\ 0 & \sqrt{2} & 0 & 0 & 0 & 0 & 0 & 0 & 0 & 0 \\ 0 & 0 & 1 & -ie^{-i\phi_{L4}} & 0 & 0 & 0 & 0 & 0 & 0 \\ 0 & 0 & -ie^{i\phi_{L4}} & 1 & 0 & 0 & 0 & 0 & 0 & 0 \\ 0 & 0 & 0 & 0 & 1 & -ie^{-i\phi_{L4}} & 0 & 0 & 0 & 0 \\ 0 & 0 & 0 & 0 & -ie^{i\phi_{L4}} & 1 & 0 & 0 & 0 & 0 \\ 0 & 0 & 0 & 0 & 0 & 0 & 1 & -ie^{-i\phi_{L4}} & 0 & 0 \\ 0 & 0 & 0 & 0 & 0 & 0 & -ie^{i\phi_{L4}} & 1 & 0 & 0 \\ 0 & 0 & 0 & 0 & 0 & 0 & 0 & 0 & 1 & -ie^{-i\phi_{L4}} \\ 0 & 0 & 0 & 0 & 0 & 0 & 0 & 0 & -ie^{i\phi_{L4}} & 1 \end{pmatrix}. \tag{2.190}$$

Neglecting the free-evolution phases, the output of the sequence is

$$\begin{aligned} &\hat{S}_{RB4}(\phi_{L4})\hat{S}_{RB3}(\phi_{L3})\hat{S}_{RB2}(\phi_{L2})\hat{S}_{RB1}(\phi_{L1})|\psi(0)\rangle = \\ &\quad\Big(-\frac{1}{2}ie^{i\phi_{L1}} \quad -\frac{1}{2}ie^{i\phi_{L2}} \quad -\frac{1}{4}e^{i(\phi_{L1}-\phi_{L2})} \quad \frac{1}{4}e^{i(\phi_{L1}-\phi_{L2}+\phi_{L4})} \quad \frac{1}{4}ie^{i(\phi_{L1}-\phi_{L2}+\phi_{L3}-\phi_{L4})} \\ &\quad\ \frac{1}{4}ie^{i(\phi_{L1}-\phi_{L2}+\phi_{L3})} \quad \frac{1}{4} \quad -\frac{1}{4}ie^{i\phi_{L4}} \quad -\frac{1}{4}e^{i(\phi_{L3}-\phi_{L4})} \quad -\frac{1}{4}ie^{i\phi_{L3}}\Big)^{\mathrm{T}}. \end{aligned} \tag{2.191}$$

We have again neglected the free-evolution phases between the pulses, which we treat below.

We ultimately detect atoms in $|b\rangle$, but we only want to account for interference between the contributions to $|b\rangle$ that interfere, namely c_{b4} and c_{b5}. So we compute

$$P_{RBb} = |c_{b1}|^2 + |c_{b2}|^2 + |c_{b3}|^2 + |c_{b4} + c_{b5}|^2 + |c_{b6}|^2. \tag{2.192}$$

The result is

$$P_{RBb} = \frac{3}{4} - \frac{1}{8}\left(1 - \cos(\Delta\phi)\right), \tag{2.193}$$

where the phase difference is $\Delta\phi = \phi_{L1} - \phi_{L2} + (\phi_{L3} - \phi_{L4})$.

2.6.4 Laser phase

Having seen some basic interferometer schemes their signals at detection, let us treat the phases in more detail. Above, we applied the beam splitter for a two-level system where only one laser phase is present in spite of the fact that we drive interferometers with stimulated Raman transitions that employ three-level systems. The treatment was nevertheless useful in recognizing two patterns.

- When an atom transitions from $|a\rangle \rightarrow |b\rangle$, the matter wave phase increases by the laser phase. When an atom transitions back from $|b\rangle \rightarrow |a\rangle$, the laser phase reduces the matter wave phase. This is evident from the two-level beam splitter in Eq. (2.48).
- The final interferometer phase difference contributed by the laser interactions is the sum over laser phases introduced to the upper interferometer arm minus the sum over laser phases introduced to the lower interferometer arm. These sums should be taken over the route that takes the input state to whichever output state is detected.

To be more explicit about the latter point, consider the Ramsey-Bordé interferometer in Fig. 2.16 where the state we detect is the opposite hyperfine state compared to the input state. The upper arm of the interferometer transitions $|a\rangle \rightarrow |b\rangle$ on the first pulse, $|b\rangle \rightarrow |a\rangle$ on the second pulse, $|a\rangle \rightarrow |b\rangle$ on the third pulse, but does not undergo a transition at the fourth pulse to end up in the final state we detect. The upper arm therefore requires accounting for three laser phases. The lower arm of the interferometer only transitions $|a\rangle \rightarrow |b\rangle$ at the fourth pulse to end up in the state we detect, so it requires accounting for one laser phase.

In contrast to the two-level system, stimulated Raman transitions involve the phases of two different laser beams $i \in \{1, 2\}$, each with frequency ω_i and wave vector $\vec{k}_i$. Each beam encounters the atom at position $\vec{z}_j$ and time t_j during the j^{th} pulse. The spatiotemporal laser phase is

$$\phi_{L(i)j} = \vec{k}_i \cdot \vec{z}_j - \omega_i t_j. \tag{2.194}$$

We may view each beam as addressing a two-level system, ω_1 addressing $|a\rangle \rightarrow |e\rangle$ and ω_2 addressing $|b\rangle \rightarrow |e\rangle$. When an atom absorbs a photon from field 1, its laser phase adds to the matter-wave phase. When an atom emits a photon into field 2, the laser phase reduces the matter-wave phase. A stimulated Raman transition therefore involves adding one beam's phase and subtracting the other beam's phase. Because the propagation vectors are anti-parallel, the product $\vec{k}_i \cdot \vec{z}_j$ appears with opposite sign for the two beams. To provide an example, consider the first beam splitter in any configuration above. The atom's amplitude that undergoes the first transition (i.e. the upper arm) begins at time t_1 in $|a\rangle$ and ends in $|b\rangle$, with $|k_1| > 0$ and $|k_2| < 0$ for the counter-propagating beams.

$$\phi_{L1} \rightarrow \phi_{L(1)1} - \phi_{L(2)1} = (k_1 z_1 - \omega_1 t_1) - (-k_2 z_1 - \omega_2 t_1) = (k_1 + k_2) z_1 - (\omega_1 - \omega_2) t_1. \tag{2.195}$$

The spatial phase imprinted the matter wave is that of the full momentum-transfer vector, but it is their frequency difference that adds to the temporal component. Calculating these phases also requires calculating the z position of the atom at the time of the pulse.

Experimenters may also intentionally modulate the laser phase in order to introduce a phase into the interferometer. If the laser oscillator spends time at a different frequency parameterized by ω_m, for example, the ωt term in the phase will integrate to $(\omega + \omega_m)t$ over the time spent oscillating at that frequency. Atom interferometry experiments performing gravimetry often introduce an ω_m ramped linearly in time. That chirp compensates against the interferometer phase introduced by the atoms' gravitational acceleration along the beam axis. Tuning the chirp rate to cancel the interferometer phase constitutes a measurement of

the acceleration of the atoms with respect to the apparatus. In this dissertation, we apply a constant ω_m to two pulses of a four-pulse interferometer in order to introduce a phase to a geometry with no native phase.

2.6.5 Free-evolution phase: the action

We have thus far neglected the phase the matter wave accrues between laser pulses. Broadly, the Hamiltonian drives these temporal dynamics. One must take care to consider the full Hamiltonian including: the internal state energy of the atom, any effect that perturbs that internal state energy like Zeeman shifts, and external kinetic energy. The final term is the one through which the recoil term enters the Ramsey-Bordé interferometer.

Computing the phase a matter wave accrues requires calculating the phase of the complex state amplitude. The complex amplitude c for an initial state starting at $|z_0\rangle$ to end its trajectory at $|z_f\rangle$ requires time-evolving the state like Eq. (2.10),

$$c(z_0, z_f) = \langle z_f|\hat{U}(t_f - t_0)|z_0\rangle, \tag{2.196}$$

We must derive the operator $\hat{U}(t_f - t_0)$, which we did previously only for eigenstates of the Hamiltonian. Operating on the state with the Hamiltonian may alter the state if it is not an eigenstate of the Hamiltonian. We account for this by performing $\mathcal{N}$ infinitesimal time evolutions using the Hamiltonian at each instant in time separated by dt. After each evolution, the state may change from $|z_i\rangle \to |z_{i+1}\rangle \neq |z_i\rangle$. The state $|\psi\rangle$ after the full evolution is

$$|\psi\rangle = e^{-i\hat{H}(t_f-dt)dt/\hbar} \cdots e^{-i\hat{H}(t_0+dt)dt/\hbar} e^{-i\hat{H}(t_0)dt/\hbar}|z_0\rangle \tag{2.197}$$

$$= \left(\prod_{i=1}^{\mathcal{N}} e^{-i\hat{H}(t_0+(i-1)dt)dt/\hbar}\right)|z_0\rangle. \tag{2.198}$$

The amplitude for taking a specific path $Z = \{z_0, z_1, ..., z_{\mathcal{N}-1}, z_f\}$ would be the product of all the amplitudes for arriving at each intermediate state specified by Z,

$$c(z_0, z_f; Z) = \langle z_f|e^{-i\hat{H}(t_f-dt)dt/\hbar}|z_{\mathcal{N}-1}\rangle \cdots \langle z_2|e^{-i\hat{H}(t_0+dt)dt/\hbar}|z_1\rangle\langle z_1|e^{-i\hat{H}(t_0)dt/\hbar}|z_0\rangle. \tag{2.199}$$

Feynman's path integral approach takes an egalitarian stance on which path the state takes. Each path is weighted equally, so they all interfere and their amplitudes add.

$$c(z_0, z_f) = \int c(z_0, z_f, Z)dZ. \tag{2.200}$$

To integrate over paths, each intermediate state in a path deserves its own integral, since all intermediate states are equally weighted.

$$c(z_0, z_f) = \int dz_{\mathcal{N}-1} \int dz_{\mathcal{N}-2} \cdots \int dz_2 \int dz_1 \langle z_f|e^{-i\hat{H}(t_f-dt)dt/\hbar}|z_{\mathcal{N}-1}\rangle \cdots \langle z_1|e^{-i\hat{H}(t_0)dt/\hbar}|z_0\rangle. \tag{2.201}$$

We can notate all the combinations as a product of all the integrals over the intermediate states,

$$c(z_0, z_f) = \prod_{i=1}^{\mathcal{N}} \left(\int dz_i \right) \langle z_f | e^{-i\hat{H}(t_f - dt)dt/\hbar} | z_{\mathcal{N}-1} \rangle \cdots \langle z_1 | e^{-i\hat{H}(t_0)dt/\hbar} | z_0 \rangle. \tag{2.202}$$

The Hamiltonian that concerns us generally is

$$\hat{H} = \frac{\hat{p}^2}{2m} + V(\hat{z}). \tag{2.203}$$

The potential is usually a function of position, so we write it suggestively as $V(\hat{z})$. It may be gravitational potential energy mgz, it may be a spatially-varying Zeeman shift in the presence of a magnetic field gradient $\mu_b g_F m_F B(z)$, it could be a spatially-varying AC Stark shift in the presence of a light intensity gradient like a dipole trap, etc. The full potential also includes the internal state of the atom through the atomic binding potential. A single element $\langle z_{i+1} | e^{-i\hat{H}(t)dt/\hbar} | z_i \rangle$ simplifies with a resolution of the identity $\mathbb{1} = \int |p\rangle\langle p|/2\pi$,

$$\langle z_{i+1} | e^{-i\hat{H}(t)dt/\hbar} | z_i \rangle = \frac{1}{2\pi} \int dp \langle z_{i+1} | e^{-i\left(\hat{p}^2/2m + V(\hat{z})\right)dt/\hbar} | p \rangle \langle p | z_i \rangle. \tag{2.204}$$

The momentum operator can return the eigenvalue p acting on $|p\rangle$, while the potential returns $V(x_i)$ acting on $|x_i\rangle$ and is constant with respect to the dp integral.

$$\langle z_{i+1} | e^{-i\hat{H}(t)dt/\hbar} | z_i \rangle = e^{-iV(z_i)dt/\hbar} \frac{1}{2\pi} \int dp e^{-ip^2 dt/2m\hbar} \langle z_{i+1} | p \rangle \langle p | z_i \rangle \tag{2.205}$$

$$= e^{-iV(z_i)dt/\hbar} \frac{1}{2\pi} \int dp e^{-ip^2 dt/2m\hbar} e^{ip(z_{i+1} - z_i)/\hbar} \tag{2.206}$$

The final term is a straightforward gaussian integral that yields

$$\langle z_{i+1} | e^{-i\hat{H}(t)dt/\hbar} | z_i \rangle = \left(\frac{-im}{2\pi dt} \right)^{1/2} \exp\left(i \left(\frac{1}{2} m \left(\frac{z_{i+1} - z_i}{dt} \right)^2 - V(z_i) \right) dt/\hbar \right). \tag{2.207}$$

The primary upshot for stepping this far through the derivation is to illustrate how the action – the kinetic minus potential energy integrated over time – describes the matter wave's free-evolution phase.

Eq. (2.202) prescribes integrating this result for each time step over all paths. References [123, 91, 114] provide pedagogical accounts of the procedure for performing the integral. It includes recognizing the action in the exponent, Taylor expanding paths about the classical path that minimizes the action, and neglecting higher-order terms whose phases oscillate rapidly and destructively interfere. The classical action S_{cl} dominates the result.

$$c(z_f, z_i) \propto e^{iS_{cl}/\hbar} = \exp\left(i \int_{t_0}^{t_f} (K - V) dt/\hbar \right), \tag{2.208}$$

where K is the kinetic energy and V is the potential energy along the classical trajectory. This is the prescription for calculating free-evolution phases we use when the atomic state does not remain in an eigenstate of the full Hamiltonian.

The classical action conveniently depends only on the endpoints of the trajectory in a linear potential. Gravity, for example, exerts a constant downward acceleration g. In terms of the initial and final times and positions,

$$S_{cl} = \frac{m}{2}\frac{\Delta z^2}{\Delta t} - \frac{m}{2}g(z_f + z_0)\Delta t - \frac{m}{24}g^2\Delta t^3 - \hbar\omega_s\Delta t, \tag{2.209}$$

where $\Delta z = z_f - z_0$, $\Delta t = t_f - t_0$, and ω_s describes the internal state energy including any perturbations like Zeeman or AC Stark shifts. Computing the free-evolution phases in interferometers with linear external potentials just requires classically solving for the particle trajectories between laser pulses and inserting the endpoints into the equation above.

2.6.6 Other phases

There are other phase terms that enter interferometers, but are not particularly important for this dissertation. We mention a few here merely to round out the introduction to atom interferometry.

If the arms of the interferometer do not perfectly overlap at the end of the interferometer, an additional matter-wave phase difference enters given by the average of the arms' momenta $\bar{p}$ and their spatial separation Δz [59]. That is often called the separation or overlap phase.

$$\Delta\phi_{sep} = \bar{p}\Delta z. \tag{2.210}$$

This lack of overlap may result from a gravity gradient, in which the upper arm of the interferometer spends more time accelerating at a lower gravitational acceleration than the lower arm. One may also intentionally change the latter pulse separation T time with respect to the first pulse separation time. That would change the phase because the trajectories do not perfectly close. This technique is sometimes employed, not to measure phases, but to trace out contrast envelopes that herald the "size" of the matter wave packet, which decreases with temperature.

Just like the ring laser gyroscope, a Sagnac phase enters when two arms of an interferometer enclose a spatial area $\vec{A}$, whose direction is given by the unit vector normal to the enclosed area. The Sagnac phase enters when this area has any component parallel to an angular momentum $\vec{\Omega}$, [53, 54]

$$\Delta\phi_{Sag} = \frac{2m}{\hbar}\vec{A}\cdot\vec{\Omega}. \tag{2.211}$$

There also exist finite-pulse effects that account for the difference between the actual phase imprinted by the atom-laser interactions and our assumption of infinitesimally-short pulses [94]. It is rather impressive that these phases are not a larger issue, given that the laser oscillators span huge number of cycles during the course of a single pulse. Of course, the

temporal phase that really matters is the difference between the Raman beams' frequencies as evinced by Eq. (2.194). For our 160-ns pulses and 800-MHz frequency difference, that is still $\gtrsim 100$ cycles. Instability in the Raman beam intensities or pulse shape and duration[24] may introduce instability in the phases from finite-pulse effects. That may be a source of phase noise in the interferometers in this dissertation that limits our achievement of the atom-snot-noise limit.

2.6.7 Raman Ramsey-Bordé phase

The interferometer geometry employed in this dissertation to measure the lithium recoil frequency is the Ramsey-Bordé interferometer, generated with stimulated Raman atom optics. We fully treat the phase of that interferometer here.

To close a Ramsey-Bordé interferometer, whose spacetime diagram is shaped like an isosceles trapezoid, the momentum transfer must reverse for the third and fourth pulses with respect to the first and second pulses. That reverses the sign of the dot product $\vec{k}\cdot\vec{z}$ in the laser phases. To write the laser phases, we must tabulate the positions. We consider an interferometer axis perpendicular to gravity so the trajectories are not accelerated. The subscript u denotes positions for the upper arm of the interferometer and v denotes those for the lower arm.

$$z_{u1} = 0 \tag{2.212}$$
$$z_{u2} = 2v_rT \tag{2.213}$$
$$z_{u3} = 2v_rT \tag{2.214}$$
$$z_{u4} = 0 \tag{2.215}$$
$$z_{l1} = z_{l2} = z_{l3} = z_{l4} = 0 \tag{2.216}$$

The pulses occur at times $t_1 = 0$, $t_2 = T$, $t_3 = T + T'$, and $t_4 = 2T + T'$. The total laser phase difference is

$$\begin{aligned}\Delta\phi_{RBL} =&(k_1\cdot 0 - \omega_1\cdot 0) - (-k_2\cdot 0 - \omega_2\cdot 0)\\ &- (k_1(2v_rT) - \omega_1 T) + (-k_2(2v_rT) - \omega_2 T)\\ &+ (-k_1(2v_rT) - \omega_1(T+T')) - (k_2(2v_rT) - \omega_2(T+T'))\\ &- [(-k_1\cdot 0 - \omega_1(2T+T') - (k_2\cdot 0 - \omega_2(2T+T'))] \qquad (2.217)\\ =&-8kv_rT + 2(\omega_1-\omega_2)T = -16\omega_rT + 2(\omega_1-\omega_2)T \qquad (2.218)\end{aligned}$$

Any sign directly in front of a k denotes its propagation direction, any sign in front of a parenthesis denotes a photon absorption (+) or emission (−) and the term in brackets contains the laser phase of the lower arm that we subtract from the total phase difference compared to the upper arm to get the phase difference.

[24] These could easily be effects that drift due to thermal effects in the switch AOMs.

The classical action along each leg of the interferometer is

$$S_{u12} = m(4v_r^2T^2)/2T - \hbar\omega_b T, \tag{2.219}$$
$$S_{u23} = 0, \tag{2.220}$$
$$S_{u34} = m(4v_r^2T^2)/2T - \hbar\omega_b T, \tag{2.221}$$
$$S_{l14} = 0, \tag{2.222}$$

assuming $\omega_b = 0$. The total free-evolution phase is then

$$\Delta\phi_{RBFE} = (S_{u12} + S_{u23} + S_{u34} - S_{l14})/\hbar = 4v_r^2T/\hbar - 2\omega_b T = 8\omega_r T - 2\omega_b T. \tag{2.223}$$

The full Raman Ramsey-Bordé phase is

$$\Delta\phi_{RB} = \Delta\phi_{RBL} + \Delta\phi_{RBFE} = -8\omega_r T + 2\delta T. \tag{2.224}$$

Had we included an acceleration $-g$, then the positions would evolve parabolically as $z_{u2} \to 2v_rT - gT^2/2$ or $z_{l4} \to -g(2T + T')^2/2$, for example. In that case,

$$\Delta\phi_{RB} \to -8\omega_r T - 2kg(T + T')T + 2\delta T, \tag{2.225}$$

an algebraic exercise left to the reader.

Note that the two-photon detuning here $\delta = \omega_1 - \omega_2 - \omega_b$ references ω_b with the Raman light off since we restrict our treatment of matter-wave phases using the action to the time between the pulses. That is, the AC Stark shifts from the Raman pulses do not enter the phase of the interferometer, though it may include remaining effects like Zeeman shifts. One may worry that the AC-Stark-shifted internal energy during the pulses should still be integrated up in the interferometer phase. That may be true, but the effect scales with the pulse time, not the pulse separation times. We therefore categorize that as a finite pulse effect that offsets the overall phase of the interferometer but does not affect the scaling with T or T'. This effect introduces some small phase noise if the timing or intensity of the Raman beams is not controlled well.

Not all Ramsey-Bordé interferometers use Raman transitions. They may use Bragg transitions for which the internal state of the atoms does not change as a result of the pulse [72, 124]. In those cases, the internal state energy component of the $2\delta T$ phase vanishes. A $2(\omega_1 - \omega_2)T$ phase remains. The laser frequency difference should nevertheless closely match the kinetic energy difference. For an atom starting at rest, $\omega_1 - \omega_2 = 4\omega_r T$ to operate on resonance, but then then laser phase and the free-evolution phase exactly cancel. A small modulation on the laser frequencies or a noisy acceleration phase could restore a measurable phase.

Simultaneous conjugate Raman Ramsey-Bordé phase

This dissertation also utilizes a conjugate Ramsey-Bordé interferometer. In fact, the conjugate interferometer is driven unavoidably due to the high-bandwidth pulses. Upon reversing

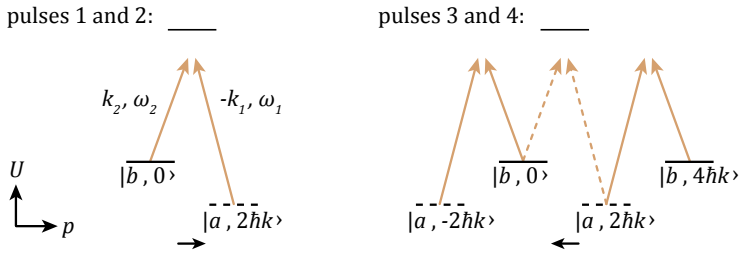

Figure 2.17: Raman transitions with reversed $\vec{k}_{1,2}$. Reversing the wave vectors to close a Ramsey-Bordé interferometer makes possible a transition to higher momentum that is ordinarily out of resonance due to its different Doppler shift. Our fast pulses drive both transitions. Note that the roles of $|a\rangle$ and $|b\rangle$ are reversed here with respect to those in Fig. 2.7 because that is how this dissertation's interferometer operates. This chapter, however, assumes that $\omega_a < \omega_b$. Section 4.2 discusses how the associated correction is just a reversal of the δ phase term.

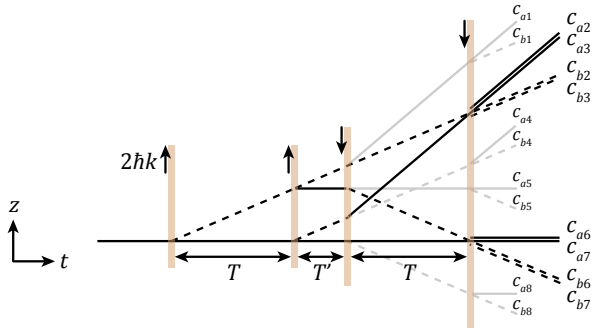

Figure 2.18: Simultaneous conjugate Ramsey-Bordé interferometers. High-bandwidth pulses simultaneously drive both interferometers unavoidably.

$\vec{k}_1$ and $\vec{k}_2$, not only may an atom in $|a, 0\rangle$ transition to $|b, -2\hbar k\rangle$ as intended, but a transition from $|b, 2\hbar k\rangle$ to $|a, 4\hbar k\rangle$ opens as Fig. 2.17 shows. The Doppler resolution between these transitions' resonances, $16\omega_r$, is well within the pulse bandwidth ~3 MHz. Driving this transition leads to closing another interferometer whose spacetime diagram is an inverted and sheared trapezoid shown in Fig. 2.18.

The conjugate interferometer has positions

$$z'_{u1} = 0, \tag{2.226}$$
$$z'_{u2} = 2v_rT, \tag{2.227}$$
$$z'_{u3} = 2v_r(T + T'), \tag{2.228}$$
$$z'_{u4} = 2v_r(2T + T'), \tag{2.229}$$
$$z'_{l1} = z'_{l2} = 0, \tag{2.230}$$
$$z'_{l3} = 2v_rT', \tag{2.231}$$
$$z'_{l4} = 2v_rT' + 4v_rT = 2v_r(2T + T'). \tag{2.232}$$

The total laser phase difference is

$$\begin{aligned}\Delta\phi'_{RBL} =&(k_1 \cdot 0 - \omega_1 \cdot 0) - (-k_2 \cdot 0 - \omega_2 \cdot 0)\\ &- \Big[(k_1 \cdot 0 - \omega_1 T) - (-k_2 \cdot 0 - \omega_2 T)\\ &\quad - (-k_1(2v_rT') - \omega_1(T + T')) + (k_2(2v_rT') - \omega_2(T + T'))\\ &\quad + (-k_1 \cdot (2v_r(2T + T')) - \omega_1(2T + T')) - (k_2 \cdot (2v_r(2T + T')) - \omega_2(2T + T'))\Big]\end{aligned} \tag{2.233}$$
$$=4(k_1 + k_2)v_rT + 2(\omega_1 - \omega_2) = 16\omega_rT + 2(\omega_1 - \omega_2)T \tag{2.234}$$

The classical action along each leg of the interferometer is

$$S'_{u14} = m(v2_r(2T + T'))^2/2(2T + T') - \hbar\omega_b(2T + T') = \hbar(4\omega_r(2T + T') - \omega_b(2T + T'), \tag{2.235}$$
$$S'_{l12} = 0, \tag{2.236}$$
$$S'_{l23} = m(2v_rT')^2/2T' - \omega_bT', \tag{2.237}$$
$$S'_{l34} = m(4v_rT)^2/2T. \tag{2.238}$$

The total free-evolution phase is then

$$\Delta\phi'_{RBFE} = (S'_{u14} - S'_{l12} - S'_{l23} - S'_{l34})/\hbar = 8\omega_rT - 2\omega_bT - 16\omega_rT = -8\omega_rT - 2\omega_bT. \tag{2.239}$$

The full conjugate Raman Ramsey-Bordé phase is

$$\Delta\phi'_{RB} = \Delta\phi'_{RBL} + \Delta\phi'_{RBFE} = 8\omega_rT + 2\delta T. \tag{2.240}$$

Had we included an acceleration $-g$,

$$\Delta\phi'_{RB} \to 8\omega_rT - 2kg(T + T')T + 2\delta T, \tag{2.241}$$

another algebraic exercise left to the reader.

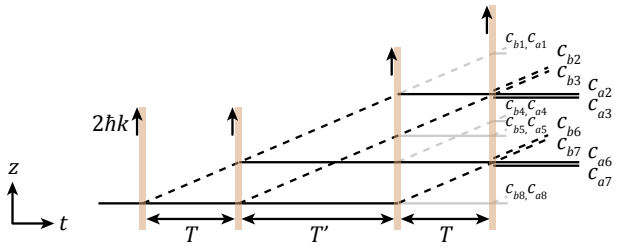

Figure 2.19: Four-pulse Mach-Zehnder interferometer.

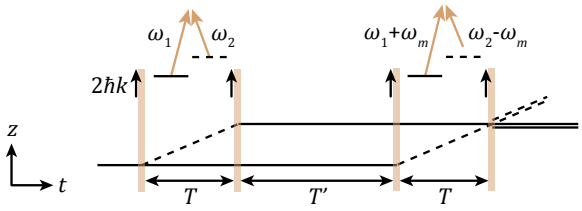

Figure 2.20: Lower four-pulse Mach-Zehnder interferometer with modulation. The laser frequencies both step by ω_m for the final two pulses.

2.6.8 Four-pulse Mach-Zehnder phase

This dissertation employs an interferometer related to the Ramsey-Bordé in order to measure ^{7}Li's red tune-out wavelength. Also four $\pi/2$ pulses, but without a k-vector reversal, we term this one the "four-pulse Mach Zehnder" and treat its phase here.

The Ramsey-Bordé interferometer brought the upper and lower arms back together by stopping the upper arm and sending it back towards the lower arm. An alternative is to send the lower arm toward the upper arm as in the Mach-Zehnder interferometer. The arms of the Mach-Zehnder are always in opposite hyperfine states, but the tune-out measurement will need an interferometer that offers time during which the arms are in the same internal state. We can simply split the Mach-Zehnder's π pulse into two $\pi/2$ pulses [125]. This interferometer has four pulses like the Ramsey-Bordé, but the k vectors never reverse.

Fig. 2.19 shows this four-pulse Mach-Zehnder interferometer. The pulses close two simultaneous interferometers. Both arms of each simultaneous interferometer are in a different hyperfine state during T'. We are interested only in the lower interferometer isolated in Fig. 2.20, whose spacetime diagram outlines a flat rhombus.

The positions are

$$z_{u1} = 0, \tag{2.242}$$
$$z_{u2} = z_{u3} = z_{u4} = 2v_rT, \tag{2.243}$$
$$z_{l1} = z_{l2} = z_{l3} = 0, \tag{2.244}$$
$$z_{l4} = 2v_rT. \tag{2.245}$$

Without any additional phases, the phase difference of this interferometer would be 0. We introduce a small modulation ω_m to the laser frequencies for the third and fourth pulses to

imprint a controlled phase onto the interferometer. Beginning the modulation at the third pulse forces the laser oscillators to advance in temporal phase at modified rates for the final T between the third and fourth pulses.[25] The wave numbers also change, but we give each beam an equal and opposite modulation to avoid any modification to the recoil energy and a spatial separation phase $(k_1+k_2) \to (k1+\omega_m/c+k_2-\omega_m/c) = (k_1+k_2)$. The laser phase is then

$$\begin{aligned}\Delta\phi_{FPMZL} =&(k_1\cdot 0-\omega_1\cdot 0)-(-k_2\cdot 0-\omega_2\cdot 0)\\ &-(k_1(2v_rT)-\omega_1 T)+(-k_2(2v_rT)-\omega_2 T)\\ &+(k_1(2v_rT)-\omega_1(T+T')-(\omega_1+\omega_m)T)\\ &-(-k_2(2v_rT)-\omega_2(T+T')-(\omega_2-\omega_m)T)\\ &-[(k_1\cdot 0-\omega_1(T+T')-(-k_2\cdot 0-\omega_2(T+T'))] \qquad (2.246)\\ =&-2\omega_m T \qquad (2.247)\end{aligned}$$

The difference in action along these trajectories is 0 in the absence of an acceleration, so the full phase is

$$\Delta\phi_{FPMZ} = -2\omega_m T. \qquad (2.248)$$

With an acceleration,

$$\Delta\phi_{FPMZ} \to -2kgT(T+T')-2\omega_m T. \qquad (2.249)$$

The sensitivity to acceleration was the impetus for this interferometer's first application at ONERA, where it was combined with Bloch oscillations to measure gravitational acceleration [125]. We use it in this dissertation to different effect.

Notice that the internal energies cancel in this interferometer since each arm spends the same amount of time in each internal state. We will perturb those energies and their cancellation in the tune-out measurement. An intensity gradient across the arms will introduce a difference in the internal energies that integrates up over the time of an AC Stark-shifting pulse.

2.6.9 Interferometer contrast

It is helpful – for planning experiments, projecting their sensitivity, and performing diagnostics – to estimate the expected contrast of interferometers. The contrast of an interferometer describes the amplitude of population oscillations from interference effects. It is half the difference between the maximum and minimum normalized populations, divided by the average.

$$\mathcal{C} = \frac{\max(P_b)-\min(P_b)}{\max(P_b)+\min(P_b)}. \qquad (2.250)$$

[25] The laser frequencies may switch to the modified frequency any time between the second and third pulses. The extra temporal phase from extra oscillation time cancels out.

This factor multiplies the $\cos(\Delta\phi)$ term in any interferometer output signal. For the Mach-Zehnder interferometer, this can be 100% for perfectly efficient pulses [126]. For the Ramsey-Bordé (or four-pulse Mach-Zehnder), it is 50% or less due to wasted beam splitter outputs that do not contribute to the interference signal.

Modeling interferometer contrast can be an integral part of projecting signals from new experiments or understanding noise and decay in mature experiments. The formalism presented in Section 2.6.3, for example, establishes a foundation from which to predict interferometer contrast. Inefficiencies in the beam splitters can be accounted for by calculating pulse efficiencies via a model like Eq. (2.115). Alternatively, one may perform Monte Carlo simulations of pulse transfer probabilities given an initial atom velocity and location in the intensity profile, each of which modifies the generalized Rabi frequency and pulse transfer probability at the experimentally fixed pulse length. The latter is a more powerful method as it allows accounting for different pulse efficiencies at each pulse, since atoms' thermal velocities cause them to wander to experience different intensities for different pulses.

Fig. 2.16 shows the output amplitudes for a simple Ramsey-Bordé interferometer. The maximum probability of detecting state $|b\rangle$ occurs when all the interference amplitude ends up in c_{b4} and c_{b5}, leaving no amplitude in c_{a4} or c_{a5}. The minimum occurs when all that amplitude diverts to c_{a4} and c_{a5} and none appears in c_{b4} or c_{b5}. Consider the pulse efficiencies along the way for ending up at c_{b4}. The atom must transfer from $|a\rangle \to |b\rangle$ at pulse 1 with efficiency η_{ab1} (ala Eq. (2.114), for example); then it must transfer from $|b\rangle \to |a\rangle$ at pulse 2 with efficiency η_{ba2}; then it must transfer from $|a\rangle \to |b\rangle$ at pulse 3 with efficiency η_{ab3}. So the maximum probability of arriving at output $b4$ is $\eta_{ab1}\eta_{ba2}\eta_{ab3}$, when pulse 4 diverts no amplitude to c_{a4} from c_{b4}. Similar reasoning produces the maximum probability for ending up in output $b5$: $\eta_{aa1}\eta_{aa2}\eta_{aa3}\eta_{ab4}$. Those signals add. The probabilities of detecting the non-interfering outputs cancel in the contrast's numerator and add in the denominator. The probability of ending up in output $b1$ is $\eta_{ab1}\eta_{bb2}$; the probability for output $b2$ is $\eta_{aa1}\eta_{ab2}$; the probability for output $b3$ is $\eta_{ab1}\eta_{ba2}\eta_{aa3}\eta_{ab4}$; the probability for output $b6$ is $\eta_{aa1}\eta_{aa2}\eta_{ab3}\eta_{bb4}$. The predicted contrast would be

$$\mathcal{C}_{RB} = \frac{\eta_{ab1}\eta_{ba2}\eta_{ab3} + \eta_{aa1}\eta_{aa2}\eta_{aa3}\eta_{ab4}}{\eta_{ab1}\eta_{ba2}\eta_{ab3}+\eta_{aa1}\eta_{aa2}\eta_{aa3}\eta_{ab4}+\eta_{ab1}\eta_{bb2}+\eta_{aa1}\eta_{ab2}+\eta_{ab1}\eta_{ba2}\eta_{aa3}\eta_{ab4}+\eta_{aa1}\eta_{aa2}\eta_{ab3}\eta_{bb4}}. \tag{2.251}$$

Perfect beam splitter efficiencies produce an output probability of $3/4 - \cos(\Delta\phi))/8$ as derived in Section 2.6.3. We could also parameterize this signal with a background probability $\mathcal{B}$ around which the population oscillates and the contrast $\mathcal{C}$.

$$P_{RBb} = \mathcal{B} - \frac{\mathcal{C}}{2}\cos(\Delta\phi). \tag{2.252}$$

2.6.10 Atom shot noise

Atoms are quantum, insofar as individual atoms are countable. The quantization of atoms produces a fundamental noise floor when detecting atom interferometer outputs. We quantify that shot noise here.

The squared amplitudes at the end of the interferometer describe output probabilities. Suppose 10 atoms each have equal probability of being detected in $|a\rangle$ or $|b\rangle$. Perhaps 6 of them end up being detected in $|b\rangle$ and 4 in $|a\rangle$. That 60/40 split is not inconsistent with the underlying probability, it is merely a consequence of detecting the probabilistic outcome of a discrete number of atoms. That deviation from the underlying probability is shot noise. Poissonian statistics show that the shot noise on N total atoms grows as $\sqrt{N}$. Interferometer experiments are not directly aimed at measuring atom numbers, but rather use the number to estimate a phase difference and measure an associated quantity of interest. We are interested in the noise $d\Delta\phi$ on the phase difference.

An interferometer's precision is best when the interferometer is most sensitive, which occurs when the signal is most highly sloped and most sensitive to phase differences. At such a "zero crossing" of the fringes, the signal is near the number of atoms around which the fringes oscillate. That value is $N\mathcal{B}$ (typically $N/2$), so the atom shot noise is $d\mathcal{S} = \sqrt{N\mathcal{B}}$ at detection. This produces an uncertainty in determining the phase difference of interest

$$d\Delta\phi = \left(\frac{d\Delta\phi}{d\mathcal{S}}\right) d\mathcal{S}. \tag{2.253}$$

The signal's phase sensitivity $d\mathcal{S}/d\Delta\phi$ depends on the signal

$$\mathcal{S} = NP_b \propto N\frac{\mathcal{C}}{2}\cos(\Delta\phi). \tag{2.254}$$

We have already assumed that the phase difference is nearly an odd half integer of π radians, where the phase sensitivity is highest. There, the interference term and signal vary linearly in $\Delta\phi$, so $\mathcal{S} \approx N\mathcal{C}\Delta\phi/2$ and $d\mathcal{S}/d\Delta\phi = N\mathcal{C}/2$ and

$$d\Delta\phi = \left(\frac{d\Delta\phi}{d\mathcal{S}}\right) d\mathcal{S} = \frac{2\sqrt{\mathcal{B}}}{\mathcal{C}\sqrt{N}}. \tag{2.255}$$

Increasing the atom number helps reduce the shot-noise-limited phase noise in an interferometer, as does increasing the contrast.

Chapter 3

Experimental tools

The experimental apparatus supporting the work in this dissertation offers several new techniques to the community's repertoire. In one, a dual-polarization imaging scheme allows for taking two cold-atom images in rapid succession without the need for an expensive camera equipped with frame transfer. That allows us to normalize detection to the atom number that fluctuates from shot to shot. We further utilize the absorption images to measure magnetic field gradients. We also describe a vacuum tube circuit that enables fast switching of two continuous-wave laser beams' directions, in far less than a microsecond. Finally, while physicists have optically pumped to other atoms' magnetically-insensitive states before, we demonstrated it for the first time in ^{7}Li and describe the setup below. Along the way, we offer a cautionary tale to folks heating an oven that loads a 2D magneto-optical trap cross. Most of the other techniques are borrowed from previous generations, though we nevertheless describe the machine in enough detail to set course for a new student building up a related a tool.

3.1 Timing and control with Cicero

Much of the digital and analog control signals are timed and controlled in Cicero, a GUI-based control software written for atomic physics experiments [127]. Cicero delivers the high-level user input to Atticus, a server that communicates with National Instruments hardware.[1] The words generated by Cicero are executed by an NI PCIe-6535 ("Dev1") that controls the digital outputs for the experiment and an NI PCI-6723 ("Dev4") that controls the analog outputs. The clock rate for the words is 100 kHz, so the finest temporal resolution we achieve through the interface is 10 μs. When we demand faster tasks, we use a digital signal from Cicero as a trigger for a faster circuit like a pulse generator.

[1] "Cicero" refers both to only the client-side portion of the architecture, as well the package of Cicero plus Atticus.

3.2 The laser system

3.2.1 Master laser

The alkalis' cooling and trapping transitions have linewidths less than 10 MHz. To stabilize lasers to such a fine feature, at least one master laser must directly interrogate an atomic sample. Our master laser is a Toptica DL pro, an external cavity diode laser (ECDL), that outputs ∼15 mW of light near 671 nm.

Modulation Transfer spectroscopy

Most of the power interrogates an aliquot of lithium separated from the main chamber. A heating belt warms the lithium only at the center of a heat pipe capped with windows that are buffered from the lithium by Argon gas [128].

The laser performs modulation transfer spectroscopy (MTS) [129] in the heat pipe [128, 114]. The beam first splits into two. A resonant electro-optical modulator (EOM) modulates the phase of one beam near 13 MHz before it propagates through the sample. The other beam remains unmodulated and propagates through the sample counter to the modulated beam. A nonlinear mixing process transfers the modulation from the modulated beam to the unmodulated beam near a spectroscopic resonance. As the laser wavelength scans, a photodiode detects the resulting modulation near the resonances. Demodulating the signal with the appropriate offset phase produces a signal that sharply crosses through 0 at any resonance. A cable of carefully selected length tunes the demodulation phase by sending the oscillator frequency through a fixed delay line.

We interrogate the lithium vapor on the D_2 line (the $2S_{1/2} \rightarrow 2P_{3/2}$ transition). There are three spectroscopic features: $|F = 1\rangle$ on D_2, $|F = 2\rangle$ on D_2, and a crossover resonance [130] in the middle. The spectroscopic features have different strengths. The crossover resonance offers a particular convenience because it symmetrically splits the two transitions, both of which are needed for cooling and trapping. The ground-state splitting between $|F = 1\rangle$ and $|F = 2\rangle$ is roughly 803.5 MHz in ^{7}Li, so each state sits 401.75 MHz from the crossover. That splitting is easily accessible by acousto-optical modulators (AOMs). The experiment previously used the error signal at the crossover resonance, but the crossover feature is weak. The transition for $|F = 2\rangle$ is larger by a factor of ∼4 and provides a steeper error signal. To take advantage of that feature, a double-passed 200-MHz AOM reduces the laser frequency by ∼400 MHz before sending it to the MTS setup. The output of the ECDL then locks to a frequency 400 MHz above the $|F = 2\rangle$ transition, very close to the crossover feature.

ECDL lockbox

The error signal enters into a servo box shown in Fig. 3.1.[2] Such a lockbox provides feedback for three ECDLs on the experiment. The servo can be configured to ramp the

[2]This figure omits the supply voltages and the regulators that stabilize them (like those in Fig. 3.2). It is also best practice to include additional shunt capacitors to ground on each power connection for each

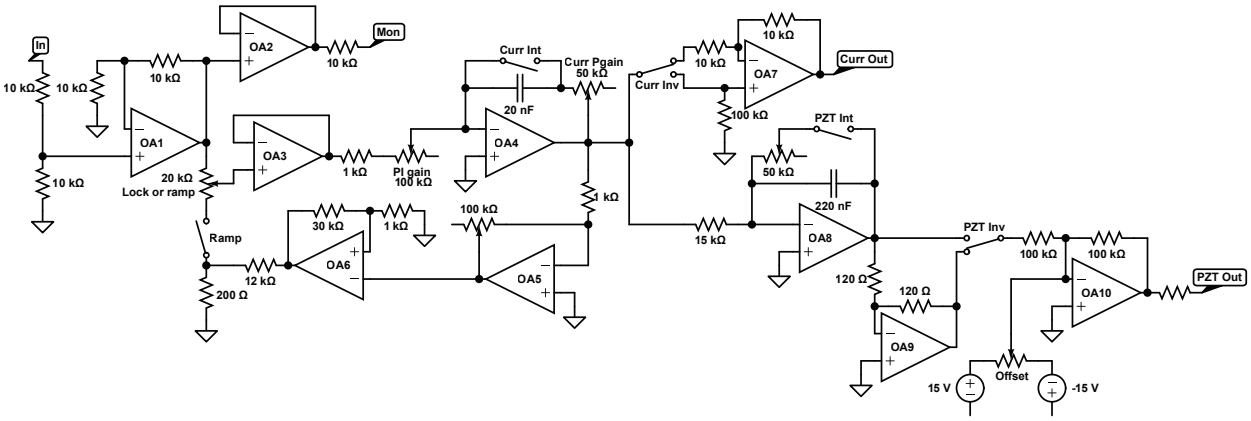

Figure 3.1: Ramping lockbox circuit for ECDLs.

laser wavelength in a triangle wave. Provided the integrator switch is open, the integrated output of OA4 is amplified by OA5 and sent into a Schmitt trigger OA6. The lock-or-ramp potentiometer functions like an adder that adds the error signal and the ramp signal, fully preferring one or the other when tuned all the way clockwise or counterclockwise. If the lock-or-ramp potentiometer passes the Schmitt trigger voltage on to OA3, the Schmitt trigger output gets integrated on OA4 until the differential input at OA6 reverses and the output rail reverses, thus reversing the ramp.

When the lock-or-ramp potentiometer selects the input error signal from MTS, OA3 receives no signal from the ramp. The box then provides proportional and integral feedback (with gains tunable by potentiometers) to the error signal for the ECDL's current and slower feedback for the piezo.

3.2.2 Injection-locked slave lasers

A few mW of optical power is sampled from the master ECDL and "injection locks" two slave lasers.[3] Lasers amplify whatever resonant mode is dominant, so sending light backwards into the diode seeds that mode and encourages the laser to amplify it. An optical isolator placed just after the diode rejects parasitic modes that may propagate backwards from farther down the setup and compete with the injected mode. The injected mode is intentionally aligned into the rejection port of the isolator so that it can pass backwards through the isolator and reach the laser diode. Injection locking diode lasers serves as a first stage of amplification, amplifying roughly 1 mW of injected light into ∼100 mW output.

Efficient and stable injection locking requires a few steps. First, the temperature and current of the diode should be stabilized to values that provide considerable power at a

operational amplifier at its location. This helps redirect AC noise that may have been induced between the opamp and supply.

[3]The master-slave nomenclature is standard but quite unfortunate. The slaves should revolt and demand promotion to "apprentices".

wavelength within 10 GHz of the target. Increasing the temperature increases the length of the cavity set by the diode facets, which increases the resonant wavelength. Tuning the current also slightly modifies the diode temperature, so increasing the current increases the wavelength. We stabilize the current with homebuilt, low-noise current controllers [131]. The temperature is controlled by a thermo-electric cooler (TEC) attached to the housing and a thermistor (Thorlabs TH10K) through which a feedback controller (Wavelength Electronics PTC2.5K-CH, e.g.) sends 100 μA. We heat diode lasers manufactured for 660 nm (e.g. Opnext HL6545MG) to $\sim$50°C to increase the wavelength to 671 nm.

Second, the seed's spatial mode should be matched with the diode's output as well as possible. The propagation axes must also be overlapped, by walking the injection seed's mirrors before it enters the isolator. Even when the diode's polarization is matched to the isolator's axis, some optical power will still be rejected, providing a target after the isolator for overlapping the two beams. The diode may output a rather poor spatial mode, so it is often best to try to overlap the injection seed with the most intense lobe of the diode's mode. Once the modes are overlapped, tuning the current within a range of several mA should indicate evidence of locking, evinced by a spectral peak that remains stationary with small perturbations to the current.[4] Tweaking the injection seed alignment or temperature may improve the current range over which the laser locks, a 1 mA range being a strong and stable lock.

A slave laser can even injection lock to the sideband of a frequency-modulated source [132] with appropriate optimization of the current and temperature. Sideband injection locking can be useful for atoms other than lithium where the ground-state hyperfine splitting exceeds the range of AOMs, but is within the range of EOMs. Employing this technique for ^{7}Li would provide access to the D_1 in ^{7}Li or to the D-line transitions of ^{6}Li.

Lock monitoring

Sampling the laser spectrum is critical for operating the apparatus. We use a homebuilt Fabry-Perot cavity with one mirror mounted on a piezo that allows tuning of the resonant condition. A triangle wave voltage applied to the piezo ramps the resonant frequency of the cavity back and forth, while a reverse-biased photodiode terminated at an oscilloscope detects the transmitted light.

The circuit in Fig. 3.2 generates a low-voltage triangle wave that serves as an external control input to the high-voltage piezo controller (Thorlabs MDT693A), which drives the piezo. Fig. 3.3 shows the trace for the triangle wave and a locked slave.

3.2.3 Frequency manipulation

An alkali MOT requires two optical frequencies. One cools the atoms, stimulating the absorption of thousands of photons and their momenta that oppose the initial momentum

[4] If no stationary peak is observable, at least an influence should be observable in which the spectrum changes reproducibly when blocking and unblocking the injection seed.

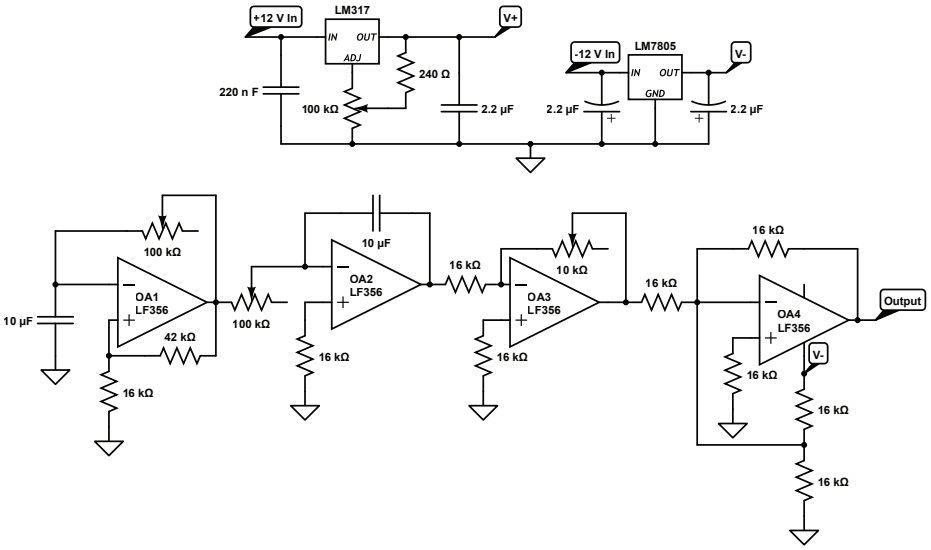

Figure 3.2: Triangle wave generator for lock monitoring cavity. Above are the regulators used to generate stable voltage references. Below is a circuit that integrates (at OA2) the output of a bistable multivibrator (OA1) and produces a triangle wave. OA3 provides a tunable gain stage and OA4 both inverts the signal and offsets it from 0 V. This circuit connects to the control input of a high-voltage piezo controller that drives the piezo on the Fabry-Perot cavity used for monitoring laser locks.

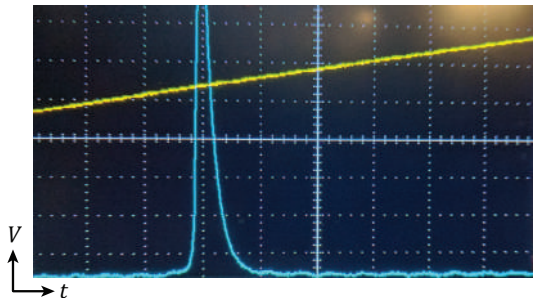

Figure 3.3: Locked slave laser. The yellow trace shows a ramp in the triangle wave modulating the Fabry-Perot cavity length. The blue trace shows the transmitted spectrum of an injection-locked locked slave laser.

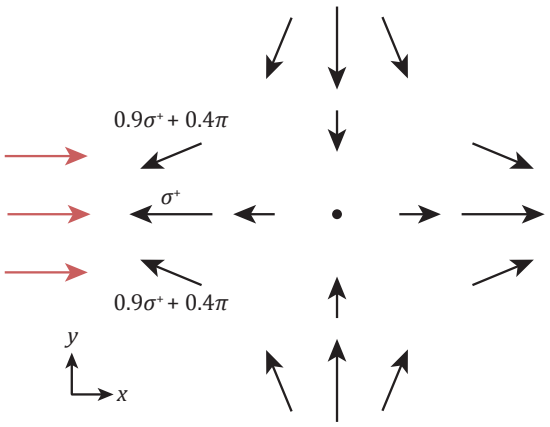

Figure 3.4: Polarization impurity in a quadrupole field. Black arrows represent the quadrupole magnetic field for anti-Helmholtz coils. Red arrows represent the propagation of MOT light. Light polarization is defined with respect to the local magnetic field direction. Even if a polarization is purely σ^+ along an axis (here x), the angle of the field off axis precludes a pure polarization. This polarization impurity prohibits a closed cycling transition and requires repump light for multi-dimensional MOTs.

of the atom. The cooling transition should be closed so that an atom scattering a photon has no choice but to decay back to the same state and continue absorbing photons and momentum. For example, a ^{7}Li atom in $|F = 2, m_F = 2\rangle$ could absorb σ^+-polarized light to $|F' = 3, m_F = 3\rangle$, from which the only dipole-allowed transition back to the ground state is to $|F = 2, m_F = 2\rangle$. Rinse, lather, repeat. In one dimension, cooling light alone is sufficient provided that the polarization and magnetic field to which its referenced are pure.

In three dimensions, a quadrupole magnetic field (from anti-Helmholtz coils) generates magnetic field gradients in all three directions. Precisely on one axis, the gradient points purely along that direction. The field direction points at an angle off axis. For a beam propagating along an axis, the angle introduces a nonzero projection of the polarization onto the field axis that corresponds to a π polarization component. The presence of the π component allows transitions outside the cooling transition and opens decay paths to the $|F = 1\rangle$ state.

Including a repump frequency recovers atoms that decay into $|F = 1\rangle$ and allows them to continue cycling on the cooling transition. For atoms with unresolved excited-state hyperfine structure like Li, the polarization impurity not only permits the $|F = 2, m_F = 2\rangle \rightarrow |F' = 3, m_F = 2\rangle$ transition, but also those to other hyperfine states like $|F = 2, m_F = 2\rangle \rightarrow |F' = 2, m_F = 2\rangle$, further opening the cooling transition to leakage. Our Li MOT uses roughly equal optical powers for cooling and repump.

The cooling and repump light originates from a single slave laser injection locked by the master laser near the ground state D_2 crossover frequency. A polarizing beam splitter (PBS) cube splits the optical power. Half the power double passes through a 200-MHz AOM to

lower optical frequency that serves as cooling light on the $|F = 2\rangle$ D_2 transition, while the other half double passes through a different 200-MHz AOM to higher optical frequency that serves as repump light on the $|F = 1\rangle$ D_2 transition.

The cooling and repump light overlap with orthogonal polarizations on a PBS. A half wave plate rotates both polarizations and subsequent PBS projects power from both frequencies onto the same polarization axis.[5] The combined repump and cooling frequencies enter an optical fiber then a tapered amplifier before cooling and trapping atoms in the vacuum chamber.

Two separate slave lasers contribute light manipulated in this way, one for a 2D MOT that traps hot atoms out of the oven and one for the 3D MOT that traps atoms pre-cooled by the 2D MOT. The four AOMs allow for independent optimization of the 2D and 3D MOTs.

3.2.4 Tapered amplifiers

The slave lasers amplify an injection seed available from the master laser from ∼1 mW to ∼100 mW. Much of that power is sacrificed to AOM efficiencies or fiber-coupling efficiencies, depending on the application. Tapered amplifiers (TAs) provide another means of increasing the optical power.

A TA is a diode laser with a geometrically tapered gain region [133]. The optical gain in diode lasers originates from the level dynamics of charge carriers in the junction, so the gain must saturate as the stimulated emission rate approaches the carrier injection rate. The tapered geometry offers a clever way around the gain saturation. The gain saturates sooner for regions with higher optical intensity. By focusing the beam into the gain region and matching the taper angle to the divergence angle of the beam, the edges of the beam profile where the intensity remains low may still experience gain even though the center of the beam has saturated the gain of the diode. Furthermore, the taper distributes the amplified optical power over a larger area at the output facet, which helps to avoid the diode's material damage threshold at high power. Optimizing the output power of the TA requires finely optimizing the placement of the lens that focuses the input beam into the gain region. The output of the TA is nearly a top-hat in intensity (not a Gaussian).

The taper is only helpful perpendicular to the diode junction where emission occurs, so the output facet of a TA has a dramatic aspect ratio and leads to a beam that diverges astigmatically. To couple the beam into an optical fiber, we use an output coupling lens to collimate the beam on a single axis. A cylindrical lens collimates the other axis, ideally placed where the waists of the two axes are identical. The placement of both lenses effects the fiber-coupling efficiency.

Three 500-mW TAs amplify optical power in this experiment. The TA inside a Toptica DL Pro (housed along with the master laser) amplifies the cooling and repump light for the

[5] This recombination tactic wastes half the optical power. In principle, these polarizations can be left orthogonal and coupled into an optical fiber, one along the slow axis and one along the fast axis. If the destination is a tapered amplifier, doing so would not help tremendously because the amplifier will prefer one polarization over the other.

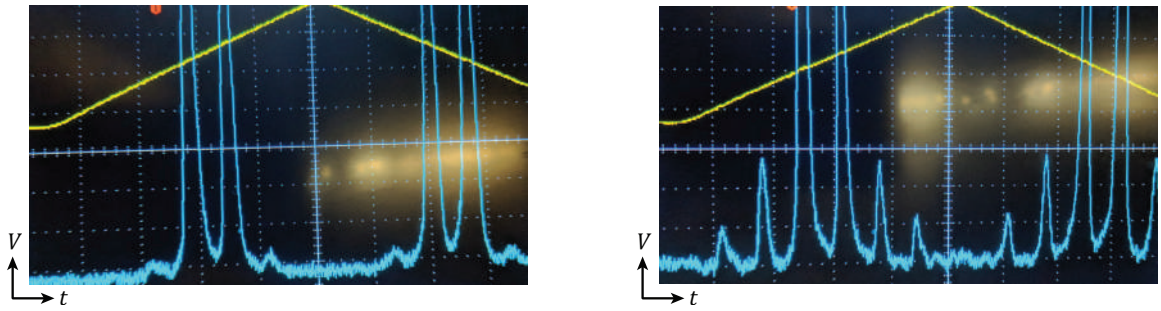

(a) "Unlocked" TA (b) "Locked" TA

Figure 3.5: Locking a dual-seeded TA. Tuning the current and temperature of the TA modifies the output modes, monitored here on the Fabry-Perot cavity. On the left, the two modes of interest (here, 3D MOT cooling and repump) appear to be stronger than the sidebands. On the right, while the TA seems distracted by its sidebands, operating here always produces better results.

3D MOT. A Toptica DC 110 controls its current (DCC 110) and temperature (DTC 110). A Toptica BoosTA with built-in current and temperature control amplifies the cooling and repump light for the 2D MOT. A homebuilt assembly amplifies light for driving the Raman transitions that generate the interferometer. A homebuilt circuit controls its current, limited to 1 A, and a Wavelength Electronics servo controls the temperature. Unlike the slave diodes, the TA chips we use output more power when cooled below room temperature.[6] All three TA chips were replaced over the course of the experiment, each housing volunteering its own vagaries.[7] We purchase our replacement chips (Eagleyard TPA-0670-0500) from XSoptix, a women-owned small business.

We seed the 2D MOT and 3D MOT TAs with combinations of cooling and repump light, two modes that compete for gain in the TA. Under this dual-seeded condition, nonlinear processes in the TAs produce output in sideband modes that are removed from the dual seeds by the seed splitting. While these sidebands seem like distractions from the desired modes, they proved to be positive indicators of TA behavior. A TA with strong and well-resolved sidebands always trapped more atoms at lower temperature. Tuning the temperature and current of the TA modifies this mode structure, so optimizing those parameters has a powerful impact on the health of the experiment.

The output of the 3D MOT TA is fiber-coupled and enters a homebuilt one-to-six-beam fiber splitter atop the vacuum chamber (Fig. 3.6). The six output beams are distributed, circularly polarized, telescoped, and enter the main chamber to generate the 3D MOT.

[6] Cooling introduces the opportunity for condensation of moisture onto the chip, which shorts the leads and destroys it. We take care to avoid the dew point and keep the chip above ∼14°C.

[7] The BoosTA disallows realignment of the output beam, which was no longer exiting the output window of the box after replacement. I glued a mirror inside and drilled a hole in the box to send the beam out the side. Not to worry - I colored the rim of the drilled hole in black Sharpie to prevent nefarious and deleterious reflections.

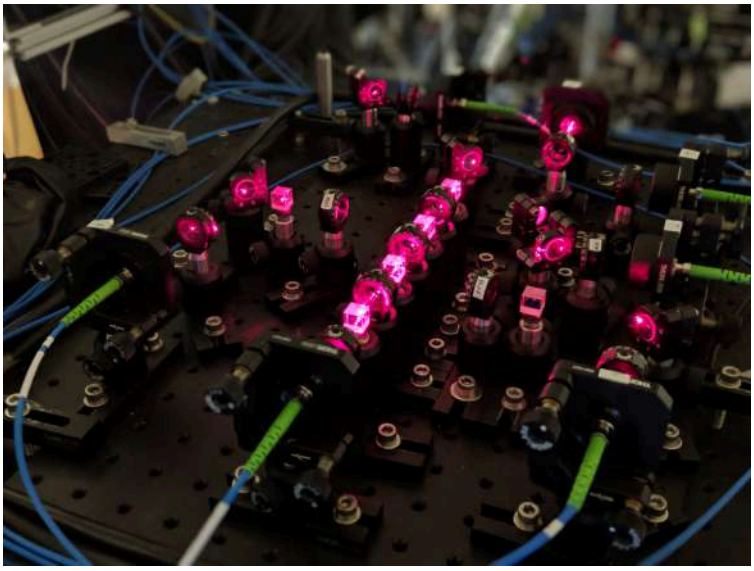

Figure 3.6: Fiber splitter. A single input beam splits into six through a cascade of half-wave plates and polarizing beam splitters. Quinn Simmons and Simon Budker built this subsystem.

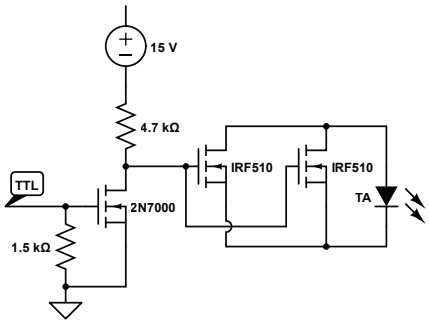

Figure 3.7: Current thief for 3D MOT TA. A TTL signal controlled by Cicero switches the MOSFETs on or off. When the TTL is high, the 2N7000 conducts and pulls the IRF510 gates low to turn them off, permitting current to pass through the TA chip. For high TTL, the voltage drops from -0.439 V to -2.769 V from anode to cathode. When the TTL is low, the 2N7000 does not conduct, sending the IRF510 gates high and allowing them to conduct and steal the current from the TA. There are two IRF510s in parallel because one did not sink enough current alone. For low TTL, the voltage drops from -1.669 V to -1.784 V from anode to cathode.

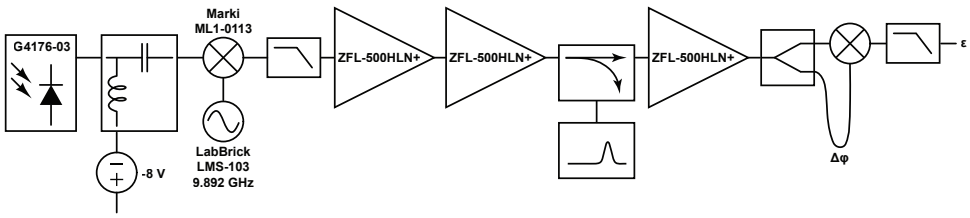

Figure 3.8: Frequency offset "trombone" lock. An optical beat note mixes with an LO into a low-frequency signal. Tuning the length of the delay line, like a trombone, tunes the amount of phase $\Delta\phi$ the low-frequency signal accrues before recombining with itself.

It is important during interferometry that no stray light close to an atomic resonance can scatter off an atom and destroy its coherence. 3D MOT light leaking into the chamber poses such a risk. While extinguishing the AOMs that generate the 3D MOT TA seeds reduces the light, the TA still outputs light when unseeded. We further extinguish the light in the chamber during interferometry with a current thief in Fig. 3.7 that steals the current from the TA in response to a digital control voltage. Removing the current source from the TA prevents any light from entering the chamber.

3.2.5 External cavity diode lasers

Three ECDLs serve the experiment, including the master laser. The laser used to measure the tune-out wavelength (the "Stark ECDL"[8]) is a commercial ECDL, a Toptica DL Pro with current and temperature control provided by a DLC Pro.

A homebuilt ECDL [128] generates ∼20 mW of light for optically pumping (OP) ^{7}Li to the $|F = 2, m_F = 0\rangle$ ground state. Circuits designed by Brent Young in 1991 control the current and temperature of the OP ECDL. The diode in the homebuilt TA is an Opnext HL6555G, which has been discontinued. A power outage claimed the original diode and the final replacement occupies the housing now. Should a new diode be required in the future, the Ushio HL65051DG should be a suitable substitute.

A servo like that in Fig. 3.1 locks each ECDL. The error signals for the servos are generated differently. MTS provides the error signal for locking the master laser. Both the OP ECDL and the Stark ECDL generate error signals using electronically-detected optical beat notes as described below.

Frequency offset "trombone" lock

The OP ECDL uses a frequency offset "trombone" lock for the error signal [134]. The OP ECDL beats against light from the injection-locked 2D MOT slave. Mixing the beat

[8]Throughout this thesis, I enjoy artistic liberty in referring to this laser and its emission as the Stark ECDL, Stark laser, Stark-shifting beam, Stark beam, or related terms that suit the mood.

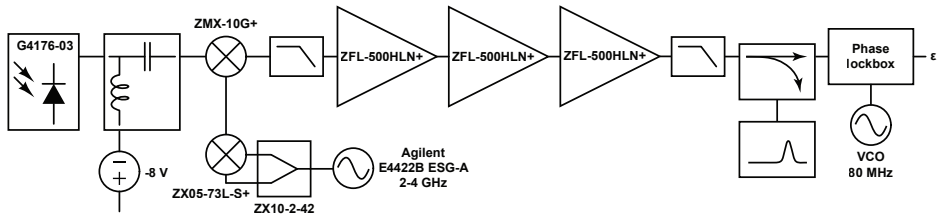

Figure 3.9: Frequency generation for phase lock. A phase lock stabilizes the optical beat note of the Stark ECDL against the Raman slave. Fig. 3.10 details the "Phase lockbox" referenced above.

note against an LO at nearby frequency produces an intermediate frequency at the mixed-down beat note f_{MDBN}. The signal at f_{MDBN} gets amplified and split. One output of a power splitter goes directly into a mixer while the other output travels through a cable of fixed length before entering the mixer. The delay line of length L introduces a phase shift $\Delta\phi = 2\pi f_{MDBN} L/(2c/3)$, where the speed of the signal in the cable is roughly 2/3 the speed of light. Multiplying $\cos(\omega_{MDBN} t)$ by $\cos(\omega_{MDBN} t + \Delta\phi)$ yields a term $\cos(\Delta\phi)$. The error signal is 0 when that term is 0. Depending on the sign of the inversion switch in the lockbox, the trombone lock will lock either when the delay line introduces an even- or odd-integer multiple of π. This OP ECDL locks at f_{MDBN} around 600 MHz.

The trombone lock is particularly simple to set up, involving mostly commercial Mini-Circuits components and a standard servo. A trombone lock originally stabilized the Stark ECDL, but tuning the LO changed both the amplitude of the error signal and the f_{MDBN}. That inadvertent frequency tuning introduced a systematic error into the tune-out measurement and was difficult to track.

Phase lock

Stabilizing the Stark ECDL with a phase lock provided far better stability with tuning. The circuit begins by manipulating an optical beat note as shown in Fig. 3.9. A fast photodetector detects the optical beat note between a sample from the Stark ECDL and the Raman slave that is injection-locked near the D_2 crossover resonance. The beat note mixes against an oscillator derived from a 4-GHz Agilent signal generator. The Agilent does not output frequencies large enough to shift the Stark laser to tune-out, so we multiply the Agilent frequency by splitting its power and mixing it against itself. That produces higher harmonics, including a component at the tripled frequency and the quadrupled frequency, albeit at reduced amplitude. To lock near the tune-out wavelength about 6.7 GHz below the D_2 reference, we lock to the tripled harmonic with the Agilent tuned near 2.5 GHz (7.5 GHz). To perform D_1 spectroscopy about 10 GHz below the D_2 reference, we lock to the quadrupled harmonic with the Agilent tuned near 2.7 GHz (10.7 GHz). The mixed-down beat note near 80 MHz enters into a phase lockbox that compares it to an 80-MHz LO signal from the Aux output of the VCO that drives the 80-MHz AOM switch that shutters the OP

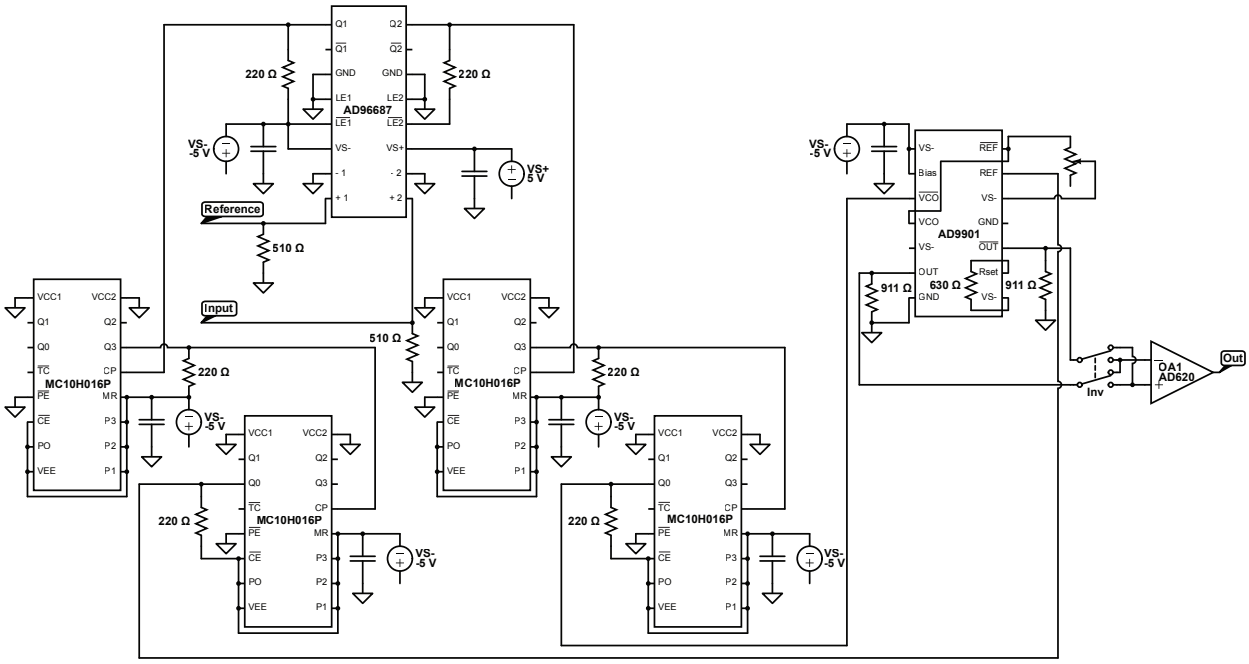

Figure 3.10: Phase lockbox. The circuit inputs two signals at different radio frequencies and outputs a voltage proportional to their phase difference. Weicheng Zhong built this box and graciously donated it to the tune-out cause.

light. The lockbox, described below, locks the mixed-down beat note to 79.67(1) MHz. The error in the lock tone is the standard deviation of measurements from a frequency counter over the range of frequencies we use to measure tune out.

Fig. 3.10 shows the phase lockbox that compares the mixed-down beat note and the 80-MHz VCO. Note that the box operates on ECL logic as opposed to TTL, which improves the speed. The AD96687 is an ultrafast comparator that converts each sine-wave input into a square wave at that frequency. To improve the capture range of the lockbox, which is limited by the frequency response of the AD9901 phase discriminator, we divide down the 80-MHz frequency. The Q3 output of the MC10H016P divides the input CP by 16 and the Q0 output divides CP by 2, so the cascaded chips divide the 80-MHz frequency by a factor of 32 to ∼2.5 MHz. The two frequencies drive the REF and VCO inputs of the AD9901 phase discriminator, but with opposite sign. At lock, these two inputs are 2.5-MHz square waves 180° out of phase. The discriminator then outputs a square wave at 2.5 MHz. The AD620 performs two functions. At lock, we want the error signal output to be 0 V, not the average of the ECL levels, which is closer to -1.4 V. The AD620 acts as a comparator and shifts the average level back up to 0 V. Furthermore, the signal should no longer be a square wave. It should be the cycle-averaged level of the square wave. The AD620 has a slow frequency response, with a gain-bandwidth product around 120 kHz. It therefore acts like a low-pass filter on the much higher 2.5-MHz input frequency and averages the square

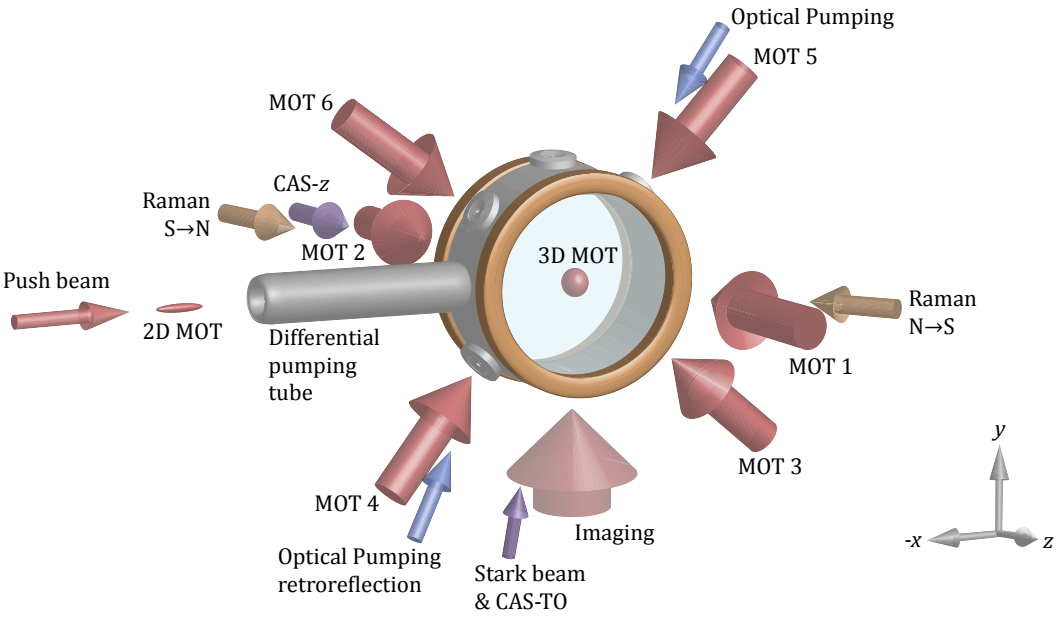

Figure 3.11: Vacuum chamber and beam axes. The 2D MOT portion of the chamber is omitted so as not to obscure the view. The gold annuli attached to the chamber are the quadrupole magnetic field coils.

wave. The resulting output is a voltage linear in the phase difference between the two input frequencies.

3.3 The chamber

Lithium is metallic at room temperature. To generate appreciable vapor pressure, we heat a sample with natural isotopic abundance[9] to around 400°C[10]. A Variac tuned near 80 V AC drives a heating belt wrapped around the oven. A 2D MOT with a permanent magnet traps the hot gas and provides an initial stage of cooling. The design is similar to that in [135] and is described in [136, 128]. If the oven temperature is too low, too little vapor is available for trapping. If the oven temperature is too high, collisions of the atoms trapped in the 2D MOT with background atoms are too frequent. Optimizing the oven temperature for atom flux can significantly improve atom loading rates.

The 2D MOT remains untrapped along one axis. Along that axis, we send a push beam resonant with the $|F = 2\rangle$ transition on the D_2 line to push the atoms through a differential pumping tube into the 3D MOT chamber. The differential pumping tube isolates the interferometry chamber from the high-pressure flux from the oven.

[9] Natural abundance is roughly 92% for ^{7}Li and 8% for ^{6}Li.

[10] A thermocouple fixed to the oven chamber underneath the heating belt reads 386°C.

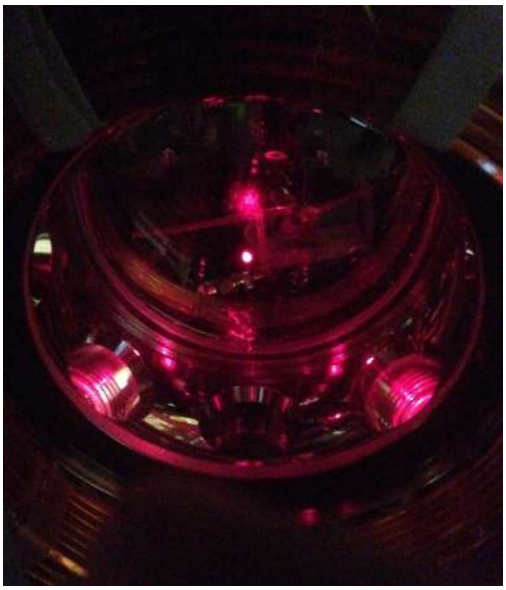

Figure 3.12: 3D MOT. In the best of times, the 3D MOT (the red orb at center stage) glows with a sanguine vigor. (10/18/2017)

The 3D MOT chamber has a total of 8 viewports (see Fig. 3.11). The two large viewports face north and south and their perimeter supports the 3D MOT anti-Helmholtz coils that generate the tunable magnetic quadrupole field for trapping (the gold annuli in Fig. 3.11). They have a hollow core through which tap water flows to cool them.

An ion gauge registers the pressure on the 2D MOT side of chamber as $\sim 10^{-7}$ torr. An ion pump (Varian StarCell VacIon Plus 40 L/s) attached to the science chamber maintains the pressure, likely around $\sim 10^{-9}$ torr. The current output of our ion pump lost credibility many moons ago. The MOT lifetime of ∼1-2 s, judged by eye, suggests that the pressure is on the order of 10^{-9} torr. The MOT lifetime is limited by collisions with background gas molecules, which increase with pressure. Given collision cross-sections with background gases, the MOT lifetime is a probe of the vacuum pressure [137].

3.3.1 Sample maintenance

Lithium corrodes glass. This behavior motivated the inert buffer gas that protects the viewports in our MTS spectroscopy cell.[11] It also contributed to a vacuum leak whose culprit is shown in Fig. 3.13

Light-induced atomic desorption (LIAD) discourages lithium atoms' excursions into the glass substrate [138]. The threshold wavelength for desorbing lithium from fused silica is 470 nm, so we illuminate the window that replaced the one shown in Fig. 3.13 at 405 nm with

[11] It is also an alleged reason that the Cronin group in Arizona never attempted to measure lithium's tune-out wavelength or polarizability.

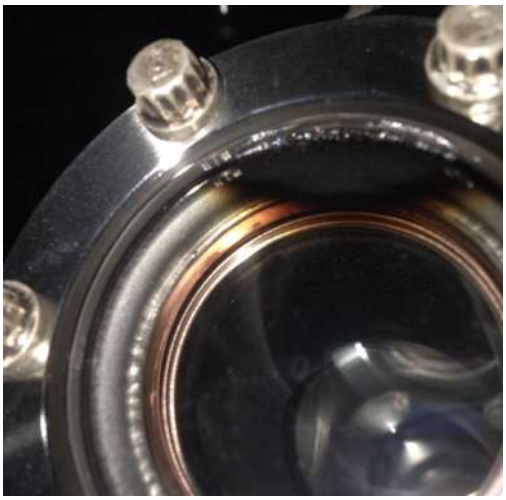

Figure 3.13: Derelict viewport. Hot lithium ejected from the oven destroyed a vacuum seal in the 2D MOT chamber in April 2015, here visible in the black pollution of the viewport and the bubbling at the glass-metal interface. A UV LED can discourage this failure mode. (04/17/2015)

a Thorlabs M405LP1.[12] The LED produces a noticeable reduction in the blackening of the window in the region of the illumination.

Atomic lithium reacts rapidly with atmospheric gases upon exposure, requiring the sample to remain under vacuum for purity. Lithium reacts with hydrogen gas to form lithium hydride LiH and water to form lithium hydroxide LiOH. Any vacuum leak, like that recorded in Fig. 3.13, compromises the sample's integrity. Atomic lithium appears metallic, so any diffuse grayscale is a harbinger of future work.

To recover the sample after a leak, we first close the gate valve separating the 2D MOT and 3D MOT chambers and wrap the 2D MOT chamber in a disposable glove bag. With all the necessary tools packed into the glove bag, we seal the bag's open end around the differential pumping tube, flow inert gas (Ar, for example) into the chamber through an inlet, and create a small slit in the bag that serves as an outlet. Replacing the derelict vacuum port, we opened the oven to find a blackened sample surface. We scraped off the black surface layer to reveal the metallic lithium below. The molten lithium had condensed around the nickel gasket that mates the oven to the 2D MOT chamber and created a seal that was incredibly difficult to erode.[13] Future samples should not be overfill the oven well. After replacing the gasket, we replaced the window, and resealed the vacuum.

For experiments, we heat the oven to $\sim 400°C$ using heating belts. To avoid heating the viewports, we heat less the neck that connects the oven well to the 2D MOT chamber. That introduces a thermal gradient such that the coldest spot along the neck is at the mating

[12] David Weld's group at the University of California, Santa Barbara tipped us off to this strategy.

[13] We slowly scraped it away with a box cutter to free the gasket. I can neither confirm nor deny that I injured myself in this process.

(a) Plugged oven neck (04/15/2016) (b) Cleared plug (04/15/2016)

Figure 3.14: Condensed lithium plugs oven flux. On the left, the metallic structure has grown into the center of the oven neck and capped off the oven exitance. On the right, deliberate heating melted the plug and removed the occlusion.

between the neck and 2D MOT "X". Hot lithium vapor flies up into the chamber from the oven and atoms that evade or escape the trap rain back down onto the cold mating and quietly condense there. The condensed metal protrudes farther and farther into the center of the neck over time. After a few years of continuous operation, this constriction sealed and prevented any vapor from exiting the oven.

The left photo of Fig. 3.14 shows the condensed lithium closing off the oven. To remove the solid plug, we uninstalled the permanent 2D MOT magnets and addressed the neck with a heat gun for ∼1 hour. That melted the plug back into the neck and liberated the lithium vapor for experiments.

3.4 Magnetic fields

A pair of anti-Helmholtz coils generates the magnetic quadrupole field for the MOT. There are 64 windings of wire, with an 8×8-wire square cross section. The inner diameter of the annulus is 14 cm and the outer diameter is 22 cm. The separation between the two coils' inner-most layer is 11 cm and the separation between the outer-most layers is 19 cm. The coils have a resistance of ∼0.15 Ω and generate a field gradient of ∼20 G/cm at an operating current of ∼20 A. The current is controlled by a control voltage set in Cicero and sent to the stabilization circuit in Fig. 3.15.

There are also three sets of Helmholtz coils that control the bias magnetic field, composed of 14 AWG gauge wire. The circuit in Fig. 3.16 controls the coil current powered by Tenma power supplies. They generate ∼0.5-G fields at the atoms. The parameters of the coils are recorded in Tab. 3.1.

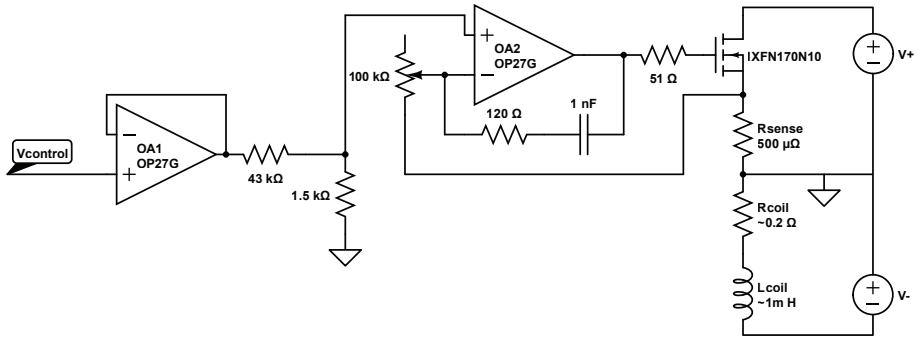

Figure 3.15: MOT coil feedback. An analog voltage controlled by Cicero serves as the control signal for this feedback circuit.

Coil axis	Winding number	x width / cm	y width / cm	z width cm
x	80	38	30	61
y	80	38	30	61
z	120	28	38	15

Table 3.1: Bias coil parameters. For each coil axis, the width along its own axis represents the distance to the atoms of the center of the coil.

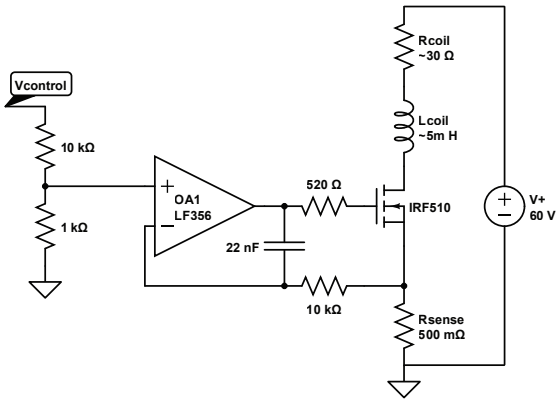

Figure 3.16: Bias coil feedback. The voltage divider at the beginning increases the tuning precision.

The fields and field gradients from each set of coils can be computed at the atoms using the Biot-Savart law, integrating the current around approximate current paths. It is straightforward, though tedious, to calculate the integrals by hand and code the formulas for plotting and prototyping.

3.5 Microwave antenna

A homebuilt Yagi Uda antenna (with one driven element and no directors) drives magnetic transitions between $|2S_{1/2}, F = 1\rangle$ and $|2S_{1/2}, F = 2\rangle$ within the ground state. The driven element is partially visible behind the rear window in Fig. 3.12. An Agilent E4422B ESG-A generates a signal at the ∼800-MHz hyperfine splitting, which is shuttered by a microwave switch and amplified by a 10-W microwave amplifier. Taking care to impedance-match to the antenna improves the coupling efficiency and microwave Rabi frequency. Optimizing our impedance was substantially improved by the addition of a small piece of foil that capped the end of the driving element. Even still, we drive a π pulse only after ∼500 μs. While the emitted polarization is parallel to the driven element, the microwaves reflect and rotate inside the vacuum chamber at the atoms. Population transfer arguments can help to recover the fraction of power in each polarization when necessary.

3.6 Imaging

Atom interferometers translate matter-wave phase differences into changes in the number of atoms in each output port, so interferometers must somehow detect total numbers of atoms. Absorption and emission of resonant light makes photons a convenient way to detect cold atoms. Fluorescence imaging drives repeated absorption-emission cycles on a transition and images the photons emitted into the solid angle subtended by a collection lens. For a lens with focal length f placed f away from the atoms and a lens of diameter D, the fraction of photons collected is only $\sim \pi(D/2)^2/4\pi f^2 \approx D^2/16f^2$. Lithium's inefficient cycling transition permits only a couple of photons to be emitted before the atom falls into a dark state, so fluorescence imaging with a small solid angle is challenging because of the low signal. Absorption imaging inverts the problem by detecting the number of photons that get scattered away from the field of view, effectively detecting the photons scattered into a solid angle $4\pi(1 - D^2/16f^2)$. Of course, sending a beam with many photons directly onto the camera increases the photon shot noise in detection.[14]

[14]For readers concerned about photon shot noise, a technique called diffractive dark-ground imaging [139, 140] records the shadow but removes most of the illuminating beam's photons and their shot noise. There is also a dispersive variant for off-resonant probes.

3.6.1 Absorption imaging

Consider a nearly-resonant beam propagating along z through a gas of atoms. Atoms will absorb photons from the beam, reducing the intensity from I. The change in intensity dI should scale as $dI \propto I$ because the more photons there are, the higher the likelihood one will get absorbed (assuming the intensity is well below the saturation intensity). The deeper into the sample the light penetrates dy, the more likely the beam is to have encountered an absorbing atom, so $dI \propto dy$. Finally, the total absorption should scale both with the number density n of the atoms and the absorption cross section σ (which depends on detuning, light polarization, atomic state, etc. [90]). Altogether, $dI = -n\sigma I dy$. The solution of this simple separable equation is the well-known Beer-Lambert law.

$$I(y) = I_0 e^{-n\sigma y}. \tag{3.1}$$

Studying the intensity of the light as it passes through a sample provides access to the number density n, which can be integrated over a volume to find the total number of atoms. To do so, one needs to know the initial intensity of the light I_0 before it encountered the sample.

Absorption imaging performs this feat by taking two images of the beam on a camera with pixels imaging the $x-z$ plane. The first is an image of the beam with the atoms present, $I_a(x,z)$, and the next is an image of the beam without the atoms, $I_b(x,z)$. The atoms cast a shadow in the first image and the second image calibrates how deep the shadow is. Because the atoms were absent in the second image, it plays the role of I_0 in Eq. (3.1). The light's propagation along y projects out that dimension, so each pixel probes the column density $\tilde{n}(x,z) = \int n(x,y,z)dy$ corresponding to that column in the sample. For example, assuming a uniform density distribution over a length l along y would give $\tilde{n}(x,z) = nl$. Taking the ratio of the two images' intensities (or counts after detection) accesses the column density.

$$\frac{I_a(x,z)}{I_b(x,z)} = \exp\left(-\int n(x,y,z)\sigma dy\right) = \exp\left(-\tilde{n}(x,z)\sigma\right). \tag{3.2}$$

The column density is[15]

$$\tilde{n}(x,z) = -\ln\left(I_a(x,z)/I_b(x,z)\right)/\sigma. \tag{3.3}$$

The total number of imaged atoms N is just the product of $\tilde{n}$ and the area that each pixel images, summed over an area that contains the full density distribution. Most atom interferometers detect matter-wave phase differences by summing up the entire density distribution in this way. For experiments where the total atom number is a critical parameter,

[15] A camera pixel measures a count of electrons, including dark counts at each pixel. If the number of counts in the image of atoms is $a(x,z)$, the number of counts in the image without atoms is $b(x,z)$, and the number of dark counts is $c(x,z)$, then technically the proper ratio to take is not $I_a(x,z)/I_b(x,z)$, but is $\left(a(x,z) - c(x,z)\right) / \left(b(x,z) - c(x,z)\right)$. In practice, one may use an average image of the pixel array's response in the dark $c(x,z)$ because the dark counts are relatively unchanging.

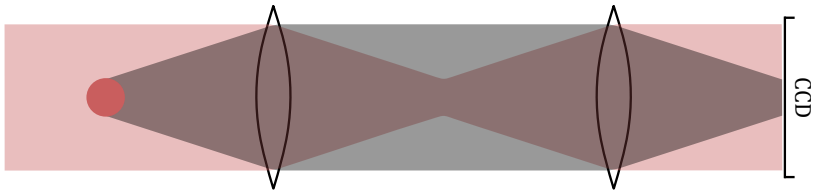

Figure 3.17: Absorption imaging schematic. The cloud absorbs resonant light and casts a shadow. In an absorption imaging setup like this, the cloud should be at the focal length of the first lens and the CCD should be at the focal length of the second lens. Because the shadow is collimated between, it is not critical to place the lens' focal points together (though not doing so would confuse the atom number calibration).

it is necessary to properly calibrate the scattering cross section and image magnification. In interferometer experiments, only changes in the relative atom number are interesting. The atom number calibration in this experiment not trustworthy because it was never necessary to get accurate atom number counts.[16] In the Wollaston imaging scheme described below, for example, there are two images taken with different light polarizations for which the scattering cross section is different, though we never bother to account for the difference.

Summing the full density profile averages over noise entering each pixel, but it also averages over differences in the signal at each pixel. Averaging in this way sacrifices any spatial features the signal may furnish.

We use light tuned to resonance with the $|2S_{1/2}, F = 1\rangle \rightarrow |2P_{3/2}, F' = 0, 1, 2\rangle$ transition to image atoms in $|2S_{1/2}, F = 1\rangle$. We choose to detect this state because we prepare the ensemble for interferometry by optically pumping into $|2S_{1/2}, F = 2, m_F = 0\rangle$ and it is preferable to detect interferometer signals on a null background using the state to which the interferometer transfers atoms.

3.6.2 Camera

A PCO pixelfly qe 12-bit charge-coupled device (CCD) camera images the atoms. A LabVIEW program controls the exposure time, triggering, and readout. The exposure time can be controlled to ∼5-μs precision, but the camera's 150-ms readout time dramatically limits the frame rate. Each single pixel images a 12.6-μm×12.6-μm area. We bin the pixels in 2×2 squares at the hardware level to improve the noise.

This camera has a problem. Fig. 3.18 shows striations in a dark image that change unpredictably with every iteration. PCO support suggested that they had seen this issue before and the resolution was to exchange the ethernet cable that connects the camera to a PCI card in the computer. The problem remained. PCO offered to test the camera if we

[16] So if we claim that we trap, say 10^7 atoms, it should be taken with a grain of salt. More importantly, our estimates of the atom-shot-noise limit would be relatively inaccurate.

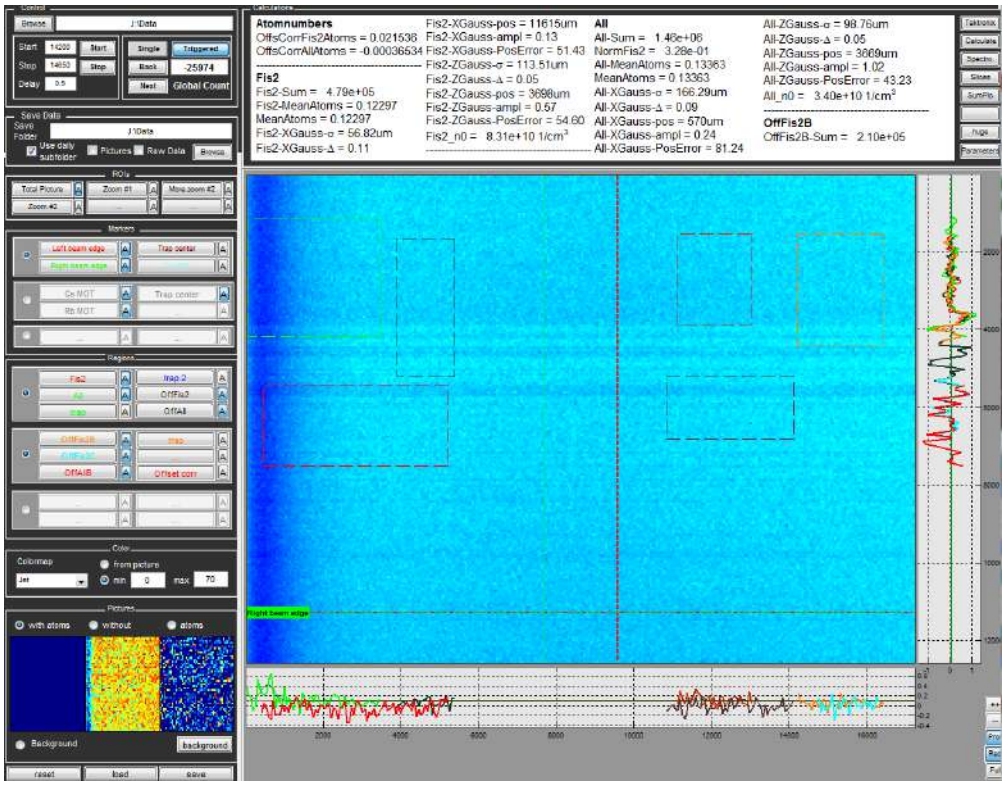

Figure 3.18: Camera noise. This is a post-processed image of the "column density" (i.e. the ln of the ratio of two images) in the dark. The lines in the image are different on every iteration. The interface is a Matlab GUI was written at Innsbruck that we modified slightly for our purposes. (06/02/2018, GCs -25989 to -25983 and -25981 to -25974, shown here is -25974)

sent it to them, but we were unable to take advantage of the kind offer. This imaging noise was likely a major source of noise in the tune-out measurement.

3.6.3 Magnetic gradient imaging

We use images of microwave excitations in the ground-state manifold to calibrate the magnetic field strength and its gradient. The magnetic field strength Zeeman-shifts the resonances. If there is a spatial gradient in the field strength, then the Zeeman-shifted transition frequency also varies spatially. Images of the microwave excitation and its position expose the spatial variation of the field.

We begin with OP to $|2S_{1/2}, F = 2, m_F = 0\rangle$. Just after, 20 μs of MOT repump fully depopulates atoms loitering in $|2S_{1/2}, F = 1\rangle$ and prepares a pure $|2S_{1/2}, F = 2\rangle$ state before applying a microwave pulse. Any atoms subsequently detected in the $|2S_{1/2}, F = 1\rangle$ must have been transferred by the microwave. Fig. 3.19 depicts the excitation from $|F = 2, m_F =$

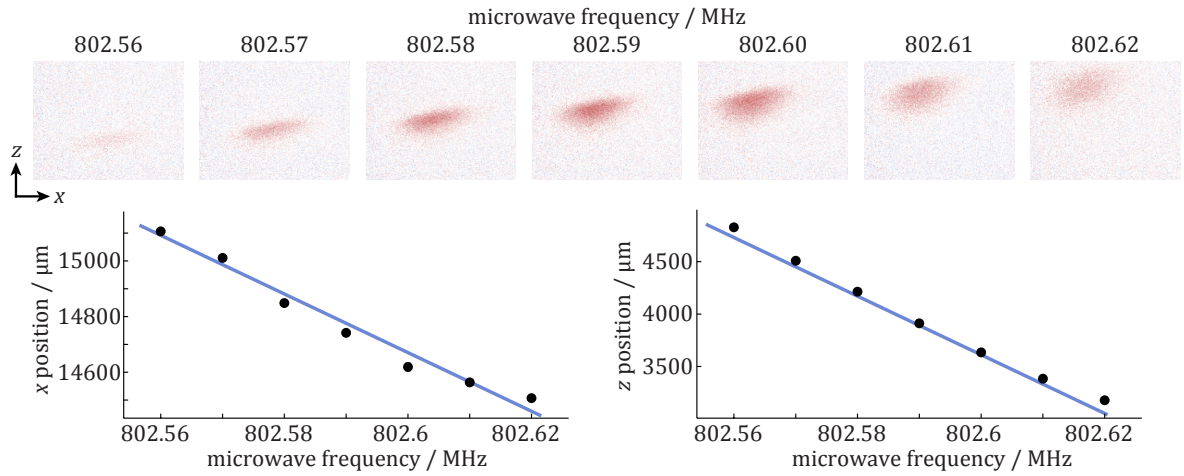

Figure 3.19: Magnetic gradient imaging. The position of a microwave excitation moves as a function of frequency due to the magnetic field gradient. (08/01/2018, GCs 3360 to 3366)

$0\rangle \rightarrow |F = 1, m'_F = -1\rangle$[17] We fit the center of the excitation in the x and z coordinates as a function of microwave frequency. The slope of each plot, m_x and m_z, represents the change in position as a function of change in frequency, $m_x = \Delta x/\Delta f_{MW}$. The quadrature sum of the slopes gives the full magnitude of the spatial variation.

$$m_r = \sqrt{m_x^2 + m_z^2} = \sqrt{\frac{\Delta x^2 + \Delta z^2}{\Delta f_{MW}^2}} = \frac{\Delta r}{\Delta f_{MW}}. \tag{3.4}$$

The magnitude of the magnetic gradient in the imaging plane is then

$$\frac{\Delta B}{\Delta r} = \frac{\Delta f_{MW}}{\Delta r}\frac{\Delta B/(m_F + m'_F)}{\Delta f_{MW}} = \frac{1}{m_r}\frac{\Delta B}{\Delta f_{MW}}\frac{1}{m_F + m'_F}. \tag{3.5}$$

We normalize the magnetic field change to the number of Zeeman shifts that contribute to the transition, which is the sum of the magnetic quantum numbers involved in the transition. The magnetic field sensitivity $\Delta f_{MW}/\Delta B$ for ^{7}Li's ground state is roughly 0.7 MHz/G (for a transition with a single Zeeman shift). The field gradient measured from Fig. 3.19 is about 0.5 G/cm, 2 ms after switching off the MOT's quadrupole field.

3.6.4 Normalized imaging

Interferometry experiments trace out signals and average down noise by performing many shots of the experiment at an appreciable repetition rate. The MOT traps an atom number that fluctuates by roughly 20% from shot to shot. Those number fluctuations would be

[17] Note that this transition is co-resonant with $|F = 2, m_F = -1\rangle \rightarrow |F = 1, m'_F = 0\rangle$. While this excitation may conflate those transitions, we do not detect any atoms in $m_F = \pm 1$ after optical pumping.

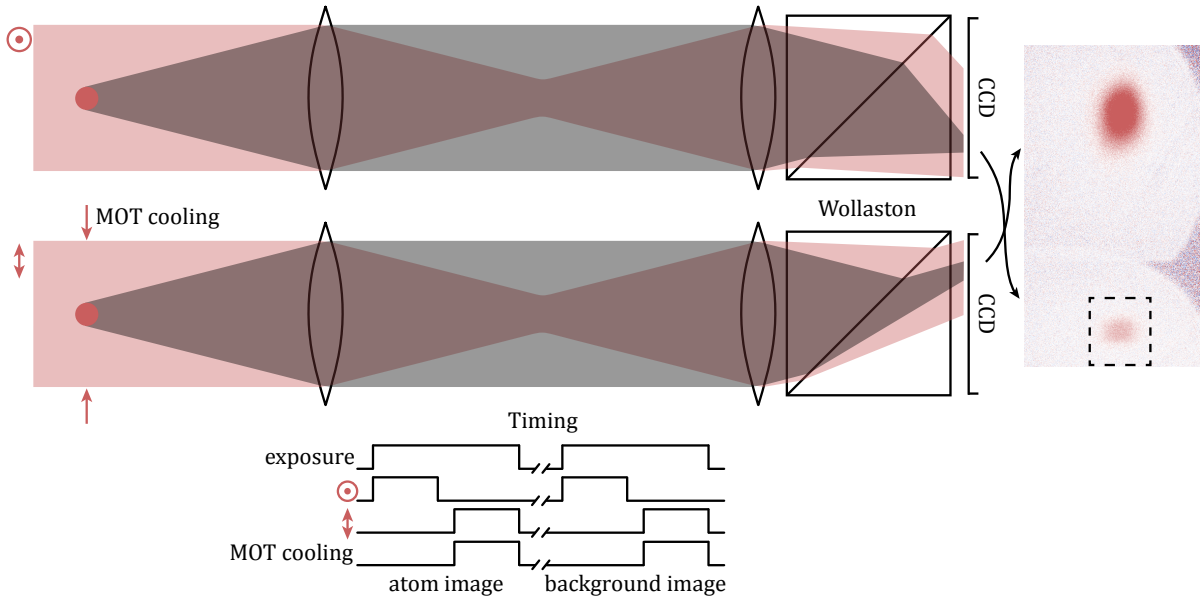

dissertation

Figure 3.20: Normalized Wollaston imaging. Shuttering two polarizations independently and separating them before the camera with a Wollaston prism forms two images on a CCD during a single exposure. The dashed box represents the region where the image of $|2S_{1/2}F = 1\rangle$ forms. That is the region almost all image data presented in this dissertation originate from, including images contributing to the tune-out wavelength measurement.

imprinted onto the interferometer signal as noise unless each shot can be normalized to the number of atoms trapped on that iteration. This requires counting atoms in both output states each shot. Experiments with state-labeled outputs may push one output off to the side to simultaneously image spatially-resolved output states. Li's inefficient cycling transition does not impart enough momentum to make this strategy viable. Furthermore, the camera readout takes 150 ms, after which the lukewarm cloud has thermally expanded and diluted beyond the field of view. The ability to take two images in rapid succession would solve the issue, allowing for counting one state and then the other.

A camera hardware technique called "frame transfer" allows multiple images to be taken during a single exposure without the readout delay. In frame transfer, only a portion of the array is illuminated. The technique shelves those pixel values by shuttling them into a dark region of the array before a subsequent illumination. Multiple illuminations can be recorded during a single exposure. This is a premium feature in expensive cameras and our pixelfly camera cannot do it.

We devise a new technique inspired by frame transfer to form two images during a single exposure and normalize the detection (Figs. 3.20 and 3.21). A Wollaston prism inserted just before the CCD array splits the two orthogonal polarizations at a 16°-angle to one another with high extinction. Just after beginning a 190-μs exposure[18], we illuminate the atoms

[18]Note that there is a 40-μs pretrigger, so we instruct the camera to expose for 230 μs.

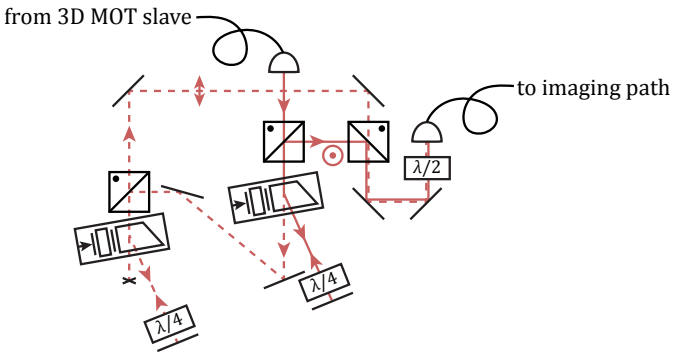

Figure 3.21: Wollaston imaging switches. The same frequency source drives two cascaded AOMs. Separate switches independently shutter each polarization for the normalized Wollaston imaging scheme. The solid (dashed) line represents the optical path for when the AOM shutter for the vertically (horizontally) polarized beam is on.

for 90 μs with horizontally polarized light resonant with the $|2S_{1/2}, F = 1\rangle \rightarrow |2P_{3/2}, F'\rangle$ transition. That detects atoms in $|F = 1\rangle$. After a 10-μs delay, we illuminate the atoms with the same frequency of imaging light but orthogonal polarization. We also turn on MOT cooling light, which depumps atoms from $|F = 2\rangle$ into $|F = 1\rangle$. The second image therefore detects atoms in both of the hyperfine ground states simultaenously. The Wollaston prism sends the two signals to opposite sides of the camera. After the atoms disperse during the CCD readout of the first exposure, we take a background image with the same pulse protocol and use the two exposures to calculate the optical density. We sum the atom numbers in a detection region on each side of the CCD. The normalized excitation is the sum from the vertically-polarized image divided by the sum from the horizontally-polarized image.

This scheme does not exactly normalize to 1. During the first image, if an atom falls out of $|F = 1\rangle$, it stops contributing signal. On average, each atom contributes about 2 signal photons[19] before decaying to $|F = 2\rangle$ and becoming dark. During the second image, however, each atom can contribute more than 2 photons on average because the cooling light can repump it back into the bright state. Measurements indicate that our detection normalization factor is 0.45. Throughout the dissertation, we multiply the number this scheme outputs by a convenient factor of 2 before reporting an axis as a "normalized" $P_{F=1}$.

The shadow in absorption imaging is collimated between the lenses. The shadow must come to a focus at the CCD to form an image. The beam tends to be collimated at the camera in absorption imaging, but that is not strictly required for experiments like ours in which an accurate count of the atom number is inconsequential. We moved the second lens closer to the first lens such that the imaging beam slightly converges onto the CCD (as depicted in Fig. 3.20). Even if the scattering cross sections for the two polarizations were calibrated, this focusing of the illumination light would worsen the calibration.

[19]The 2-photon figure is the result of a Monte Carlo simulation with the decay probabilities governed by Clebsch-Gordan coefficients.

3.6.5 Time-of-flight imaging

We may take the liberty to allow the sample to evolve for some amount of time before exposing an image. The dynamics of the cloud become evident by scanning out this time of flight t_{TOF}. This accesses two important quantities: the sample's temperature and its center-of-mass velocity.

Temperature

Measuring the temperature provides a crucial diagnostic about the experiment and allows us to tune control parameters in order to optimize it. The thermal speed of each atom determines the Doppler shift it sees on the Raman beams and sets a requirement for the bandwidth of the interferometry pulses. Efforts to lower the temperature relax the bandwidth requirement, making the pulse transfers more efficient. Furthermore, the thermal velocities lead to an important thermal dephasing process that limits the signal-to-noise ratio of the phase patterning technique. Knowing the thermal distribution helps in modeling the severity of the problem.

The temperature of the cloud manifests in the Maxwell-Boltzmann distribution of the atoms' thermal velocities along each dimension [141]. We will consider a one-dimensional probability distribution and fit each axis' temperature independently.

$$f_{MB}(v) = \sqrt{\frac{m}{2\pi k_B \mathcal{T}}} \exp\left(-mv^2/2k_B\mathcal{T}\right). \tag{3.6}$$

This is a Gaussian distribution with standard deviation

$$\sigma_v = \sqrt{\frac{k_B\mathcal{T}}{m}}, \tag{3.7}$$

where k_B is the Boltzmann constant, $\mathcal{T}$ is the temperature, and m is the atomic mass.

In spatial coordinates, each atom begins its expansion from position x_0. The Gaussian position probability distribution has some initial width σ_0.

$$p(x_0, 0) = \frac{1}{\sqrt{2\pi\sigma_0^2}} \exp\left(-x_0^2/2\sigma_0^2\right). \tag{3.8}$$

We are interested in the final position distribution. The final positions are related to the velocity, whose distribution we know via Eq. (3.6),

$$v = \frac{x - x_0}{t_{TOF}}. \tag{3.9}$$

To find the final distribution, we must integrate over all the initial positions weighted by the probability of having started at that position

$$p(x, t_{TOF}) = \frac{1}{\sqrt{2\pi\sigma_0^2}} \frac{1}{\sqrt{2\pi\sigma_v^2}} \int dx_0 \exp\left(-x_0^2/2\sigma_0^2\right) \exp\left(-v^2/2\sigma_v^2\right) \tag{3.10}$$

$$= \frac{1}{2\pi\sigma_0\sigma_v} \int dx_0 \exp\left(-x_0^2/2\sigma_0^2\right) \exp\left(-(x - x_0)^2/2\sigma_v^2 t_{TOF}^2\right). \tag{3.11}$$

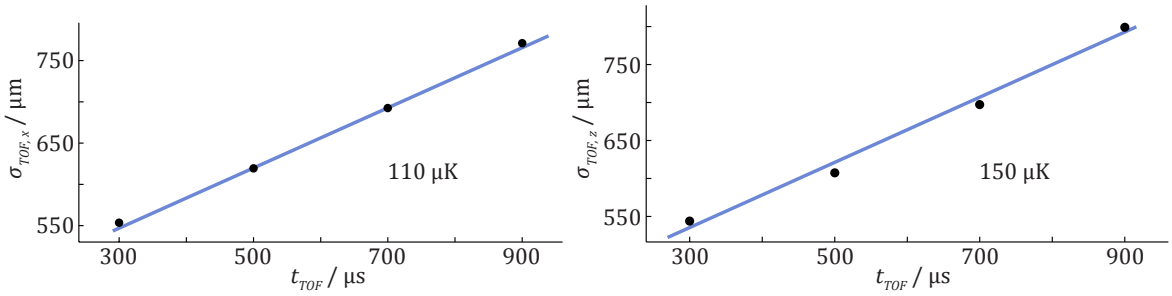

Figure 3.22: Time-of-flight thermometry. At long times, the velocity distribution width is just the linear slope of the gaussian width as a function of time. (07/02/2018, GCs -31963 to -31912)

This is a simple Gaussian integral and its result can be manipulated into the form

$$p(x, t_{TOF}) = \frac{1}{\sqrt{2\pi(\sigma_0^2 + \sigma_v^2 t_{TOF}^2)}} \exp\left(-x^2/2(\sigma_0^2 + \sigma_v^2 t_{TOF}^2)\right). \tag{3.12}$$

After a time of flight t_{TOF}, the position distribution has a gaussian width

$$\sigma_{TOF} = \sqrt{\sigma_0^2 + \sigma_v^2 t_{TOF}^2} \tag{3.13}$$

that is related to the temperature.

For short times, one can fit a series of gaussian density distributions from images taken at varying t_{TOF} with both σ_0 and σ_v as free parameters. Alternatively, at long t_{TOF}, the second term dominates and the width simplifies to $\sigma_v t_{TOF}$. At long t_{TOF}, σ_v is just the linear slope of $\sigma_{TOF}(t_{TOF})$. We fit these points as in Fig. 3.22 to determine the temperature. The temperature along z is likely to be underestimated, since the curvature from the initial width remains quite visible. The 110-μK temperature recorded along x is significantly below the 140-μK Doppler temperature.

This derivation assumes a thermal velocity distribution, so it does not accurately apply to quantum-degenerate gases. Experiments with Bose-Einstein condensates sometimes perform thermometry on the thermal portion of the ensemble and assume the BEC is in thermal equilibrium with it. For deeply low temperatures where there are too few thermal atoms for fitting, the community must develop new and clever thermometry techniques, e.g. [142].

Velocity

We fit the center of the Gaussian distribution as a function of t_{TOF} to x_{TOF} and z_{TOF}. The evolution of the center gives the center-of-mass velocity of the sample $\sim$1 m/s. This quantity is critical in the tune-out measurement because the velocity introduces a Doppler shift on the tune-out beam. The Doppler shift is large enough to introduce a substantial systematic shift. Time-of-flight imaging can only measure the velocity in the plane perpendicular to the

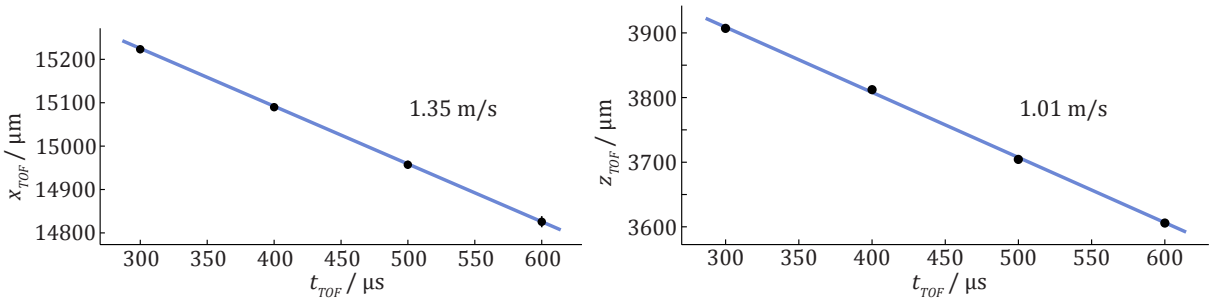

Figure 3.23: Time-of-flight velocimetry. The center-of-mass velocity is the slope of the position as a function of time of flight. (07/30/2018, GCs -4606 to -4563)

imaging beam, so calibrating the Doppler shift the atoms see on the tune-out beam requires a different method. Measuring the velocity in time-of-flight images nevertheless helps to calibrate the systematic.

3.7 Optical pumping

The varying magnetic-field dependence of the Zeeman sublevels' energies is a nuisance at best. Preparing atoms in an $m_F = 0$ state helps to alleviate a constellation of related issues. Atom interferometer experiments prepare $m_F = 0$ states for interferometry using a variety of methods. For example, one might optically pump atoms to an extremal m_F ("stretched state") using a closed MOT cooling transition and perform a series of well-resolved, high-efficiency microwave transfers [91]. We cannot afford this approach, due to lithium's leaky cycling transition and our sluggish microwave Rabi frequency compared to the thermal expansion rate.

3.7.1 Optical pumping light

We can take advantage of a dipole selection rule that prohibits transitions with $F' = F$ for $m_F = m'_F = 0$. We cannot pump efficiently on any such transition for $|2S_{1/2}, F\rangle \to |2P_{3/2}, F'\rangle$ because of the lack of resolution on the D_2 line. Transitions to nearby $F' \neq F$ for $m_F = m'_F = 0$ would be ubiquitous. The $|2S_{1/2}, F\rangle \to |2P_{1/2}, F'\rangle$ transitions offer much better resolution, 15 times the linewidth. Of course, atoms may decay to the wrong hyperfine ground state after excitation, so the process requires repumping. One could perform this pumping on either the $|2S_{1/2}, F = 1\rangle \to |2P_{1/2}, F' = 1\rangle$ transition or the $|2S_{1/2}, F = 2\rangle \to |2P_{1/2}, F' = 2\rangle$. Since there are more states in $|F = 2\rangle$ to which atoms can leak from $|F = 1\rangle$, repumping for the $|2S_{1/2}, F = 2\rangle \to |2P_{1/2}, F' = 2\rangle$ option is more efficient. We repump atoms decaying into $|F = 1\rangle$ with MOT repump light.

We frequency offset lock a homebuilt ECDL near the $|2S_{1/2}, F = 2\rangle \to |2P_{1/2}, F' = 2\rangle$ transition. In an early design, we had a single optical isolator providing about 40 dB of

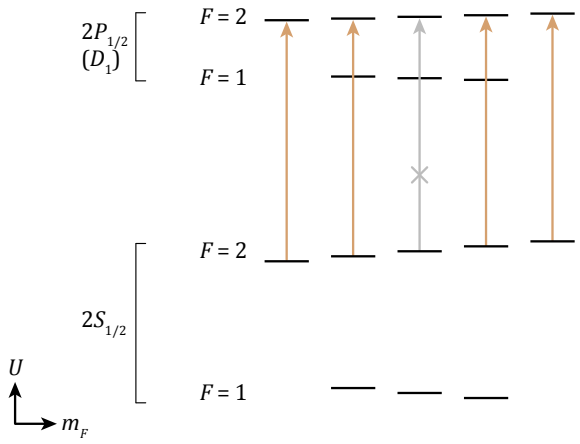

Figure 3.24: Optical pumping levels. Light tuned to the $|2S_{1/2}, F = 2\rangle \rightarrow |2P_{1/2}, F = 2\rangle$ transition pumps atoms to the $|2S_{1/2}, F = 2, m_F = 0\rangle$ state, darkened by a forbidden optical dipole transition.

isolation (Thorlabs IO-5-670-HP). The light couples into an optical fiber between the laser and the vacuum chamber, but reflections from the fiber port injected feedback into the laser despite the isolator. It was crucial to insert a second 40-dB isolator before the fiber port to achieve stability.

After the optical fiber, an 80-MHz AOM shutters optical pumping light. It passes through a polarizing beam splitter to purify the polarization and enters the vacuum chamber roughly coaxially with MOT arm 5 (see Fig. 3.11 and [114]). Propagating in the $x - y$ plane, its polarization is along the z axis. If the pumping beam propagates only in one direction, it biases the momentum transfer of pumping photons along that direction. For symmetry and to increase the scattering rate, a mirror retroreflects the beam back into the chamber for a second, counter-propagating the interaction.

The z axis is defined by the direction of the magnetic field, described below, so there may be a small angle between the polarization and the field. Only after the MOT quadrupole field decays can the bias coils establish a homogeneous, uniform magnetic field such that the light can be π polarized parallel to the field.

3.7.2 Magnetic field for optical pumping

Conceptually, the $m_F = 0$ state is one whose magnetic moment points perpendicular to the magnetic field. The MOT pumps atoms into a stretched state, which means the spins align parallel to the magnetic field (or anti-parallel depending on the g factor). Because the field points in different directions at different spots in the quadrupole field, the spins also point in different directions. Consider Fig. 3.4. The directions of the arrows on axis indicate the direction of the stretched-state spin vector. The field points in different directions so the spins point in different directions. To prepare a pure $m_F = 0$ state, all the spins must point

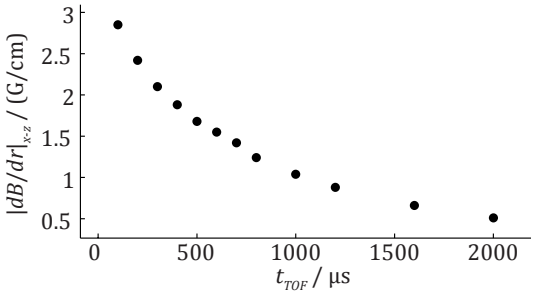

Figure 3.25: Magnetic field gradient decay. The magnetic field gradient decays with a time constant of roughly 1.5 ms. (11/08/2017)

in the same direction and they must be perpendicular to the field.

The spatially-varying MOT field makes pumping to $m_F = 0$ very difficult since the field varies spatially. We must switch off the anti-Helmholtz coils and wait for the gradients from the quadrupole field to decay well below the magnitude of the bias field divided by the size of the cloud. Only then can we establish very purely π-polarized light to minimize any circularly-polarized transitions that pollute the pumping process. The current in the quadrupole coils decays after only 250 μs, but eddy currents in the steel vacuum chamber invigorate the gradients for much longer. We measure the field gradient *in situ* using the magnetic gradient imaging method at varying times of flight after current shutoff.[20] As Fig. 3.26 shows, the gradient decays with a τ_B =1.5-ms time constant, far longer than the coil current.

3.7.3 Molasses and launch

The field gradient decays to 0.5 G/cm after 2 ms. That is a substantial amount of time for the rapidly thermally expanding cloud. To limit the ballistic expansion of the cloud during that time, we leave on the MOT cooling and repump light after switching off the quadrupole field coils. This tactic, in principle, would just create an optical molasses without a restoring force for trapping [42]. The molasses limits expansion more effectively than anticipated, due to the fact that it is not simply a molasses.

The Helmholtz coils turn on well before the anti-Helmholtz coils switch off, which is required due to the switching speed limitation imposed by the large inductance of the bias coils. In the presence of the strong quadrupole field during the MOT stage, the small bias field is of little import. While the quadrupole field decays, on the other hand, its strength begins to diminish with respect to the bias field. The quadrupole field gradient decays from some strength $(dB/dz)_0$ ~20 G/cm proportionally to $\exp(-t_{TOF}/\tau_B)$ as in Fig. 3.26. The

[20]Note that the microwave pulse takes 500 μs, which is a substantial fraction of the times of flight. The measured gradient is therefore some gradient integrated over the 500-μs pulse period just after t_{TOF}. This helps explain why the initial gradient measured in this way is far smaller than the ~20 G/cm we expect for the MOT gradient.

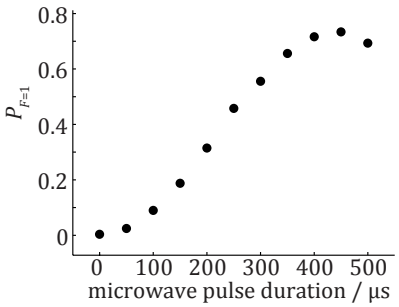

Figure 3.26: Transfer probability for a microwave pulse. A microwave resonant with the ground-state $|F = 2, m_F = 0\rangle \rightarrow |F = 1, m_F = 0\rangle$ transition transfers atoms from $|F = 2, m_F = 0\rangle$ into the detected $|F = 1\rangle$ state with a π pulse duration of $\sim$450 μs. (08/01/3018, GCs 3155 to 3187)

fixed coils place the center at a fixed position we label the origin. Denoting the bias field as B_b, the total field is

$$B(z, t_{TOF}) = \left(\frac{dB}{dz}\right)_0 z \exp\left(-t_{TOF}/\tau_B\right) + B_b. \tag{3.14}$$

The position z_0 where the total field is 0 evolves exponentially in time.

$$z_0(t_{TOF}) = -\left(\frac{dB}{dz}\right)_0^{-1} \exp\left(t_{TOF}/\tau_B\right) B_b \tag{3.15}$$

The sample cannot follow this moving MOT position indefinitely. The finite photon scattering rate from the MOT beam propagating along the direction of the launch eventually becomes insufficient to transfer enough momentum to keep up. The sample quickly reaches a terminal velocity $\sim$1 m/s and z_0 runs away from it.

3.7.4 Microwave spectrum

Optical pumping takes place after the quadrupole field decays and the field is homogeneous across the sample. The $\sim$4-mW OP beam pumps the atoms with a $1/e^2$-intensity waist of $\sim$4 mm. To probe the optical pumping efficiency, we scan the microwave frequency to resolve each transition. The $|F = 2, m_F = 0\rangle \rightarrow |F = 1, m_F = 0\rangle$ microwave transition is strongest when the pumping efficiency is maximal. We tune the control parameters for the three axes of Helmholtz coils to maximize the pumping efficiency.

The spectrum reveals the magnitude of the bias field. A microwave transition involving one singly-Zeeman-shifted level (e.g. $m_F = 0 \rightarrow m'_F = 1$) is 700 kHz per 1 G field in the ^{7}Li ground state. The zero-field resonance is 803.504 MHz, so the peak centers in Fig. 3.27 indicate that the bias field is $\sim$1.3 G. The Earth's magnetic field is about 0.5 G in Berkeley and runs roughly North and down, so we choose to orient the field Northward so the Earth's

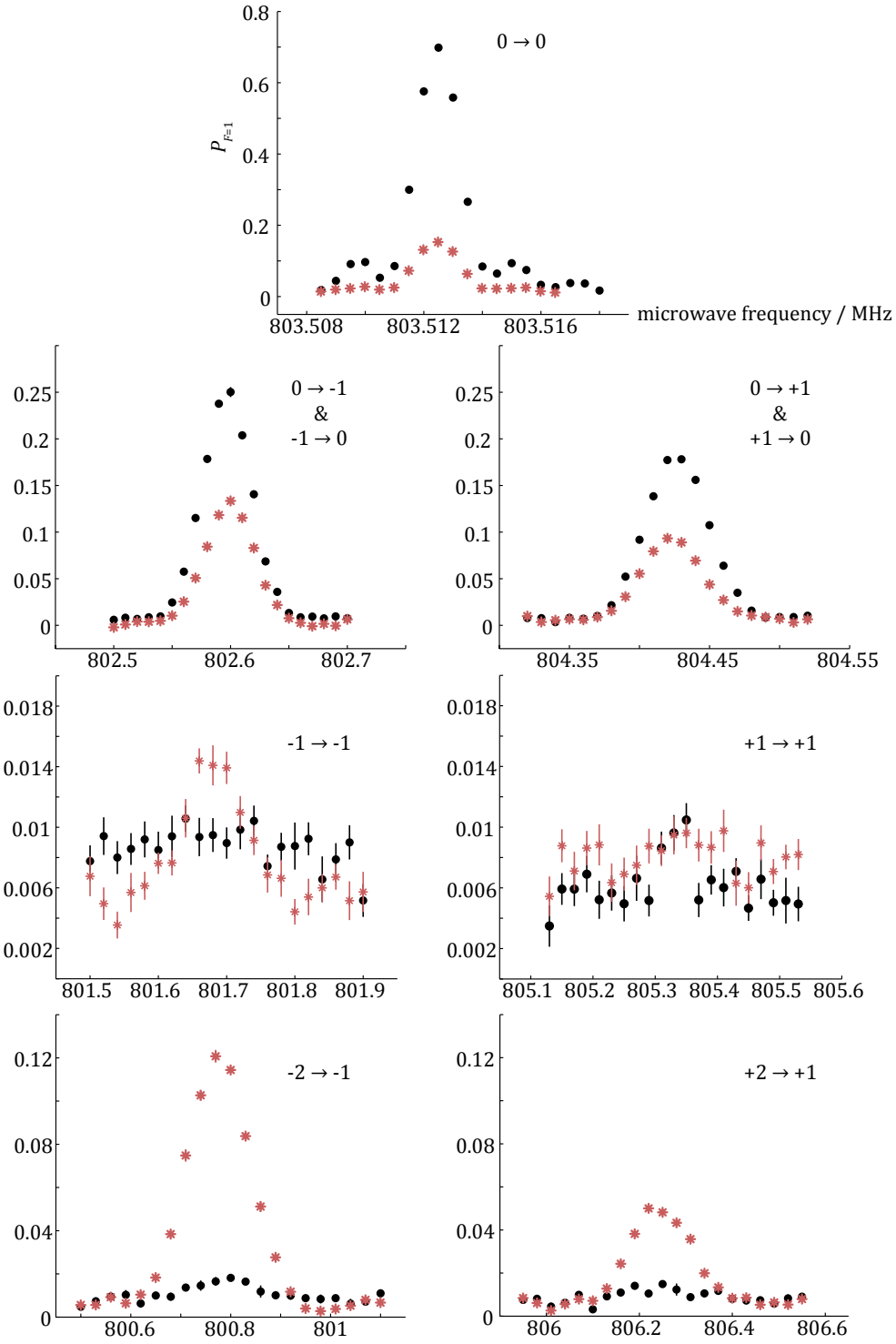

Figure 3.27: Microwave spectra with and without optical pumping. Black circles (red asterisks) indicate pulse transfers with (without) optical pumping with a 500-μs pulse. Labels specify $m_F \to m'_F$ for $|F = 2, m_F\rangle \to |F = 1, m'_F\rangle$. (08/01/3018, GCs 2992 to 6409)

field adds to the field from the bias coils.[21] Otherwise, much of the coils' limit would be dedicated to first cancelling Earth's field before generating a non-zero bias contribution in the opposite direction.

Zeeman population estimates

It is important to obtain rough estimates the populations in each of the Zeeman sublevels after optical pumping. No atoms appear in $|2S_{1/2}, F = 1\rangle$ due to the strong MOT repump that is on during optical pumping.

The $m_F = 0 \to 0$ resonance is only slightly broadened by the quadratic Zeeman gradient, so we assume that the peak height of the $0 \to 0$ resonance represents the full population in $m_F = 0$: 80%.[22]

The $m_F = \pm 1 \to \pm 1$ peaks do not register any signal beyond imaging noise after optical pumping. That absence is not due to a lack of π polarization in the microwave field because the $m_F = 0 \to 0$ resonance is healthy. We therefore assume that no population in the $m_F = \pm 1$ states survives optical pumping.

That assumption allows us to estimate the polarization using the $m_F = 0 \to 0$, $0 \to +1$, $0 \to -1$ resonances. Each resonance originates from the same population, so the relative peak heights in the σ^+ and σ_- transitions give the ratio of microwave power in each polarization. The $0 \to +1$ peak is 3/4 as high as the $0 \to -1$ peak, so the ratio of powers in the circular polarizations is $I^+ = (3/4)I^-$.

With 80% in $m_F = 0$ and no population in the $m_F = \pm 1$ states, the remaining 20% is distributed among $m_F = \pm 2$: $P_{+2} + P_{-2} = 0.2$. The power ratio multiplies the relative peak heights of the $+2 \to +1$ and $-2 \to -1$ transitions. The peak height (A) ratio is equal to the ratio of populations multiplied by the fraction of microwave power driving each transition: $A_{+2\to+1}/A_{-2\to-1} = P_{+2}I^-/P_{-2}I^+$, so $P_{+2}/P_{-2} = A_{+2\to+1}I^+/A_{-2\to-1}I^- = (3/4)A_{+2\to+1}/A_{-2\to-1} \approx (3/4)0.022/0.06 = 0.275$. Through $(1 + .275)P_{-2} = 0.2$, this yields populations of $P_{-2} = 0.16$ and $P_{+2} = 0.04$.

After optical pumping, the fractional populations in the m_F sublevels of $|2S_{1/2}, F = 2\rangle$

[21] Though Earth's field reported by NOAA has an equal component downward towards the ground, we do not use the y axis coils for the tune-out measurement. Our earlier projects did energize those coils, but we believe the installation of of the LIAD LED at the 2D MOT in late 2017 modified the local field to cancel Earth's vertical component. Let this be a warning that adding new components can substantially change local fields.

[22] The peak height is admittedly closer to 70% in Fig. 3.27. That is because I multiply detected populations by a convenient factor of 2 to get a number that is close to properly normalized given the Wollaston imaging technique. A more accurate factor to use throughout the dissertation would have been 2.2. The more accurate factor yields a population of 80% in $m_F = 0$.

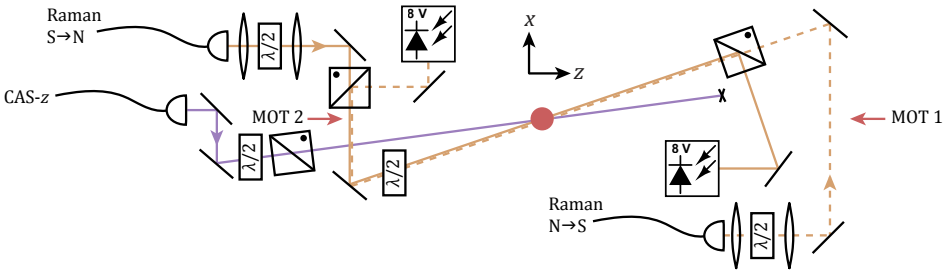

Figure 3.28: Raman and cold-atom spectroscopy (CAS)-z beam path to sample.

are

$$P_{m_F=0} = 0.80(2) \tag{3.16}$$
$$P_{m_F=-1} = P_{m_F=+1} = 0.00(2) \tag{3.17}$$
$$P_{m_F=-2} = 0.16(2) \tag{3.18}$$
$$P_{m_F=+2} = 0.04(2), \tag{3.19}$$

where the uncertainties come from imaging noise and peak height estimations.

In considerations like those above, one should only compare peak heights for transitions with the same number of total Zeeman shifts since they are broadened by the gradient similarly. Comparing peak heights across transitions of different total number of Zeeman shifts would require accounting for different suppression factors that describe how the gradient broadens each peak and reduces its height.

3.8 Raman beams

Fig. 3.28 shows how the Raman beams enter the sample along the North-South axis, tilted by $\sim 4^\circ$ with respect to z in the imaging plane. They have orthogonal linear polarizations.

3.8.1 Raman frequency generation and modulation f_m

The splitting between the Raman frequencies must match the 803-MHz hyperfine splitting in the ground state. The unbalanced intensities of the Raman beams introduce a differential AC Stark shift between the levels, so the most efficient pulse transfer occurs on the Stark-shifted resonance about 1 MHz away from the bare resonance. For the recoil project with a Ramsey-Bordé interferometer phase that depends on the detuning from bare resonance, we are forced to tune the splitting near the bare resonance as opposed to the Stark-shifted resonance. That reduced the pulse transfer efficiency for that project.

The 2D MOT slave laser, injection-locked to the master laser, injection locks the Raman slave laser. Two cascaded 400-MHz AOMs (IntraAction ATM-4001A1) shift a portion of the optical power up and down in frequency (see Fig. 3.29). Since the slave laser locks near the

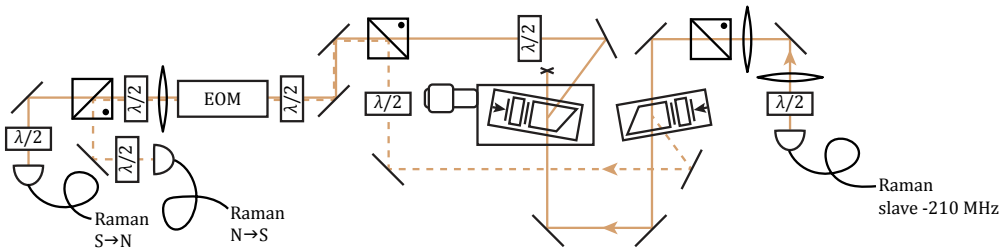

Figure 3.29: Raman beam generation. Two cascaded 400-MHz AOMs shift the solid line up in frequency and the dashed line down. The EOM acts as a voltage-controlled $\lambda/2$ wave plate to reverse the frequencies' propagation vectors at the atoms. We removed the EOM for the tune-out measurement to get more Raman power at the atoms.

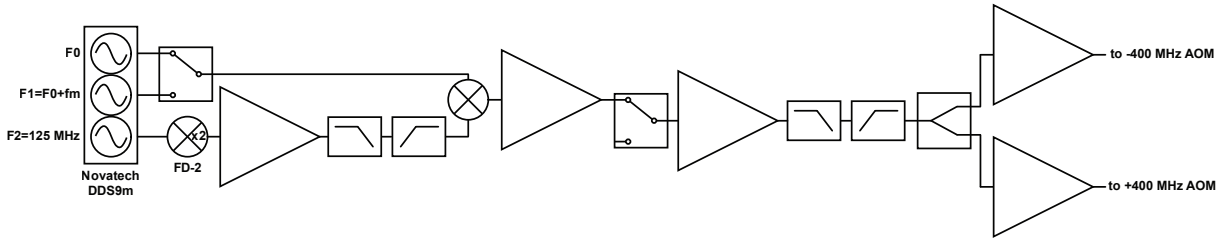

Figure 3.30: Raman frequency generation.

cross-over resonance 400 MHz between the $|2S_{1/2}, F = 1\rangle \rightarrow |2P_{3/2}, F'\rangle$ and $|2S_{1/2}, F = 2\rangle \rightarrow |2P_{3/2}, F'\rangle$ transitions, these 400-MHz AOMs would shift the two frequencies onto resonance. To introduce an appreciable single-photon detuning to drive ground-state Raman transitions, a continuously operating 210-MHz AOM shifts the optical frequency downward before the cascaded 400-MHz AOMs. A TA also amplifies the optical power before it arrives at the cascaded 400-MHz AOMs. Roughly 180 mW enter the setup in Fig. 3.29 via an optical fiber.

A Novatech DDS9m direct digital synthesizer (DDS) provides the frequencies that drive the 400-MHz AOMs (see Fig. 3.30). Its four channels step with terrific 0.1-Hz precision, but each can only reach a maximum of 171 MHz. We first double one channel at F2 = 125 MHz to generate 250 MHz. The 250-MHz signal mixes with one of two other channels as selected by a microwave switch. Those two channels operate near F0=151.75 MHz so that twice the drive frequency matches the 803.5-MHz ground-state hyperfine splitting. We operate those two channels at slightly different frequencies in order to introduce a frequency hop on the AOMs. The second of four interferometer pulses triggers a latch that switches which channel mixes with the 250-MHz tone. That introduces a modulation frequency f_m onto the final two pulses of a four-pulse sequence (F1 = F0 + f_m) that we use to tune the phase of the interferometer.

The two Raman frequencies must arrive at the atoms simultaneously to drive a transition. When a microwave switch passes the 400-MHz tone to an amplifier that drives the AOMs, a

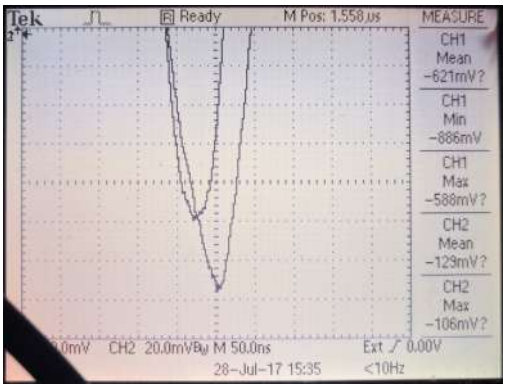

Figure 3.31: Temporally overlapped Raman pulse. Two photodetectors sense each of the Raman beams after they pass through the chamber. Mounting one of the 400-MHz AOMs on a translation stage permits temporal overlap. (07/28/2017)

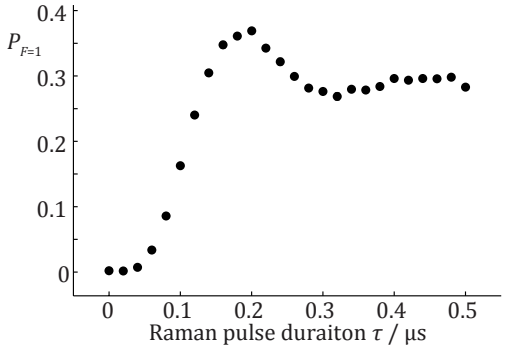

Figure 3.32: Raman pulse transfer probability. The dephasing is worse than Fig. 2.9, likely due to the intensity profile of the beam. (07/17/2018 GCs -32025 to -31842)

sound wave begins propagating through the tellurium dioxide crystal from the piezoelectric transducer. The speed of sound in tellurium dioxide is about 4 km/s. If the beams enter each of the AOMs at a different distance to the piezoelectric transducer, it will take a different amount of time for the sound wave to reach the beam and shutter it. To match the shutter time, it is crucial to place one of the AOMs on a translation stage and tune it so that the two Raman beams shutter simultaneously. A bare, reverse-biased photodiode (Thorlabs FDS010) detects each Raman beam after it has passed through the chamber. Each signal drops across a terminator at an oscilloscope. We tune the translation stage to overlap the leading edge of the two pulse traces (see Fig. 3.31).

3.8.2 Fast pulses

Each atom in the thermal distribution sees a different Doppler shift on each of the Raman beams. Because the beams propagate along opposite directions and drive velocity-sensitive

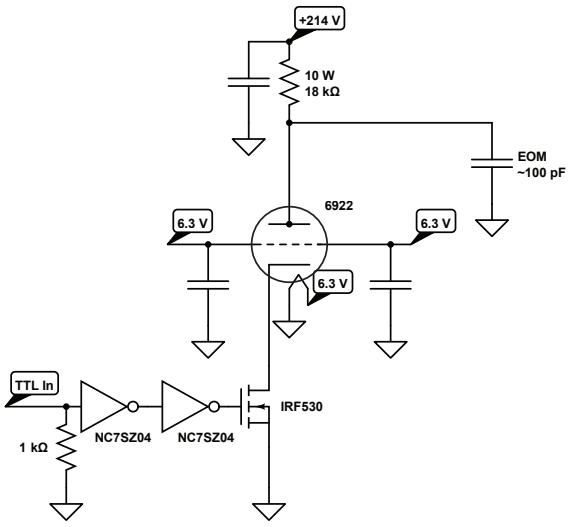

Figure 3.33: Vacuum tube switch for EOM. The vacuum tube can handle a much higher voltage in the off state than the MOSFET.

Raman transitions, an atom moving towards one beam at velocity v sees it shifted to the blue and the opposite beam shifted to the red. So the total Doppler shift on the two-photon transition is $\sim 2v/(671\text{ nm})$. The velocity width $2\sigma_v$ sets the range of Doppler shifts for the $\sim$140 μK sample, $4\sigma_v/(671\text{ nm})$=2.4 MHz. The Raman pulses must span this spectral bandwidth to address the entire sample.

We use a fast beam splitter pulse with τ =160 ns that offers a Fourier-limited bandwidth $1/2\pi\tau \sim 1$ MHz. Roughly 30 mW of light 200 MHz below the $|2S_{1/2}, F = 2\rangle \rightarrow |2P_{3/2}, F'\rangle$ transition and 15 mW of light 200 MHz below the $|2S_{1/2}, F = 1\rangle \rightarrow |2P_{3/2}, F'\rangle$ transition arrive at the atoms. The beams have a $1/e^2$ gaussian intensity waist of 3.6 mm. They follow a lin-$\perp$-lin scheme where one is polarized roughly along x and the other along y. The propagate close to the z axis, tilted with respect to it by 4°. Scanning the pulse duration τ produces Rabi flopping (Fig. 3.32) that decoheres due to the varying Rabi frequency across the ensemble (due to the intensity profile of the beams and the Doppler width of the thermal sample).

3.8.3 Raman switching

The rapid Raman transition demands rapid pulse shuttering. Cicero's 10-μs resolution is insufficient, so a Cicero pulse triggers a SRS DG645 digital delay/pulse generator that drives the pulse sequences for interferometry.

Furthermore, a Ramsey-Bordé interferometer requires that the momentum transfer for the third and fourth pulses is opposite to the momentum transfer of the first and second pulses. The direction of the Raman vectors must reverse between the second and third pulses. Each Raman frequency launches towards the atoms out of an optical fiber from either side

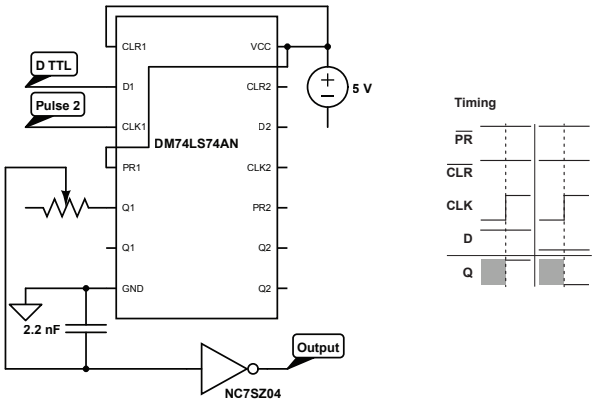

Figure 3.34: Latching switch. The second of four Ramsey-Bordé pulses is teed off and input into the CLK input. The output of the positive-edge-triggered flip-flop is slightly delayed by a low-pass filter and inverted to control the MOSFET in the vacuum tube switch. This circuit also controls the DDS' switching between F0 and F1 for Raman frequency generation.

of the optical table. To switch the direction, the fiber from which each frequency launches must reverse. We insert an EOM before a PBS that splits the polarization-labeled Raman frequencies into one fiber or the other. Switching the voltage on the EOM to its "half-wave" voltage turns it into a $\lambda/2$ wave plate (see Fig. 3.29).

The half-wave voltage may be identified by polarizing a beam that transmits through a polarizer, inserting the EOM, and tuning its DC voltage until the polarizer extinguishes the beam. For our EOM, this voltage is near 214 V. A standard MOSFET does not typically offer a sufficiently high drain-source voltage, but vacuum tubes do. Fig. 3.33 shows the circuit that rapidly switches the high voltage on the EOM. A MOSFET acts as a voltage-controlled switch, while a vacuum tube (here a 6922) handles the high voltage. For an ∼100-pF EOM capacitance and a 18-kΩ load resistor, the switch operates much faster than 2 μs.

Fig. 3.34 illustrates the trigger that drives the MOSFET in Fig. 3.33. A tee samples the second of four interferometry pulses from the SRS DG645, which drives a positive-edge-triggered flip flop that latches the logic state driving the MOSFET. A second trigger of the pulse sequence resets the latch at the end of each experimental shot, after the atoms have diluted for the background absorption imaging exposure.

This latch circuit also drives the microwave switch that determines which DDS frequency mixes into the Raman frequencies, adding f_m to the third and fourth pulses in the tune-out measurement.

3.9 Tune-out setup

The beam measuring the tune-out wavelength originates from the path in Fig. 3.35. The reference light for the optical beat note phase lock comes from the Raman slave laser. It is the undiffracted light in the 210-MHz AOM that generates the single-photon detuning for

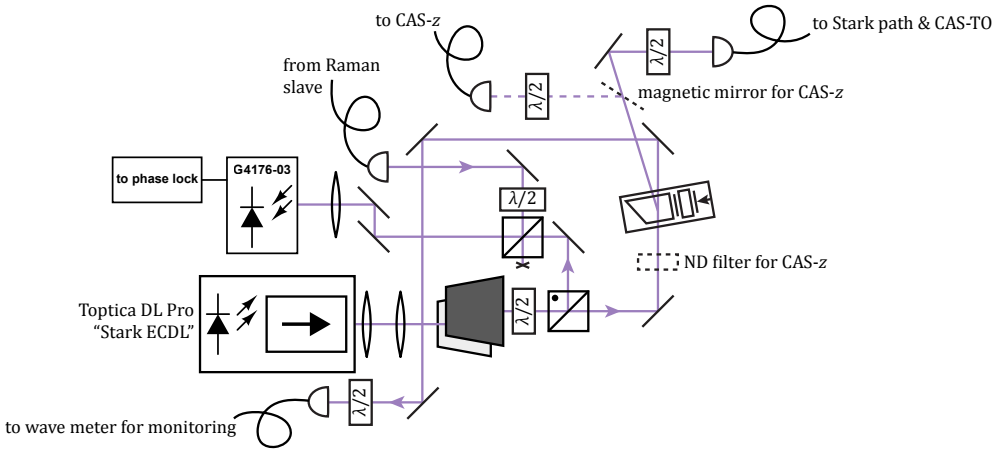

Figure 3.35: Stark ECDL optics.

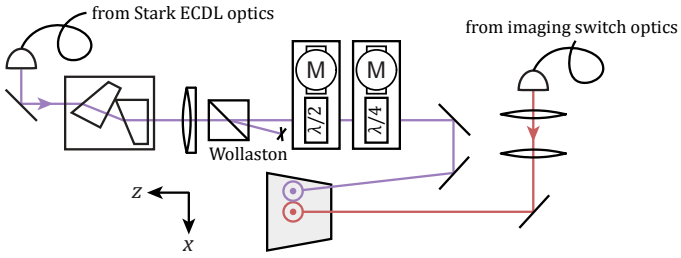

Figure 3.36: Tune-out and CAS-TO optics.

the Raman transitions, so this reference light is locked to the $|2S_{1/2}\rangle \rightarrow |2P_{3/2}\rangle$ crossover resonance.

The tune-out measurement requires the Stark-shifting light to propagate as parallel to the imaging axis as possible, here offset by $\sim 5°$. Fig. 3.36 illustrates the beam path for measuring the tune-out wavelength. The beam enters an anamorphic prism pair (Thorlabs PS883-A) that elongates the beam to an aspect ratio of 4 before it encounters the 500-mm achromatic lens that focuses the beam onto the sample. The elongated axis is the vertical axis perpendicular to the optical table.[23] The lens focuses the elongated (non-elongated) axis with a higher (lower) numerical aperture to a size of ~ 150 μm (~ 600 μm) at the atomic sample. Two motorized wave plates, one $\lambda/2$ and one $\lambda/4$, control the polarization of the Stark-shifting beam. We also perform CAS-TO spectroscopy along the y axis. Fig. 3.28 shows how the CAS-z beam enters the sample along the North-South axis tilted by $\sim 2°$. Its polarization is very nearly along x.

[23] Fig. 3.36 shows the anamorphic prism pair elongating the beam along the axis parallel to the table. That is an artistic liberty taken for the purposes of the diagram. The beam is truly elongated along the axis perpendicular to the table.

Parameter	Value
Sample temperature	$\sim$140 μK
Thermal speeds	$\sim$1/2 m/s
Magnetic field for optical pumping and interferometry	1.3 G
Microwave π pulse time	450 μs
Optical pumping beam waist	4 mm
Optical pumping power	4 mW
Raman beam waist ($1/e^2$ intensity)	3.6 mm
ω_1, $\omega_2 (< \omega_1)$ Raman beam powers	15, 30 mW
Raman single-photon detuning	-2$\pi\times$ 210 MHz
Raman $\pi/2$ pulse time	160 ns
Stark (tune out) x, z beam waists ($1/e^2$ intensity)	600, 150 μm
Stark (tune out) beam power	3 mW
CAS-z beam waist ($1/e^2$ intensity)	1.5 mm
CAS-z beam power	0.4 mW
Interferometer contrast	10%

Table 3.2: Experimental parameters.

3.10 Collected relevant parameters

This section houses Table 3.2, a quick lookup of some of the experimental parameters of most interest to readers.

Chapter 4

Sensing atomic recoil above the temperature

Atom interferometry has produced one of the preferred methods for measuring the fine-structure constant α_{fsc}. Previous measurements have required that the samples entering the interferometer have kinetic energy distributions below the recoil temperature. Achieving such narrow velocity distributions is nontrivial, lossy, and only works very well for a small handful of atomic species. Here, we demonstrate and describe a technique that allows measuring the fine-structure constant without requiring sub-recoil temperatures [143].

Developing interferometry techniques that work at high temperatures would open up new candidates for interferometry, like electrons. Since lithium is also difficult to cool, it volunteers a testbed for proving out such techniques. While lithium does not offer quite as high of a recoil frequency as an electron, its $2\pi\times$63-kHz recoil is still substantially larger than that of Cs. In this chapter, we focus on extending recoil interferometry to higher temperatures.

4.1 Prior techniques

Two different atom interferometry techniques have produced terrific measurements of α_{fsc}.

The first is based on simultaneous conjugate Ramsey-Bordé interferometers. A single Ramsey-Bordé (Fig. 2.16) establishes a kinetic energy difference between the upper and lower arms by only allowing the upper arm of the interferometer to spend time with the excess kinetic energy of photon recoil. Integrating a substantial phase requires increasing the pulse separation time T and the baseline along which the arms separate, so having the long baseline of an atomic fountain improves the measurement precision. Doing so on Earth's surface where most labs are currently located[1] also subjects the atoms to the local gravitational acceleration. The $2kgT(T+T')$ phase accrued as a result confounds the

[1]NASA's Cold Atom Laboratory announced that it had successfully cooled atoms on the International Space Station in 2018.

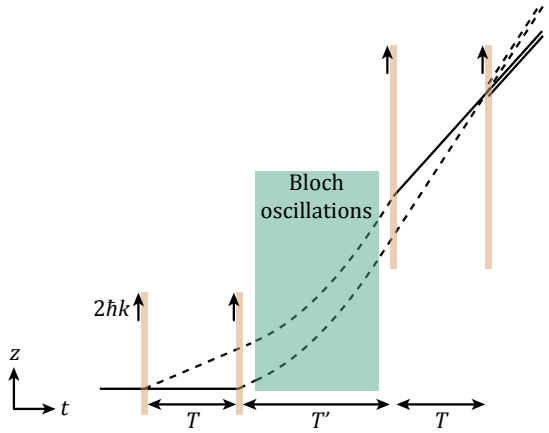

Figure 4.1: Accelerated four-pulse Mach-Zehnder interferometer. This interferometer measured the fine-structure constant to 0.62 ppb [73].

measurement of the atoms' recoil frequency. Running two interferometers simultaneously as in Fig. 2.18 produces two signals that depend on the recoil with opposite sign but gravity with the same sign. By subtracting the two simultaneous conjugate interferometers' phases, the gravity term cancels and only the recoil term remains. This requires independently measuring the two interferometers' phases by independently detecting all four interfering outputs. Detecting each output separately demands a sample whose velocity spread is much smaller than the velocity with which the arms separate. In other words, the velocity spread needs to be "sub-recoil". Warm samples like our lithium sample do not satisfy this criterion. Our sample's thermal speeds are nearly 10 times higher than the recoil speed. Nevertheless, this technique achieved a 0.20-ppb precision on α_{fsc} using a sub-recoil sample of ^{133}Cs.

A different technique does not require two simultaneous interferometers. In contrast to the previous measurement, it uses Raman transitions as beam splitters. That labels the outputs according to the internal atomic state, so state-specific detection obviates the need for spatially resolving the outputs that set the cooling demands above. The interferometer scheme is based on a four-pulse Mach-Zehnder like Fig. 2.19. That interferometer has no recoil phase because each arm spends the same time recoiling with the same energy. We must recognize that it is not the difference in speed between the arms that determines the phase, but the difference in energy. Because the energy of an arm scales with the square of the number of photon momenta it has absorbed, it still is possible to achieve a large kinetic energy difference between two arms distinguished by only two photon momenta provided that each is biased to a large offset speed. Accelerating two arms of an interferometer using Bloch oscillations in a swept optical lattice as in Fig. 4.1 produces this bias in speeds [144]. After N_{BO} photon momenta transferred from Bloch oscillations during T', the final T boasts an upper arm recoiling with N_{BO} photon momenta and a lower arm recoiling with $N_{BO}+2$ photon momenta. The difference in kinetic energy between the states is $\hbar(4N_{BO}+2)\omega_r$,

which accrues phase over T.[2] Despite offering state-labeled outputs, this technique requires a sample cold enough to efficiently undergo Bloch oscillations for coherent acceleration. Thus, it is also not suitable for warm samples. Nevertheless, this technique achieved a 0.62-ppb precision on α_{fsc} using a sub-recoil sample of ^{87}Rb [73].

4.2 Beating fringes

A lukewarm sample of 300-μK ^{7}Li demands a new toolkit for recoil interferometry. The thermal speeds are much larger than the recoil speed, so spatially-resolved detection is impossible. One could filter the velocity of the sample using a long velocity-selective Raman transition with a sub-recoil Fourier-limited bandwidth, but that would sacrifice any signal from the majority of the sample whose thermal speeds and Doppler shifts preclude satisfying the resonance condition. We instead use the entire sample, addressing it with short, high-bandwidth Raman pulses that cover the Doppler spread (see Figs. 2.8 and 2.9 for theory and Fig. 3.32 for data).

Covering the Doppler spread with high-bandwidth pulses also fails to resolve the different Doppler-shifted resonances of the transitions involved in each of the conjugate Ramsey-Bordé interferometers (see Fig. 2.17). Therefore, these high-bandwidth pulses drive each of the conjugate interferometers in Fig. 2.18 simultaneously and unavoidably. Sub-recoil samples do discriminate between those Doppler shifts, so driving each transition historically required intentionally modulating the beam splitter frequencies to address them [124, 72].

The presence of both simultaneous conjugate interferometers and the lack of spatial resolution produces two overlapped signals, one from each interferometer. Summing the output probabilities of Fig. 2.18 like in Eq. (2.192):

$$P_{SCRBb} = |c_{b1}|^2 + |c_{b2} + c_{b3}|^2 + |c_{b4}|^2 + |c_{b5}|^2 + |c_{b6} + c_{b7}|^2 + |c_{b8}|^2, \tag{4.1}$$

producing two separate interference terms that add. We assign a contrast to each of the interferometers, $\mathcal{C}^+$ for the upper, conjugate interferometer and $\mathcal{C}^-$ for the conventional interferometer. The two interferometers have phase differences $\Delta\phi^{\pm} = \pm 8\omega_r T - 2\delta T$.[3] With a background population of $\mathcal{B}$, the interferometer signal becomes

$$s_{SCRB} = \mathcal{B} - \frac{\mathcal{C}^+}{2}\cos(8\omega_r T - 2\delta T) - \frac{\mathcal{C}^-}{2}\cos(-8\omega_r T - 2\delta T). \tag{4.2}$$

We neglect the acceleration phase here since we operate the interferometer perpendicular to gravity. The two interferometers' contrasts are roughly equal $\mathcal{C}^+ \approx \mathcal{C}^- \equiv \mathcal{C}^{\pm}$ because the

[2] The total phase difference $4N_{BO}\omega_r T$ is less by the $2\omega_r T$ phase accrued by the upper arm during the first T.

[3] The sign on δ has suddenly reversed with respect to what appears in Eqs. (2.225) and (2.241). Those previous derivations assumed the interferometer starts in the lower-energy hyperfine state $|a\rangle$ and recoils into the higher-energy state $|b\rangle$ (as is canonical). In the interferometry results henceforth in this dissertation, we optically pump to $|b\rangle = |2S_{1/2}, F = 2\rangle$, which recoils into $|a\rangle = |2S_{1/2}, F = 1\rangle$. The roles of ω_1 and ω_2, as well as ω_a and ω_b are all reversed under this state reversal. That flips the sign that appears in front of δ.

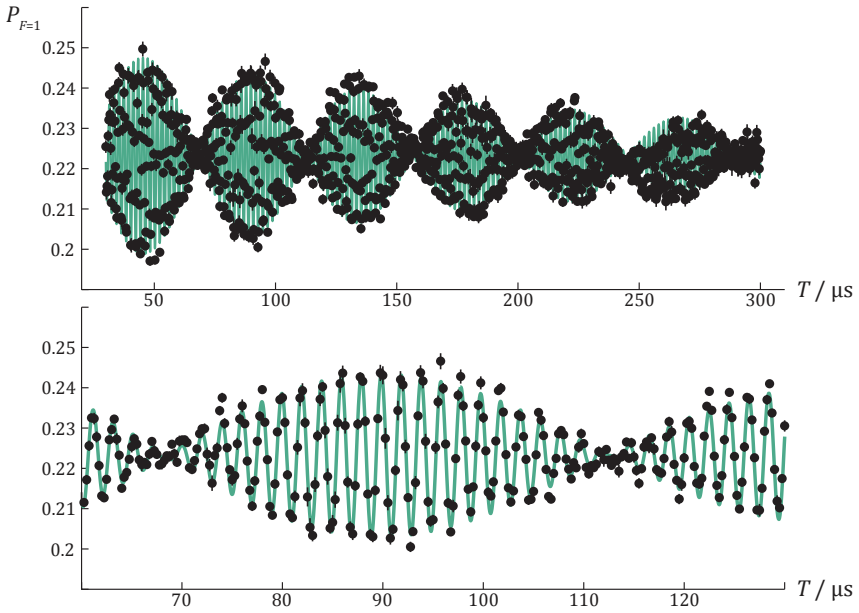

Figure 4.2: Beating fringes for $\omega_1 - \omega_2 = 2\pi \times 803.518$ MHz. (08/29/2016 GCs 25205 to 30726)

difference in resonant Doppler shifts involved in each interferometer is well within the pulse bandwidth. Then,

$$s_{SCRB} = \mathcal{B} - \frac{1}{2}\mathcal{C}^{\pm}\left(\cos(8\omega_r T - 2\delta T) + \cos(-8\omega_r T - 2\delta T)\right). \tag{4.3}$$

The sum of cosines adheres to $\cos(a+b) + \cos(a-b) = 2\cos(a)\cos(b)$.

$$s_{SCRB} = \mathcal{B} - \mathcal{C}^{\pm}\cos(8\omega_r T)\cos(2\delta T). \tag{4.4}$$

The overlapped signals from the simultaneous conjugate interferometers advance at different phase rates for nonzero two-photon detuning δ. Recall that the detuning this references is the difference between the laser frequency difference and the hyperfine splitting with the light off. The latter includes any Zeeman shifts that accompany local magnetic fields. For nonzero δ, the two signals beat.

Fig. 4.2 shows beating fringes for a laser frequency difference of $\omega_1 - \omega_2 = 2\pi \times 803.518$ MHz. We tune the laser frequency difference by tuning the frequency of a DDS channel that produces the Raman splitting.[4] There is a slow modulation of the fringe amplitude from the $\cos(2\delta T)$ term that multiplies the fast $\cos(8\omega_r T)$ fringes. The roughly 3 full rotations of the

[4]There are two channels involved. One parks at 125 MHz and doubles to 250 MHz. The other ("rf1"≈151.755 MHz) mixes against the 250-MHz tone to produce 410.755 MHz. This frequency drives two AOMs. One AOM increases a Raman beam's frequency to ω_1 and the other AOM decreases the other Raman beam's frequency to ω_2. The difference between the two beams is twice that of either single AOM's frequency: ≈ 803.510 MHz.

$\omega_1 - \omega_2$ / 2π MHz	ω_r / 2π kHz	decay time / μs
803.500	63.1611(37)	252(12)
803.502	63.1654(45)	245(13)
803.504	63.1609(32)	281(12)
803.506	63.1600(28)	277(11)
803.508	63.1648(19)	297.5(8.3)
803.510	63.1610(43)	248(14)
803.512	63.137(18)	260(260)
803.514	63.1661(27)	314(13)
803.516	63.1262(38)	228(10)
803.518	63.1629(23)	234.5(6.4)
803.520	63.1664(49)	261(17)

Table 4.1: Fit parameters from beating fringes. The parenthesis specify the 1-σ fit uncertainty on each parameter.

amplitude oscillation in 270 μs implies that $\delta \approx 2\pi$ 5.5 kHz, though the sign is not immediately obvious. We know from the microwave spectra (Fig. 3.27)[5] that the quadratically-Zeeman-shifted resonance between $|2S_{1/2}, F = 2, m_F = 0\rangle$ and $|2S_{1/2}, F = 1, m_F = 0\rangle$ is about 803.5125 MHz. That resonance is 5.5 MHz from the laser frequency difference, just as we would expect.

The separation of time scales between a small 2δ and a comparatively large $8\omega_r$ isolates the recoil frequency as the sole contributor to the fast oscillations. We may fit the fringes to determine ω_r. In addition to the contrast, δ, ω_r, and background population as they appear in Eq. (4.4), we also include a decay term on the fringe amplitude. Due to the high number of fit parameters and the nonlinear fit function, faithfully fitting the fringes requires a careful choice of seed parameters.

Fig. 4.3 shows beating fringes for a range of δ, each with its own fit.[6] At the time, the thermal fluctuations in the position of the sample were rather dramatic (prior to installing the curtains in Fig. 5.9 for the tune-out measurement). The drifting position led to a drifting pulse transfer efficiency. Unique contrasts and background populations for each scan are the combined result of those thermal effects and a newly tuned $\pi/2$ pulse time for each scan.

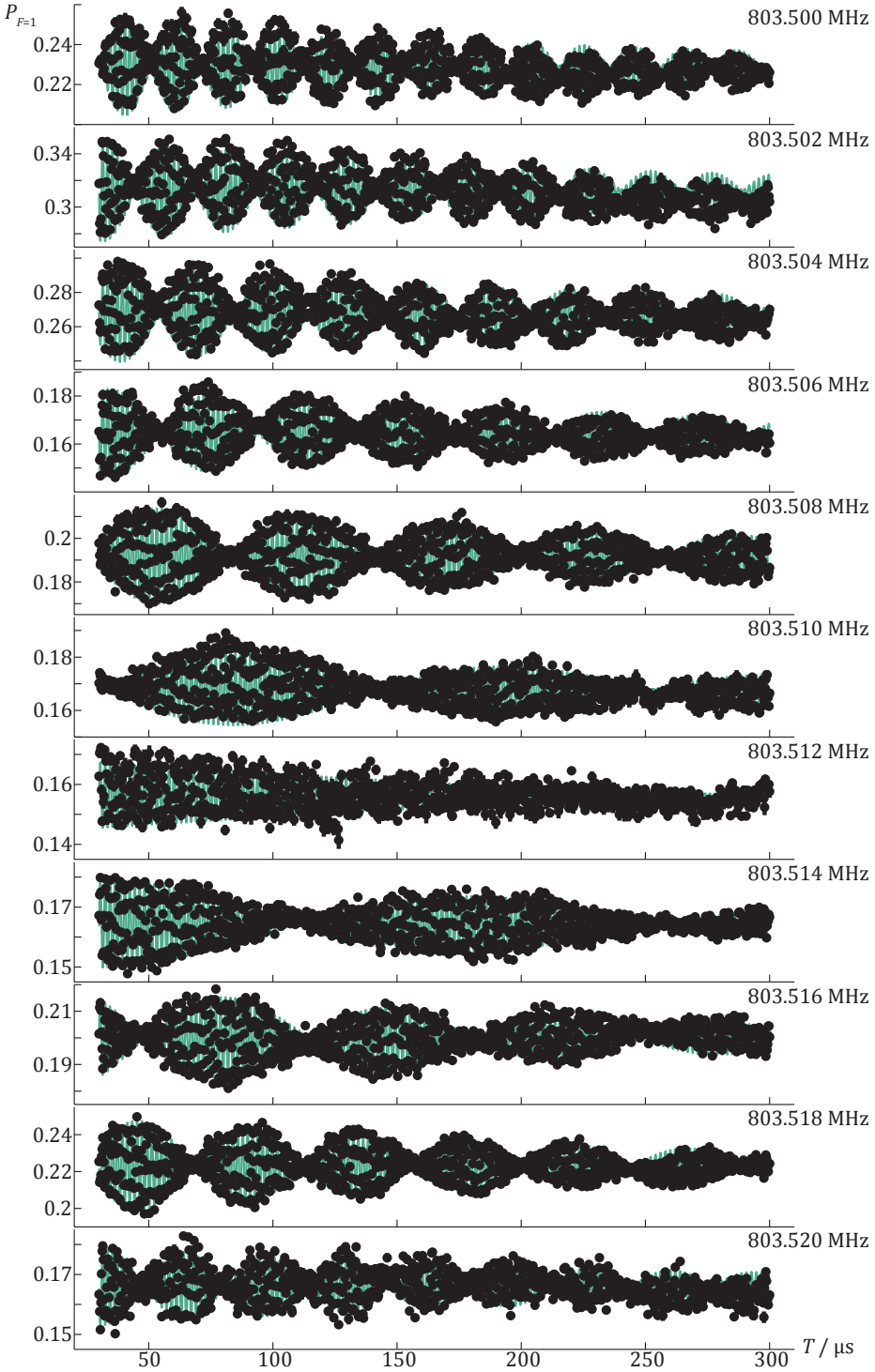

Figure 4.3: Beating fringes for several $\omega_1 - \omega_2$.

4.2.1 Recoil frequency

The most interesting parameters from the fits in Fig. 4.3, collected in Tab. 4.1, are the recoil frequency ω_r and the $1/e$ contrast decay time constant. The weighted average of the fits to the recoil frequency gives $2\pi \times 63.161(1)$ kHz. While we did not precisely measure the wave number of the light, we do know it far better than the statistical uncertainty on that fit, to 20 MHz easily. The wavelength of the Raman light tuned 200 MHz below the D_2 crossover resonance is $\lambda = c/(446810090(20)\text{ MHz})$=670.96171(3) nm. Given $\hbar/m = \omega_r\lambda^2/2\pi^2$, we achieve

$$\frac{\hbar}{m} = 9.0510 \times 10^{-9}\ \text{m}^2/\text{s}, \tag{4.5}$$

with a statistical uncertainty given by

$$d\left(\frac{\hbar}{m}\right)_{\text{stat}} = \sqrt{\left(\frac{\partial(\hbar/m)}{\partial\omega_r}\right)^2 d\omega_r^2 + \left(\frac{\partial(\hbar/m)}{\partial\lambda}\right)^2 d\lambda^2} \tag{4.6}$$

$$= \sqrt{\frac{(670.96171\text{ nm})^4}{\pi^2}(1\text{ Hz})^2 + \frac{4(63.161\text{ kHz})^2(670.96171\text{ nm})^2}{\pi^2}(30\text{ fm})^2} \tag{4.7}$$

$$= 1.4 \times 10^{-13}\ \text{m}^2/\text{s}. \tag{4.8}$$

Thus,

$$\alpha_{fsc} = 0.00729699(6)_{\text{stat}}. \tag{4.9}$$

The reported error is purely statistical because we have made no effort to restrain, control, or estimate systematic effects. Without such efforts, we emphasize that this should not be construed as a measurement at all. Note that it is a mere 7-σ away from the bona fide measurement in Ref. [72].

This precision could be improved by taking the data differently. We recorded much of the data at low T where the precision is low, preferring to demonstrate the features of the beating fringe technique. An attempt focused on precision would specify to long T where the phase accrued is high. In addition to other systematics, one would need to consider the offset phase from finite pulse effects, as well as the 0 or π phase introduced depending on whether the $\cos(2\delta T)$ term is in a peak or a trough.

4.2.2 Contrast decay

The weighted average of the contrast decay time constant is 260(3) μs. Atoms transit through the beam at thermal speeds v_{th} ~0.5 m/s for a total time $2T$ (neglecting $T' = 10\ \mu\text{s} \ll T$).

[5]Note that the experimental parameters were slightly different in 2018 when we obtained that spectrum, compared to 2016 when we took these beating fringes. They are very similar though.

[6]I was only able to identify the GCs for half the data sets: (803.500 MHz – 08/25/2016 GCs -19963 to -14565); (803.502 MHz – 08/25/2016 GCs -8487 to -3078); (803.504 MHz – 08/25/2016 GCs -2962 to 2565); (803.516 MHz – 08/29/2016 GCs 15661 to 21069); (803.518 MHz – 08/29/2016 GCs 25205 to 30726); (803.520 MHz – 08/29/2016 GCs -31686 to -26787)

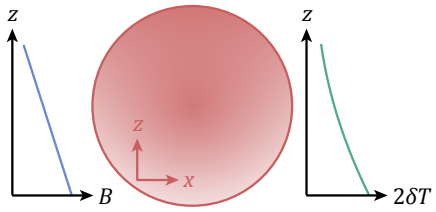

Figure 4.4: Magnetic gradient dephasing.

For contrast decay limited by thermal excursions out of the interferometry beam, we should expect to see contrasts out to $T = (3.6\text{ mm})/2v_{th} = 3.6$ ms. That limit is ten times longer than the contrast decay we observe, so another decoherence mechanism must be at play.

We optically pump the atoms to a magnetically-insensitive $m_F = 0$ state in order to avoid dephasing from different Zeeman sublevels. Each Zeeman sublevel would have a different internal energy splitting due to the Zeeman shift, so each would accrue a different $2\delta T$ phase. While the $m_F = 0$ state is insensitive to magnetic fields, it is not immune. Furthermore, a nonzero gradient in the magnetic field persists in spite of our attempt to let it decay. The gradient is ~ 1 G/cm after 1.5 ms of molasses time. The bias field is around 1.3 G, so the field on one end of the $\sim$ 1-mm-diameter cloud is about 1.25 G and about 1.35 G on the other side. Given a quadratic Zeeman shift of 2.5 kHz/G^2, the difference in $2\delta T$ phases after $T = 300$ μs would be $2(2\pi \times 2.5\,\text{kHz/G}^2)((1.35\text{ G})^2 - (1.25\text{ G})^2)(300\,\mu\text{s}) \sim \pi$. Evidently the spatially varying quadratic Zeeman shift dephases one side of the cloud with respect to the other side of the cloud. In principle, one could recover fringes at different spots in the cloud [145].

4.2.3 Vibration immunity

It is valuable to reinsert the phase due to accelerations and recognize the vibration immunity of this configuration. The acceleration follows the same sign as the $2\delta T$ phase, so it appears alongside it.

$$s_{SCRB} \to \mathcal{B} - \mathcal{C}^{\pm}\cos(8\omega_r T)\cos(2\delta T + 2ka_z T(T + T')), \tag{4.10}$$

where a_z is any acceleration along the interferometer axis, gravity or otherwise. Vibrations enter as such accelerations, for example. Accelerations from vibrations randomize the long-T fringes in Refs. [124, 72], requiring ellipse fitting to accomplish the differential phase detection. Small-phase accelerations only perturb the amplitude of this interferometer signal, not the precious high-frequency recoil phase. The separation between timescales is admittedly a function of T, but accelerations remain little concern below even $T = 10$ ms [84], well beyond the interrogation time on our experiment.

4.3 Motivating the fine-structure constant

Here, we take the opportunity to motivate the fine-structure constant and measurements of it, which are capable of heralding physics yet undiscovered.

The fine-structure constant is a dimensionless fundamental constant of nature, describing the strength of the electromagnetic interaction. For example, the fine-structure constant can be expressed as the number of Compton wavelengths ($\lambda_C = h/m_e c$) that fit in the lowest Bohr orbit. While that number is not an integer – or even of order 1 – it helps establish how the fine-structure constant relates an electromagnetic interaction energy that binds an atom to the fundamental rest energy of an electron m_e.

We may write the fine-structure constant in terms of the infinite-mass Rydberg constant R_∞,

$$\alpha_{fsc}^2 = 4\pi R_\infty \frac{\hbar}{m_e c}. \tag{4.11}$$

This view of the fine-structure constant suffers with $\hbar/m_e$ as the least precisely-known parameter. Rewriting this expression with atomic mass units (amu) and an atomic mass m_a does not appear illuminating at first.

$$\alpha_{fsc}^2 = 4\pi \frac{R_\infty}{c} \left(\frac{1 \text{ amu}}{m_e}\right) \left(\frac{m_a}{1 \text{ amu}}\right) \frac{\hbar}{m_a}. \tag{4.12}$$

This view of the fine-structure enjoys relatively more precise measurements of the electron mass in amu [146] and many atomic masses measured in amu (i.e. relative to carbon) in Penning traps [147, 118]. On the other hand, it suffers a new bottleneck: $\hbar/m_a$. That ratio also appears in an atom's recoil frequency:

$$\omega_r = \frac{1}{2}\left(\frac{\hbar}{m}\right) k^2. \tag{4.13}$$

The only other uncertainty in the recoil frequency comes from the light's wave number k, which a frequency comb can measure very accurately and precisely. Precision measurements of atomic recoil frequencies can therefore be turned into precision measurements of the fine-structure constant.

There is another route to achieving a precision measurement of α_{fsc}, by measuring the magnetic moment of a single electron via its cyclotron frequency in a Penning trap [148, 149]. That tactic measured α_{fsc} to 0.28 ppb and efforts to improve the measurement are underway [150]. The Standard Model predicts the electron's magnetic moment in Bohr magnetons ($-\mu_-/\mu_B$) as a power series of contributions from α_{fsc} and a couple terms from hadronic and weak physics. It is possible that physics beyond the standard model (BSM) contributes other terms yet to be discovered.

$$-\frac{\mu_-}{\mu_B} = 1 + C_2\left(\frac{\alpha_{fsc}}{\pi}\right) + C_4\left(\frac{\alpha_{fsc}}{\pi}\right)^2 + C_6\left(\frac{\alpha_{fsc}}{\pi}\right)^3 + C_8\left(\frac{\alpha_{fsc}}{\pi}\right)^4 + ... + a_{\text{hadronic}} + a_{\text{weak}} + a_{\text{BSM}}, \tag{4.14}$$

where the C's are coefficients determined by precise QED calculations (C_2, C_4, C_6, and C_8 [151] have all been calculated analytically). The final term is merely a suggestion of what might be hiding at the frontier of precision.

Probing BSM physics requires both the measurement of α_{fsc} through the electron's magnetic moment, as well as an independent method. Any discrepancy between the two methods could be due to BSM physics. The most precise measurement by atom interferometry with ^{133}Cs [72] measured α_{fsc} to 0.20 ppb, producing a fruitful comparison with an intriguing tension and potential implications for BSM physics.

It is admittedly not always true that $\hbar/m_a$ is the least precise parameter in Eq. (4.12). It is true for ^{133}Cs, so a measurement of $\hbar/m_{\mathrm{Cs}}$ constitutes a measurement of the fine-structure constant. The measurements of the ^{7}Li mass lag enough that a precision measurement of $\hbar/m_{\mathrm{Li}}$ would not yet produce a competitive precision for α_{fsc}. Of course, a precision measurement of $\hbar/m_{\mathrm{Li}}$ could motivate better mass measurements.

Measuring atomic masses is not required for an independent measurement of α_{fsc}, it merely circumvents the lack of precision in $\hbar/m_e$. Directly measuring the electron recoil would determine α_{fsc} through Eq. (4.11) without needing to insert any mass ratios. Electrons behave as matter waves just atoms do, so electron interferometry could be a path to precise measurements of α_{fsc}. The precision that an recoil-interferometric technique confers on α_{fsc} scales with the recoil frequency; the recoil frequency for an electrons that diffract off a 1064-nm photon is an indomitable ∼GHz [152], compared to ^{133}Cs' paltry $2\pi \times 2$ kHz.

There are a host of severe complications when considering how to perform interferometry with electrons. Like lithium, electrons do not enjoy the same advanced cooling techniques that Rb and Cs do. Warmer samples lead to similar complications to those we battled with lithium. Unlike atoms, electrons are electrically charged, so Coulomb repulsion becomes a concern for plasmas with many electrons. The charge also requires that electrons be trapped with electric and magnetic fields like those of a Penning trap, whose blackbody emission limits the temperatures to which the plasmas can be cooled [153].

Chapter 5

Tune-out measurement with phase-patterned atom interferometry

Tune-out wavelengths lend themselves nicely to precision measurement with atom interferometers. A tune-out wavelength is essentially the wavelength of light between a pair of atomic transitions where the transitions contribute equal and opposite AC Stark shifts. Nearby tune out, small AC Stark shifts perturb the atomic energy. An atom interferometer is a terrific tool to translate those small energy shifts into a matter-wave phase shift observable in the output populations. At tune out alone, there is no phase shift.

Our sample's diverse thermal speeds necessitate a new method, since previous techniques could not work. We present a new method for measuring the tune-out wavelength and target a precision of ~ 1 MHz, at the level of the theoretical prediction. This chapter details the work reported in Ref. [154].

5.1 Previous tune-out techniques

We aim to construct an atom interferometer that measures a phase shift due to the AC Stark shift. The first thought may be to drive any interferometer, for example a Mach-Zehnder, in which the arms spatially separate. Once spatially resolved, shining a laser onto a single interferometer arm selectively phase shifts that arm relative to the other. Fig. 5.1 displays

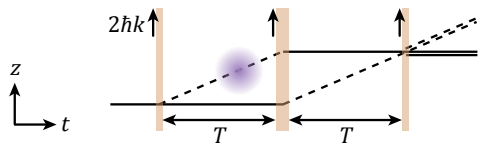

Figure 5.1: A Mach-Zehnder for tune out. A laser beam (purple) selectively addresses one arm of the interferometer, inducing an AC Stark shift and interferometer phase shift that vanish at tune out.

this concept. Comparing the interference signal with the pulse of the beam to the interference signal in the absence of the beam recovers the phase shift due to the beam. The phase shift vanishes when tuning the wavelength of the laser precisely to the tune-out wavelength.

Methods like Fig. 5.1 have measured tune-out wavelengths for Rb [29] and K [26, 27]. Other methods beyond interferometry may sense the polarizability differently. Any dipole potential created by light vanishes at tune out, including any Kapitza-Dirac scattering off a pulsed lattice. Kapitza-Dirac probes have measured tune out in Rb [30, 31] and Dy [32]. In another method, a radio frequency knife continuously out-coupled He from a magnetic trap. An additional dipole potential from a laser beam modified the outcoupling rate at every wavelength except at the tune-out wavelength [7].

The sample in this dissertation subsists at a balmy ∼140 μK. With thermal speeds $\sigma_v \sim 40$ cm/s and a much lower recoil speed of $v_r = 8.5$ cm/s, the arms of the interferometer do not separate quickly enough to overcome the rapid thermal expansion. Spatially resolving the interferometer arms for the entire sample is impossible.

Let us consider Fig. 5.1 differently. It is not important that the AC Stark-shifting beam addresses one interferometer arm and not the other. What is important is that the AC Stark shift is different for the two arms. In other words, the arms sample a gradient of the AC Stark shift or a gradient of the intensity (for fixed laser wavelength). The idea behind our application of phase patterning is to introduce a pulsed intensity gradient to the interferometer that imprints a spatially-varying interferometer phase.

Magic versus tune-out wavelengths

There is some conflation and confusion between two distinct terms in the community: magic wavelengths and tune-out wavelengths. The majority of mentions adopt the following nomenclature.

A "tune-out wavelength" is one at which a particular state in a particular species has a polarizability equal to 0 [117, 12]. This appears to be synonymous with a "magic-zero wavelength" [27, 155, 156] for added confusion. There is no AC Stark shift, no dipole trapping, and no effect that relies on dipole polarizability.

A "magic wavelength" is one at which the differential shift (or difference in polarizability) between two levels vanishes. Each state may still have a nonzero overall AC Stark shift, but the splitting between them is equal to the splitting in the absence of light. Magic wavelengths can still generate a trapping potential, but leave a clock transition unperturbed [145, 104]. Tuning other parameters may also yield magic conditions, like polarization [157] or intensity [105].

5.2 Applications of tune-out wavelengths

Light at a tune-out wavelength tunes out only for a particular state in a particular atomic species. Other states in the same atom or other atoms still likely have a nonzero polarizability

and experience dipole potentials. Tune-out wavelengths therefore aid in engineering quantum states in a state- or species-dependent manner. The theory and applications for alkali atoms are discussed in Ref. [117], while Ref. [158] treats relevant wavelengths for various pairs of species.

Let us touch on several interesting applications of tune-out wavelengths to pique readers' interests.

- Trap two species of gas, a target gas and a probe gas. Drive the target gas into a Mott insulator state with a dipole potential tuned to the probe species' tune-out wavelength. The probe species remains a superfluid [159].
- Build a quantum computer using two separate lattices that address the $^1S_0$ and metastable $^3P_0$ states of alkaline-earth atoms like ^{87}Sr. One lattice tunes out to $^3P_0$ and stores the qubit state encoded in the $^1S_0$ nuclear magnetic state. The other lattice tunes out to $^1S_0$ and transports the qubits [160].
- Measure collisional scattering between different species confined to a different number of dimensions [31].
- Selectively compress one gas of K using a tune-out wavelength for Rb, so that the heat from compression dissipates into the Rb. [161]
- Place a species impurity into a gas. Investigate the dynamics of the impurity in one dimension, an analogue to the diffusion of a spin flip in a one-dimensional ferromagnet [162]. A similar experiment operates in three dimensions [163].
- Launch each of two species with its own lattice tuned to a tune-out wavelength for the other, for use in atom-interferometric tests of the equivalence principle [156].
- Probe an ultracold gas with off-resonant probe light at a tune-out wavelength. The probe does not generate a dipole force so it avoids classical backaction that perturbs the state [155].

Precision measurements of tune-out wavelengths help inform a dialogue between experiment and atomic theory. The measurement in He [7], for example, has inspired a rich body of theory working to include QED effects into the polarizability calculations [8, 9, 11].

Li, a small and theoretically simple atom that permits Hylleraas calculations like He, presents a new opportunity to drive progress in collaboration between theory and experiment. Atom interferometry with a supersonic beam measured the static DC polarizability of lithium [24], but no scientist has yet measured a tune-out wavelength or the dynamic polarizability in lithium. The lack of precedent motivates a study. There is a significant isotope shift in the tune-out wavelengths of the two isotopes ^{6}Li and ^{7}Li that is of considerable interest to theorists [12, 117]. Li's small D-line splitting also places its tune-out wavelength very close to each transition, a proximity that enhances the possible sensitivity of a tune-out

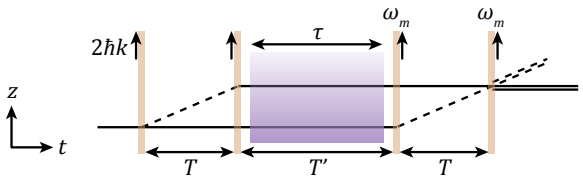

Figure 5.2: Tune-out measurement interferometer geometry. A four-pulse Mach-Zehnder produces two interferometer arms in the same internal state during T'. The arms sample the intensity gradient of a pulsed laser beam (purple central pulse). The Raman frequencies step by ω_m for the final two pulses in order to introduce a tunable phase difference to the interferometer. The effect of the beam vanishes at tune out.

wavelength measurement. In combination with the precise calculations in the Hylleraas basis and beyond, the polarizability of Li is among the most precisely calculable and measurable across the periodic table, making it a prime candidate to serve as a reference species for dynamic polarizability. One experiment has already demonstrated a method employing a reference species (K) to measure the polarizability of another exotic species (Dy) using the oscillation frequency in a dipole trap [164].

5.3 Phase-patterned atom interferometry

The impossibility of addressing a single arm of our lithium interferometer motivates reframing Fig. 5.1 as sampling an intensity gradient. Here, we present the concept of phase-patterned atom interferometry.

5.3.1 Interferometer geometry

There is a significant difference between each of the hyperfine ground state's tune-out wavelengths. It is not satisfactory to pulse a beam that simultaneously addresses multiple hyperfine states because when the beam tunes out for one state, a nonzero effect on the other state remains. We must pulse a beam that addresses a single hyperfine state and whose effect vanishes at a tune-out wavelength for that state. The four-pulse Mach Zehnder volunteers a time T' during which the arms are in the same internal state. The Ramsey-Bordé also does, but has the disadvantages of sporting a recoil phase that does not interest us and of requiring that the k vectors be reversed in the middle.[1] The four-pulse Mach-Zehnder is the tool of choice.

Forgoing a reversal of the k vectors removes the $8\omega_r T$ and $2\delta T$ phases from the recoil energy and two-photon detuning. Operating perpendicular to gravity removes the $2kgT(T+$

[1] We perform k reversal for the Ramsey-Bordé with an EOM, which sacrificies some of the Raman optical power. Removing the EOM and not having to reverse k vectors recovers some optical power and increases the efficiency of the beam splitters.

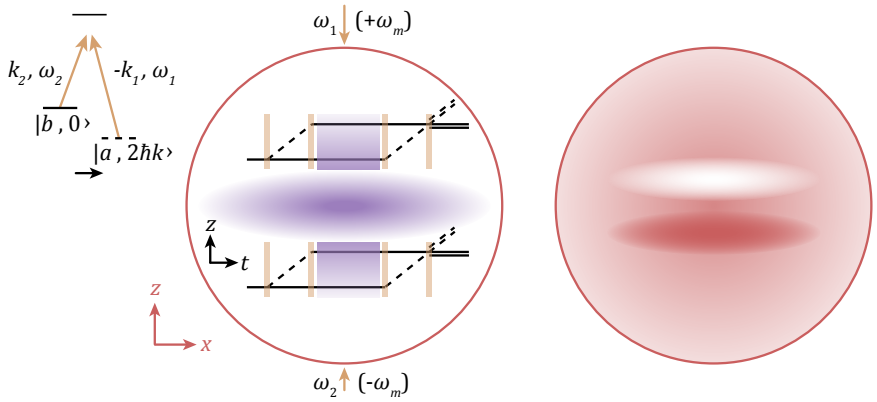

Figure 5.3: Phase-patterned atom interferometry. Left shows a tightly focused Stark-shifting beam (purple intensity profile) that pulses through the center of the sample (red outline), both shown on spatial axes. Spacetime diagrams of the interferometer scheme lie within the sample. For an atom below (above) the center of the beam, the interferometer samples a positive (negative) intensity gradient. Right shows the resulting atomic density profile. The interferometer translates the opposite phase differences from opposite intensity gradients into opposite population differences.

T') phase from accelerations. This interferometer has no phase difference. We modify the Raman frequencies of the final two pulses ($\omega_1 \to \omega_1 + \omega_m$ and $\omega_2 \to \omega_2 - \omega_m$) in order to introduce a nonzero and controllable $2\omega_m T$ phase difference to the interferometer.

A laser beam tuned near the tune-out wavelength pulses while the arms are in the same internal state. The matter wave along each arm advances in phase according to the internal energy as perturbed by the local AC Stark shift. In the presence of a nonzero AC Stark shift, i.e. away from tune out, the arms' matter waves advance at different rates since they sample different local intensities. The phase difference is proportional to the intensity difference $\Delta\phi \propto (dI/dz)\Delta z$, where Δz is the arm separation.

If the entire cloud sampled the same intensity gradient, there would be an overall phase shift in the interferometer common to the whole sample, present if and only if the beam pulses. One could, in principle, align a laser beam's center beyond the edge of the sample and induce such a uniform phase shift. The beam would have to be large in order to produce a uniform intensity gradient across the entire ∼1-mm-wide sample and the power would need to be substantial to produce an appreciable gradient. We could not achieve the specifications to make this method viable.

Tightly focusing a beam produces larger intensity gradients for a fixed power, albeit on a smaller length scale. Sending the beam directly through the center of the sample presents atoms below (above) the center of the beam with a positive (negative) intensity gradient. The opposite intensity gradients produce opposite phase differences that the interferometer translates into opposite population differences. The intensity gradient directly patterns a density profile onto the sample, so we term the technique "phase-patterned atom interfer-

Line	F'	$\Delta_{0;Di,F'}$ / MHz
D_1	1	-91.88
D_1	2	0
D_2	3	10011.99
D_2	2	10021.46
D_2	1	10027.27
D_2	0	10030.03

Table 5.1: ^{7}Li hyperfine detunings from $f_0 = 446,799,862.994(2)$ MHz, the $|2S_{1/2}, F = 2\rangle \rightarrow |2P_{1/2}, F' = 2\rangle$ transition. Data are from Ref. [115].

ometry".

Atom interferometry experiments nearly always sum the output populations across the entire size of the sample. Here, the region of excess density would cancel the region of reduced density and the signal summed across the sample would be 0. This technique requires sensing spatial features within the output populations.

5.3.2 The signal

Each arm of the interferometer samples the local AC Stark shift; the matter-wave phase advances at the internal state frequency ω_b plus the perturbation. The phase difference between the arms is their matter-wave frequency difference between upper and lower arms, integrated over the pulse time τ.

$$\Delta\phi(x,z) = -\frac{1}{\hbar}(\Delta U_{AC,u}(x,z) - \Delta U_{AC,l}(x,z))\tau = -\frac{1}{\hbar}\Delta(\Delta U_{AC}(x,z))\tau. \tag{5.1}$$

We may neglect hyperfine structure and use the effective saturation intensities for each line. We reference laser detunings Δ_0 to the $|2S_{1/2}, F = 2\rangle \rightarrow |2P_{1/2}, F = 2\rangle$ transition at frequency f_0. At the tune-out wavelength between the D_1 and D_2 lines, the detuning from D_1 (D_2) is positive (negative), the difference set by the fine-structure splitting.

Let us consider the local AC Stark shifts. Neglecting the hyperfine structure, using the effective saturation frequencies for circular polarization, and assuming $\gamma_{D1} \approx \gamma_{D2} \equiv \gamma$, we would find

$$\Delta U_{AC}(x,z) \approx \frac{\gamma^2}{8} I(x,z) \left(\frac{1}{\Delta_0 I^*_{sat,D1,TO}} + \frac{1}{(\Delta_0 - \Delta_{FS}) I^*_{sat,D2,TO}} \right), \tag{5.2}$$

where $\Delta_{FS} \sim 10$ GHz is the fine-structure splitting.

More accurately, each hyperfine transition adds its own contribution to the AC Stark shift. We label the detuning from f_0 as $\Delta_{0;Di,F'}$. Fig. 2.14 shows these detunings and Table 5.1 tabulates them.

$$\Delta U_{AC}(x,z) = \frac{1}{8} I(x,z) \sum_{i\in\{1,2\},F',m'_F,q} \frac{\gamma^2_{Di} |\epsilon_q|^2 C^2(JFm_F; J'F'm'_F; q)}{(\Delta_0 - \Delta_{0;Di,F'}) I_{sat,Di}}. \tag{5.3}$$

For this measurement, the ground state has $J = 1/2$, $F = 2$, $m_F = 0$.

Even Eq. (5.3) is not truly exact and would require some modifications for better precision. First, we sum here only over the hyperfine structure on the D_1 and D_2 lines, while truly all excited states n' contribute an AC Stark shift. Lithium's small Δ_{FS} does, however, render the D-line contributions far more potent than any of the distant $n' \geq 3$ transitions. Second, this simple form $\Delta U_{AC} = \hbar\Omega^2/4\Delta$ assumed the RWA. The RWA accurately approximates the Stark shift for transition frequencies near the laser frequency, but neglects an important term for detunings approaching the laser frequency. Given the small D-line detunings for Li's tune-out wavelength, those terms are negligible in this experiment. Third, the hyperfine detunings should technically contain any Zeeman shifts or other perturbations [28]. All these effects are small in our system, so we can safely neglect them in this work when it is convenient. Eq. (2.139) and the definitions that follow it are more cumbersome, but more accurate.

The intensity profile of the beam follows a Gaussian profile

$$I(x,z) = \frac{2P}{\pi w_x w_z} e^{-2x^2/w_x^2} e^{-2z^2/w_z^2} \tag{5.4}$$

with power P, waist w_z along the interferometry axis and waist w_x perpendicular to the interferometry axis. The interferometer only samples an intensity gradient along the interferometry axis z, so

$$\Delta(\Delta U_{AC}(x,z)) \approx \frac{dI(x,z)}{dz}\Delta z = \frac{dI(x,z)}{dz}(2v_r T), \tag{5.5}$$

where Δz is the interferometer's arm separation along the interferometry axis. We have assumed that the arm separation is small compared to the intensity profile. Differentiating the intensity profile, we find

$$\Delta\phi(x,z) \propto -\frac{Pz}{\pi w_x w_z^3} e^{-2z^2/w_z^2} v_r T\tau. \tag{5.6}$$

The intensity gradient reaches a maximum at $|z| = w_z/2$, so the phase difference reaches a maximum absolute value of

$$\max(|\Delta\phi(x,z)|) \propto \frac{P}{w_x w_z^2} v_r T\tau. \tag{5.7}$$

The more favorable scaling of the signal with w_z compared to w_x motivates an asymmetric beam with a tighter waist along the interferometry axis. Tightening the waist along x does still help increase the maximum intensity gradient, but making it smaller than the size of the sample reduces the number of atoms that get to participate in the signal.

Figure 5.4: Thermally Dephased Signal. Numerical integration of the signal over the thermal velocity distribution and beam profile shows a reduction in contrast due to the thermal motion of the atoms.

5.3.3 Dephasing from thermal and launch speeds

The reasoning towards the maximum phase difference Eq. (5.7) considers atoms at rest. The high thermal speeds $\sim 1/2$ m/s are a detriment to the signal. The arms do not necessarily sample a constant intensity gradient as atoms wander through the intensity profile during the pulse. An atom at $|z| = w_z/2$ is unlikely to achieve the maximum phase difference as its trajectory removes it from that most sensitive position. Even after the pulse imprints the interferometer phase, atoms continue along their trajectories both between the pulse and the end of the interferometer, as well as between the end of the interferometer and detection. This itineracy smears out the resulting density profile of interest. Furthermore, our sample enters the interferometer with a nonzero launch speed along the intensity profile, $v_{lx}\hat{x} + v_{lz}\hat{z}$ in the $x - z$ plane. That also reduces the signal contrast since atoms are biased to be transiting across the beam profile during the pulse

Consider a single atom beginning the interferometer at a position (x_0, z_0) and moving at a velocity $v_x\hat{x} + v_z\hat{z}$ in the $x - z$ plane. It integrates a phase difference during the pulse time

$$\Delta\phi_{SA} = \frac{\Delta U_{ACp}}{\hbar}\int_0^\tau dt\, e^{-2(x_0+v_x(t+T))^2/w_x^2}\left(e^{-2(z_0+2v_rT+v_z(t+T))^2/w_z^2} - e^{-2(z_0+v_z(t+T))^2/w_z^2}\right), \tag{5.8}$$

where ΔU_{ACp} is the peak AC Stark shift at the center of the beam.

We image the atoms at final positions after the interferometer $x_f = x_0 + v_x(2T + T')$ and $z_f = z_0 + 2v_rT + v_z(2T + T')$. The final signal as a function of position integrates over the atomic density and Maxwell-Botlzmann distributions.

$$\begin{aligned} s(x_f, z_f) =& \frac{\mathcal{C}}{2(2\pi)^{3/2}\sigma_{vx}\sigma_{vz}\sigma_a} \\ &\times \int_{-\infty}^{\infty} e^{-(x_f^2+z_f^2)/2\sigma_a^2} e^{-(v_x-v_{lx})^2/2\sigma_{vx}^2} e^{-(v_z-v_{lz})^2/2\sigma_{vz}^2} \cos(\Delta\phi_{SA})\, dx_f\, dz_f\, dv_x\, dv_z, \end{aligned} \tag{5.9}$$

where σ_{vx} and σ_{vz} are the standard deviations of the Maxwell-Boltzmann speed distributions along each axis and we assume a Gaussian atomic density distribution with standard deviation $\sigma_a \sim 500$ μs.

Numerically integrating the signal in Mathematica served as a useful tool for projecting the sensitivity of the interferometer. Fig. 5.4 shows an example result of the atomic density

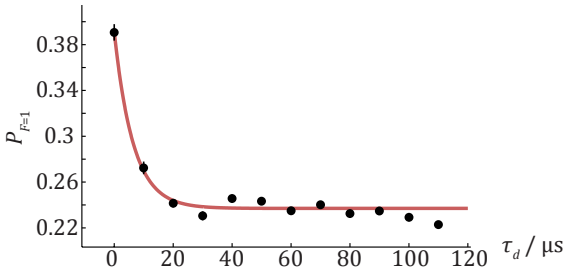

Figure 5.5: Decoherence of complementary $F = 1$ interferometer. With $f_m = 14.5$ kHz, a pulse of MOT repump light during T' decoheres the complementary interferometer occupying $|2S_{1/2}, F = 1\rangle$. (05/23/2018, GCs -29126 to -29042).

from the numeric integration. As a proxy for the sensitivity, we used the signal strength at $z_f = w_z/2$ for different values of Δ_0 and predicted its slope as it crossed through zero. Multiplying this sensitivity by the noise amplitude from different sources predicts the precision of the measurement.

5.3.4 Population selection

Optical pumping delivers atoms in $|2S_{1/2}, F = 2, m_F = 0\rangle$ to the interferometer. Roughly, 80% of the atoms occupy $m_F = 0$, 16% occupy $m_F = +2$, 4% occupy $m_F = -2$ and there are essentially none in $m_F = \pm 1$.

The interferometer itself generates amplitude in both $F = 1$ and $F = 2$ during T' in spite of the input state preparation. The $F = 2$ interferometer is a flat rhombus, while the recoiling $F = 1$ component closes a separate interferometer shaped like an angled rhombus. The two interferometers are complementary in the sense that they have precisely the same phase difference, $2\omega_m T$. The two signals add.

Introducing the phase patterning pulse breaks the equality of the interferometers, since the light perturbs each state differently. Each state contributes a different phase pattern at every wavelength and each advertises a tune-out wavelength different by roughly the 800-MHz ground-state hyperfine splitting. A precision measurement at the 1-MHz level must isolate one hyperfine state or the other, so we decohere the interferometer in $F = 1$ during T'.

A pulse of MOT repump light specifically addresses $F = 1$, driving incoherent scattering events on the D_2 line. It spoils the coherence of that interferometer and reduces the contrast. The peak population stands as a proxy for the total contrast since $\mathcal{C} \propto \max(P_{F=1})$. We fix $\omega_m = 2\pi \times 14.5$ kHz at the top of an interference fringe and scan the decohering pulse length τ_d. The peak population decays with a time constant 6.5(1.7) μs (Fig. 5.5).

The coherence of the $F = 2$ interferometer should persist regardless of the MOT repump pulse. Fig. 5.6 shows the $2\omega_m T$ fringes with both populations (upper), as well as the fringes that remain after a 70-μs pulse to decohere the $F = 1$ interferometer (lower). Both

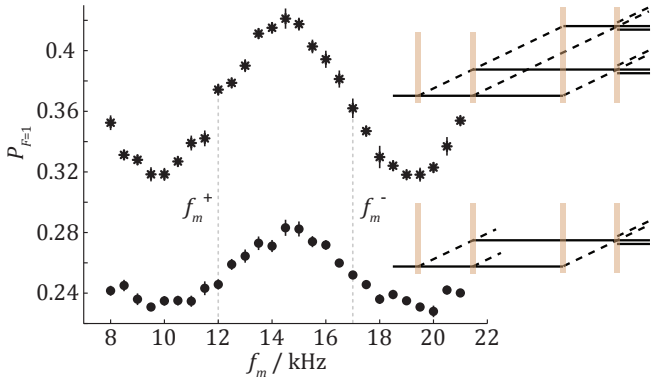

Figure 5.6: Four-pulse Mach-Zehnder fringes. Both interferometers' signals add in the fringes above (asterisks) (07/17/2018, GCs -31652 to -31464). Fringes only contain the lower interferometer signal (circles) after a pulse decoheres the complementary interferometer (07/17/2018, GCs -31066 to -30847). Pulse separation times are $T = 53$ μs and $T' = 110$ μs.

interferometers produce a contrast of $\sim$20%, while the $F = 2$ interferometer alone produces half the contrast, $\sim$10%, as expected.

5.3.5 Bias phase for sensitivity

Detection measures a population, not the interferometer phase difference directly. Measuring the population registers a normalized signal

$$s = \mathcal{B} + \frac{\mathcal{C}}{2}\cos(\Delta\phi(x,z)), \tag{5.10}$$

where $\mathcal{B}$ is the normalized background population. The sensitivity therefore depends on the phase difference.

$$\frac{ds}{d\Delta\phi} \propto \mathcal{C}\sin(\Delta\phi(x,z)). \tag{5.11}$$

To maximize the sensitivity to additional phase shifts due to the intensity gradient, we bias the phase difference to an odd multiple of $\pi/2$ using the modulation frequency on the third and fourth Raman pulses.

We tune the sensitivity to be positive at f_m^+ or negative at f_m^-. At f_m^+ (f_m^-), an additional positive phase difference produces a maximal positive (negative) change in the observed population. Pulsing the Stark-shifting beam during T' introduces an additional phase difference that is spatially dependent. The sign of the population difference depends on the sign of the sensitivity, so reversing the sensitivity from f_m^+ to f_m^- reverses the signal imprinted onto the atomic density.

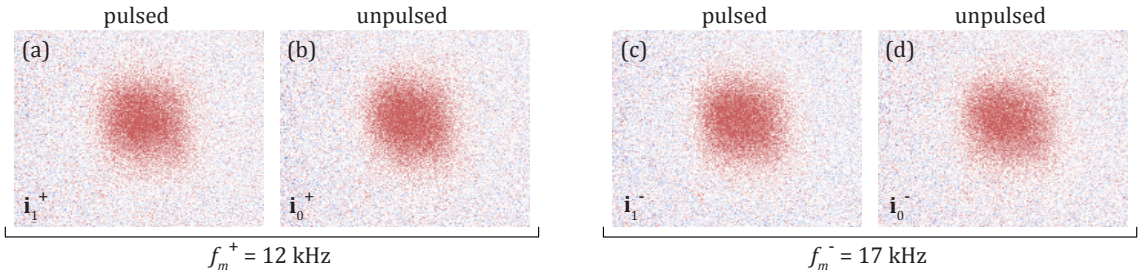

Figure 5.7: Raw images. Even at our furthest detuning from tune out where the signal should be strongest, opposite sensitivities for which the pattern should reverse look nearly identical (a and c). Unpulsed images without the Stark pulse and its effect (b and d) also look nearly indistinguishable from the pulsed images (07/17/2018, GCs left to right: -19702, -19705, -19701, -19692).

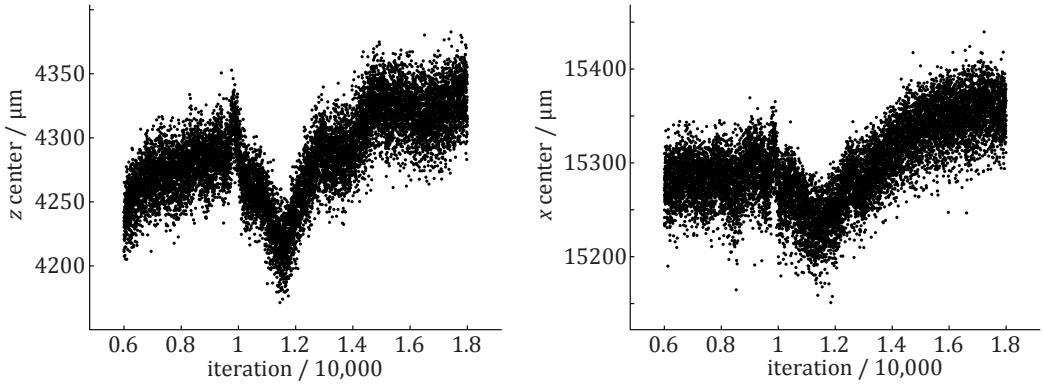

Figure 5.8: Position drifts. The fitted center of the sample fluctuates on short time scales and drifts on long time scales, on a length scale comparable to the size of the Stark-shifting beam. The data span $\sim$ 7 hours (08/07/2018, GCs 6000 to 18000).

5.4 Image Processing

Multiple factors make make reading out the signal in this experiment very challenging. First, the signals are small. While the largest expected phase shift for a stationary atom at $|z| = w_z/2$ and $x = 0$ for our largest detuning from tune out is $\sim 3\pi$ radians, but thermal dephasing significantly mutes the pattern. Second, the interferometer has a paltry contrast of only $\sim 10\%$. Fig. 5.7 displays raw images, including two images ((a) and (c)) for which the signal is maximal and opposite in sign. Third, thermal effects in the laboratory deflect MOT mirrors that sit atop tall aluminum posts. This changes an étalon interference pattern MOT arms 1 and 2 generate as they propagate through the large North/South vacuum viewports that are not anti-reflection coated. It results in changes in the launch velocity of the sample and produces both fast fluctuations and slow drifts in the position of the cloud, each of which is on the order of the size of the Stark-shifting beam waist (see Fig. 5.8). Shrouding the

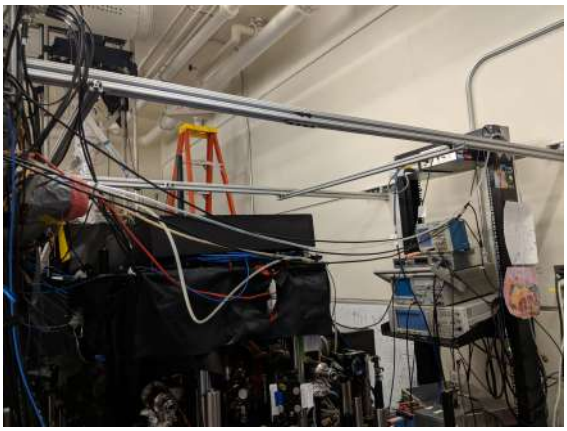

(a) Frame for curtains (02/13/2018)

(b) Experiment in curtains (07/18/2018)

Figure 5.9: Curtains for thermal stability.

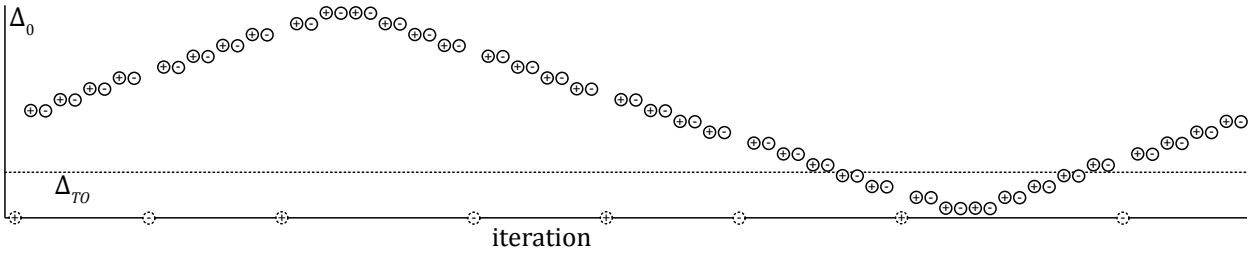

Figure 5.10: Modulated parameters for tune-out scan. Pluses (minuses) represent shots with positive (negative) phase sensitivity using f_m^+ (f_m^-). Solid (dashed) circles represent pulsed (unpulsed) shots.

experiment in curtains (see Fig. 5.9) reduced the excursions by at least a factor of 2, but the problem remained.

5.4.1 Modulated data set

As Fig. 5.7 shows, we generate one of four image types on each experimental iteration. We take images for each sensitivity where the Stark-shifting beam does pulse and some where it does not pulse. As the wavelength of the laser scans across tune out for the pulsed shots, unpulsed shots regularly interrupt the scan. The difference between the pulsed and unpulsed shots should isolate the effect of the beam. We take pulsed and unpulsed shots for each sensitivity. Any effects that alter the interferometer phase difference reverse their contribution to the signal upon sensitivity reversal, whether or not the effect is associated with the Stark-shifting pulse.

The scan spans a wavelength range that is not symmetric about tune out, as Fig. 5.10 shows. The asymmetry is primarily the consequence of a technical limitation; the Agilent E4422B ESG-A signal generator that controls the Stark laser wavelength switches between

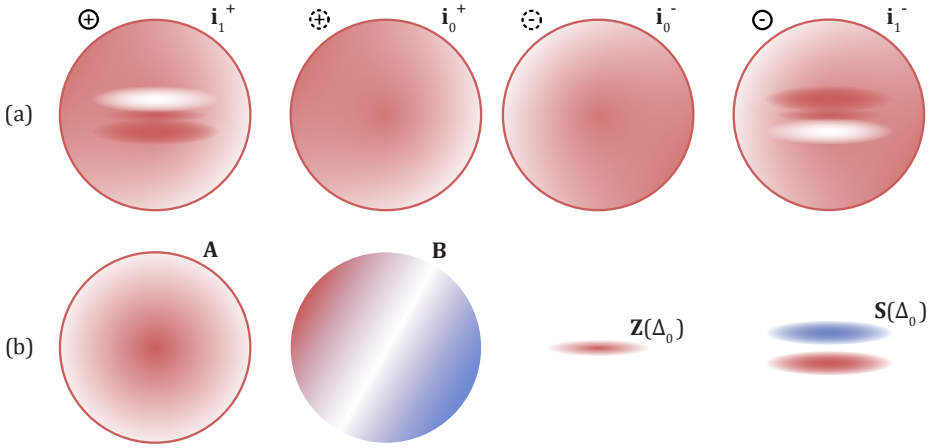

Figure 5.11: Image types and their components. (a) schematically represents the four image types. (b) schematically represents individual components that sum to the image types in (a).

sources to cover its specified range. One such source switch sits at the edge of our scan around $\Delta_0 \approx 2\pi \times 3465$ MHz. The reference tone in the phase lock falls silent momentarily, which destroys the lock when the source switches and precludes automating the scan over the chasm. The maximum detuning from tune out is roughly

$$\Delta_M \equiv \max(|\Delta_0 - \Delta_{TO}|) \sim 2\pi \times 400 \text{ MHz}. \tag{5.12}$$

We parameterize the four image types with the presence (lack) of a pulse $p = 1$ ($p = 0$) and the $\pm$ phase sensitivity: $\mathbf{i}^{\pm}_{p,j}$. Each image indexed by j can be approximated as a sum over five main components (Fig. 5.11): $\mathbf{A}$ is the underlying atomic density profile, $\mathbf{B}$ is any pattern not associated with the Stark-shifting pulse that is imprinted onto the cloud as a result of the interferometer, $\mathbf{Z}(\Delta_{0,j})$ is a monopole-shaped pattern that results from single-photon scattering from the Stark-shifting pulse, the coherent interaction with the Stark-shifting beam imprints the phase-patterned signal $\mathbf{S}(\Delta_{0,j})$ that reverses across tune out, and $\mathbf{N}_j$ is noise.

$$\mathbf{i}^{\pm}_{p\in[0,1],j} = a_j\mathbf{A} \pm b_j\mathbf{B} + p\left(\zeta_j\mathbf{Z}(\Delta_{0,j}) \pm \varsigma_j\mathbf{S}(\Delta_{0,j})\right) + \mathbf{N}_j. \tag{5.13}$$

The bold-face type emphasizes the matrix representation of each image and component.[2]

Each weight is a projection of the image onto a static matrix that represents the compo-

[2]Fun fact: In Greek, when σ ends a word, the character changes to ς. For example, the island Mykonos is spelled Μυκονος, not Μυκονοσ.

nent.

$$a_j = \left(\mathbf{i}^{\pm}_{p,j} \cdot \mathbf{A}\right) \tag{5.14}$$
$$b_j = \left(\mathbf{i}^{\pm}_{p,j} \cdot \mathbf{B}\right) \tag{5.15}$$
$$\zeta_j = \left(\mathbf{i}^{\pm}_{p,j} \cdot \mathbf{Z}(\Delta_{0,j})\right) \tag{5.16}$$
$$\varsigma_j = \left(\mathbf{i}^{\pm}_{p,j} \cdot \mathbf{S}(\Delta_{0,j})\right), \tag{5.17}$$

where the projection, or dot product, is a normalized sum over pixel-by-pixel products

$$(\mathbf{V} \cdot \mathbf{W}) = \frac{\sum_{x,z} V(x,z)W(x,z)}{\sum_{x,z} W(x,z)W(x,z)}. \tag{5.18}$$

Altogether, roughly 330,000 of these images comprise the data set that we use to determine tune out.

5.4.2 Averaging

The most straightforward way to improve the signal-to-noise ratio beyond that in Fig. 5.7 is to average down the noise. We partition the images into subsets ξ and average images of each type at a fixed Stark laser wavelength within each subset. Residual images, the difference between pulsed and unpulsed, contain both the signal of interest and the effect of scattering.

$$\langle \mathbf{R}^{\pm}(\Delta_0)\rangle_{j\in\xi} \equiv \langle \mathbf{i}^{\pm}_{1,k}(\Delta_{0,k} = \Delta_0)\rangle_{k\in\xi} - \langle \mathbf{i}^{\pm}_{0,l}\rangle_{l\in\xi}. \tag{5.19}$$

With sufficient averaging, imaging noise $\langle \mathbf{N}\rangle \approx 0$ and both $\mathbf{A}$ and $\mathbf{B}$ should cancel between the pulsed and unpulsed images. Only the signal of interest and scattering should remain, both with patterns and projections that are a function of wavelength.

$$\langle \mathbf{R}^{\pm}(\Delta_0)\rangle_{j\in\xi}(\Delta_0) \approx \langle \zeta_j\rangle_{j\in\xi}\mathbf{Z}(\Delta_0) \pm \langle \varsigma_k\rangle_{k\in\xi}\mathbf{S}(\Delta_0). \tag{5.20}$$

Taking the difference between the two residuals produces a difference image for which the scattering should cancel and leave only the signal.

$$\langle \mathbf{D}(\Delta_0)\rangle_{j\in\xi} \equiv \langle \mathbf{R}^{+}(\Delta_0)\rangle_{j\in\xi} - \langle \mathbf{R}^{-}(\Delta_0)\rangle_{j\in\xi} \approx 2\langle \varsigma_j\rangle_{j\in\xi}\mathbf{S}(\Delta_0). \tag{5.21}$$

The subsets should be large enough to capture the full range of the fast fluctuations in position, atom number[3], etc., and they should be small enough to sample only a stable portion of the slow drift. We ultimately optimize the size of the subset for the lowest error in the tune-out measurement, resulting in subsets of roughly 1,000 images spanning ∼30 minutes. Fig. 5.8, for example, contains 12 1,000-image subsets.

[3]Note that the normalized imaging scheme no longer helps in processing the images for the tune out wavelength (other than producing cleaner $2\omega_m T$ fringes for Fig. 5.6). One could normalize each image to the total number of atoms on that shot, but we opted not to because doing so produced slightly larger errors.

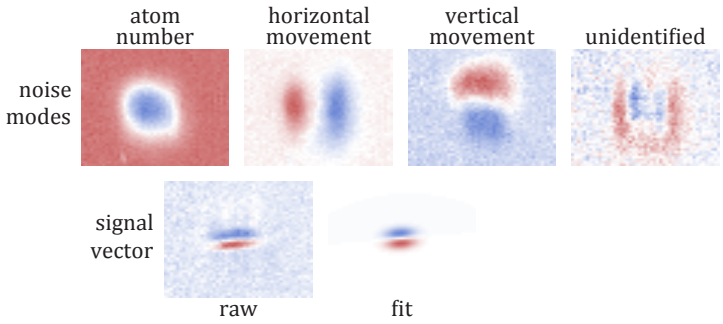

Figure 5.12: Noise and signal vectors from principal component analysis (PCA). This is just a sampling of the vectors PCA returned for our data set. (07/30/2018)

5.4.3 An aside on principal component analysis

We originally planned to use principal component analysis (PCA) to read out the faint signal from noisy images [114]. Complications with its results precluded its application in our precision measurement. Before presenting our final method of choice, here we briefly mention the concept and inconsistencies that disfavored it.

PCA applies straightforward linear algebra to reduce the dimensionality of data, details perspicuously described in [165]. Images are typically represented as matrices of pixel values. The dimension of the image is simply the number of pixels, each image being the sum over pixel vectors (each a matrix with all 0s, except for a single 1 at the location of the pixel in the detector array), each multiplied by the detected intensity at that pixel.

Cold-atom experiments rarely concern themselves about such fine details as to require detailed pixel-by-pixel information. They are instead interested in more global properties of the sample, like its summed atom number or movement within a region. PCA finds these vectors of interest like atom number and movement, making obsolete the unnecessarily large number of single-pixel vectors. Then, each experimental shot may be described as a sum of how many atoms there are multiplied by the atom-number vector, how far the sample has moved along x multiplied by the x-movement vector, etc. Calculating these vectors with PCA amounts to finding the eigenmodes of pixel variations in the image array. Note that specifying to eigenmodes of "variation" among images implies first removing the average of the images, which is the first step of PCA. In this case, we first subtracted the average unpulsed image for each sensitivity to avoid subtracting the signal out of the images.

We envisioned identifying the signal vector using PCA (i.e. the density pattern induced by the Stark shifting beam) and projecting each image onto the signal vector to quantify how strong the signal was in each image. That signal strength should cross through 0 at tune out, similar to projections curves in the following sections. A series of issues arose in implementing this simple idea.

The signal vector of interest looks like an excess of atoms above the beam center and a dearth of atoms below (or the reverse). That signal vector looks substantially like a significant source of noise: movement of the sample (specifically along the interferometry axis). Even

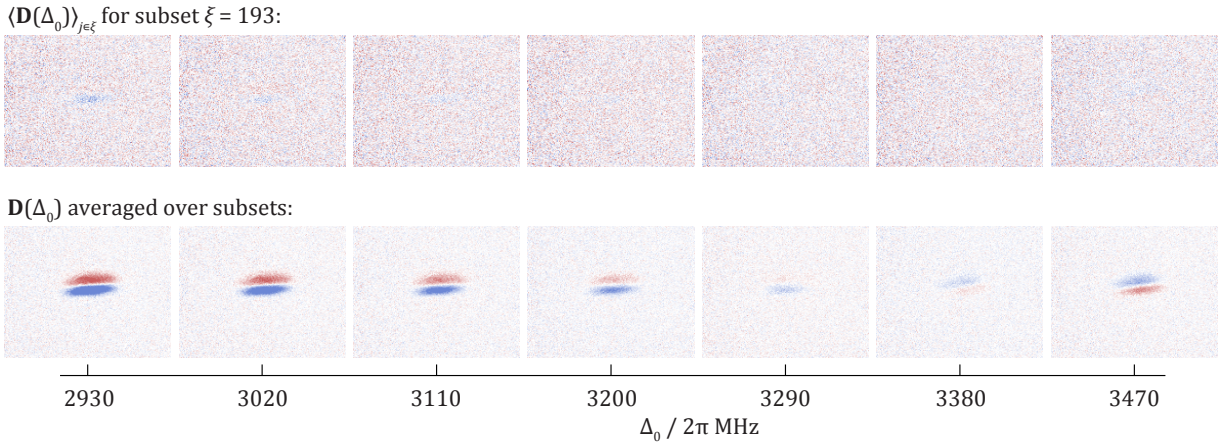

Figure 5.13: Residual images.

when the signal should vanish at tune out, nothing more than movement of the sample might masquerade as signal. We attempted to remove the effect of noise by "deprojecting" it. That is, we computed the projection of each image onto each vector describing a noise mode and subtracted the noise vector weighted by that projection. Deprojection could, in principle, remove everything but the remaining signal, in particular when the noise is orthogonal to the signal. Our noise is not necessarily orthogonal to the signal. A cartoon linear algebra analysis showed that this should only introduce a noise term that averages to 0 with a large enough data set. Nevertheless, we did try to orthogonalize the noise vectors to a signal model using a Gram-Schmidt routine prior to deprojecting.

All our attempts to identify tune out from subsets of the data led to results that varied by roughly 20 MHz in tune out and nearly 10 times the error bar on each point. Modifying aspects of the analysis that should have had no effect on the result did have significant effects on the results well beyond their error bars. We never identified the precise reason that PCA failed to deliver consistent results on our data set, but we caution that a decision to apply PCA in precision measurement should be treated with extreme care.

We now describe the simpler method that delivered more consistent results.

5.5 Phase patterning results

5.5.1 The signal

Fig. 5.13 shows several of the difference images as a function of wavelength. The difference images for a single subset have relatively low signal-to-noise ratio, but the signal is visible. The signal of interest becomes more prominent after averaging each wavelength's difference image over all subsets.

The signal reverses sign as the Stark laser scans across tune out. To find where the sign reversal occurs, we first fit the signal to a particular geometry that describes the expected

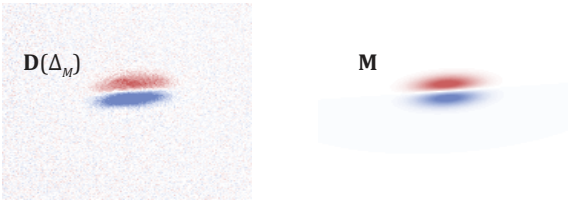

Figure 5.14: Stark signal model.

signal. The difference image with the highest signal-to-noise ratio is the one tuned furthest from tune out: $\mathbf{D}(\Delta_M)$. The model $\mathbf{M}$ follows a functional form fixed by Eq. (5.6). The signal is a sine of that phase difference[4], but for the small phase differences we observe, the signal is essentially the phase difference. The model contains six free parameters:

$$\mathbf{M}(a, \theta, x_0, z_0, \sigma_{\tilde{x}}, \sigma_{\tilde{z}}) = a\tilde{z}e^{-(\tilde{z}-z_0)^2/2\sigma_{\tilde{z}}^2}e^{-(\tilde{x}-x_0)^2/2\sigma_{\tilde{x}}^2}, \tag{5.22}$$

where a is an amplitude, (x_0, z_0) is the center of the pattern, and the coordinates $(\tilde{x}, \tilde{z})$ are tilted to an angle θ about (x_0, z_0).[5]

$$\tilde{x} = x_0 - ((x - x_0)\cos(\theta) - (z - z_0)\sin(\theta)) \tag{5.23}$$
$$\tilde{z} = z_0 - ((x - x_0)\sin(\theta) + (z - z_0)\cos(\theta)) \tag{5.24}$$

A χ^2 minimization routine optimizes the parameters to fit $\mathbf{M}$ to $\mathbf{D}(\Delta_M)$ and Fig. 5.14 displays the result.

Projections of $\mathbf{D}(\Delta_0)$ onto $\mathbf{M}$ cross through zero and reverse sign across tune out. Each subset ξ returns one projection per Δ_0: $\langle \mathbf{D}(\Delta_0)\rangle_{j\in\xi} \cdot \mathbf{M}$ (left in Fig. 5.15). A fit to that curve crosses through zero at $\Delta_{\mathrm{TO},\xi}$, the subset's estimate of tune out.[6]

Two routes produce error bars to satisfy any curiosity about the distribution of errors. First, we average each single subset's $\langle \mathbf{D}(\Delta_0)\rangle_{j\in\xi} \cdot \mathbf{M}$ curve over the entire data set. That produces a projection curve with error bars on each point, plotted on the right in Fig. 5.15. The errors are too small to be visible on the projection curve, though a plot of the fit residuals makes them visible. The residuals are consistent with zero.

Alternatively, the subsets generate 320 individual estimates $\Delta_{\mathrm{TO},\xi}$ amenable to statistical analysis. Fig. 5.16 shows these 320 results along with a histogram binning the data and a gaussian fit to the histogram. The results pass goodness-of-fit normality tests (Lilliefors, Jarque-Bera, χ^2, and Kolmogorov-Smirnov) and appear as convincingly Gaussian as a reasonable person could want. The normality of the distribution justifies using a standard error as the uncertainty metric.

$$\langle \Delta_{\mathrm{TO},\xi} \rangle = 2\pi \times 3335.5(1.1)\ \mathrm{MHz}. \tag{5.25}$$

[4]The interferometer signal for a four-pulse Mach-Zehnder looks like a cosine, but tuning the phase difference to an odd multiple of $\pi/2$ using the bias from $f_m^{\pm}$ makes it look like a sine for which $\sin(\Delta\phi) \approx \Delta\phi$.

[5]The tilt is a consequence of the Raman beams not being aligned precisely to the z axis the CCD images.

[6]The fit also returns a fit uncertainty on the parameter, but we found those errors to underestimate the error. that is, they are small compared to the scatter in the data, so we ignore them.

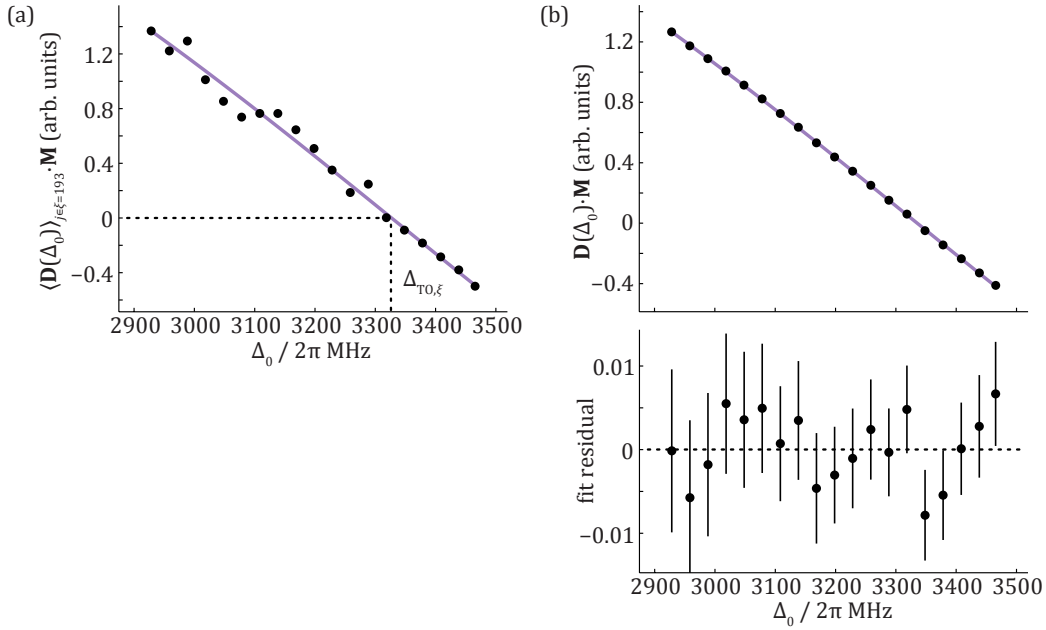

Figure 5.15: Projections of residual images **D** onto the model **M**. In (a), difference images from a single subset s of the data are projected onto the model. In (b), we reduce the noise in the curve by constructing a curve such as in (a) for each subset s. Averaging over each of those curves produces (b), where error bars are shown but are smaller than the markers. The fit residuals for the averaged curve are consistent with 0.

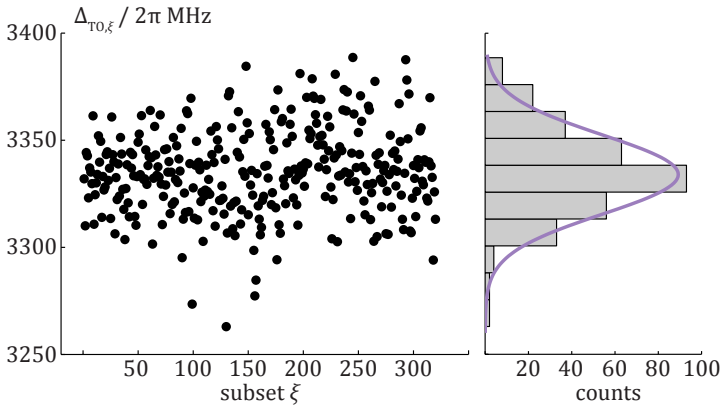

Figure 5.16: Statistics of subsets' results. Each subset returns one of 320 estimates of tune out. The results bin to a gaussian distribution (fit in purple).

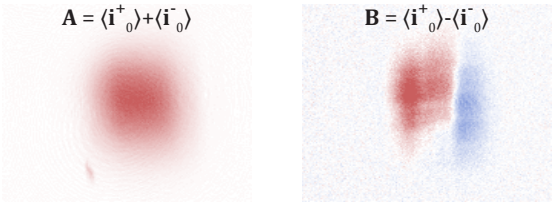

Figure 5.17: **A** and **B** from unpulsed images. The unpulsed averages are taken over the entire data set.

We also computed the overlapped Allan deviation [154] and observe that the uncertainty integrates down with a power of -0.4 in the measurement time, slightly slower than the expected square-root scaling.

5.5.2 Scattering and other features

The difference images are the most relevant to the tune-out signal, but the other base components are also accessible via Eq. (5.13). The underlying atomic density **A** should be the sum of the two sensitivities' unpulsed averages (left of Fig. 5.17). Taking the difference between the unpulsed averages of the two sensitivities should cancel **A** and reveal **B**.

The manifestation of **B** in the data (right of Fig. 5.17) remains a mystery of the data set. It is unclear what process generates this interferometer- and sensitivity-dependent background signal.[7] It is unlikely to be a magnetic field gradient, since the pattern is effectively perpendicular to the interferometer axis and the interferometer could only sample magnetic field gradients along the interferometer axis. It is probable that the Raman beam centers are not precisely aligned to the center of the sample. Misalignment would produce an intensity gradient across the sample that might result result in a position-dependent offset phase through finite pulse effects. The sensitivity reversal could not be tuned properly for the entire sample simultaneously, resulting in population gradients that change sign with the sensitivity.

Alert or skeptical readers may notice an asymmetry in the difference images of Fig. 5.13. The blue lobe of the signal appears consistently stronger than the red lobe. The asymmetry could result if the scattering monopole **Z** does not appear with equal strength in $\mathbf{R}^{\pm}$.

We isolate the scattering monopole in the data not by taking the difference of residual images as in Eq. (5.21), but by summing them. The signal should cancel and reveal the pattern due to scattering. Fig. 5.18 shows these images averaged over the entire data set. The wavelength dependence is weak, so we can achieve a higher signal-to-noise image by averaging over wavelengths as well (bottom left of Fig. 5.18). Computing the projection

[7] We discovered the dependence of the unpulsed images on interferometer sensitivity well after the data campaign. Early analysis treated all unpulsed shots equally, irrespective of sensitivity, so finding the dependence was critical in developing a consistent analysis method. I am unbelievably grateful to my prior, prescient self for deciding to take unpulsed shots with both sensitivities.

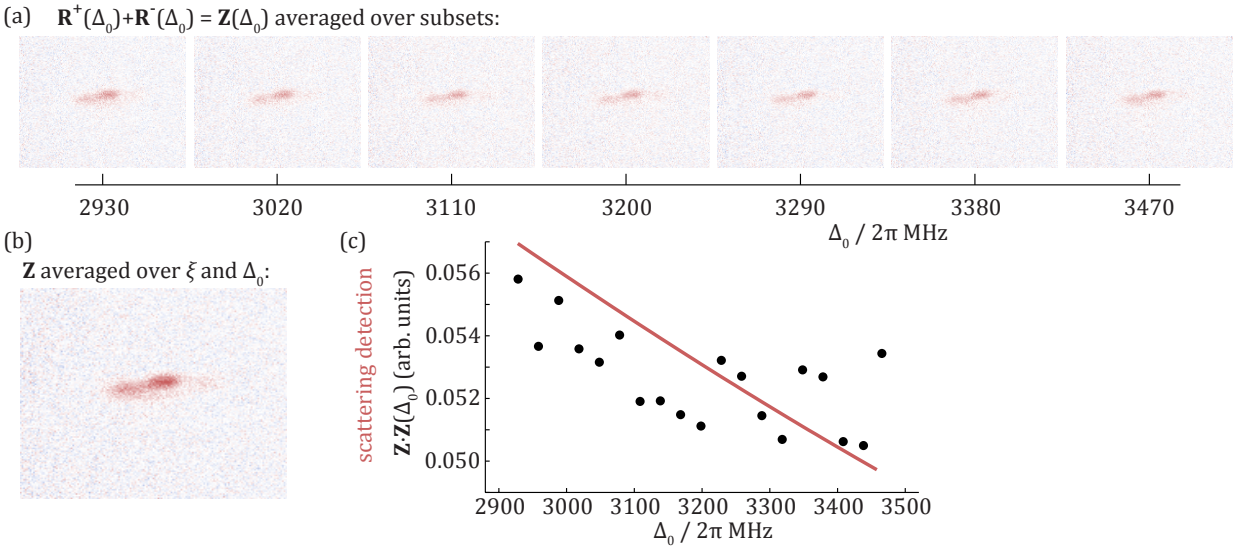

Figure 5.18: Scattering images. The sum of residual images cancels the signal of interest and isolates single-photon scattering. The pattern (shown in (a) at each wavelength) is largely independent of wavelength, permitting an average, shown in (b). In (c), projections of each wavelength's image onto the average show a small dependence on wavelength. A calculation of the probability that an atom scatters and falls into the detected $F = 1$ state produces the red curve, which is rescaled to match the projections' units.

of each wavelength's image onto the average illustrates the weak wavelength dependence of the scattering rate near tune out. The total scattering rate is not the quantity that should reproduce this dependence, but rather the probability that an atom that scatters decays into $F = 1$ to be detected. Computing that quantity reproduces the dependence, at least qualitatively.

The fact that the scattering survives Eq. (5.21) to produce the blue-lobe preference is another outstanding mystery of the data set. It is unclear why the scattering appears stronger in $\mathbf{R}^-$ compared to $\mathbf{R}^+$. Taken alone, it should not be concerning, assuming the scattering pattern and the signal pattern are centered on each other. At tune out, there would be no signal and a monopole scattering pattern that is even about the center. The model $\mathbf{M}$ is odd about the center, so the projection should be 0 and there should[8] be no systematic shift to the projection curves in Fig. 5.15.

Any position offset between the the monopole scattering pattern and the dipole signal pattern spoils this assumption. If $\mathbf{M}$ is offset with respect to $\mathbf{Z}$, then even at tune out when only $\mathbf{Z}$ remains, there would be a nonzero projection onto $\mathbf{M}$, systematically shifting the entire projection curve. With that, we arrive at our analysis of systematic effects.

[8]My undergraduate advisor Prof. Jutta Luettmer-Strathmann likes to say, "'Should' is a four-letter word". I hear this refrain quite often in the back of my head.

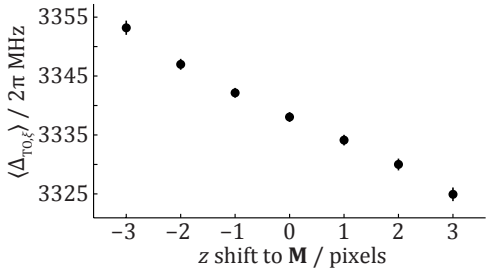

Figure 5.19: Projective result versus pixel offset. If **M** is not centered on the scattering pattern, it shifts the result by ~ 4.5 MHz per pixel offset.

5.6 Systematic effects

5.6.1 Scattering recoil and one-dimensional analysis

If **Z** and **S** are not centered on each other, the projective analysis presented above suffers a systematic shift. The two patterns both originate from the same Stark-shifting beam profile, so we might expect them to be centered on each other. There is nevertheless an important difference between the processes that generate the two patterns. The coherent effect of the beam that generates **S** remains effectively stationary and centered on the beam because the dipole forces due to the small AC Stark shifts are small.

Any atom that scatters, however, recoils with an average velocity v_r along the beam's propagation direction. The Stark-shifting beam axis cannot be perfectly aligned to the imaging beam axis, so there is a projection of the Stark beam axis onto the imaging plane. Consider a $\sim 5°$ tilt between the beams. The scattering pattern drifts at v_r from the moment of scattering through to detection. Assuming an atom scatters halfway through $T' = 110$ μs, it continues through the final $T = 53$ μs to detection. That totals to ~ 100 μs recoiling at a speed $\sim v_r \sin(5°)$ in the imaging plane, a distance of about 1 μm.

We can quantify the effect by intentionally shifting **M** by a number of pixels and performing the full analysis. Fig. 5.19 shows the results, yielding a systematic shift of about 4.5 MHz per pixel offset. This is large enough to warrant further investigation.

Phase patterning can produce nontrivial patterns in multiple dimensions. Our measurement utilizes information only along the interferometer axis, so we may integrate pixels perpendicular to the interferometer axis. The fit of $\mathbf{D}(\Delta_M)$ to **M** returns an angle 4.4°, so we rotate the difference images by that angle, using a bicubic interpolation, before integrating. Fig. 5.20 shows the resulting one-dimensional trace for $\mathbf{D}(\Delta_M)$, which exhibits a dramatic asymmetry due to scattering.

We fit each one-dimensional trace to the sum of a signal portion of the fit and a scattering portion of the fit (top of Fig. 5.21).[9] Both the signal portion and scattering portion of the fit deliver their own amplitudes. We plot the amplitude of the signal portion of the fit and

[9]Before fitting, we generate error bars that weight for the atomic density. That procedure suppresses the importance of points away from the center where the signal sits.

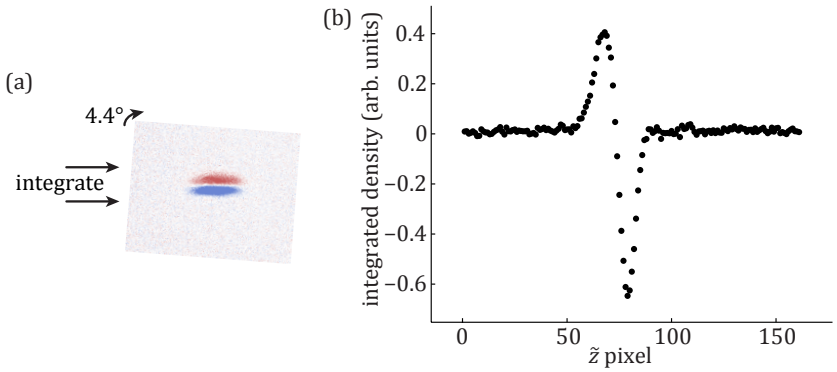

Figure 5.20: Dimension reduction. As shown in (a), we tilt out the angle appearing in the difference images and integrate the pixel values perpendicular to the interferometer axis to generate a one-dimensional signal as shown in (b).

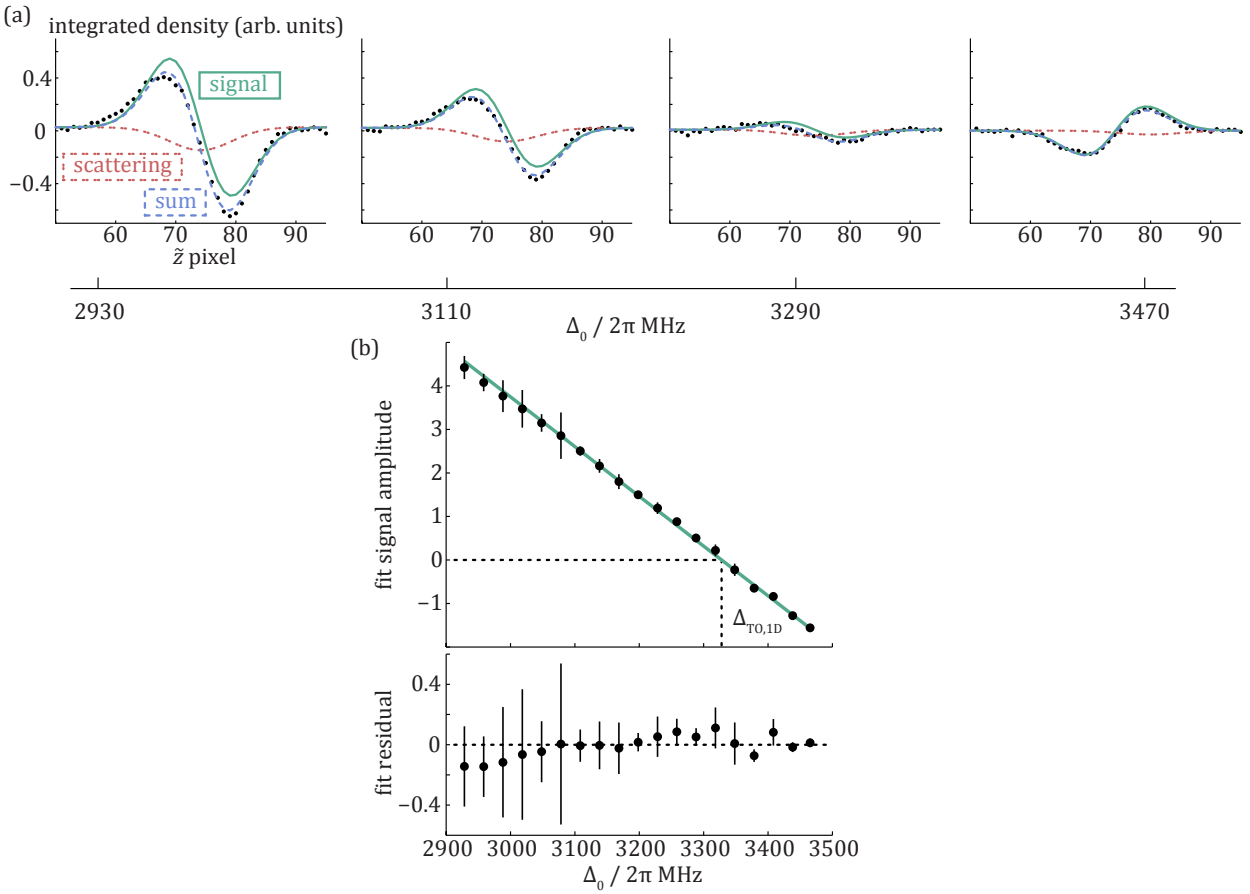

Figure 5.21: One-dimensional analysis. In (a), we fit each one-dimensional trace to the sum (blue dashed line) of a signal portion (green line) and a scattering portion (red dot-dot line). Tune out is where the amplitudes of just the signal portion of the fit cross through zero, shown in (b) with fit residuals that do show clear structure.

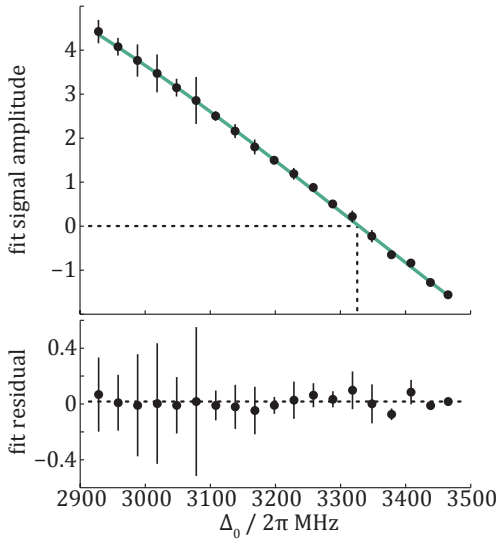

Figure 5.22: Cubic fit to one-dimensional signal amplitudes. We do not report this value.

estimate tune out $\Delta_{\mathrm{TO,1D}}$ as the frequency at which a fit to the amplitudes crosses through 0 (bottom of Fig. 5.21). To estimate the error, we compute the standard deviation of jackknife estimates of the zero crossing. That is, we fit for the zero crossing neglecting each point on the curve, one at a time, and calculate the square root of the variance among the estimates. Jackknifing the error here results in an error bar 40% larger than the fit uncertainty. This should account for what may be nontrivial structure in the fit residuals.

$$\Delta_{\mathrm{TO,1D}} = 2\pi \times 3328.0(1.4)\ \mathrm{MHz}. \tag{5.26}$$

This value is shifted down by about 8 MHz compared to the two-dimensional projective analysis. We see a one-to-two pixel offset between the signal portion of the fit and the total fit in the one-dimensional trace for $\mathbf{D}(\Delta_M)$, consistent with the rough estimate of 4.5 MHz per pixel offset.

The structure in the residuals of the fit in Fig. 5.21 might make some readers uncomfortable. In Fig. 5.22, we include a cubic term in the fit function. The residuals qualitatively improve and the fit crosses through zero at 3328.86(1.42) MHz. Nevertheless, we choose to report the result from Fig. 5.21 with the linear fit because that fit more closely matches the result of a fit that excludes the first 5 points where the curvature is most dramatic (3329.30(1.40) MHz).

5.6.2 Cold-atom spectroscopy

Spectroscopy of the cold-atom sample itself solves two problems. First, it allows us to calibrate and determine the Doppler shift the atoms see on the Stark-shifting beam during the tune-out measurement. Second, it allows us to set a baseline f_0 to which we reference

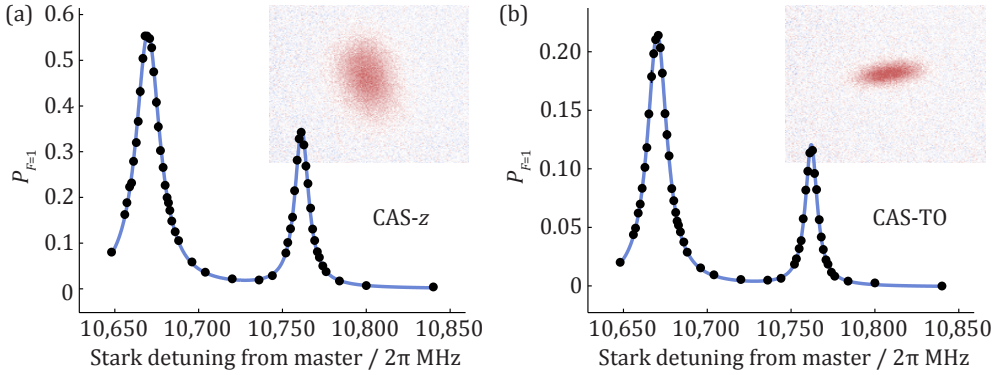

Figure 5.23: Cold-atom spectra. Spectroscopy of the cold atomic sample measures the D_1 resonances along two axes: z in (a) and along the axis we use to measure tune out in (b). The spectra establish a spectroscopic baseline and calibrate a Doppler systematic. Insets show an example of the excitation whose sum is plotted. (CAS-z: 07/30/2018, GCs -4558 to -3851) (CAS-TO: 07/30/2018, GCs -3850 to -3143)

detunings Δ_0. The latter establishes a method to measuring the wavelength of the laser (in combination with laser spectroscopy data), alternative to using a frequency comb for a direct wavelength measurement.

Doppler shift and f_0 reference

Magnetic field dynamics launch the cold atomic sample. Time-of-flight imaging records a speed of roughly 1 m/s in the imaging plane, but cannot access the component perpendicular to the imaging plane. The Stark-shifting beam necessarily propagates perpendicular to the imaging plane, so a different method must probe the velocity component along the Stark beam axis. Any velocity along that axis produces a Doppler shift that the atoms register in the tune-out measurement, so it is imperative to determine the launch velocity component along the Stark beam axis.

We first establish a spectroscopic baseline by performing cold-atom spectroscopy (CAS) along an axis for which we know the Doppler shift, $\hat{z}$ in the $x-z$ imaging plane. We divert the Stark beam via a magnetic mirror to an axis close to the Raman beam axis, which is essentially parallel to $\hat{z}$[10], so we call it CAS-z.

We phase lock the Stark laser near the D_1 line using a local oscillator frequency near 2700 MHz, quadrupled to the $\sim$ 10-GHz $2P$ fine-structure splitting. The CAS-z beam transmits through a polarizing beam splitter cube establishing a polarization very close to $\hat{x} \sim \sigma^{\pm}$. Scanning the laser wavelength exposes two resonances, $|2S_{1/2}, F = 2, m_F = 0\rangle \rightarrow |2S_{1/2}, F = 1, m_F = \pm 1\rangle$ at lower laser frequency (higher local oscillator frequency) and $|2S_{1/2}, F = 2, m_F = 0\rangle \rightarrow |2S_{1/2}, F = 2, m_F = \pm 1\rangle$ at higher laser frequency (lower local

[10]There is a small, $\sim 2^{\circ}$ offset between $\hat{z}$ and the CAS-z axis.

oscillator frequency). We fit the excitations to the sum of two Lorentzians as Fig. 5.23 shows.

Just before or after spectroscopy, time-of-flight imaging measures the launch velocity along z. The velocity determines the size of the Doppler effect that shifts the resonances. To determine the direction of the launch, we insert an object between the vacuum chamber and the first imaging lens. Matching the object movement and the launch direction establishes the launch direction to be North-to-South, opposite the propagation of the CAS-z beam. The atoms therefore see the CAS-z beam shifted to the blue and they resonate at a frequency lower than the true resonance. At $v_z \sim -1$ m/s for 670.962 nm, we correct the CAS-z resonance upward by $\sim 2\pi \times 1.4$ MHz.[11] Correcting the optical frequency upward corresponds to correcting the local oscillator (that sets the Stark laser's detuning from the master laser) downward. The Doppler-corrected resonance establishes the frequency f_0 that detunings Δ_0 reference. Averaging 14 measurements throughout the tune-out measurement campaign gives a quadrupled local oscillator frequency of $2\pi \times (10669.72 - 1.36) = 2\pi \times 10668.36(5)$ MHz. The 0.05-MHz error is the standard error among the 14 Doppler-corrected measurements; any errors due to drift in the master spectroscopy would manifest there. Referencing optical detunings to this frequency for the tune-out measurement requires subtracting the tripled local oscillator frequency $2\pi \times f_{LO}$ that scans the laser about tune out.

$$\Delta_0 = 2\pi \times (10668.36 - 3f_{LO}) \text{ MHz}. \tag{5.27}$$

The Doppler-free spectroscopic baseline from CAS-z permits calibration of the Doppler shift atoms see on the Stark-shifting beam axis in the tune-out measurement. We again tune the Stark laser near the D_1 line, but allow it to propagate along the tune-out path along which it induces AC Stark shift gradients in the interferometer. This CAS-TO spectroscopy records a resonance at $4f_{LO}$ that is shifted by an average of $2\pi \times 1.58(6)$ MHz upward from $2\pi \times 10668.36$ MHz in the same direction as the CAS-z resonance. The atoms must also see the Stark-shifting laser blue-shifted. We therefore correct the measured tune-out frequency upward by $2\pi \times 1.58(6)$ MHz to account for this Doppler shift.

Imperfect optical pumping

Cold-atom spectroscopy does not isolate $|2S_{1/2}, F = 2, m_F = 0\rangle$. It interrogates the Zeeman populations delivered to it by optical pumping: $P_{m_F=0} = 0.80(2)$, $P_{m_F=\pm} = 0.00(2)$, $P_{m_F=-2} = 0.16(2)$, and $P_{m_F=+2} = 0.04(2)$. The Zeeman effect perturbs each state and its transition energies. The shifts contributed by the $m_F = +2$ and $m_F = -2$ are equal and opposite, but they do not cancel here due to the population asymmetry.

The shift due to 4% in $m_F = +2$ cancels 4% of the 16% in $m_F = -2$, leaving a 12% asymmetry towards $m_F = -2$ to induce a shift. The transition is Zeeman-shifted by the difference in Zeeman shifts in the ground and excited states. For the CAS-z $\hat{x}$-polarized light, only a σ^+ transition contributes from $|2S_{1/2}, F = 2, m_F = -2\rangle \rightarrow |2P_{1/2}, F = 2, m_F = -1\rangle$,

[11] Each of the 14 measurements is slightly different, so we only quote an approximate value here.

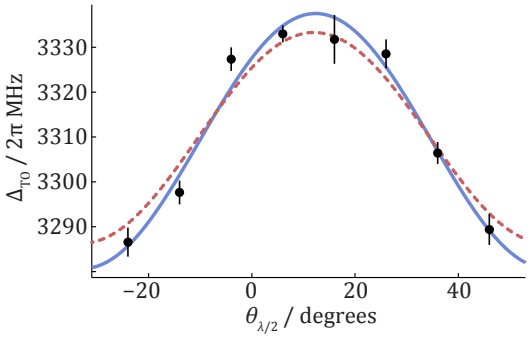

Figure 5.24: Variation of tune out with polarization. The tune out measurement at several angles of linear polarization traces out the variation due to the tensor polarizability. A fit with free amplitude (blue line) returns a variation of $2\pi \times 56.8(4.7)$ MHz. Another fit has its amplitude constrained to the theoretically predicted $2\pi \times 47$ MHz (red dot-dot line).

reducing the potency by a factor of 2 since only half the total optical power contributes to the transition.

The transition itself is perturbed by the difference in Zeeman-shifted energies of $|2S_{1/2}, F = 2, m_F = -2\rangle$ and $|2P_{1/2}, F = 2, m_F = -1\rangle$; the former with $g_F = 1/2$ and the latter with $g_F = 1/6$. The transition is perturbed by $\Delta U_e - \Delta U_g = \mu_B((1/6)(-1) - (1/2)(-2))(1.3)\,\mathrm{G} = \hbar(+2\pi \times 1.52\ \mathrm{MHz})$. Multiplied by the factor accounting for population asymmetry and half the optical power, 0.06, the total shift to the spectroscopic baseline due to the Zeeman population asymmetry is $2\pi \times 0.09(2)$ MHz. The transition frequency we measure is higher than f_0 by this amount, which makes detunings from it look too low, so we correct the final reported tune-out detuning upward.

The shift due to uncertainty in the $m_F = \pm 1$ populations is much smaller than this effect, so we do not consider it here.

5.6.3 Polarization

The polarization of the Stark-shifting light can have a significant impact on tune out. Different polarizations couple with different strengths to the excited states. The difference between tune outs for $|2S_{1/2}, F = 2, m_F = 0\rangle$ using $\sigma^{\pm}$ and π polarization is $2\pi \times 47$ MHz, assuming the theoretical matrix elements in Ref. [12].

Our experimental geometry allows for a nonzero projection of the Stark-shifting beam onto $\hat{z}$. That precludes a perfectly π-polarized beam. We can, however, achieve a pure polarization along $\hat{x}$, a linear combination of $\sigma^{\pm}$. Both σ^{+} and σ^{-} produce identical tune-out wavelengths for $m_F = 0$. We therefore pursue $\sigma^{\pm}$ polarization, which maximizes Δ_{TO}. A Wollaston prism outside the vacuum chamber ensures the polarization purity. Then, a half wave plate at angle $\theta_{\lambda/2}$ and a quarter wave plate at angle $\theta_{\lambda/4}$ control the polarization entering the chamber (see Fig. 3.36).

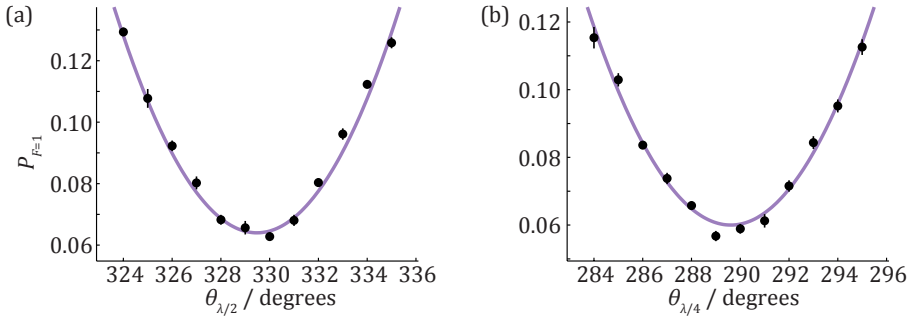

Figure 5.25: Finding π polarization for the Stark beam. When the Stark-shifting beam performs spectroscopy on the optical pumping transition, scattering is minimized when the polarization most closely resembles π polarization at the minima of the curves above. (a) shows the scattering minimum tuning the half-wave plate, while (b) shows the scattering minimum tuning the quarter-wave plate. ($\lambda/2$ scan: 07/25/2018, GCs -23780 to -23660) ($\lambda/2$ scan: 07/25/2018 GCs -23659 to -23539)

We can roughly set the polarization outside the vacuum chamber. To do so, we temporarily insert a PBS cube just before the periscoping mirror that sends the Stark-shifting beam into the chamber. Polarization along $\hat{x}$ is nearly parallel to the optical table, so we tune the waveplates to minimize the reflection at the cube. The minimum occurs at angles $\theta_{\mathrm{PBS},\lambda/2} = 6°$ and $\theta_{\mathrm{PBS},\lambda/4} = 4°$. From this baseline, we perform tune-out measurements at incremental values of polarization. We use the two-dimensional projective analysis for these data, not the one-dimensional analysis. Each value may be systematically shifted, but we are only interested in obtaining the amplitude of tune-out variation with polarization. Tuning the half wave plate by 1° tilts the polarization by 2°, so for every angle we tilt the quarter wave plate by twice as much to follow the half wave plate and preserve linear polarization. The wave plate angles therefore respect a relationship $\theta_{\lambda/4} - \theta_{\mathrm{PBS},\lambda/4} = 2(\theta_{\lambda/2} - \theta_{\mathrm{PBS},\lambda/2})$ as we scan the linear polarization.

Fig. 5.24 shows the variation in tune out with polarization. Because the $m_F = 0$ state has no vector polarizability, the variation in this plot traces out the variation due to the tensor polarizability. We fit the variation with a period constrained to 90°, since a 90° rotation on the half wave plate restores a polarization. The red dotted fit assumes an amplitude equal to the $2\pi \times 47$-MHz variation predicted by theory, which is worse than the solid blue fit with free amplitude. The free-amplitude fit returns a variation of $2\pi \times 56.8(4.7)$ MHz, 2-σ larger than the predicted value.

The free amplitude fit also suggests the wave plate angle that maximizes tune out, which is the polarization that most closely matches $\hat{x} \sim \sigma^{\pm}$. The maximum occurs at $\theta_{0,\lambda/2} = 12.4(1.0)°$.

Setting the polarization outside the vacuum chamber may not be sufficient. Vacuum viewports can exhibit significant birefringence that rotate the polarization [166]. The optical pumping transition that forbids $|2S_{1/2}, F = 2, m_F = 0\rangle \rightarrow |2P_{1/2}, F = 2, m_F = 0\rangle$ permits

an *in situ* measurement of the polarization. Of course, probing that transition requires π polarization, 90° rotated from the $\sigma^{\pm}$ polarization we seek. We may nevertheless perform spectroscopy on the optical pumping transition using the Stark-shifting beam and rotate 90° from there. The wave plate angles that minimize the scattering rate identify π polarization.

We perform CAS-TO on the $|2S_{1/2}, F = 2\rangle \rightarrow |2P_{1/2}, F = 2\rangle$ resonance in Fig. 5.23 and scan the wave plates to find π polarization. Fig. 5.25 shows the variation of the single-photon scattering excitation for the $|2S_{1/2}, F = 2, m_F = 0\rangle \rightarrow |2P_{1/2}, F = 2, m_F = 0\rangle$ transition as a function of wave plate angles. The angles that minimize scattering are $\theta_{\mathrm{OP},\lambda/2} = 329.5(1)°$ and $\theta_{\mathrm{OP},\lambda/4} = 289.6(1)°$. We can achieve $\sigma^{\pm}$ polarization by rotating the half wave plate by 45° to $\theta_{\mathrm{TO},\lambda/2} = 14.5°$ and the quarter wave plate by 90° to $\theta_{\mathrm{TO},\lambda/2} = 19.6°$. Because this method probes the polarization *in situ*, we expect the results to be more accurate than the previous method and use these wave plate angles for the 330,000-image tune-out measurement campaign.[12]

We assume the error in our polarization is set by the discrepancy between the two methods: $\Delta\theta_{\lambda/2} = \theta_{\mathrm{TO},\lambda/2} - \theta_{0,\lambda/2} = 2.1(9)°$ and $\Delta\theta_{\lambda/4} = \theta_{\mathrm{TO},\lambda/4} - \theta_{0,\lambda/4} = 3(2)°$. We treat each error independently by assuming the half wave plate introduces only error in the angle of linear polarization to $\hat{x}$ and that the quarter wave plate introduces only an ellipticity. Tuning the angle of the linear polarization can trace out the full 57-MHz polarization-dependent variation between $\hat{x}$ and $\hat{z}$. Coupling strengths depend on the square of the polarization component magnitude. That is, the fraction of the optical power that contributes to the wrong polarization follows the square of the projection, $\sin^2$. Further, 1° error on the half wave plate translates to a 2° error in the polarization angle. The total uncertainty contributed by the half wave plate is therefore $\sin^2(2\Delta\theta_{\lambda/2})2\pi \times 57$ MHz $= 2\pi \times 0.31$ MHz. The quarter wave plate can only produce half the full variation, since it tunes the polarization between $\hat{x}$ and an equal linear combination of $\hat{x}$ and $\hat{z}$: $\sin^2(\Delta\theta_{\lambda/4})2\pi \times 57/2$ MHz $= 2\pi \times 0.08$ MHz. Their quadrature sum of the errors is $2\pi \times 0.32$ MHz.

Reference [29] reports an effort to monitor and control the polarization throughout the tune-out measurement campaign. We assume the polarization is stable and do not make any effort to compensate for drifts.

5.6.4 Interferometer population impurities

Hyperfine impurity: complementary interferometer

The four-pulse Mach-Zehnder closes two interferometers that occupy different F during T'. The tune out of $|2S_{1/2}, F = 1, m_F = 0\rangle$ is larger than that of $F = 2$ by roughly the ground-state hyperfine splitting ~ 804 MHz. We aim to measure only where $F = 2$ tunes out, so we destroy the decoherence of the $F = 1$ interferometer by addressing it with MOT repump

[12] Also note that we do not include the data that contribute to Fig. 5.24 in the precision measurement of tune out. Doing so would improve the precision on the tune-out measurement, but requires knowledge of the tensor shift present at each point. Given the tension between our measurement and theory, we do not attempt these corrections.

light during T'. The contrast of that interferometer decays with a time constant of 6.5(1.7) μs (see Fig. 5.5). After the 70-μs pulse, a fraction $e^{-70/6.5} \sim 0.00002$ of the $F = 1$ atoms remains. Only half the atoms that would go on to interfere are recoiling in $F = 1$ during T', while the other half are in $F = 2$, so only a total fraction of 0.00001 in $F = 1$ contributes to the shift. The shift is $0.00001(2\pi \times 804)$ MHz $\sim 2\pi \times 0.01$ MHz. This signal would increase the measured tune-out frequency, so we correct our measurement downward.

Zeeman impurity

Imperfect optical pumping sends Zeeman populations into the interferometer that are in $F = 2$, but not the $m_F = 0$ state of interest.

The $m_F = \pm 2$ states where most of the Zeeman population impurity resides do not undergo the interferometer. The Raman polarizations follow a lin-$\perp$-lin scheme with polarizations close to $(\sigma^+ + \sigma^-)/\sqrt{2}$ and $(\sigma^+ - \sigma^-)/\sqrt{2}$. The only routes for $|2S_{1/2}, F = 2, m_F = \pm 2\rangle$ to transition to $F = 1$ with circular polarization are to absorb a $\sigma^\mp$ photon from one Raman beam (ω_2) and emit a $\sigma^\pm$ into the other (ω_1), arriving at $|2S_{1/2}, F = 1, m_F = 0\rangle$ via $F' = 1$ or $F' = 2$ on the D_2 line. Because the hyperfine structure is unresolved on the D_2 line, the $\sim$200-MHz single-photon detunings of the Raman beams to $F' = 1$ and $F' = 2$ are approximately equal. Neglecting the difference in detunings, the signs in the polarization components and the signs in the Clebsch-Gordan coefficients for the Raman routes collaborate to prohibit the $m_F = \pm 2$ states from undergoing a Raman transition.

Let us consider the $m_F = 2$ case explicitly. Sec. 2.4.2 outlines the calculation. Given lin-$\perp$-lin polarization, the components for the beam addressing $|2S_{1/2}, F = 2\rangle \to |2P_{3/2}, F' = 1, 2\rangle$ are $\epsilon_{ab,+1} = \epsilon_{ab,-1} = 1/\sqrt{2}$ and those addressing $|2S_{1/2}, F = 1\rangle \to |2P_{3/2}, F' = 1, 2\rangle$ are $\epsilon_{bc,-1} = 1/\sqrt{2} = -\epsilon_{bc,+1}$. There are two Raman routes with nonzero Rabi frequency that add to the total two-photon Rabi frequency:

(i) the atom absorbs a σ^- photon from $|2S_{1/2}, F = 2, m_F = 2\rangle$ to $|2P_{3/2}, F' = 2, m'_F = 1\rangle$ with $\epsilon_{ab,+1} = 1/\sqrt{2}$, then emits a σ^+ photon to $|2S_{1/2}, F'' = 1, m''_F = 0\rangle$ with $\epsilon_{bc,-1} = 1/\sqrt{2}$,

(ii) or the atom absorbs σ^- with $\epsilon_{ab,+1} = 1/\sqrt{2}$ to $|2P_{3/2}, F' = 1, m'_F = 1\rangle$, then emits σ^+ to $|2S_{1/2}, F'' = 1, m''_F = 0\rangle$ with $\epsilon_{bc,-1} = 1/\sqrt{2}$,

The products of the two polarization components and two Clebsch-Gordan coefficients for these routes are $\left(\sqrt{1/2}\right)\left(\sqrt{1/20}\right)$, $\left(\sqrt{1/2}\right)\left(\sqrt{5/24}\right)$, $\left(\sqrt{1/2}\right)\left(-\sqrt{1/12}\right)$, and $\left(\sqrt{1/2}\right)\left(\sqrt{1/8}\right)$, respectively. The sum of the Raman routes' Rabi frequencies vanish: $(1/2)\left(\sqrt{1/20}\right)\left(\sqrt{5/24}\right) + (1/2)\left(-\sqrt{1/12}\right)\left(\sqrt{1/8}\right) = 0$. The routes are calculated similarly for $m_F = -2$. Since the total Raman Rabi rate vanishes for both states, they do not undergo the interferometer and do not shift the tune-out result.

Now let us consider the $m_F = 1$ state. It has five routes it can take to undergo a Raman transition from $|2S_{1/2}, F = 2, m_F = 0\rangle$ to $|2S_{1/2}, F = 1\rangle$.

(i) the atom absorbs a σ^+ photon from $|2S_{1/2}, F = 2, m_F = 1\rangle$ to $|2P_{3/2}, F' = 2, m'_F = 2\rangle$ with $\epsilon_{ab,-1} = 1/\sqrt{2}$, then emits a σ^+ photon to $|2S_{1/2}, F'' = 1, m''_F = 1\rangle$ with $\epsilon_{bc,-1} = 1/\sqrt{2}$,

(ii) the atom absorbs a σ^- photon from $|2S_{1/2}, F = 2, m_F = 1\rangle$ to $|2P_{3/2}, F' = 2, m'_F = 0\rangle$ with $\epsilon_{ab,+1} = 1/\sqrt{2}$, then emits a σ^- photon to $|2S_{1/2}, F'' = 1, m''_F = 1\rangle$ with $\epsilon_{bc,+1} = -1/\sqrt{2}$,

(iii) the atom absorbs a σ^- photon from $|2S_{1/2}, F = 2, m_F = 1\rangle$ to $|2P_{3/2}, F' = 1, m'_F = 0\rangle$ with $\epsilon_{ab,+1} = 1/\sqrt{2}$, then emits a σ^- photon to $|2S_{1/2}, F'' = 1, m''_F = 1\rangle$ with $\epsilon_{bc,+1} = -1/\sqrt{2}$,

(iv) the atom absorbs a σ^- photon from $|2S_{1/2}, F = 2, m_F = 1\rangle$ to $|2P_{3/2}, F' = 2, m'_F = 0\rangle$ with $\epsilon_{ab,+1} = 1/\sqrt{2}$, then emits a σ^+ photon to $|2S_{1/2}, F'' = 1, m''_F = -1\rangle$ with $\epsilon_{bc,-1} = 1/\sqrt{2}$,

(v) the atom absorbs a σ^- photon from $|2S_{1/2}, F = 2, m_F = 1\rangle$ to $|2P_{3/2}, F' = 1, m'_F = 0\rangle$ with $\epsilon_{ab,+1} = 1/\sqrt{2}$, then emits a σ^+ photon to $|2S_{1/2}, F'' = 1, m''_F = -1\rangle$ with $\epsilon_{bc,-1} = 1/\sqrt{2}$.

The polarization-component times Clebsch-Gordan product for each route respectively is

(i) $\left(\sqrt{1/2}\right)\left(\sqrt{1/12}\right) \times \left(\sqrt{1/2}\right)\left(\sqrt{1/4}\right)$,

(ii) $\left(\sqrt{1/2}\right)\left(-\sqrt{1/8}\right) \times \left(-\sqrt{1/2}\right)\left(\sqrt{1/24}\right)$,

(iii) $\left(\sqrt{1/2}\right)\left(\sqrt{1/40}\right) \times \left(-\sqrt{1/2}\right)\left(-\sqrt{5/24}\right)$,

(iv) $\left(\sqrt{1/2}\right)\left(-\sqrt{1/8}\right) \times \left(\sqrt{1/2}\right)\left(\sqrt{1/24}\right)$,

(v) $\left(\sqrt{1/2}\right)\left(\sqrt{1/40}\right) \times \left(\sqrt{1/2}\right)\left(\sqrt{5/24}\right)$.

The sum of these factors is 0.144.

Performing a similar summation for the $m_F = 0$ state yields a factor of 0.167. That implies that the Raman Rabi frequency for the $m_F = +1$ state is a factor of 0.144/0.167=0.86 that of the $m_F = 0$ state. We set the $\pi/2$ pulse time using the Rabi frequency of the $m_F = 0$ state. Each pulse transfers $m_F = 1$ atoms with an efficiency reduced by that amount and there are four pulses. The relative contrast is therefore $(\sin^2(0.86\pi/4)/\sin^2(\pi/4))^4 = 0.37$ (multiplying the efficiencies from Eq. (2.43) once for each pulse). That is, any atoms undergoing the interferometer from $m_F = \pm 1$ interfere with 37% the contrast of the $m_F = 0$ atoms. Neglecting small changes due to the Zeeman shift [28], their tune out is shifted downward by $2\pi \times 7.71$ MHz.

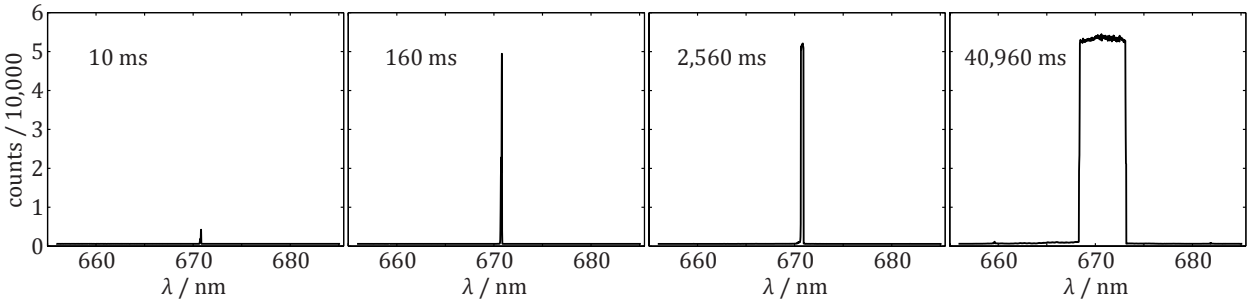

Figure 5.26: Intensity counts with a grating spectrometer. Calculating the power spectral density requires recording raw spectra at an array of exposure times.

Recall that we do not actually detect any atoms in the $m_F = \pm 1$ states after optical pumping. We can, however, derive an uncertainty in the contribution of this state assuming the 0.02 fractional uncertainty in the population from imaging noise and uncertainty in the population estimation. While the fractional population in $m_F = \pm 1$ is 0.02, half those atoms are destined to follow the $F = 1$ complementary interferometer and decohere, so only a fractional population of 0.01 might interfere. Each of the states adds an uncertainty $0.37 \cdot 0.01 \cdot (2\pi \times 7.71 \text{ MHz}) = 2\pi \times 0.03$ MHz. Adding the two $m_F = \pm 1$ populations' uncertainties in quadrature, we arrive at an uncertainty $2\pi \times 0.04$ MHz.

5.6.5 Broadband emission

Diode lasers generally do not emit perfectly monochromatic light. The Stark ECDL we use to measure tune out is no exception. The laser emits the majority of its optical power in the lasing peak, but it also emits a small fraction of the total power over a large bandwidth. The broadband emission is called amplified spontaneous emission (ASE) [167]. Each component of that spectrum contributes to the total Stark shift and the gradient that the interferometer samples for the tune-out measurement. Even when the lasing peak sits at tune out, the remnant Stark shifts from the rest of the ASE spectrum could contribute a nonzero signal that systematically shifts our result.

We record the spectrum of the laser with a grating spectrometer (Princeton Instruments Acton SpectraPro SP-2300 with PIXIS 400 CCD, borrowed from Norm Yao's group). The dynamic range of the camera is too small to measure the spectrum across the requisite range of power spectral densities.

We build the power spectral density (PSD) by covering the spectrometer in a dark curtain to block room light, attenuating the laser light, and then exposing the spectrometer for an array of times, each twice the previous: 10, 20, 40, 80, 160, 320, 640, 1280, 2560, 5120, 10240, 20480, 40960, and 81920 ms. Five repetitions through this scan of exposures help to smooth out noise. Fig. 5.26 shows four of the exposures. The highest exposures saturate the detector around the lasing peak but provide valuable information about wavelengths at very low PSD. Low exposures provide information about the power in the lasing peak before

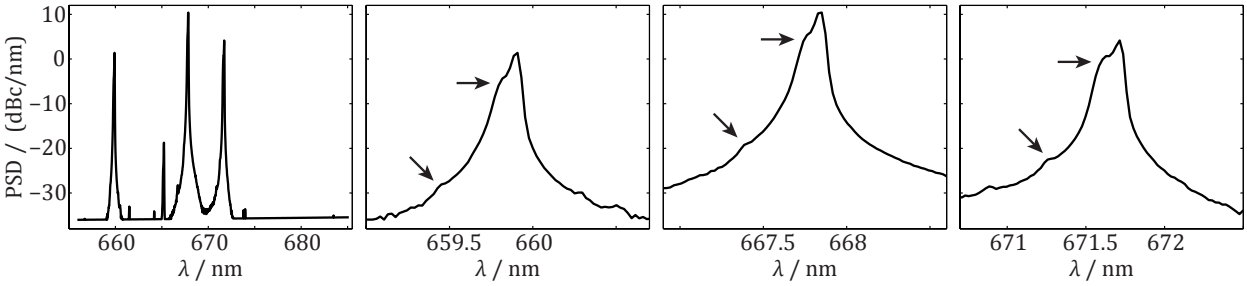

Figure 5.27: PSD of neon calibration source. The recorded PSD of a neon calibration source shows pathologies (black arrows) that are conserved across monochromatic peaks.

it saturates the detector. Stitching together the scans into a PSD requires some processing. We first subtract the value from an averaged scan of the spectrometer in the dark to find the counts above the noise floor at each wavelength.[13] We identify the valid points in each scan as the wavelengths whose counts lie comfortably between the detector's noise floor and saturation. For those points, we divide the higher-exposure scan's count by 2 (the relative factor between adjacent exposures) and average the two values. Across the five repetitions of this kind of scan, we choose the median of each value.

We report the power in dB relative to the carrier (dBc). Doing so requires summing the counts in the carrier peak across the noise bandwidth of the detector to get the total peak counts. Then we divide each count by the peak count and divide by the resolution bandwidth. Taking $10\log_{10}$ of those values gives the PSD in dBc/nm. Though the resolution bandwidth (RBW) of the spectrometer is 0.022 nm, errors in the imaging system spread photons across a series of pixels. Notice the two artifacts conserved across each peak of a neon calibration source in Fig. 5.27. The artifacts imply that the grating spectrometer's imaging system distributes the photons of a single peak across a range of pixels spanning ∼1 nm, the noise bandwidth. We therefore calculate the carrier counts by summing all counts within a 1-nm window and normalize to that value to report a dBc.

Fig. 5.28 shows the resulting PSD for the Stark-shifting laser. Because the noise bandwidth spans ∼1 nm, we consider PSD within a 1-nm window around the peak to originate from lasing peak itself. We truncate the lasing peak across the noise bandwidth and consider the remaining spectrum the PSD of the ASE.

For a total laser power P, the power at wavelength λ is $P10^{\mathrm{PSD}(\lambda)/10}(\mathrm{RBW})$. The associated systematic shift is the sum of interferometer phase differences (ala Eq. 5.6) induced by the power at each wavelength in the spectrum. We compare the result for the laser peak's detuning Δ_0 at which the phase shift for $z = w_z/2$ crosses through zero both with and without this extra phase shift contributed by the ASE. The ASE shifts the zero crossing upward by $2\pi \times 0.09$ MHz, so we correct our final result downward by that amount. This systematic is independent of total laser power, but does depend on the wavelength calibration of the spectrometer and errors that result from how we stitch together the array of exposures. A

[13] The average dark counts are around 590, the subtle vertical offsets in Fig. 5.26.

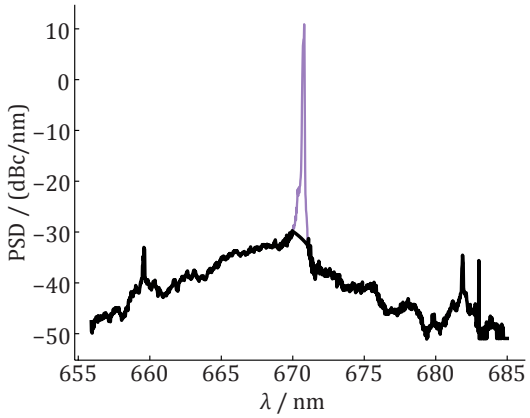

Figure 5.28: PSD of Stark ECDL. We truncate the lasing peak (thin purple) across a window the size of the spectrometer noise bandwidth and calculate the total systematic Stark shift contributed by the remaining spectrum (thick black).

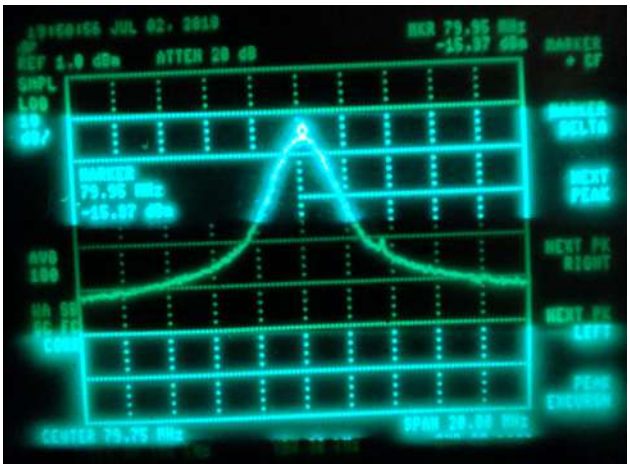

Figure 5.29: Electronic beat note of Stark laser. The laser has a symmetric spectrum and full-width-half-max linewidth of 1.4 MHz. (07/02/2018)

$2\pi \times 0.1$-MHz uncertainty in this systematic originates from the spread of shifts we calculate within an expected range of wavelength and power calibration errors.

The grating spectrometer only accesses information outside a 1-nm window from the lasing peak. Any irregularities in the laser spectrum within that window could contribute large systematics, especially if there are asymmetries across the D-line resonances. The electronic beat note in the phase lock does provide information very close to the lasing peak, as Fig. 5.29 shows, but also does not spawn any concerns.

In principle, even a symmetric laser peak could couple asymmetrically to the D lines. Since tune out is not equidistant to each line, the coupling strength $\propto 1/\Delta$ varies at different rates for each of the lines on either side of the lasing peak's center. The laser inherits a 1.4-

MHz linewidth from the master laser lock, small enough compared to the fine-structure splitting to quell worries about these kinds of asymmetries.

A final class of suspicions may lie between the regimes above. The spectrometer's noise bandwidth is too large to probe any spectral features near or within the D lines and any record of the beat note in the phase lock is too narrow. If there were any anomalous features in the laser spectrum close to the D-line resonances, it could have introduced systematic asymmetries in the coupling. We cannot rule out this possibility definitively, though no signs point to such anomalies. For example, there are no anomalies in the D_1 spectroscopy scans in Fig. 5.23. Rogue peaks in the laser spectrum could have manifested there as excitations that appear removed from the resonances. Even the nonzero slope of the ASE around the resonances could be unsettling. Calculations with Eq. (2.57) confirmed that the slope of the ASE is small enough that the coupling remains symmetric enough about the resonances that any contribution to the Stark shift just above a resonance effectively cancels an equal and opposite contribution just below the resonance.

5.6.6 Phase lock stability

Throughout the tune-out measurement, we use the local oscillator frequency in the phase lock as a proxy for the Stark laser wavelength. It establishes f_0 as a detuning from the master laser and all detunings Δ_0 that parameterize the laser wavelength reference it. If the lock tone in the phase lock varied with the local oscillator frequency, then the local oscillator frequency would not be a good metric. An early version of the lock with a frequency-offset "trombone" lock varied by up to several MHz as a function of local oscillator frequency. The phase lock, in blissful contrast, is stable to 10 kHz, around 79.69 MHz.

5.6.7 Effects that contribute insignificant shifts

Some effects in this section could contribute systematic effects, but we reason here that the effects are negligible. Other effects could be significant, but would not systemically shift our result – for example, the Sagnac effect shifts the overall phase of the interferometer so as to be calibrated into f_m. We include examples of both these effects to anticipate any questions readers may have.

Mechanical dipole forces

The AC Stark shift creates a potential that follows the intensity profile of the beam just like a dipole trap. The gradient in the potential produces a force $F_z = -dU/dz$ that can kick the atoms over the interaction time with the Stark beam. At $x = 0$ where the gradient and this kick is largest,

$$F = -\frac{\hbar\gamma^2}{2}\left(\frac{2P}{\pi w_x w_z^2}\right)\left(\frac{4z}{w_z^2}\right)e^{-2z^2/w_z^2}\left(\frac{1}{4}\right)\left(\frac{1}{\Delta I^*_{sat,D1,TO}} + \frac{1}{(\Delta - \Delta_{FS})I^*_{sat,D1,TO}}\right). \quad (5.28)$$

The magnitude of the force is maximal at $z = w_z/2$. The acceleration $a = F/m$ that acts on the atom for the pulse length τ =0.1 ms to produce a displacement $a\tau^2/2$ that is merely $\sim$0.5 microns at maximum.

This displacement is not the same in character as the displacement from scattering that motivated the one-dimensional analysis. That was a displacement of the dipole signal pattern relative to a monopole scattering pattern. Here, the displacement would be a common perturbation to both the dipole and monopole positions. Furthermore, the effect is symmetric about the center of the cloud. When the total Stark shift is negative (positive), atoms drift into (away from) the center of the beam.

Sagnac

The sample's launch velocity is not parallel to the interferometry axis. That means that the interferometer arms do enclose a spatial area during the interferometer. A small Sagnac phase enters, but it is common to the entire sample and only potentially changes how we tune f_m to set the bias phase of the interferometer. It does not affect the measurement.

Hyperpolarizability

The hyperpolarizability vanishes at tune out, at least for a three-level system[14]. On the other hand, our wavelength scan is not symmetric about tune out and the hyperpolarizability shift is nonlinear. That leads to the possibility that the hyperpolarizability shifts the points more strongly on one side of the scan, systematically shifting the zero crossing of the fit.

Fig. 2.13 presents an approximation of the hyperpolarizability we expect in our system. We accounted for the Clebsch-Gordan coefficients for our state and polarization by summing the squared Clebsch-Gordan coefficients across allowed transitions on each line, neglecting differences in detuning from the small excited-state hyperfine splittings. The squared coefficients sum to 1/3 for both the D_1 line and the D_2 line, so we suppressed each squared dipole matrix element in that calculation by 1/3. That reduces the polarizability by a factor of 3 and reduces the hyperpolarizability by a factor of 9, compared to the result for the full transition dipole matrix element.

Our measurement technique is sensitive to gradients in the hyperpolarizability. The peak shift for our maximum detuning is $\sim$20 Hz at the center of the beam. For a 10-μm arm separation on a 150-μm beam, the interferometer would sample a maximum 2-Hz difference in the hyperpolarizability shift at $w_z/\sqrt{8}$ where the slope of the hyperpolarizability is highest on the I^2 profile.

$$20\ \text{Hz}\Big((\exp(-2((0.15/\sqrt{8}+0.01)\ \text{mm})^2/(0.15\ \text{mm})^2))^2 - (\exp(-2(0.15/\sqrt{8}\ \text{mm})^2/(0.15\ \text{mm})^2))^2\Big) \sim 2\ \text{Hz}. \quad (5.29)$$

[14] While the atomic system has many more than three levels, the transitions outside the three-level system are so far off-resonance that they modify this result only negligibly.

The interferometer would accrue 0.001 radians of phase over the 100-μs Stark-shifting pulse.

Now we consider how large of a systematic shift that produces. The prediction for the polarizability in Fig. 2.13 suggests a ∼100-kHz polarizability shift. The 10-μm arm separation samples a 10-kHz difference on the intensity profile, accruing $\sim 2\pi$ radian of phase over the 100-μs pulse.[15] These phase shifts are estimated near our maximal detuning from tune out, around 400 MHz away. The largest shift the hyperpolarizability could introduce would be

$$\frac{400\ \text{MHz}}{2\pi\ \text{rad}}(0.001\ \text{rad}) \sim 0.06\ \text{MHz}. \tag{5.30}$$

While this is in the regime of shifts we consider, the real shift will only be much smaller than this for multiple reasons. First, the hyperpolarizability only affects points far away from tune out. It would introduce a curvature to the fits and a contribution to a cubic term in the fit. We fit the signal amplitudes with both cubic (Fig. 5.22) and linear (Fig. 5.21) functions and showed that the cubic term was not important. Second, thermal dephasing affects the smaller length scales of the hyperpolarizability's I^2 profile more strongly than that of the Stark shift. The 2 Hz we calculate above is for an atom at rest at the most sensitive position. The Stark shifts predicted are highly optimistic and the experimentally relevant phase shifts are much smaller.

5.7 The result

Tab. 5.2 collects the significant systematic effects, uncertainties, and the fit result.

5.7.1 Comparison to theory

The measurement result is most interesting contextualized by contemporary atomic theory. Reference [12] calculates lithium's dipole matrix elements for the purpose of finding tune-out and magic wavelengths. It uses a fine-structure basis to calculate tune out for $|2S_{1/2}\rangle$. Hyperfine effects are important to our spin-polarized measurement for tune out of $|2S_{1/2}, F = 2, m_F = 0\rangle$, so we must perform our own calculation using the transition dipole matrix elements the theorists calculated[16] using experimental transition energies.

$$d_{D1} = 3.3169(6)\ \text{a.u.} = 2.8122(5) \times 10^{-29}\ \text{C} \cdot \text{m} \tag{5.31}$$

$$d_{D2} = 4.6909(8)\ \text{a.u.} = 3.9771(7) \times 10^{-29}\ \text{C} \cdot \text{m}. \tag{5.32}$$

[15] We report elsewhere that the maximum phase shift we observe is more like $\pi/10$ radians. That is something of an estimate, averaged over the signal across the thermally-dephased signal. Here, we are considering the absolute maximum phase shift any single atom could accrue and comparing that condition for both for the polarizability and the hyperpolarizability.

[16] Here we remain vigilant and notice that the dipole matrix elements contain a factor of $\sqrt{2J_l + 1}$. These matrix elements are not in disagreement with the values reported in Tab. 2.2, they just use an inconveniently different convention.

Effect	Correction	1-σ uncertainty
Doppler shift along Stark beam axis (5.6.2)	+1.58	0.06
Broadband laser emission (5.6.5)	−0.09	0.1
Complementary $F = 1$ interferometer (5.3.4, 5.6.4)	−0.01	0.04
Interference from $m_F = \pm 1$ interferometer (5.6.4)		0.09
Zeeman shift to measured f_0 (5.6.2)	+0.09	0.02
Statistical uncertainty in measured f_0		0.05
Polarization impurity (5.6.3)		0.3
Total	+1.59	0.34
One-dimensional fit (5.6.1)	3327.95	1.40
Final result	3329.54	1.44

Table 5.2: Tune-out measurement systematics. Systematic effects in measuring ^{7}Li's tune out for $|2S_{1/2}, F = 2, m_F = 0\rangle$ with $\sigma^{\pm}$ ($\hat{x}$) polarization. Parentheses after each effect refer to the germane section. The detuning references the $|2S_{1/2}, F = 2\rangle \rightarrow |2P_{1/2}, F' = 2\rangle$ transition. All frequencies are given in MHz divided by 2π.

The conversion factor between atomic units and SI is ($1 = 8.47836 \times 10^{-30}$ C·m/a.u.).

To compare our measurement to theory, we use these theoretical matrix elements to calculate where the AC Stark shift or the polarizability vanish. There is no need to consider the gradiometer configuration of our interferometer because the gradient vanishes if the total shift vanishes. One may either build a calculator to find the zero crossing either by using Eq. (2.137) and Clebsch-Gordan coefficients or by using a cascade of Eqs. (2.139), (2.140), (2.141), (2.142), and (2.143). Each should specify to a particular hyperfine Zeeman sublevel and light polarization. The two approaches should produce identical results, up to differences due to the RWA that have no import here. Validating these calculators' predictions against the Rb measurement in [28] and [29] (using Rb's parameters for dipole matrix elements and transition energies) helped assuage our trepidations about us experimentalists performing calculations.

Higher $n > 2$

There are some important differences between our calculator and the full theory. First, we do not consider transitions to principle quantum number higher than $n = 2$. We consider only the $|2S_{1/2}\rangle \rightarrow |2P_{1/2}\rangle$ and $|2S_{1/2}\rangle \rightarrow |2P_{3/2}\rangle$ transitions. We did modify the calculator to account for the $n = 3$ transitions with[17]

$$d_{2S1/2\rightarrow 3P1/2} = 0.183(3) \text{ a.u.} \tag{5.33}$$

$$d_{2S1/2\rightarrow 3P3/2} = 0.259(4) \text{ a.u..} \tag{5.34}$$

[17] Again, these values have the factor of $\sqrt{J_l + 1}$ built into them.

and experimental transition energies from the NIST database [120], but the inclusion had no effect near our level of precision. This is likely due to the minuscule detunings of tune out to the D-lines relative to all other transitions in lithium. We can amplify the effect by a factor of 100 by multiplying the dipole matrix elements by a factor of 10 (also multiplying the corresponding linewidths by 10 if they are defined separately), which produces a shift of 20 kHz, so we estimate the effect of the $n = 3$ levels to produce a shift at the 0.2-kHz level. As in Rb [29], the nearest n level dominates the polarizability contributed from higher n. Since even $n = 3$ produces no observable shift, we do not consider higher n.

Core polarizability

Second, we do not account for the polarizability of the core electrons. Transitions out of the core are higher in energy than any frequency that addresses the valence electron. The red 671-nm light we use to measure tune out appears as essentially DC to the core and we may approximate the core polarizability with the static core polarizability. Ionizing lithium exposes the core, so the core polarizability of Li is approximately equal to the static polarizability of Li^+ [16]:

$$\alpha_c = 0.1883(20) \text{ a.u.} \tag{5.35}$$

We account for this by simply adding this static core polarizability to the total polarizability in our calculator. It does not shift the zero crossing near our level of precision. We can estimate the effect by multiplying this factor by 100 to observe a 10-kHz shift. That implies that the core polarizability shifts tune-out at the 0.1-kHz level. There also exist core-valence interactions that we do not consider. They appear at a level in Rb a factor of 10 smaller than even the higher n contributions.

Zeeman shifts

Including Zeeman shifts merely changes the transition energies and detuning factors in the polarizability calculation [28]. Because we use a light polarization that is an equal combination of σ^+ and σ^- polarizations, Zeeman shifts to transitions are equal and opposite for the two components, so their effects roughly cancel. Furthermore, we use a relatively small bias field in our experiment produces only $\sim$ 1-MHz transition energy shifts. Increasing the field strength by a factor of 10 in the calculations produces a shift near 10 kHz, so we expect this effect to enter at the 1-kHz level.

Multipole transitions

The atomic theory we use does not account for transitions beyond the dipole transitions of the electric dipole approximation. Atoms do couple to higher-multipole components of the electric field, which can drive quadrupole, octupole, etc. transitions. Those transitions follow different selection rules. For example, quadrupole transitions do not couple the S states to higher S or P states. The $3D$ states are detuned far enough from the Stark laser

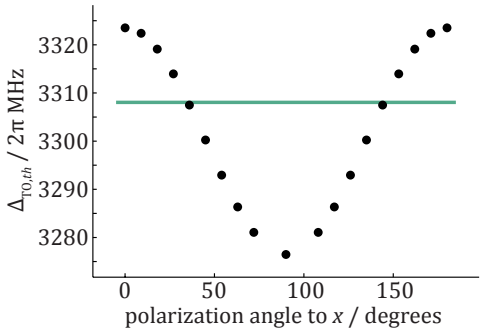

Figure 5.30: Variation of tune out prediction with polarization angle. The green line shows the prediction for scalar tune out.

frequency not to worry us. Multipolar effects on the polarizability and hyperpolarizability are discussed in Refs. [109, 110, 105].

Predictions

With the theoretical matrix elements above and experimental transition energies [115], we predict that $|2S_{1/2}, F = 2, m_F = 0\rangle$ tunes out with $\sigma^{\pm}$-polarized light at

$$\Delta_{\mathrm{TO}\pm,th} = 2\pi \times 3323.52(1.3)\ \text{MHz}. \tag{5.36}$$

For π-polarized light,

$$\Delta_{\mathrm{TO}\pi,th} = 2\pi \times 3276.47(1.3)\ \text{MHz}. \tag{5.37}$$

The $F = 1$ state tunes out for $\sigma^{\pm}$-polarized light at

$$\Delta_{\mathrm{TO}\pm,th,F=1} = 2\pi \times 4130.08(1.3)\ \text{MHz}, \tag{5.38}$$

806.56 MHz above where $F = 2$ tunes out. Note that the difference is not exactly equal to the ground-state hyperfine splitting.

5.7.2 Tensor tension and scalar agreement

Our tensor-shifted tune-out measurement at 3329.5(1.4) is in 3-σ tension with the theory prediction 3323.5(1.3). Furthermore, we observe a 2-σ tension in the magnitude of variation in tune out between the tensor-shifted tune outs of $\sigma^{\pm}$ and π polarizations; we measure a variation of 56.9(4.7) MHz compared to theory's 47.1(1.3) MHz prediction.

The variation of tune out with polarization for the $m_F = 0$ state arises solely from the tensor polarizability. We calculate tune out for several linear polarizations at an angle to the x axis. Fig. 5.30 shows the results. The variation follows a $(3/4)\cos^2(\theta) - (1/2)$ dependence (see Eq. (4) of Ref. [29]). It is not symmetric about the value where the scalar polarizability alone crosses through zero, $\alpha^s(\Delta^s_{\mathrm{TO}}) = 0$.

$$\Delta^s_{\mathrm{TO},th} = 2\pi \times 3308.05\ \text{MHz}. \tag{5.39}$$

The tensor-shifted tune out for $\sigma^{\pm}$-polarized light is 1/3 of the full tensor variation above the scalar tune out.

We can combine our measurement of the tensor-shifted tune out of $|2S_{1/2}, F = 2, m_F = 0\rangle$ for σ^{π}-polarized light with our measurement of the variation of tune out with polarization to

$$\Delta^{s}_{\mathrm{TO}} = 2\pi \times (3329.5(1.4) - 56.9(4.7)/3)\ \mathrm{MHz} = 2\pi \times 3310.5(4.9)\ \mathrm{MHz}, \tag{5.40}$$

which agrees with theory. Inputting our measured value of the tensor shift produces better agreement than if we were to use the theoretically-calculated value.

Speculation

Our measurement of the tensor-shifted tune out and the full magnitude of the tensor shift both disagree with theory, but our measured value of scalar tune out agrees with theory. This suggests that the disagreement may be due to a polarization-related effect, either in the theory or in the experiment.

We offer one possibility for a polarization-related effect we did not account for. We measure the variation of tune out with polarization by tuning the angle of the polarization with respect to the x axis (Fig. 5.24). The polarization of the ASE or any power-spectral anomalies also vary in those measurements. If there were a feature in the Stark laser's PSD close to one of the resonances that we were unable to identify, its polarization would have varied in that scan. The Clebsch-Gordan coefficients that describe that such a feature's coupling to the resonances have a strong polarization dependence, some completely vanish at certain polarizations and not at others. Thus, there could be a spectral feature near resonance with a strong polarization dependence that introduces an undetected systematic into our 56.9(4.7)-MHz measurement of the full tensor variation. Such a feature would also have introduced a Stark shift contribution that systematically shifts our precision measurement tune out for $\sigma^{\pm}$ light. We have no reason to suspect that the Stark ECDL emits such a spectral feature, but dutifully report this as a possible source of undetected error.

Chapter 6

Prospecting

6.1 A polarizing future

6.1.1 Measuring hyperpolarizability

One of lithium's advantages in measuring the tune-out wavelength is the small $2P$ fine-structure splitting that produces a highly-sloped polarizability near tune out. That large slope allows for proportionally increased precision in measuring tune out. The hyperpolarizability must also be relatively highly-sloped near tune out due to the fine-structure splitting, permitting a tantalizing opportunity to measure it.

Hyperpolarizability produces energy shifts proportional to the square of light intensity. This has become important physics with the advent of optical lattice clocks [168], in which experimenters extend the interrogation time of an atomic clock by trapping atoms with long-lived excited states in an optical lattice. These versatile experiments can turn an eye toward an impressive array of important physics, from many-body physics to searching for dark matter candidates through time-variation of fundamental constants.

Ordinary lattice light would systematically perturb the precious clock transition, so scientists choose a magic wavelength for the trap. The two clock states have equal polarizability at a magic wavelength, so the transition should be unperturbed. It is unlikely, however, that the two states have equal hyperpolarizability at the magic wavelength, producing a shift to the transition that depends on the intensity of the trapping light. Hyperpolarization in lattice clocks can introduce a systematic shift to the clock transition, as well as broadening due to fluctuations in intensity or due to the varying intensity with the trap topography. The broadening in particular may become a leading uncertainty for these experiments.

Lattice clock experiments have investigated the effects of hyperpolarizability before [104, 105, 106, 103] and it remains an active field of inquiry [108, 107, 145]. Theorists have also attended to these shifts, but disagreements between theory and experiment remain [110, 109]. Precision measurements of hyperpolarizability in lithium could be indispensable in remedying the disagreement between theory and experiment.

Measuring the hyperpolarizability in our experiment is challenging. At tune out, its

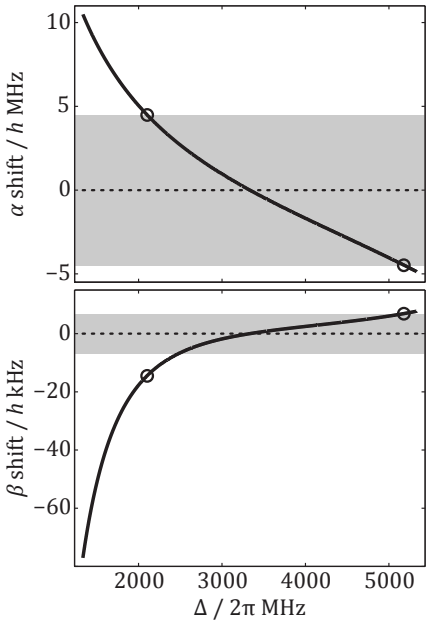

Figure 6.1: Dual-wavelength hyperpolarizability scheme. A light field with equal power at two wavelengths (black circles) samples equal and opposite polarizabilities and the total polarizability shift cancels (gray box). The hyperpolarizability shift does not fully cancel.

effect vanishes. Away from tune out, its shift sits atop a large background signal from the polarizability. The lattice clock community tends to scan the intensity of the trap light and look for and a variation in the clock frequency that is quadratic in the intensity. Here, one could consider measuring tune out at several values of intensity and looking for a quadratic variation in the measurement sensitivity, or the slope through tune out. This strategy is possible, but unlikely to be particularly sensitive because the hyperpolarizability is so small near tune out. It would be better to tune the laser further away from tune out where the hyperpolarizability is larger. Of course, the polarizability is also larger, so a scheme that rids the signal of the effects of polarizability is preferable.

Here we offer a scheme to cancel the polarizability's effect and leave only the effect of the hyperpolarizability. Consider a light field with equal power at two different wavelengths, wavelengths chosen such that the polarizability is equal and opposite for each of them. The wavelengths are not precisely symmetric about tune out because the polarizability varies nonlinearly and asymmetrically away from tune out. We send this light field at the atoms in the same manner we have done with our phase-patterned tune-out measurement. Because the two wavelengths contribute equal and opposite polarizabilities and the powers are matched, there is no total polarizability shift. The more dramatic nonlinearity for the hyperpolarizability, however, means that the effect of the hyperpolarizability does not fully cancel. A signal proportional to the difference between the two wavelengths' hyperpolarizability survives. It is not ideal that hyperpolarizability's effect largely cancels, but it is likely

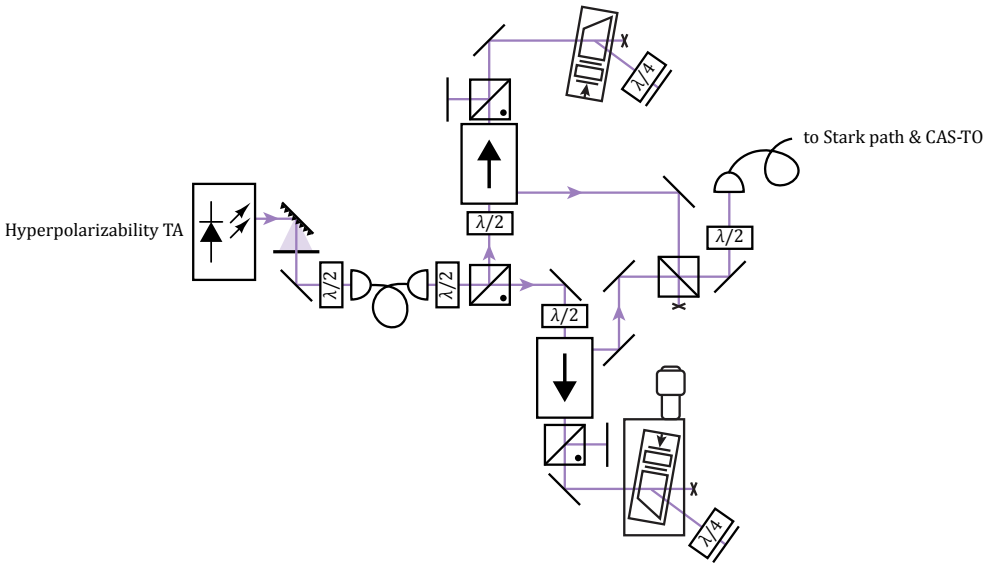

Figure 6.2: Dual-wavelength hyperpolarizability optics setup. Two quadruply-passed AOMs generate two wavelengths of light whose polarizability cancels, but whose hyperpolarizability does not.

worth cancelling the large background from the polarizability.

Fig. 6.1 shows the energy shifts in a three-level model from polarizability and hyperpolarizability at each wavelength in this scheme. We have retained the beam parameters for this plot, but have increased the power by a factor of 10. Increasing the power by a factor of 10 amplifies the polarizability shift by a factor of 10 and amplifies the hyperpolarizability shift by a factor of 100. One might accomplish this with an optical setup similar to Fig. 6.2. The Stark ECDL would seed a standard 500-mW, 671-nm TA. The output of the TA should be spectrally filtered with a grating and pinhole because the ASE from a TA will be much stronger relative to the carrier compared to an ECDL's direct output. An optical fiber may spatially filter the mode before the beam divides into two and double-passes through two AOMs in opposite directions. Two quadruply-passed 400-MHz AOMs would generate light with ∼3 GHz splitting. A 50/50 beam splitter would recombine the beams at identical polarization and send them along the tune-out measurement path. This should deliver ∼10 times our current ∼ 3-mW power in each wavelength. Another route to well-matched powers in each wavelength may be to pass the beam through an EOM and drive sidebands that serve as the two wavelengths. There are several disadvantages like the carrier not being precisely at tune out and higher-order sidebands sitting near the atomic resonances, but it may be worth further consideration.

Assuming the tuning perfectly cancels the polarizability, the phase shift is proportional to the difference in the hyperpolarizability between the two wavelengths. We choose detunings from the modeled D_1 line near 2125 MHz and 5130 MHz. The difference in the points' hyperpolarizability gives a differential remnant difference in hyperpolarizabilities of $\sim 3.5 \times$

10^{20} a.u. and a remnant peak shift of $\sim 2\pi \times 7$ kHz. The interferometer with will sample the gradient in the squared intensity profile, yielding a maximal difference of $\sim 2\pi \times 1$ kHz. That gives a substantial peak phase difference near 2π. This peak phase difference is for an atom at rest at the most sensitive position. While the observable phase shifts will be smaller due to thermal dephasing, this is similar to the phase shifts we measured for tune out and should be easily accessible with similar averaging. There is a difference between the phase pattern in our tune out measurement and the phase pattern this would imprint; the hyperpolarizability shift follows the squared intensity profile, so the pattern will be $\sqrt{2}$ smaller in size. The size of the pattern in our tune-out measurement was manageable enough, so we do not expect the imaging or thermal dephasing would pose unique challenges to the slightly smaller feature at our current beam size.

The approach here faces multiple obstacles. First, scattering will be an even larger issue in this scheme because the detunings we suggest more closely approach the D_1 resonance. One could take the same modulated approach as our tune-out measurement, taking the difference between pulsed and unpulsed images for two opposite sensitivities, and subtracting the two residual images. It is important to recognize that scattering remained an issue for us regardless of our attempts to cancel it (and for unknown reasons), so it could present a larger hurdle here. Second, it is not obvious how to take the signal we propose here and turn it into an absolute measurement of a nonzero hyperpolarizability. Obtaining the signal in the first place would likely motivate folks to solve this problem.

6.1.2 Ultraviolet tune out

The next tune-out wavelength in ^{7}Li sits between the $|2S_{1/2}\rangle \rightarrow |3P_{1/2,3/2}\rangle$ ultraviolet transitions near 323 nm. That tune out is arguably far more interesting than the 671-nm tune-out wavelength. First, relativistic effects begin to come into play, as discussed in Ref. [114]. Second, the hyperpolarizability becomes more interesting.

Recall that hyperpolarizability is the result of four-photon processes. The perturbation may ride two photons upward and two photons back downward to the perturbed state. For the red tune out, the two-photon transitions upward are still quite far from resonance with the $|3S\rangle$ and $|3D\rangle$ states, so the hyperpolarizability contains huge (cancelling) contributions from the up-down-up-down processes via the $|2P\rangle$ states and almost no contribution from any up-up-down-down process.

The story is radically different for the ultraviolet tune out. Two photons at 323 nm excite the valence electron in ^{7}Li beyond ionization. That means the up-up-down-down processes couple resonantly into a continuum of unbound, free-electron states. That is a far more exciting problem for many theorists than precise computations of features on the D lines.[1] There is considerable disagreement in the community about how to treat this and theorists are still working to develop methods that properly account for this kind of behavior [95]. A

[1] D stands for Dull, amirite?

direct measurement of hyperpolarizability effects around the $|2S\rangle \rightarrow |3P\rangle$ transitions would provide tremendous insights that theorists would undoubtedly find valuable.

Entertaining the ultraviolet tune out requires considering optics that properly transport the ultraviolet light. Generating the light and working with it also opens the door to cooling lithium on the $|2S\rangle \rightarrow |3P\rangle$ line, which is much narrower and offers temperatures approaching 50 μK [113]. Parallelizing efforts for deeper cooling, measuring tune out, and measuring hyperpolarizability in the ultraviolet should make this an attractive direction.

6.1.3 Tuning out ^{6}Li

Theorists have worked to account for isotopic differences between ^{6}Li and ^{7}Li and have expressed a keen interest in investigating the shift between their tune outs [12] and hyperpolarizability [18, 169].

Many of our ^{7}Li techniques would carry over to ^{6}Li. Adding the capability to work with it is a straightforward, albeit time-consuming, endeavor. The cooling and trapping light for ^{6}Li is near the D_1 line of ^{7}Li. Most of the lasers we use for ^{7}Li can therefore be used for addressing either isotope. The master laser spectroscopy would first need to modified to enable switching to locking at a ^{6}Li reference instead of only the ^{7}Li resonance it currently supports. That requires including an isotopically-enriched sample with a substantial fraction of ^{6}Li in both the spectroscopy cell and the main chamber. The ground-state hyperfine difference in ^{6}Li is only $\sim$230 MHz, nearly 4 times smaller than that of ^{7}Li. The same AOMs we use to generate the cooling and trapping light for ^{7}Li could not be repurposed for ^{6}Li. Instead, a cascaded AOM scheme with 80-MHz double-passed AOMs after the 200-MHz AOMS we currently use for ^{7}Li could switch to cooling and trapping ^{6}Li by simply extinguishing the ^{7}Li AOMs and turning on those for ^{6}Li. The beam paths would otherwise be identical. We have observed the TAs to be rather particular about their tuning, so it may be necessary to retune them (and potentially the slave lasers) upon switching between isotopes.

Perhaps the largest challenge to working with ^{6}Li is its hyperfine structure. ^{7}Li volunteers a magnetically-insensitive $m_F = 0$ state. ^{6}Li does not, with $F = 1/2, 3/2$ in the ground state. One might consider optically pumping to each of the $|2S_{1/2}, F = 3/2, m_F = \pm 3/2\rangle$ with $\sigma^{\pm}$-polarized light on ^{6}Li's D_2 line, but the pumping would be inefficient. Measuring tune out for each of the states could cancel linear Zeeman effects, but it might require controlling the magnetic gradients better than was required in our $m_F = 0$ work.

6.1.4 An independent tune-out wavelength measurement

Our measurement registers a tension with theory. While our measurement is the first of a tune-out wavelength in lithium, other apparatuses routinely produce ultracold samples of ^{7}Li [170, 171, 172, 173, 174, 175, 176] and ^{6}Li [177, 178, 179, 180, 181, 182] and any one of them may be positioned well to precisely measure of the lithium tune-out wavelength. We extend a warm invitation to these ultracold experiments to perform an independent measurement that would provide a check on both our methods and theory.

6.1.5 Polarizability reference species

Lithium's relatively simple electronic structure imbues calculations of its polarizability with more precision than other species. An experiment in Ref. [164] used K as a reference species to determine the polarizability of Dy, a more exotic species. They simultaneously trap both species in an optical dipole trap; suddenly displacing the trap center excites mechanical oscillations at a frequency proportional to the square root of the polarizability. Using the well-known polarizability of the reference species and its measured oscillation frequency allows a measurement of the exotic species' polarizability through its oscillation frequency. Such a procedure might be adapted instead for Li, whose polarizability is the most precisely calculable of the alkalis. One could imagine a cottage industry of precisely measuring species' polarizabilities against Li.

6.2 Extensions and applications of phase patterning

We developed phase patterning out of necessity to measure ^{7}Li's tune-out wavelength with a thermal sample. In doing so, we stumbled on a much more broadly applicable technique. Phase patterning enables control or sensing of spatially-varying interferometer phases. While we leveraged it for a sample with thermal speeds much higher than the recoil speed, it is generally applicable to any experiment where the arm separation is smaller than the size of the sample along a particular axis, which could be a necessity or a design choice. In our tune-out measurement, the interferometer sampled an intensity gradient to generate a phase; away from tune out, there was a spatially-labeled AC Stark shift and phase difference. We also imagine similar applications where the intensity itself directly patterns phase profiles using the differential polarizability of superposed states. We now dream of a few options for how else phase patterning might be useful.

6.2.1 Correcting systematic phase gradients

Our recoil measurement was frustrated by a phase gradient imprinted on the interferometer by the magnetic field gradient. Atoms at one end of the sample accrued more $2\delta T$ phase than atoms at the other end of the sample. The signals dephased and decohered when summing the interferometer output signal over the sample, as is most convenient and sensitive. We could have corrected the component of the phase gradient along the interferometer axis by applying an intensity gradient across the sample during T'. To compensate for the phase gradient, the light could be tuned to a wavelength with a high polarizability where modest light intensity produces substantial gradients.

Experiments that produce large spacetime separations may sample regions of the vacuum chamber distinct in their gravitational [183], magnetic [184], or thermal environments [6, 4, 5]. Gradients in these fields may imprint a spatially-varying phase shift on the interferometer that spatially dephases the interferometer singal. Phase patterning can compensate for these systematic dephasing mechanisms. For example, consider a four-pulse Mach-Zehnder

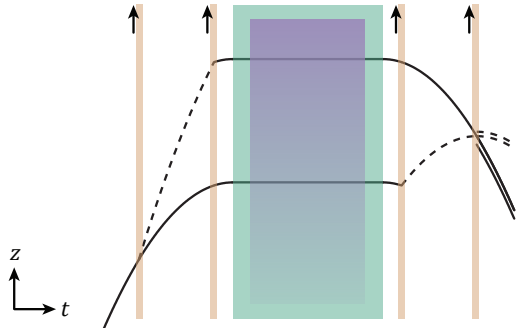

Figure 6.3: Phase patterning during a lattice hold. The green central pulse represents a lattice that drives Bloch oscillations to hold an atom against gravity. The purple pulse therein represents a phase patterning pulse that compensates for systematic gradients.

interferometer that allows the interferometer to accrue phase in place during T' by holding them in a lattice as in Ref. [185, 186]. Any curvature in the blackbody power spectral density across the matter-wave separation imprints a phase that depends on the height of an atom within the sample.[2] Such a phase gradient could be compensated by applying a phase patterning pulse during the lattice hold as Fig. 6.3 shows. One would choose a laser wavelength with nonzero polarizability and design the intensity profile to imprint a height-dependent phase difference.

Phase patterning does not require the arms of an interferometer to sample an intensity gradient. A phase-patterning pulse may alternatively address state-labeled trajectories with a differential polarizability. The local intensity, rather than the local intensity gradient, would imprint a phase as the two Stark-shifted, superposed states accrue phase at different rates during the pulse. Consider, for example, an optical lattice clock whose phase depends on spatially-varying systematic effects as in Ref. [145]. One could measure the systematic phase as a function of position and pattern an intensity profile to pulse during the measurement time. A differential polarizability between the clock states at the pulse wavelength would add a phase in proportion to the local intensity of the pulse. Nontrivial phase profiles may be imprinted by patterning the intensity profile with a spatial light modulator (SLM).

6.2.2 Sensing spatially-varying fields

Cold atoms are exquisite sensors. In many applications like sensing current loops from the transition into a high-temperature superconducting state, accessing the relevant physics requires sensing spatial variations in fields of interest [187]. Some applications might aim to sense small deviations from a default background pattern. Our tune-out measurement benefitted from biasing the interferometer phase to points of maximal phase sensitivity. For

[2] A simple gradient imprints a phase common to the entire sample. A curvature in the field produces a gradient that depends on the height in the sample. A curvature in the intensity profile of the phase patterning pulse is also required for the same reason.

a pre-determined default pattern, one could use phase patterning to imprint a spatially-varying bias phase such that the interferometer is maximally sensitive to deviations from the default pattern at every position in space. Certain experiments may even provide the opportunity to switch the signal of interest on and off as we do in our measurement. Even when they do not, one might achieve the same result by flipping the spatially-tuned bias phase between positive and negative phase sensitivity and subtracting the results.

6.2.3 Patterning density profiles

Creating designer atomic density profiles, a strength of phase patterning, is important in multiple arenas like quantum gas microscopes [179, 180, 188, 189, 190, 191] and atom lithography [192, 193, 194]. Multiple geometries may be useful for fashioning these density distributions. Assembling non-trivial profiles will likely require a SLM. Our tune-out interferometer generated a spatial separation that sampled an intensity gradient along the interferometer axis to pattern a density distribution. There, the phase patterning pulse must propagate perpendicular to the interferometer axis. A phase patterning pulse may propagate parallel to the interferometry axis if the wave packets are in differentially-polarizable states during the application of the pulse (as in Fig. 5.1). Some experiments may not offer differentially polarizable states, like interferometers operating on Bragg transitions [72, 124]. In those cases, one could consider spatially modulating the phase on the interferometry beam itself. An atomic fountain, for example, might install a deformable mirror as its retroreflection mirror. Deforming the mirror only for the final recombination pulse would imprint that spatially-varying phase onto the atomic sample. One might purge the opposite interferometer output with a blow-away pulse to leave only the density-patterned result for the next stage of the experiment. The final atomic densities could be lensed [195, 196, 194] to increase feature sizes or reduce them below the diffraction limit of the phase-patterning light. Multi-dimensional patterning may also be of interest [197].

6.3 Extending interrogation time

Atom interferometry with lithium has been very challenging for several reasons, the most daunting being those related to the large distribution of thermal speeds. It still may be useful to improve on the methods presented in this dissertation. We first suggest a couple modest improvements to the existing apparatus before dreaming a little more loftily.

Interrogation times are ultimately limited by atoms thermally expanding out of the beam that drives the interferometry pulses. Most sequences release atoms from any trapping potential for interferometry. Entering at velocity v, the atom travels a distance $x = v\Upsilon$, where Υ is the total time between the first and last pulse of an interferometer sequence. If am atom transits a distance comparable to the beam waist of the interferometry beam $x \sim w$, the pulses can no longer manipulate and interfere the atom and the atom is lost to the dark abyss. Since thermal speeds $\sim \sqrt{k_B \mathcal{T}/m}$ scale with the square root of the temperature,

reducing the temperature by some factor only increases the maximum interrogation time by the square root of that factor. Widening the interferometry beam by some factor increases the maximum interrogation time with the same factor, at the expense of the pulses' Rabi frequency and bandwidth. In this section, we will discuss several approaches that would extend our interrogation times.

6.3.1 Improving our apparatus

The persistent magnetic field gradient set the strictest coherence limit on our recoil-sensitive interferometer. Spatially-varying quadratic Zeeman shifts dephased atoms across the sample through the $2\delta T$ phase. Lower gradients would allow our current apparatus to improve the interrogation time and recoil sensitivity by a factor of ~ 10, but eddy currents in the steel vacuum chamber sustain the gradient for times long compared to the thermal expansion rate. Installing an H bridge is one option for mitigating the gradient on accessible timescales. It would permit switching the polarity of the voltage on the MOT's anti-Helmholtz coils to generate a negative gradient that would counteract the slowly-decaying gradient from the chamber. Lowering the gradient to ~ 0.02 G/cm would saturate the available interferometry time allowed by our current 3.6-mm Raman beams.

Increasing the available power for driving Raman transitions would grant longer interferometry times. A simple way to do this at limited cost would be to install a second Raman TA, so that each of two Raman TAs would be dedicated to one of the Raman frequencies. To preserve the Rabi frequency and bandwidth, the peak intensity should be kept constant. Since the intensity scales inversely with the area of the beam, doubling the Raman power only enables an increase of the beam size and interrogation time by $\sqrt{2}$.

Replacing or repairing our camera could be an important upgrade for future work on our apparatus. We did not explicitly quantify the level of imaging noise from the defects in Fig. 3.18, but it quite probably introduced a leading source of uncertainty in the fit. While it is not directly in the interest of extending interrogation time, it could increase the sensitivity and reduce the integration time of phase-patterned data.

6.3.2 Advanced cooling

While the D_2 line's poor resolution makes sub-Doppler cooling less effective than other species, advanced laser-cooling techniques can reduce the temperature by a factor of 2 or 3 [136, 198, 113]. The thermal speeds reduce by only the square root of that factor, so one more advanced cooling stage would not increase the interrogation time significantly. Furthermore, techniques like gray molasses [198] preserve phase-space density, so it would deliver a lower temperature at the expense of a larger sample requiring a larger interferometry beam. Evaporation can further cool below the recoil limit, but that requires thermalization through collisions between evaporative purges. Lithium has an unfavorable s-wave scattering length for thermalizing, one of the reasons ^{7}Li lost the race to Bose-Einstein condensation in the early 1990s [199].

Lithium does have a broad Feshbach resonance [200, 201] that permits tuning the interactions. A few teams have begun to use the Feshbach resonance $\gtrsim$700 G to produce BECs of ^{7}Li at Rice [174], MIT [172, 181], UCSB [170, 202], CNRS [173], in Tokyo [203], and in Korea [175].[3] The atom numbers routinely exceed 10^6, competitive with the atom numbers used in this dissertation, albeit at generally lower experimental repetition rates. Interferometers with BECs must consider a systematic phase shift from mean-field atom-atom interactions [204], but manipulating lithium's scattering length further opens the door to squelching it altogether during interferometry [205] at ∼544 G [200]. Exploiting the features of this magnetic Feshbach resonance require unfortunately large magnetic fields. Much smaller magnetic fields have already limited the interferometer coherence in this dissertation, so introducing a larger field could introduce more problems. The Feshbach resonance operates on the magnetically-sensitive $|2S_{1/2}, F = 1, m_F = 1\rangle$. One could form the BEC in that state and transfer to the magnetically-insensitive $|2S_{1/2}, F = 2, m_F = 0\rangle$ with a single microwave pulse to avoid the heating our optical pumping strategy would generate. Alternatively, there are two narrow Feshbach resonances near ∼850 G for $|2S_{1/2}, F = 1, m_F = 0\rangle$ [206] that might support evaporation and suppressing interactions.

Non-uniform quadratic Zeeman shifts from the persistent magnetic gradient limited the coherence in our recoil-sensitive interferometer, but a colder sample trapped in an optical dipole trap would allow for a more patient delay between shutting off the MOT magnetic field and performing interferometry. A uniform field, even if nonzero, would no longer provoke decoherence from the quadratic Zeeman shift. Magnetic gradients can even be compensated in two dimensions if need be.[4] Readers concerned about other aspects of the magnetic fields might consider controlling the Feshbach resonance optically [207].

It is likely that anyone pursuing or maintaining a BEC of lithium would have a harmonic optical dipole trap. That opens a very interesting sphere of possibilities.

6.4 Free-oscillation interferometers

An alternative strategy to increase interrogation times is to trap the atoms so they stay within the interferometry beam. After all, even tossing atoms upwards in an atomic fountain [124, 72] with length L only improves the free fall time $\propto \sqrt{L}$. A trapped interferometer can be made in a compact apparatus. Several groups have explored atom interferometry with harmonically-confined samples. Some have investigated Michelson interferometers with weak confinement [208] or strong confinement [209, 210] that may be used for Sagnac interferometry to sense rotations with atoms [211] or ions [53]. Some have run Ramsey-type clocks on a microwave transition [212, 213, 214] or on a nearly-co-propagating Raman transition with a tunable momentum kick [215].

[3] Related efforts produce Fermi-degenerate gases of ^{6}Li [171, 182].

[4] Maxwell's equations prohibit compensating generic gradients in all three dimensions.

6.4.1 Free-oscillation recoil interferometer

No group has performed recoil-sensitive interferometry in a harmonic trap. There is a unique challenge to constructing such an interferometer. Recall that the recoil energy emerges in the Ramsey-Bordé interferometer through the classical action; however, the classical action vanishes for any integer of half-periods of harmonic oscillation. In order to generate a nonzero recoil phase, we can engineer an interferometer that operates on quarter-periods of the oscillation. Such a scheme was proposed for Bragg-diffracting electrons in a Penning trap [216], but there are important differences between that geometry and the case for neutral atoms subject to counter-propagating Raman transitions.

Consider an atom in a one-dimensional harmonic potential with axial trap frequency ω_z and period

$$\tilde{T} = 2\pi/\omega_z. \tag{6.1}$$

The potential could be created by an optical dipole trap, for example. The equation of motion $\ddot{z} + \omega_z^2 z = 0$ is solved by $z(t) = A\cos(\omega_z t) + B\sin(\omega_z t)$. For an arbitrary initial position z_i and velocity v_i, the trajectories and velocities follow

$$z = z_i \cos(\omega_z t) + \frac{v_i}{\omega_z}\sin(\omega_z t), \tag{6.2}$$

$$\dot{z} = -\omega_z z_i \sin(\omega_z t) + v_i \cos(\omega_z t). \tag{6.3}$$

It will be useful to recognize the positions and velocities after quarter- and half-period evolutions: $z(\tilde{T}/4) = v_i/\omega_z$, $\dot{z}(\tilde{T}/4) = -\omega_z z_i$, $z(\tilde{T}/2) = -z_i$, and $\dot{z}(\tilde{T}/2) = -v_i$.

The matter-wave accrues phase during free evolution according to the action along the classically-expected trajectory, which no longer depends only on the endpoints as it did in a linear potential.[5]

$$S_{cl} = \frac{m}{2}\int_0^t (\dot{z}(t')^2 - \omega_z^2 z(t')^2)dt'. \tag{6.4}$$

Inserting the expressions,

$$S_{cl} = \frac{m}{2}\int_0^t \Big(\omega_z^2 z_i^2 \sin^2(\omega_z t') - 2\omega_z z_i v_i \sin(\omega_z t')\cos(\omega_z t') + v_i^2\cos^2(\omega_z t') \\ - \omega_z^2 z_i^2 \cos^2(\omega_z t') - 2\omega_z z_i v_i \sin(\omega_z t')\cos(\omega_z t') - v_i^2 \sin^2(\omega_z t')\Big)dt' \tag{6.5}$$

[5] One may wonder if the quantization of harmonic oscillator vibrational levels has any consequence here. The derivation for the matter-wave phase that prescribes the action along the classically-expected trajectory is sufficiently general to apply here without caveat. Interested readers may find guidance from the ion community [217, 218], who takes up residence in phase space and considers displacement operators. Here, one might displace the state and expand the coherent state in a Fock basis that supports energy eigenvalues. The Fock components would evolve as eigenestates under the Hamiltonian and one could calculate interferometer phases according to App. A. Alternatively, the optical lattice clock community has also considered interferometry operating between vibrational levels of a harmonic trap [219].

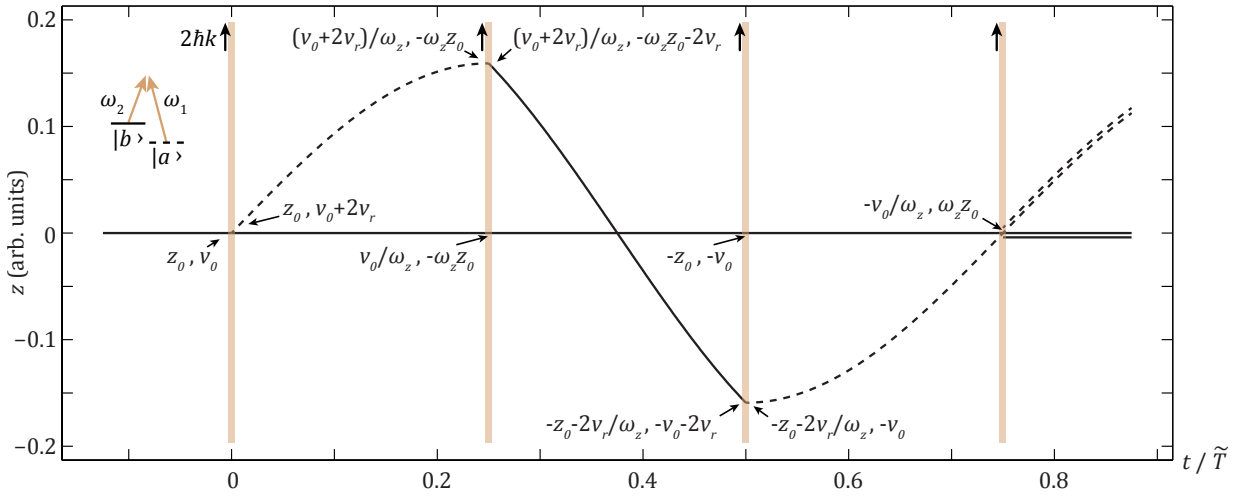

Figure 6.4: Free-oscillation recoil interferometer trajectories. Labels indicate the position and velocity of the arms at critical instants just before or after a Raman pulse.

Performing the integrals, the action indeed vanishes for half periods $S_{cl}(\tilde{T}/2) = 0$, but is nonzero for quarter periods

$$S_{cl}(\tilde{T}/4) = -mz_i v_i. \tag{6.6}$$

We can exploit the appearance of v_i in the action for quarter-period evolutions, imparting recoil velocities through Raman pulses.

The free-oscillation recoil interferometer consists of four $\pi/2$ pulses, each separated in time by a quarter of the trap period $\tilde{T}/4$ as Fig. 6.4 shows. Labelling the trajectories with the positions and velocities aids in computing the trajectories, as well as the laser and free-evolution phases of the interferometer. We label the arm with the recoils the upper arm u and the arm without recoils the lower arm l. Consider an atom in the trap with position z_0 and velocity v_0 at the moment of the first Raman pulse.

$$z_{u1} = z_{l1} = z_0, \tag{6.7}$$
$$z_{u2} = (v_0 + 2v_r)/\omega_z, \tag{6.8}$$
$$z_{u3} = -z_0 - 2v_r/\omega z, \tag{6.9}$$
$$z_{u4} = -v_0/\omega_z, \tag{6.10}$$
$$z_{l2} = v_0/\omega_z, \tag{6.11}$$
$$z_{l3} = -z_0, \tag{6.12}$$
$$z_{l4} = -v_0/\omega_z. \tag{6.13}$$

The laser phases from wave vectors k_2 and $-k_1$ sum to

$$\begin{aligned}\Delta\phi_{FOL} =&(k_2 \cdot z_{u1} - \omega_2 \cdot 0) - (-k_1 \cdot z_{u1} - \omega_1 \cdot 0) \\ &- (k_2 z_{u2} - \omega_2 \tilde{T}/4) + (-k_1 z_{u2} - \omega_1 \tilde{T}/4) \\ &(k_2 z_{u3} - \omega_2 \tilde{T}/2) - (-k_1 z_{u3} - \omega_1 \tilde{T}/2) \\ &- \left[(k_2 \cdot z_{l4} - 3\omega_2 \tilde{T}/4) - (-k_1 \cdot z_{l4} - 3\omega_1 \tilde{T}/4)\right] \qquad (6.14) \\ =&-(\omega_1 - \omega_2)\tilde{T}/2 - \frac{8}{\pi}\omega_r \tilde{T}. \qquad (6.15)\end{aligned}$$

Notice that the free-oscillation recoil interferometer does not require reversal of the Raman k-vectors between the second and third pulses, in contrast to the Ramsey-Bordé interferometer. The free-evolution phase requires calculating the classical actions along each quarter-period leg. Including the internal state energies as well,

$$S_{u12} = -mz_0(v_0 + 2v_r) - \hbar\omega_a \tilde{T}/4, \qquad (6.16)$$

$$S_{u23} = -m\frac{v_0 + 2v_r}{\omega_z}(-\omega_z z_0 - 2v_r) - \hbar\omega_b \tilde{T}/4, \qquad (6.17)$$

$$S_{u34} = -m(-z_0 - 2v_r/\omega_z)(-v_0) - \hbar\omega_a \tilde{T}/4, \qquad (6.18)$$

$$S_{l12} = -mz_0 v_0 - \hbar\omega_b \tilde{T}/4, \qquad (6.19)$$

$$S_{l23} = -m\frac{v_0}{\omega_z}(-\omega_z z_0) - \hbar\omega_b \tilde{T}/4, \qquad (6.20)$$

$$S_{l34} = -m(-z_0)(-v_0) - \hbar\omega_b \tilde{T}/4. \qquad (6.21)$$

The difference in action along the arms gives the phase

$$\Delta\phi_{FOFE} = \frac{1}{\hbar}\left[S_{u12} + S_{u23} + S_{u34} - (S_{l12} + S_{l23} + S_{l34})\right] = 2(\omega_b - \omega_a)\frac{\tilde{T}}{4} + \frac{4}{\pi}\omega_r \tilde{T}. \qquad (6.22)$$

The total phase difference for the free-oscillation recoil interferometer is

$$\Delta\phi^{-}_{FO} = -\frac{4}{\pi}\omega_r \tilde{T} - \delta\tilde{T}/2. \qquad (6.23)$$

The $\pi/2$ pulses each produce two outputs each and it would be irresponsible not to consider the effect of those outputs. Fig. 6.5 displays those outputs and their trajectories. Notice that not all overlapping trajectories interfere. Whether they interfere depends on whether the Raman beams couple both the states and momenta of the two overlapping states. There is evidently one more interferometer that closes. We will label the arm that begins recoiling as the upper arm u and the arm that recoils at the second pulse the lower

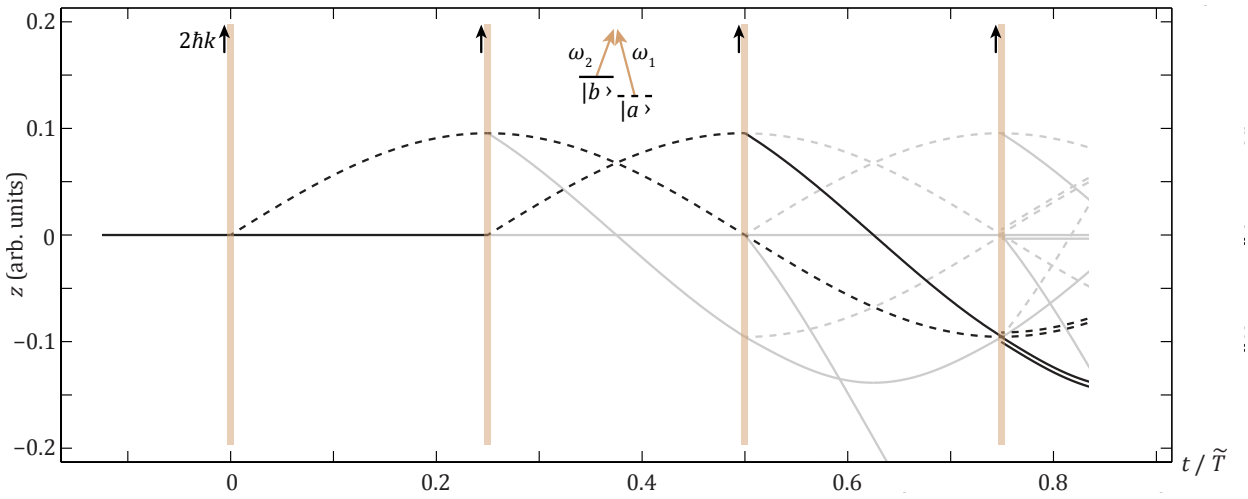

Figure 6.5: The conjugate free-oscillation interferometer. Here we show all pulse outputs, with a second closing interferometer in black.

arm l.

$$z'_{u1} = z'_{l1} = z_0, \tag{6.24}$$
$$z'_{u2} = (v_0 + 2v_r)/\omega_z, \tag{6.25}$$
$$z'_{u3} = -z_0, \tag{6.26}$$
$$z'_{u4} = -(v_0 + 2v_r)/\omega_z, \tag{6.27}$$
$$z'_{l2} = v_0/\omega_z, \tag{6.28}$$
$$z'_{l3} = -z_0 + 2v_r/\omega_z, \tag{6.29}$$
$$z'_{l4} = -(v_0 + 2v_r)/\omega_z. \tag{6.30}$$

Calculating the phase for this interferometer, we find a phase conjugate to the first interferometer.

$$\Delta\phi^+_{FO} = \frac{4}{\pi}\omega_r\tilde{T} - \delta\tilde{T}/2. \tag{6.31}$$

The two interferometers overlap and their signals beat for nonzero δ, just as in Fig. 4.2. The two-photon detuning in our previous work incorporated any perturbations to the atomic energy between the pulses, including linear and quadratic Zeeman shifts. It is interesting to consider whether the trapping potential modifies this consideration. If the trap is an optical dipole trap, for example, the trap perturbs the atomic energies through the AC Stark shift. The harmonic potential we use to generate the trajectories and compute the action in Eq. (6.4) accounts for that perturbation and one should therefore not add the perturbation again to the internal state energies.

The precision of the interferometer scales with the trap oscillation period, so improving the precision is no longer as simple as tuning the pulse separation time. The pulse separation times must match the trap period. One can tune the trap period coarsely by tuning the angle

between two beams of a crossed optical dipole trap. Tuning the intensity of the trap light achieves finer adjustments to the trap period. Alternatively, one might load into a one-dimensional optical lattice that generates a harmonic potential at each lattice site.

Crucially, neither of the interferometers' phases depends on initial position or velocity of the atom. The technique evidently allows the use of thermal samples, provided that the trap is deep enough to hold them. For sub-recoil samples, one could extinguish the trap just after the interferometer and allow the two interferometer outputs, different in velocity by $2v_r$ (or more for techniques that transfer higher momentum), to separate.

Challenges

There are several significant challenges to implementing this interferometer. We have only considered the interferometer in a single dimension. The trapping potential should also confine the atoms radially, preferably with a much higher radial trap frequency than the longitudinal axial frequency. Any misalignment between the Raman axis and the longitudinal trap axis will also excite radial motion. If the radial trap frequency is not an integer multiple of the axial trap frequency, then the interferometer arms will not overlap radially, introducing a matter-wave separation phase. It would be necessary to carefully align the Raman axis, carefully calibrate and stabilize these frequencies, and estimate the size of any residual effects.

Even if any radial separations are solved or mitigated, no trap is truly harmonic. A perfectly harmonic trap requires infinite energy, since a perfectly harmonic potential diverges with the distance from the trap center. A real potential necessarily has higher-order terms that introduce anharmonicity into the potential. Compared to a harmonic potential, the anharmonicity relaxes the real trap with increasing distance from the center. The effects of anharmonicity have been considered previously for free-oscillation interferometers [220, 217, 215].

Here, we describe the anharmonicity by adding corrections to the harmonic potential,

$$U = \frac{1}{2} m\omega_z^2 z^2 \left(1 - G_2 z^2 + ...\right), \tag{6.32}$$

where the G coefficients describe the strength of the term. We neglect the odd powers that should be small in a nearly symmetric trap. The equation of motion contains the usual force term $\propto z$ and an additional contribution $\propto z^3$.

$$\ddot{z} + \omega_z^2 z - 2G_2\omega_z^2 z^3 = 0. \tag{6.33}$$

This is an undamped Duffing equation with well-understood solutions that follow bowtie-shaped trajectories in phase space (in contrast to the harmonic oscillator's ellipses). For the quantum harmonic oscillator, the anharmonicity adds a vibrational-quanta-dependent term to the energy spacing between neighboring levels [221].

Rather than treat the interferometer phase for the real-space Duffing oscillator trajectories, we can treat the phase perturbatively for small anharmonicity. Akin to finding the perturbation to a state energy in quantum mechanics by computing the expectation value

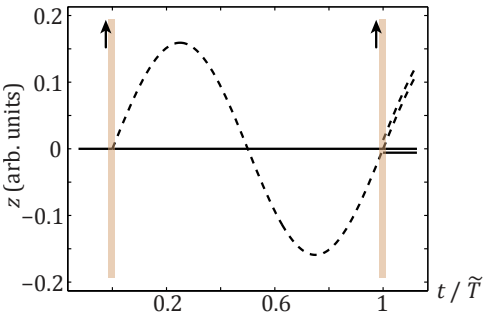

Figure 6.6: Free-oscillation interferometer for sensing AC forces.

of the perturbation with the unperturbed states, we leave the trajectories unperturbed and integrate the perturbed free-evolution phase along those trajectories [222]. The phase we integrate is $m\omega_z^2 G_2 z^4/2\hbar$, along the trajectories z laid out above. The results depend strongly on initial conditions, so here we only show the results for vanishing initial position and velocity

$$\Delta\phi^{-}_{FO,G2} = \frac{9\pi/16 - 1}{8\pi^3\hbar} m G_2 (2v_r)^4 \tilde{T}^3 \tag{6.34}$$

$$\Delta\phi^{+}_{FO,G2} = \frac{1 - 3\pi/16}{8\pi^3\hbar} m G_2 (2v_r)^4 \tilde{T}^3 \tag{6.35}$$

The challenges related to anharmonicity will be worse for hotter atoms since the initial velocities and positions will be diverse, producing larger excursions from the trap center.

Warm samples like our lithium that are limited to smaller interrogation times with standard methods as they thermally expand more rapidly out of the interferometry beams. Techniques to extend the interrogation time, like this free-oscillation technique, could make precision measurements with thermal samples more viable. Nevertheless, it might be prudent to explore effects like those from anharmonicity first in a colder sample.

6.4.2 Free-oscillation AC force sensor

We may also consider the effect of accelerations on free-oscillation interferometers. Any DC acceleration adds a linear term to the potential, like gravity's mgz. A harmonic potential plus a linear potential is still harmonic, with an offset center. Gravity and linear accelerations therefore introduce no phase to the trapped interferometer above. AC forces, on the other hand, could couple into the trajectories. AC forces have been proposed as manifestations of dark-sector physics [223]. Measuring vibrational power spectra *in situ* may another be application of interest for an AC force sensor.

To search for AC forces, we prefer to generate an interferometer insensitive to recoil, an interferometer that operates on half-periods of oscillation. Fig. 6.6 shows such an interferometer. The Raman pulses do not couple the trajectories at the first intersection after a half period (without a reversal of the k vectors), but they do couple the trajectories after

an integer number of full periods. We treat the phase due to a potential $m\tilde{a}_z \sin(\omega_F t + \phi_0) z$ that oscillates at a frequency ω_F with a phase offset by ϕ_0 with respect to the oscillations in the trap. We again treat the phase difference for small AC forces perturbatively, integrating the force term along the unperturbed trajectories. The result is

$$\Delta\phi_{FOAC} = -\delta\tilde{T} + \frac{m\tilde{a}_z}{\hbar} \frac{2v_r(\sin(\phi_0) - \sin(2\pi\omega_F/\omega_z))}{(\omega_z - \omega_F)(\omega_z + \omega_F)}, \tag{6.36}$$

where there is a δ-dependent phase for interferometers operating with Raman pulses. The dependence on the phase offset between the AC force and the free oscillation is certainly unfortunate, but ingenuity has solved harder problems.

Appendix A

Hamiltonian evolution for eigenstate interferometers

The Schrödinger equation

$$i\hbar\frac{d}{d\tau}|\psi\rangle = \hat{H}(\tau)|\psi\rangle \tag{A.1}$$

produces a feature worth appreciating for atom interferometry. The operator describing evolution of small time steps $d\tau$

$$\hat{U}(d\tau) = \exp(-i\hat{H}d\tau/\hbar), \tag{A.2}$$

integrates to

$$\hat{U}(\tau)|s\rangle = \exp(-i\hat{H}\tau/\hbar)|s\rangle = \exp(-i\omega_s\tau)|s\rangle, \tag{A.3}$$

only when $|s\rangle$ is an eigenstate of the full Hamiltonian $\hat{H}$.

After an interferometry pulse, the atom occupies a state of internal state and momentum, say $|b, 2\hbar k\rangle$. Under the influence of gravity, the acceleration constantly changes the atomic momentum, implying that the state is not an eigenstate of the Hamiltonian. In those cases, it becomes more convenient to describe the interferometer phase using a path integral with the classical action as outlined in Section 2.6.5.

Eigenstates accrue phase much more simply than the action, integrating a phase factor $\exp(-i\omega_s\tau)$, where ω_s is the eigenstate's frequency. In most of the interferometers in this thesis, the interferometer operates perpendicular to gravity, so the state evolves as an eigenstate and integrates phase in this simple way. Here we treat an example of how to use this simple Hamiltonian evolution to calculate interferometer phases for eigenstates.

The full Hamiltonian includes the atom's internal state energy, its external kinetic energy $p^2/2m$, as well as the energies of all the photons floating around to drive the transitions.[1]

[1] We treat those pulse periods as infinitesimally small periods of time during which different states are coupled. Since states are coupled, the state is obviously not an eigenstate of the full Hamiltonian at those moments. Treating them as infinitesimally small means that no phase accrues during that time anyway. Any phase that does accrue in reality there we call a "finite pulse effec".

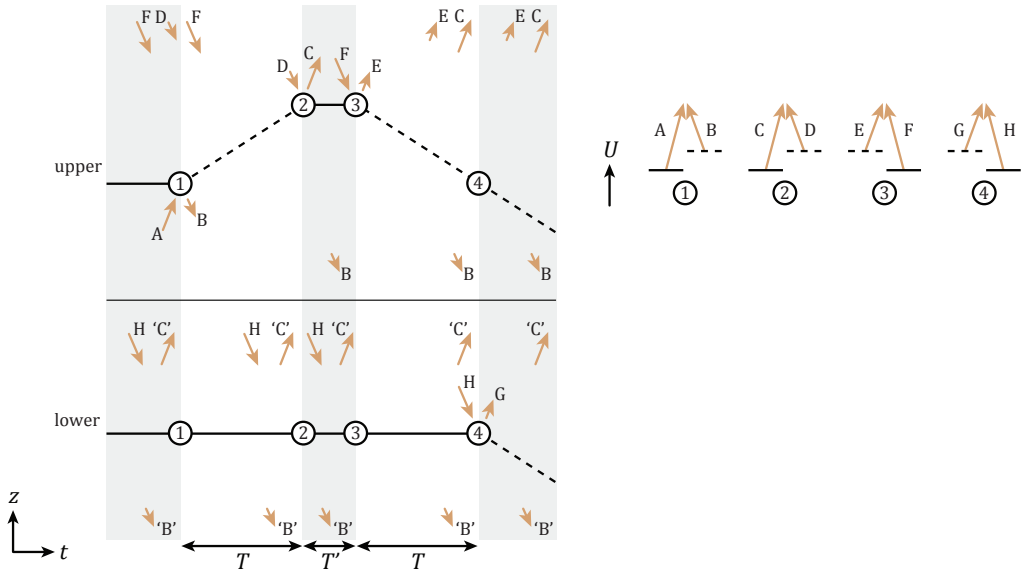

Figure A.1: Ramsey-Bordé spacetime diagram with photons. The photon frequencies $\omega_1 > \omega_2$ drive stimulated Raman transitions between hyperfine states with energy $\omega_b > \omega_a = 0$. The labeling of photons is not physical; it is for bookkeeping only.

Consider the standard Ramsey-Bordé interferometer operating perpendicular to gravity. The upper arm of the interferometer recoils away, ceases, and recoils back toward the lower arm. Photons drive stimulated Raman transitions to make this occur. We can consider the photons that drive the transitions as propagating from distant points to arrive at the atom at the moment of the transition.

Fig. A.1 separately displays the upper and lower arms of the interferometer with the photons that drive the four transitions. We label the photons A through H just to track which photon performs which function. For example, the upper arm of the interferometer absorbs photon A and emits photon B at the first pulse. Since photon B is emitted, it continues to propagate away from the atom. It remains a contribution to the total energy, so we must continue to track its contribution beyond the first pulse.

The lower arm of the interferometer only involves absorbing H and emitting G. Taken alone, those photons would fail to reproduce the same total energy as the upper arm before and after the interferometer. Integrating those different energies to infinity would cause the energetics of these situations to diverge. But the interferometer should present a difference only between the arms. The state before and after the interferometer must be identical, distinguished only by the path it took to arrive at that state. We therefore include extra photons 'B' and 'C' in scare quotes throughout the interferometer to avoid this divergence, even though they do not participate in any transitions in the lower arm of the interferometer.

Let us sum the energy to find the eigenvalue returned by the full Hamiltonian during each period between the pulses. Consider the energy, divided by $\hbar$, for the upper arm between pulses 1 and 2. The phase accrues for T as the total energy of the state, which includes

photons F, B, and D with frequencies ω_1, ω_2, and ω_2, respectively. We must not forget the minus sign in front of the Hamiltonian in the temporal evolution operator.

$$\phi_{u12} = -\omega_b T - 4\omega_r T - \omega_1 T - 2\omega_2 T. \tag{A.4}$$

Between the second and third pulses, there is no recoil energy and we set the internal energy $\omega_a = 0$ for the lower hyperfine state

$$\phi_{u34} = -2\omega_1 T' - \omega_2 T'. \tag{A.5}$$

Between the third and fourth pulses,

$$\phi_{u12} = -\omega_b T - 4\omega_r T - \omega_1 T - 2\omega_2 T. \tag{A.6}$$

Summing up these phases for the upper arm, we find

$$\phi_u = -2\omega_b T - 8\omega_r T - 2\omega_1 T - 4\omega_2 T - 2\omega_1 T' - \omega_2 T' \tag{A.7}$$

For the lower arm,

$$\phi_{l12} = -2\omega_1 T - \omega_2 T, \tag{A.8}$$
$$\phi_{l12} = -2\omega_1 T' - \omega_2 T', \tag{A.9}$$
$$\phi_{l12} = -2\omega_1 T - \omega_2 T, \tag{A.10}$$

with total phase

$$\phi_l = -4\omega_1 T - 2\omega_2 T - 2\omega'_T - \omega_1 T'. \tag{A.11}$$

The interferometer phase is the phase difference between the arms.

$$\Delta\phi = \phi_u - \phi_l = -8\omega_r T + 2(\omega_1 - \omega_2 - \omega_b)T = -8\omega_r T + 2\delta T. \tag{A.12}$$

We have reproduced the same phase as the path integral method, with arguably less effort. A similar analysis of the conjugate Ramsey-Bordé also produces the correct phase difference $+8\omega_r T + 2\delta T$.

Bibliography

[1] K. C. Cox et al. "Quantum-Limited Atomic Receiver in the Electrically Small Regime". In: *Phys. Rev. Lett.* 121 (2018), p. 110502. DOI: 10.1103/PhysRevLett.121.110502. arXiv: 1805.09808 [physics.atom-ph].

[2] R. Grimm, M. Weidemüller, and Y. B. Ovchinnikov. "Optical dipole traps for neutral atoms". In: *Advances in Atomic, Molecular and Optical Physics*. Vol. 42. Academic Press, 2000, pp. 95–170. arXiv: 9902072 [physics.atom-ph].

[3] J. D. Miller, R. A. Cline, and D. J. Heinzen. "Far-off-resonance optical trapping of atoms". In: *Phys. Rev. A* 47 (1993), R4567(R). DOI: 10.1103/PhysRevA.47.R4567.

[4] V. V. Flambaum, S. G. Porsev, and M. S. Safronova. "Energy shift due to anisotropic blackbody radiation". In: *Phys. Rev. A* 93 (2016), p. 022508. DOI: 10.1103/PhysRevA.93.022508. arXiv: 1508.01242 [physics.atom-ph].

[5] M. S. Safronova et al. "Blackbody radiation shift in the Sr optical atomic clock". In: *Phys. Rev. A* 87 (2013), p. 012509. DOI: 10.1103/PhysRevA.87.012509. arXiv: 1210.7272 [physics.atom-ph].

[6] P. Haslinger et al. "Attractive force on atoms due to blackbody radiation". In: *Nature Physics* 14 (2018), p. 257. DOI: 10.1038/s41567-017-0004-9. arXiv: 1704.03577 [physics.atom-ph].

[7] B. M. Henson et al. "Precision measurement for metastable helium atoms of the 413 nm tune-out wavelength at which the atomic polarizability vanishes". In: *Phys. Rev. Lett.* 115 (2015), p. 043004. DOI: 10.1103/PhysRevLett.115.043004. arXiv: 1505.03642 [physics.atom-ph].

[8] Y.-H. Zhang et al. "QED and relativistic nuclear recoil corrections to the 413 nm tune-out wavelength for the 2^3S_1 state of helium". In: *Phys. Rev. A* 99 (2019), 040502(R). DOI: 10.1103/PhysRevA.99.040502. arXiv: 1903.04170 [physics.atom-ph].

[9] G. Drake and J. Manalo. "QED Corrections to the Tune-out Wavelength for the 1s2s ^3S - 1s3p ^3P Transition of Helium". In: *APS Meeting Abstracts*. May 2018, Q06.003.

[10] Y.-H. Zhang et al. "Tune-out wavelength around 413 nm for the helium 2^3S_1 state including relativistic and finite-nuclear-mass corrections". In: *Phys. Rev. A* 93 (2016), p. 052516. DOI: 10.1103/PhysRevA.93.052516.

[11] Y.-H. Zhang et al. "Dynamic dipole polarizabilities for the low-lying triplet states of helium". In: *Phys. Rev. A* 92 (2015), p. 012515. DOI: 10.1103/PhysRevA.92.012515. arXiv: 1503.07300 [physics.atom-ph].

[12] M. S. Safronova, U. I. Safronova, and C. W. Clark. "Magic wavelengths for optical cooling and trapping of lithium". In: *Phys. Rev. A* 86 (2012), p. 042505. DOI: 10.1103/PhysRevA.86.042505. arXiv: 1206.7115 [physics.atom-ph].

[13] L.-Y. Tang et al. "Dynamic Stark shift of the ^{7}Li($2S \rightarrow 3S$) transition". In: *Phys. Rev. A* 87 (2013), p. 032507. DOI: 10.1103/PhysRevA.87.032507.

[14] L.-Y. Tang et al. "Dynamic dipole polarizabilities of the Li atom and the Be^+ ion". In: *Phys. Rev. A* 81 (2010), p. 042521. DOI: 10.1103/PhysRevA.81.042521. arXiv: 1001.4116 [physics.atom-ph].

[15] F. L. Kien, P. Schneeweiss, and A. Rauschenbeutal. "Dynamical polarizability of atoms in arbitrary light fields: general theory and application to cesium". In: *Eur. Phys. J. D* 67 (2013), p. 92. DOI: 10.1140/epjd/e2013-30729-x. arXiv: 1211.2673 [physics.atom-ph].

[16] J. Mitroy, M. S. Safronova, and C. W. Clark. "Theory and applications of atomic and ionic polarizabilities". In: *J. Phys. B: At. Mol. Opt. Phys.* 43 (2010), p. 202001. DOI: 10.1088/0953-4075/43/20/202001. arXiv: 1004.3567 [physics.atom-ph].

[17] M. Puchalski, D. Kędziera, and K. Pachucki. "D_1 and D_2 lines in ^{6}Li and ^{7}Li including QED effects". In: *Phys. Rev. A* 87 (2013), p. 032503. DOI: 10.1103/PhysRevA.87.032503. arXiv: 1212.3196 [physics.atom-ph].

[18] L.-Y. Tang et al. "Nonrelativistic ab initio calculations for 2^2S, 2^2P and 3^2D lithium isotopes: Applications to polarizabilities and dispersion interactions". In: *Phys. Rev. A* 79 (2009), p. 062712. DOI: 10.1103/PhysRevA.79.062712. arXiv: 0905.2110 [physics.atom-ph].

[19] Z.-C. Yan and G. W. F. Drake. "Theoretical lithium $2^2S \rightarrow 2^2P$ and $2^2P \rightarrow 3^2D$ oscillator strengths". In: *Phys. Rev. A* 52 (1995), R4316. DOI: 10.1103/PhysRevA.52.R4316.

[20] M. Puchalski, D. Kędziera, and K. Pachucki. "Erratum: Lithium electric dipole polarizability". In: *Phys. Rev. A* 85 (2012), p. 019910. DOI: 10.1103/PhysRevA.85.019910.

[21] M. Puchalski, D. Kędziera, and K. Pachucki. "Lithium electric dipole polarizability". In: *Phys. Rev. A* 84 (2011), p. 052518. DOI: 10.1103/PhysRevA.84.052518.

[22] F. W. King, B. Bederson, and H. Walther. "High-Precision Calculations for the Ground and Excited States of The Lithium Atom". In: *Adv. At. Mol. Opt. Phys.* 40 (1999), p. 57. DOI: 10.1016/S1049-250X(08)60111-1.

[23] F. W. King. "Progress on high precision calculations for the ground state of atomic lithium". In: *J. Mol. Struct.* 400 (1997), p. 7. DOI: 10.1016/S0166-1280(97)90265-7.

[24] A. Miffre et al. "Measurement of the electric polarizability of lithium by atom interferometry". In: *Phys. Rev. A* 73 (2006), 011603(R). DOI: 10.1103/PhysRevA.73.011603. arXiv: 0506106 [quant-ph].

[25] M. D. Gregoire et al. "Measurements of the ground-state polarizabilities of Cs, Rb and K using atom interferometry". In: *Phys. Rev. A* 92 (2015), p. 052513. DOI: 10.1103/PhysRevA.73.011603. arXiv: 1509.07091 [physics.atom-ph].

[26] R. Trubko et al. "Potassium tune-out-wavelength measurement using atom interferometry and a multipass optical cavity". In: *Phys. Rev. A* 95 (2017), p. 052507. DOI: 10.1103/PhysRevA.95.052507.

[27] W. F. Holmgren et al. "Measurement of a wavelength of light for which the energy shift for an atom vanishes". In: *Phys. Rev. Lett.* 109 (2012), p. 243004. DOI: 10.1103/PhysRevLett.109.243004. arXiv: 1208.4653 [physics.atom-ph].

[28] R. H. Leonard et al. "Erratum: High-precision measurements of the ^{87}Rb D-line tune-out wavelength (Phys. Rev. A 92, 052501 (2015))". In: *Phys. Rev. A* 95 (2017), 059901(E). DOI: 10.1103/PhysRevA.95.059901.

[29] R. H. Leonard et al. "High-precision measurements of the ^{87}Rb D-line tune-out wavelength". In: *Phys. Rev. A* 92 (2015), p. 052501. DOI: 10.1103/PhysRevA.92.052501. arXiv: 1507.07898 [physics.atom-ph].

[30] F. Schmidt et al. "Precision measurement of the ^{87}Rb tune-out wavelength in the hyperfine ground state $F = 1$ at 790 nm". In: *Phys. Rev. A* 93 (2016), p. 022507. DOI: 10.1103/PhysRevA.93.022507. arXiv: 1512.03578 [quant-ph].

[31] G. Lamporesi et al. "Scattering in mixed dimensions with ultracold gases". In: *Phys. Rev. Lett.* 104 (2010), p. 153202. DOI: 10.1103/PhysRevLett.104.153202. arXiv: 1002.0114 [cond-mat.quant-gas].

[32] W. Kao et al. "Anisotropic dependence of tune-out wavelength near Dy 741-nm transition". In: *Opt. Express* 25 (2017), pp. 3411–3419. DOI: 10.1364/OE.25.003411. arXiv: 1609.02111 [physics.atom-ph].

[33] G. W. Biedermann et al. "Atom interferometry in a warm vapor". In: *Phys. Rev. Lett.* 118 (2017), p. 163601. DOI: 10.1103/PhysRevLett.118.163601. arXiv: 1610.02451 [physics.atom-ph].

[34] O. Carnal and J. Mlynek. "Young's double-slit experiment with atoms: A simple atom interferometer". In: *Phys. Rev. Lett.* 66 (1991), p. 2689. DOI: 10.1103/PhysRevLett.66.2689.

[35] M. Kasevich and S. Chu. "Atomic interferometry using stimulated Raman transitions". In: *Phys. Rev. Lett.* 67 (1991), p. 181. DOI: 10.1103/PhysRevLett.67.181.

[36] W. W. Chow et al. "The ring laser gyro". In: *Rev. Mod. Phys.* 57 (1985), p. 61. DOI: 10.1103/RevModPhys.57.61.

[37] B. P. Abbott et al. "Observation of Gravitational Waves from a Binary Black Hole Merger". In: *Phys. Rev. Lett.* 116 (2016), p. 061102. DOI: 10.1103/PhysRevLett.116.061102. arXiv: 1602.03837 [gr-qc].

[38] Z. Y. Ou C. K. Hong and L. Mandel. "Measurement of subpicosecond time intervals between two photons by interference". In: *Phys. Rev. Lett* 59 (1987), p. 2044. DOI: 10.1103/PhysRevLett.59.2044.

[39] D. W. Keith et al. "Diffraction of Atoms by a Transmission Grating". In: *Phys. Rev. Lett.* 61 (1988), p. 1580. DOI: 10.1103/PhysRevLett.61.1580.

[40] P. E. Moskowitz et al. "Diffraction of an Atomic Beam by Standing-Wave Radiation". In: *Phys. Rev. Lett.* 51 (1983), p. 370. DOI: 10.1103/PhysRevLett.51.370.

[41] P. L. Gould, G. A. Ruff, and D. E. Pritchard. "Diffraction of atoms by light: The near-resonant Kapitza-Dirac effect". In: *Phys. Rev. Lett.* 56 (1986), p. 827. DOI: 10.1103/PhysRevLett.56.827.

[42] S. Chu et al. "Three-dimensional viscous confinement and cooling of atoms by resonance radiation pressure". In: *Phys. Rev. Lett.* 55 (1985), p. 48. DOI: 10.1103/PhysRevLett.55.48.

[43] E. L. Raab et al. "Trapping of Neutral Sodium Atoms with Radiation Pressure". In: *Phys. Rev. Lett.* 59 (1987), p. 2631. DOI: 10.1103/PhysRevLett.59.2631.

[44] A. D. Cronin, J. Schmiedmayer, and D. E. Pritchard. "Optics and interferometry with atoms and molecules". In: *Rev. Mod. Phys.* 81 (2009), p. 1051. DOI: 10.1103/RevModPhys.81.1051. arXiv: 0712.3703 [quant-ph].

[45] L. Duca et al. "An Aharonov-Bohm interferometer for determining Bloch band topology". In: *Science* 347 (2015), p. 288. DOI: 10.1126/science.1259052. arXiv: 1407.5635 [cond-mat.quant-gas].

[46] T. Maudlin. "Three measurement problems". In: *Topoi* 14 (1995), p. 7. DOI: 10.1007/BF00763473.

[47] G. C. Ghirardi, A. Rimini, and T. Weber. "Unified dynamics for microscopic and macroscopic systems". In: *Phys. Rev. D* 34 (1986), p. 470. DOI: 10.1103/PhysRevD.34.470.

[48] R. Penrose. "On Gravity's role in Quantum State Reduction". In: *Gen. Relat. Gravit.* 28 (1996), p. 581. DOI: 10.1007/BF02105068.

[49] M. J. Weaver et al. "Phonon interferometry for measuring quantum decoherence". In: *Phys. Rev. A* 97 (2018), p. 063832. DOI: 10.1103/PhysRevA.97.063832. arXiv: 1802.08399 [quant-ph].

[50] W. Marshall et al. "Towards Quantum Superpositions of a Mirror". In: *Phys. Rev. Lett.* 28 (2003), p. 130401. DOI: 10.1103/PhysRevLett.91.130401. arXiv: 0210001 [quant-ph].

[51] T. Kovachy et al. "Quantum superposition at the half-metre scale". In: *Nature* 528 (2015), pp. 530–533. DOI: 10.1038/nature16155.

[52] X. Wu et al. "Multiaxis atom interferometry with a single diode laser and a pyramidal magneto-optical trap". In: *Optica* 4 (2017), p. 1545. DOI: 10.1364/OPTICA.4.001545. arXiv: 1707.08693 [physics.atom-ph].

[53] W. C. Campbell and P. Hamilton. "Rotation sensing with trapped ions". In: *J. Phys. B: At. Mol. Opt. Phys.* 50 (2017), p. 064002. DOI: 10.1088/1361-6455/aa5a8f. arXiv: 1609.00659 [physics.atom-ph].

[54] R. Trubko et al. "Atom Interferometer Gyroscope with Spin-Dependent Phase Shifts Induced by Light near a Tune-Out Wavelength". In: *Phys. Rev. Lett.* 14 (2015), p. 140404. DOI: 10.1103/PhysRevLett.114.140404. arXiv: 1510.06241 [physics.atom-ph].

[55] P. W. Graham et al. "Mid-band gravitational wave detection with precision atomic sensors". In: (2017). arXiv: 1711.02225 [astro-ph.IM].

[56] P. W. Graham et al. "A Resonant Mode for Gravitational Wave Detectors based on Atom Interferometry". In: *Phys. Rev. D* 94 (2016), p. 104022. DOI: 10.1103/PhysRevD.94.104022. arXiv: 1606.01860 [physics.atom-ph].

[57] S. Loriani et al. "Atomic source selection in space-borne gravitational wave detection". In: (2018). arXiv: 1812.11348 [physics.atom-ph].

[58] A. M. Kaufman et al. "Hong-Ou-Mandel atom interferometry in tunnel-coupled optical tweezers". In: *Science* 345 (2014), p. 306. DOI: 10.1126/science.1250057. arXiv: 1312.7182 [cond-mat.quant-gas].

[59] J. M. Hogan, D. M. S. Johnson, and M. A. Kasevich. "Light-pulse atom interferometry". In: (2008). arXiv: 0806.3261 [physics.atom-ph].

[60] Y. Bidel et al. "Absolute marine gravimetry with matter-wave interferometry". In: *Nat. Commun.* 9 (2018), p. 627. DOI: 10.1038/s41467-018-03040-2.

[61] L. Hu et al. "Sr atom interferometry with the optical clock transition as a gravimeter and a gravity gradiometer". In: (2019). arXiv: 1907.10537 [physics.atom-ph].

[62] D. Savoie et al. "Interleaved atom interferometry for high-sensitivity inertial measurements". In: *Science Advances* 4 (2018), p. 033608. DOI: 10.1126/sciadv.aau7948. arXiv: 1808.10801 [physics.atom-ph].

[63] C. Freier et al. "Mobile quantum gravity sensor with unprecedented stability". In: *J. Phys. Conf. Ser.* 723 (2016), p. 012050. DOI: 10.1088/1742-6596/723/1/012050. arXiv: 1512.05660 [physics.atom-ph].

[64] S. M. Dickerson et al. "Multiaxis inertial sensing with long-time point source atom interferometry". In: *Phys. Rev. Lett.* 111 (2013), p. 083001. DOI: 10.1103/PhysRevLett.111.083001. arXiv: 1305.1700 [physics.atom-ph].

[65] R. P. del Aguila et al. "Bragg gravity-gradiometer using the $^1S_0-^3P_1$ intercombination transition of ^{88}Sr". In: *New J. Phys.* 20 (2018), p. 019502. DOI: 10.1088/1367-2630/aab088. arXiv: 1712.01388 [physics.atom-ph].

[66] A. Bertoldi et al. "Atom interferometry gravity-gradiometer for the determination of the Newtonian gravitational constant G". In: *Eur. Phys. J. D* 40 (2008), p. 271. DOI: 10.1140/epjd/e2006-00212-2. arXiv: 0606126 [physics.atom-ph].

[67] G. W. Biedermann et al. "Testing gravity with cold-atom interferometers". In: *Phys. Rev. A* 91 (2015), p. 033629. DOI: 10.1103/PhysRevA.91.033629. arXiv: 1412.3210 [physics.atom-ph].

[68] J. M. McGuirk et al. "Sensitive absolute-gravity gradiometry using atom interferometry". In: *Phys. Rev. A* 65 (2002), p. 033608. DOI: 10.1103/PhysRevA.65.033608. arXiv: 0105088 [physics.atom-ph].

[69] G. Rosi et al. "Precision measurement of the Newtonian gravitational constant using cold atoms". In: *Nature* 510 (2014), p. 518. DOI: 10.1038/nature13433. arXiv: 1412.7954 [physics.atom-ph].

[70] G. Lamporesi et al. "Determination of the Newtonian gravitational constant using atom interferometry". In: *Phys. Rev. Lett.* 100 (2008), p. 050801. DOI: 10.1103/PhysRevLett.100.050801. arXiv: 0801.1580 [physics.atom-ph].

[71] J. B. Fixler et al. "Atom interferometer measurement of the Newtonian constant of gravity". In: *Science* 315 (2007), p. 74. DOI: 10.1088/1742-6596/723/1/012050.

[72] R. H. Parker et al. "Measurement of the fine-structure constant as a test of the Standard Model". In: *Science* 360 (2018), pp. 191–195. DOI: 10.1126/science.aap7706. arXiv: 1812.04130 [physics.atom-ph].

[73] R. Bouchendira et al. "New determination of the fine structure constant and test of quantum electrodynamics". In: *Phys. Rev. Lett.* 106 (2011), p. 080801. DOI: 10.1103/PhysRevLett.106.080801. arXiv: 1012.3627 [physics.atom-ph].

[74] B. Plotkin-Swing et al. "Three-path atom interferometry with large momentum splitting". In: *Phys. Rev. Lett.* 121 (2018), p. 133201. DOI: 10.1103/PhysRevLett.121.133201. arXiv: 1712.06738 [physics.atom-ph].

[75] L. Zhou et al. "Test of the Equivalence Principle at the 10^{-8} level by a dual-species double-diffraction Raman atom interferometer". In: *Phys. Rev. Lett.* 115 (2015), p. 013004. DOI: 10.1103/PhysRevLett.115.013004. arXiv: 1503.00401 [physics.atom-ph].

[76] C. Overstreet et al. "Effective inertial frame in an atom interferometric test of the equivalence principle". In: *Phys. Rev. Lett.* 120 (2018), p. 183604. DOI: 10.1103/PhysRevLett.120.183604. arXiv: 1711.09986 [physics.atom-ph].

[77] D. Schlippert et al. "Quantum test of the universality of free fall". In: *Phys. Rev. Lett.* 112 (2014), p. 203002. DOI: 10.1103/PhysRevLett.112.203002. arXiv: 1406.4979 [physics.atom-ph].

[78] G. Rosi et al. "Quantum test of the equivalence principle for atoms in coherent superposition of internal energy states". In: *Nat. Commun.* 8 (2017), p. 15529. DOI: 10.1038/ncomms15529. arXiv: 1704.02296 [physics.atom-ph].

[79] A. Bonnin et al. "Simultaneous dual-species matter-wave interferometer". In: *Phys. Rev. A* 88 (2013), p. 043615. DOI: 10.1103/PhysRevA.88.043615. arXiv: 1307.2734 [physics.atom-ph].

[80] X.-C. Duan et al. "Test of the universality of free fall with atoms in different spin orientations". In: *Phys. Rev. Lett.* 117 (2016), p. 023001. DOI: 10.1103/PhysRevLett.117.023001. arXiv: 1602.06377 [physics.atom-ph].

[81] M. A. Hohensee, H. Müller, and R. B. Wiringa. "Equivalence Principle and Bound Kinetic Energy". In: *Phys. Rev. Lett.* 111 (2013), p. 151102. DOI: 10.1103/PhysRevLett.111.151102. arXiv: 1308.2936 [gr-qc].

[82] K.-Y. Chung et al. "Atom interferometry tests of local Lorentz invariance in gravity and electrodynamics". In: *Phys. Rev. D* 80 (2009), p. 016002. DOI: 10.1103/PhysRevD.80.016002. arXiv: 0905.1929 [gr.qc].

[83] M. Jaffe et al. "Testing sub-gravitational forces on atoms from a miniature in-vacuum source mass". In: *Nat. Phys.* 13 (2017), p. 938. DOI: 10.1038/NPHYS4189. arXiv: 1612.05171 [physics.atom-ph].

[84] P. Hamilton et al. "Atom interferometer constraints on dark energy". In: *Science* 349 (2015), pp. 849–851. DOI: 10.1126/science.aaa8883. arXiv: 1502.03888 [physics.atom-ph].

[85] L. Salvi et al. "Squeezing on Momentum States for Atom Interferometry". In: *Phys. Rev. Lett* 120 (2018), p. 033601. DOI: 10.1103/PhysRevLett.120.033601. arXiv: 1708.05112 [physics.atom-ph].

[86] K. C. Cox et al. "Spatially homogeneous entanglement for matter-wave interferometry created with time-averaged measurements". In: *Phys. Rev. A* 94 (2016), 061601(R). DOI: 10.1103/PhysRevA.94.061601. arXiv: 1608.06234 [physics.atom-ph].

[87] O. Hosten et al. "Measurement noise 100 times lower than the quantum-projection limit using entangled atoms". In: *Nature* 529 (2016), p. 505. DOI: 10.1038/nature16176. arXiv: 1708.05112 [physics.atom-ph].

[88] A. Sugarbaker et al. "Enhanced atom interferometer readout through the application of phase shear". In: *Phys. Rev. Lett.* 111 (2013), p. 113002. DOI: 10.1103/PhysRevLett.111.113002. arXiv: 1305.3298 [physics.atom-ph].

[89] P. B. Wigley et al. "Readout-delay-free Bragg atom interferometry using overlapped spatial fringes". In: *Phys. Rev. A* 99 (2019), p. 023615. DOI: 10.1103/PhysRevA.99.023615. arXiv: 1812.09076 [quant-ph].

[90] Daniel A. Steck. *Quantum and Atom Optics*. Available online at http://steck.us/teaching (revision 0.10.1, 30 April 2015). 2007.

[91] Matthew Jaffe. "Atom interferometry in an optical cavity". PhD thesis. University of California, Berkeley, 2018.

[92] C. Brand et al. "An atomically thin matter-wave beamsplitter". In: *Nat. Nanotechnol.* 10 (2015), p. 845. DOI: 10.1038/nnano.2015.179. arXiv: 1602.07578 [quant-ph].

[93] Paul R. Berman. *Atom Interferometry*. 1st ed. 525 B Street, Suite 1900, San Diego, CA 92101-4495, USA: Academic Press, Inc., Jan. 1997. ISBN: 0120924609. URL: https://www.sciencedirect.com/book/9780120924608/atom-interferometry.

[94] Chenghui Yu. "Measuring the fine structure constant with a state-of-the-art atom interferometer". PhD thesis. University of California, Berkeley, 2018.

[95] Swaantje-Johanna Grunefeld. "A Pseudostate Method for Computing Photon-Atom Scattering Cross-sections". PhD thesis. University of Queensland, 2017.

[96] W. I. McAlexander, E. R. I. Abraham, and R. G. Hulet. "Radiative lifetime of the $2P$ state of lithium". In: *Phys. Rev. A* 54 (1996), R5–R8. DOI: 10.1103/PhysRevA.54.R5.

[97] L. Hu et al. "Atom Interferometry with the Sr Optical Clock Transition". In: *Phys. Rev. Lett.* 119 (2017), p. 263601. DOI: 10.1103/PhysRevLett.119.263601. arXiv: 1708.05116 [physics.atom-ph].

[98] V. Paulisch et al. "Beyond adiabatic elimination: A hierarchy of approximations for multi-photon processes". In: *Eur. Phys. J. Plus* 129 (2014), p. 12. DOI: 10.1140/epjp/i2014-14012-8. arXiv: 1209.6568 [quant-ph].

[99] K. Moler et al. "Theoretical analysis of velocity-selective Raman transitions". In: *Phys. Rev. A* 45 (1992), p. 342. DOI: 10.1103/PhysRevA.45.342.

[100] F.-F. Wu et al. "Relativistic full-configuration-interaction calculations of magic wavelengths for the 23S1 to 21S0 transition of helium isotopes". In: *Phys. Rev. A* 98 (2018), 040501(R). DOI: 10.1103/PhysRevA.98.040501. arXiv: 1804.01218 [physics.atom-ph].

[101] H. Katori. "Optical lattice clocks and quantum metrology". In: *Nat. Photonics* 5 (2011), p. 203. DOI: 10.1038/nphoton.2011.45.

[102] A. Derevianko and H. Katori. "Colloquium: Physics of optical lattice clocks". In: *Rev. Mod. Phys.* 83 (2011), p. 331. DOI: 10.1103/RevModPhys.83.331. arXiv: 1011.4622 [physics.atom-ph].

[103] A. Brusch et al. "Hyperpolarizability Effects in a Sr Optical Lattice Clock". In: *Phys. Rev. Lett.* 96 (2006), p. 103003. DOI: 10.1103/PhysRevLett.96.103003. arXiv: 0512201 [physics.atom-ph].

[104] R. C. Brown et al. "Hyperpolarizability and Operational Magic Wavelength in an Optical Lattice Clock". In: *Phys. Rev. Lett.* 119 (2017), p. 253001. DOI: 10.1103/PhysRevLett.119.253001. arXiv: 1708.08829 [physics.atom-ph].

[105] I. Ushijima, M. Takamoto, and H. Katori. "Operational Magic Intensity for Sr Optical Lattice Clocks". In: *Phys. Rev. Lett.* 121 (2018), p. 263202. DOI: 10.1103/PhysRevLett.121.263202. arXiv: 1812.11815 [physics.atom-ph].

[106] P. G. Westergaard et al. "Lattice-Induced Frequency Shifts in Sr Optical Lattice Clocks at the 10^{-17} Level". In: *Phys. Rev. Lett.* 106 (2011), p. 210801. DOI: 10.1103/PhysRevLett.106.210801. arXiv: 1102.1797 [physics.atom-ph].

[107] N. Nemitz et al. "Modeling light shifts in optical lattice clocks". In: *Phys. Rev. A* 99 (2019), p. 033424. DOI: 10.1103/PhysRevA.99.033424. arXiv: 1904.06070 [physics.atom-ph].

[108] T. Bothwell et al. "JILA SrI Optical Lattice Clock with Uncertainty of 2.0×10^{-18}". In: (2019). arXiv: 1906.06004 [physics.atom-ph].

[109] S. G. Porsev et al. "Multipolar Polarizabilities and Hyperpolarizabilities in the Sr Optical Lattice Clock". In: *Phys. Rev. Lett.* 120 (2018), p. 063204. DOI: 10.1103/PhysRevLett.120.063204. arXiv: 1711.03957 [physics.atom-ph].

[110] F.-F. Wu et al. "Multipolar and higher-order lattice shifts in the Sr and Mg clocks". In: (2019). arXiv: 1906.02024 [physics.atom-ph].

[111] Daniel A. Steck. *Rubidium 87 D Line Data*. Available online at https://steck.us/alkalidata/rubidium87numbers.1.6.pdf (revision 1.6, 14 October 2003). 2001.

[112] Alexander J. Dunning. "Coherent atomic manipulation and cooling using composite optical pulse sequences". PhD thesis. University of Southampton, 2014.

[113] P. M. Duarte et al. "All-optical production of a lithium quantum gas using narrow-line laser cooling". In: *Phys. Rev. A* 84 (2011), 061406(R). DOI: 10.1103/PhysRevA.84.061406. arXiv: 1109.6635 [cond-mat.quant-gas].

[114] Kayleigh Cassella. "Hot beats and tune outs: atom interferometry with laser-cooled lithium". PhD thesis. University of California, Berkeley, 2018.

[115] C. J. Sansonetti et al. "Absolute transition frequencies and quantum interference in a frequency comb based measurement of the ^{6,7}Li D lines". In: *Phys. Rev. Lett.* 107 (2011), p. 023001. DOI: 10.1103/PhysRevLett.107.023001.

[116] A. Beckmann, K. D. Böklen, and D. Elke. "Precision Measurements of the Nuclear Magnetic Dipole Moments of ^{6}Li, ^{7}Li, ^{23}Na, ^{39}K and ^{41}K". In: *Z. Physik* 270 (1974), p. 173. DOI: 10.1007/BF01680407.

[117] B. Arora, M. S. Safronova, and C. W. Clark. "Tune-out wavelengths of alkali-metal atoms and their applications". In: *Phys. Rev. A* 84 (2011), p. 043401. DOI: 10.1103/PhysRevA.84.043401. arXiv: 1107.2060 [physics.atom-ph].

[118] E. Myers. "High-Precision Atomic Mass Measurements for Fundamental Constants". In: *Atoms* 7 (2019), p. 37. DOI: 10.3390/atoms7010037.

[119] Sz. Nagy et al. "New mass value for ^{7}Li". In: *Phys. Rev. Lett.* 96 (2006), p. 163004. DOI: 10.1103/PhysRevLett.96.163004. arXiv: 1209.5281 [nucl-ex].

[120] National Institute of Standards and Technology. *Atomic Spectra Database*. Available online at https://www.nist.gov/pml/atomic-spectra-database (revision 5.6, October 2018). 2007. DOI: 10.18434/T4W30F.

[121] J. Pipin and D. M. Bishop. "Accurate variational calculations of the 2^2S, 2^2P and 3^2D states and the dipole, quadrupole and dipole-quadrupole polarizabilities and hyperpolarizabilities of the lithium atom". In: *Phys. Rev. A* 45 (1992), pp. 2736–2743. DOI: 10.1103/PhysRevA.45.2736.

[122] F. J. Gálvez, E. Buendía, and A. Sarsa. "Correlated one-electron and two-electron densities for the ground state of the lithium atom". In: *Phys. Rev. A* 61 (2000), p. 052505. DOI: 10.1103/PhysRevA.61.052505.

[123] Brian Estey. "Precision measurement in atom interferometry using Bragg diffraction". PhD thesis. University of California, Berkeley, 2016.

[124] B. Estey et al. "High- Resolution Atom Interferometers with Suppressed Diffraction Phases". In: *Phys. Rev. Lett.* 115 (2015), p. 083002. DOI: 10.1103/PhysRevLett.115.083002. arXiv: 1410.8486 [physics.atom-ph].

[125] R. Charriére et al. "Local gravity measurement with the combination of atom interferometry and Bloch oscillations". In: *Phys. Rev. A* 85 (2012), p. 013639. DOI: 10.1103/PhysRevA.85.013639. arXiv: 1109.3605 [physics.atom-ph].

[126] M. Jaffe et al. "Efficient Adiabatic Spin-Dependent Kicks in an Atom Interferometer". In: *Phys. Rev. Lett.* 121 (2018), p. 040402. DOI: 10.1103/PhysRevLett.121.040402. arXiv: 1803.09024 [physics.atom-ph].

[127] A. Keshet and W. Ketterle. "A distributed, graphical user interface based, computer control system for atomic physics experiments". In: *Rev. Sci. Instrum.* 84 (2013), p. 015105. DOI: 10.1063/1.4773536. arXiv: 1208.2607 [physics.atom-ph].

[128] Geena Kim. "A new laser cooling method for lithium atom interferometry". PhD thesis. University of California, Berkeley, 2014.

[129] D. J. McCarron, S. A. King, and S. L. Cornish. "Modulation transfer spectroscopy in atomic rubidium". In: *Meas. Sci. Technol.* 19 (2008), p. 105601. DOI: 10.1088/0957-0233/19/10/105601. arXiv: 0805.2708 [physics.atom-ph].

[130] Christopher J. Foot. *Atomic Physics*. 1st ed. Great Clarendon St., Oxford OX2 6DP, UK: Oxford University Press, 2005. ISBN: 0198506953. URL: https://global.oup.com/academic/product/atomic-physics-9780198506966?cc=us&lang=en&.

[131] K. G. Libbrecht. "A low-noise high-speed diode laser current controller". In: *Rev. Sci. Instrum.* 64 (1993), p. 2133. DOI: 10.1063/1.1143949.

[132] K. Szymaniec et al. "Injection locking of diode lasers to frequency modulated source". In: *Opt. Commun.* 144 (1997), p. 50. DOI: 10.1016/S0030-4018(97)00390-8.

[133] J. N. Walpole. "Semiconductor amplifiers and lasers with tapered gain regions". In: *Opt. Quant. Electron.* 28 (1996), p. 623. DOI: 10.1007/BF00411298.

[134] G. Puentes. "Laser frequency offset locking scheme for high-field imaging of cold atoms". In: *Appl. Phys. B* 107 (2012), p. 11. DOI: 10.1007/s00340-012-4898-8. arXiv: 1108.6045 [physics.ins-det].

[135] T. G. Tiecke et al. "High-flux two-dimensional magneto-optical-trap source for cold lithium atoms". In: *Phys. Rev. A* 80 (2009), p. 013409. DOI: 10.1103/PhysRevA.80.013409. arXiv: 0905.1063 [cond-mat.quant-gas].

[136] P. Hamilton et al. "Sisyphus cooling of lithium". In: *Phys. Rev. A* 89 (2014), p. 023409. DOI: 10.1103/PhysRevLett.118.233201. arXiv: 1308.1935 [physics.atom-ph].

[137] T. Arpornthip, C. A. Sackett, and K. J. Hughes. "Vacuum-pressure measurement using a magneto-optical trap". In: *Phys. Rev. A* 85 (2012), p. 033420. DOI: 10.1103/PhysRevA.85.033420. arXiv: 1203.0189 [physics.atom-ph].

[138] D. S. Barker et al. "Light-induced atomic desorption of lithium". In: *Phys. Rev. A* 98 (2018), p. 043412. DOI: 10.1103/PhysRevA.98.043412. arXiv: 1805.09862 [physics.atom-ph].

[139] M. Pappa et al. "Ultra-sensitive atom imaging for matter-wave optics". In: *New J. Phys.* 13 (2011), p. 115012. DOI: 10.1088/1367-2630/13/11/115012.

[140] Konstantinidis Gregory-Orfeus. "Diffractive Dark-Ground Imaging of Ultra-Low Atom-Numbers in a MOT". PhD thesis. University of Crete, 2011.

[141] T. M. Brzozowski et al. "Time-of-flight measurement of the temperature of cold atoms for short trap-probe beam distances". In: *J. Opt. B: Quantum Semiclass. Opt.* 4 (2002), p. 62. DOI: 10.1088/1464-4266/4/1/310.

[142] R. Olf et al. "Thermometry and cooling of a Bose gas to 0.02 times the condensation temperature". In: *Nat. Phys.* 11 (2015), p. 720. DOI: 10.1038/nphys3408. arXiv: 1505.06196 [cond-mat.quant-gas].

[143] K. Cassella et al. "Recoil-sensitive lithium interferometer without a subrecoil sample". In: *Phys. Rev. Lett.* 118 (2017), p. 233201. DOI: 10.1103/PhysRevLett.118.233201. arXiv: 1610.07588 [physics.atom-ph].

[144] M. Cadoret et al. "Combination of Bloch Oscillations with a Ramsey-Bordé Interferometer: New Determination of the Fine Structure Constant". In: *Phys. Rev. Lett.* 101 (2008), p. 230801. DOI: 10.1103/PhysRevLett.101.230801. arXiv: 0810.3152 [physics.atom-ph].

[145] G. E. Marti et al. "Imaging Optical Frequencies with 100 μHz Precision and 1.1 μm Resolution". In: *Phys. Rev. Lett.* 120 (2018), p. 103201. DOI: 10.1103/PhysRevLett.120.103201. arXiv: 1711.08540 [physics.atom-ph].

[146] S. Sturm et al. "High-precision measurement of the atomic mass of the electron". In: *Nature* 506 (2014), p. 467. DOI: 10.1038/nature13026. arXiv: 1406.5590 [physics.atom-ph].

[147] B. J. Mount, M. Redshaw, and E. Myers. "Atomic masses of ^{6}Li, ^{23}Na, ^{39,41}K, ^{85,87}Rb and ^{133}Cs". In: *Phys. Rev. A* 82 (2010), p. 042513. DOI: 10.1103/PhysRevA.82.042513.

[148] D. Hanneke, S. Fogwell Hoogerheide, and G. Gabrielse. "Cavity control of a single-electron quantum cyclotron: Measuring the electron magnetic moment". In: *Phys. Rev. A* 83 (2011), p. 052122. DOI: 10.1103/PhysRevA.83.052122. arXiv: 1009.4831 [physics.atom-ph].

[149] D. Hanneke, S. Fogwell, and G. Gabrielse. "New Measurement of the Electron Magnetic Moment and the Fine Structure Constant". In: *Phys. Rev. Lett.* 100 (2008), p. 120801. DOI: 10.1103/PhysRevLett.100.120801. arXiv: 0801.1134 [physics.atom-ph].

[150] G. Gabrielse et al. "Towards an Improved Test of the Standard Model's Most Precise Prediction". In: *Atoms* 7 (2019), p. 45. DOI: 10.3390/atoms7020045. arXiv: 1904.06174 [quant-ph].

[151] S. Laporta. "High Precision Calculation of the 4-Loop Contribution to the electron g-2 in QED". In: *Phys. Lett. B* 772 (2017), p. 232. DOI: 10.1016/j.physletb.2017.06.056. arXiv: 1704.06996 [hep-ph].

[152] K.-P. Marzlin. "Ramsey-Bordé interferometer for electrons". In: *Phys. Rev. A* 88 (2013), p. 043621. DOI: 10.1103/PhysRevA.88.043621. arXiv: 1307.4020 [quant-ph].

[153] A. P. Povilus et al. "Electron Plasmas Cooled by Cyclotron-Cavity Resonance". In: *Phys. Rev. Lett.* 117 (2016), p. 175001. DOI: 10.1103/PhysRevLett.117.175001. arXiv: 1609.08761 [physics.plasm-ph].

[154] E. Copenhaver et al. "Measurement of a ^{7}Li tune-out wavelength by phase-patterned atom interferometry". In: *Phys. Rev. A* 100 (2019), p. 063603. DOI: 10.1103/PhysRevA.100.063603. arXiv: 1904.08974 [physics.atom-ph].

[155] M. Jasperse et al. "Continuous Faraday measurement of spin precession without light shifts". In: *Phys. Rev. A* 96 (2017), p. 063402. DOI: 10.1103/PhysRevA.96.063402. arXiv: 1705.10965 [quant-ph].

[156] R. Chamakhi et al. "Species-selective launch for precision atom interferometry". In: *New J. Phys.* 17 (2015), p. 123002. DOI: 10.1088/1367-2630/17/12/123002.

[157] H. Kim, H. S. Han, and D. Cho. "Magic Polarization for Optical Trapping of Atoms without Stark-Induced Dephasing". In: *Phys. Rev. Lett.* 111 (2013), p. 243004. DOI: 10.1103/PhysRevLett.111.243004. arXiv: 1311.1290 [physics.atom-ph].

[158] L. J. LeBlanc and J. H. Thywissen. "Species-specific optical lattices". In: *Phys. Rev. A* 75 (2007), p. 053612. DOI: 10.1103/PhysRevA.75.053612. arXiv: 0702034 [cond-mat.stat-mech].

[159] B. Gadway et al. "Probing an ultracold-atom crystal with matter waves". In: *Nat. Phys.* 8 (2012), p. 544. DOI: 10.1038/nphys2320. arXiv: 1104.2564 [cond-mat.quant-gas].

[160] A. J. Daley et al. "Quantum computing with alkaline-earth-metal atoms". In: *Phys. Rev. Lett.* 101 (2008), p. 170504. DOI: 10.1103/PhysRevLett.101.170504. arXiv: 0808.1940 [quant-ph].

[161] J. Catani et al. "Entropy exchange in a mixture of ultracold atoms". In: *Phys. Rev. Lett.* 103 (2009), p. 140401. DOI: 10.1103/PhysRevLett.103.140401. arXiv: 0906.2264 [cond-mat.quant-gas].

[162] J. Catani et al. "Quantum dynamics of impurities in a one-dimensional Bose gas". In: *Phys. Rev. A* 85 (2012), p. 023623. DOI: 10.1103/PhysRevA.85.023623. arXiv: 1106.0828 [cond-mat.quant-gas].

[163] D. Mayer et al. "Controlled doping of a bosonic quantum gas with single neutral atoms". In: *J. Phys. B: At. Mol. Opt. Phys.* 52 (2019), p. 015301. DOI: 10.1088/1361-6455/aaf357. arXiv: 1805.01313 [cond-mat.quant-gas].

[164] C. Ravensbergen et al. "Accurate determination of the dynamical polarizability of dysprosium". In: *Phys. Rev. Lett.* 120 (2018), p. 223001. DOI: 10.1103/PhysRevLett.120.223001. arXiv: 1801.05658 [physics.atom-ph].

[165] Stephen R. Segal. "Progress towards an ultracold atomic Sagnac gyroscope". PhD thesis. University of Colorado, Boulder, 2010.

[166] A. Steffen et al. "Note: In situ measurement of vacuum window birefringence by atomic spectroscopy". In: *Rev. Sci. Instrum.* 84 (2013), p. 126103. DOI: 10.1063/1.4847075. arXiv: 1308.4959 [physics.atom-ph].

[167] W. W. Chow and R. R. Craig. "Amplified spontaneous emission effects in semiconductor laser amplifiers". In: *IEEE J. Quant. Elect.* 26 (1990), pp. 1363–1368. DOI: 10.1109/3.59683.

[168] A. D. Ludlow et al. "Optical atomic clocks". In: *Rev. Mod. Phys.* 87 (2015), p. 637. DOI: 10.1103/RevModPhys.87.637. arXiv: 1407.3493 [physics.atom-ph].

[169] S. Cohen and S. I. Themelis. "Construction of RKR-QDT atomic model potentials for the calculation of Lithium polarizabilities and hyper-polarizabilities". In: *J. Phys. B: At. Mol. Opt. Phys.* 38 (2005), p. 3705. DOI: 10.1088/0953-4075/38/20/007.

[170] Z. A. Geiger et al. "Observation and uses of position-space Bloch oscillations in an ultracold gas". In: *Phys. Rev. Lett.* 120 (2018), p. 213201. DOI: 10.1103/PhysRevLett.120.213201. arXiv: 1803.02456 [cond-mat.quant-gas].

[171] S. Blatt et al. "Low-noise optical lattices for ultracold ^{6}Li". In: *Phys. Rev. A* 92 (2015), 021402(R). DOI: 10.1103/PhysRevA.92.021402. arXiv: 1505.00758 [physics.atom-ph].

[172] I. Dimitrova et al. "Observation of two-beam collective scattering phenomena in a Bose-Einstein condensate". In: *Phys. Rev. A* 96 (2017), 051603(R). DOI: 10.1103/PhysRevA.96.051603. arXiv: 1709.02028 [cond-mat.quant-gas].

[173] I. Ferrier-Barbut et al. "A mixture of Bose and Fermi superfluids". In: *Science* 345 (2014), p. 1035. DOI: 10.1126/science.1255380. arXiv: 1404.2548 [cond-mat.quant-gas].

[174] J. H. V. Nguyen et al. "Collisions of matter-wave solitons". In: *Nat. Phys.* 10 (2014), p. 918. DOI: 10.1038/nphys3135. arXiv: 1407.5087 [cond-mat.quant-gas].

[175] K. Kim et al. "Rapid production of large ^{7}Li Bose-Einstein condensates using D_1 gray molasses". In: *Phys. Rev. A* 99 (2019), p. 053604. DOI: 10.1103/PhysRevA.99.053604. arXiv: 1905.03555 [cond-mat.quant-gas].

[176] P. Medley et al. "Evaporative Production of Bright Atomic Solitons". In: *Phys. Rev. Lett.* 112 (2014), p. 060401. DOI: 10.1103/PhysRevLett.112.060401.

[177] R. A. Hart et al. "Observation of antiferromagnetic correlations in the Hubbard model with ultracold atoms". In: *Nature* 519 (2015), p. 211. DOI: 10.1038/nature14223. arXiv: 1407.5932 [cond-mat.quant-gas].

[178] A. Amico et al. "Time-Resolved Observation of Competing Attractive and Repulsive Short-Range Correlations in Strongly Interacting Fermi Gases". In: *Phys. Rev. Lett.* 121 (2018), p. 253602. DOI: 10.1103/PhysRevLett.121.253602. arXiv: 1807.10208 [cond-mat.quant-gas].

[179] M. F. Parsons et al. "Site-resolved Imaging of Fermionic ^{6}Li in an Optical Lattice". In: *Phys. Rev. Lett.* 114 (2015), p. 213002. DOI: 10.1103/PhysRevLett.114.213002. arXiv: 1504.04397 [cond-mat.quant-gas].

[180] P. T. Brown et al. "Bad metallic transport in a cold atom Fermi-Hubbard system". In: *Science* 363 (2019), p. 379. DOI: 10.1126/science.aat4134. arXiv: 1802.09456 [cond-mat.quant-gas].

[181] B. Mukherjee et al. "Homogeneous Atomic Fermi Gases". In: *Phys. Rev. Lett.* 118 (2017), p. 123401. DOI: 10.1103/PhysRevLett.118.123401. arXiv: 1610.10100 [cond-mat.quant-gas].

[182] A. Omran et al. "Microscopic Observation of Pauli Blocking in Degenerate Fermionic Lattice Gases". In: *Phys. Rev. Lett.* 115 (2015), p. 263001. DOI: 10.1103/PhysRevLett.115.263001. arXiv: 1510.04599 [cond-mat.quant-gas].

[183] P. Asenbaum et al. "Phase shift in an atom interferometer due to spacetime curvature across its wave function". In: *Phys. Rev. Lett.* 118 (2017), p. 183602. DOI: 10.1103/PhysRevLett.118.183602. arXiv: 1610.03832 [physics.atom-ph].

[184] Q.-Q. Hu et al. "Mapping the absolute magnetic field and evaluating the quadratic Zeeman-effect-induced systematic error in an atom interferometer gravimeter". In: *Phys. Rev. A* 96 (2017), p. 033414. DOI: 10.1103/PhysRevA.96.033414. arXiv: 1805.05159 [physics.app-ph].

[185] V. Xu et al. "Probing gravity by holding atoms for 20 seconds". In: (2019). arXiv: 1907.03054 [physics.atom-ph].

[186] M. A. Hohensee et al. "Force-Free Gravitational Redshift: Proposed Gravitational Aharonov-Bohm Experiment". In: *Phys. Rev. Lett.* 108 (2012), p. 230404. DOI: 10.1103/PhysRevLett.108.230404. arXiv: 1109.4887 [quant-ph].

[187] F. Yang et al. "Scanning quantum cryogenic atom microscope". In: *Phys. Rev. Applied* 7 (2017), p. 034026. DOI: 10.1103/PhysRevApplied.7.034026. arXiv: 1608.06922 [cond-mat.mes-hall].

[188] L. W. Cheuk et al. "Quantum-Gas Microscope for Fermionic Atoms". In: *Phys. Rev. Lett.* 114 (2015), p. 193001. DOI: 10.1103/PhysRevLett.114.193001. arXiv: 1503.02648 [cond-mat.quant-gas].

[189] E. Haller et al. "Single-atom imaging of fermions in a quantum-gas microscope". In: *Nat. Phys.* 11 (2015), p. 738. DOI: 10.1038/nphys3403. arXiv: 1503.02005 [cond-mat.quant-gas].

[190] W. S. Bakr et al. "A quantum gas microscope for detecting single atoms in a Hubbard-regime optical lattice". In: *Nature* 462 (2009), p. 74. DOI: 10.1038/nature08482. arXiv: 0908.0174 [cond-mat.quant-gas].

[191] J. F. Sherson et al. "Single-atom-resolved fluorescence imaging of an atomic Mott insulator". In: *Nature* 467 (2010), p. 68. DOI: 10.1038/nature09378. arXiv: 1006.3799 [cond-mat.quant-gas].

[192] D. Meschede and H. Metcalf. "Atomic nanofabrication: atomic deposition and lithography by laser and magnetic forces". In: *J. Phys. D: Appl. Phys.* 36 (2003), R17. DOI: 10.1088/0022-3727/36/3/202.

[193] R. J. Clark et al. "Nanofabrication by magnetic focusing of supersonic beams". In: *Appl. Phys. B* 103 (2010), p. 547. DOI: 10.1007/s00340-010-4229-x. arXiv: 1004.5581 [physics.atom-ph].

[194] J. R. Gardner, E. M. Anciaux, and M. G. Raizen. "Neutral atom imaging using a pulsed electromagnetic lens". In: *J. Chem. Phys.* 146 (2017), p. 081102. DOI: 10.1063/1.4976986.

[195] T. Kovachy et al. "Matter wave lensing to pK temperatures". In: *Phys. Rev. Lett.* 114 (2015), p. 143004. DOI: 10.1103/PhysRevLett.114.143004. arXiv: 1407.6995 [physics.atom-ph].

[196] S. Abend et al. "Atom-chip fountain gravimeter". In: *Phys. Rev. Lett.* 117 (2016), p. 203003. DOI: 10.1103/PhysRevLett.117.203003.

[197] B. Barrett et al. "Multidimensional atom optics and interferometry". In: *Phys. Rev. Lett.* 122 (2019), p. 043604. DOI: 10.1103/PhysRevLett.122.043604. arXiv: 1901.02214 [physics.atom-ph].

[198] A. T. Grier et al. "Λ-enhanced sub-Doppler cooling of lithium atoms in D_1 gray molasses". In: *Phys. Rev. A* 87 (2013), p. 063411. DOI: 10.1103/PhysRevA.87.063411. arXiv: 1304.6971 [physics.atom-ph].

[199] C. C. Bradley et al. "Evidence of Bose-Einstein Condensation in an Atomic Gas with Attractive Interactions". In: *Phys. Rev. Lett.* 75 (1995), p. 1687. DOI: 10.1103/PhysRevLett.75.1687.

[200] S. E. Pollack et al. "Extreme Tunability of Interactions in a ^{7}Li Bose-Einstein Condensate". In: *Phys. Rev. Lett.* 102 (2009), p. 090402. DOI: 10.1103/PhysRevLett.102.090402. arXiv: 0811.4456 [cond-mat.other].

[201] C. Chin et al. "Feshbach resonances in ultracold gases". In: *Rev. Mod. Phys.* 82 (2010), p. 1225. DOI: 10.1103/RevModPhys.82.1225. arXiv: 0812.1496 [cond-mat.other].

[202] Zachary A. Geiger. "An Apparatus for Dynamical Quantum Emulation Using Ultracold Lithium". PhD thesis. University of California, Santa Barbara, 2017.

[203] T. Ikemachi et al. "All-optical production of a superfluid Bose-Fermi mixture of ^{6}Li and ^{7}Li". In: *J. Phys. B: At. Mol. Opt. Phys.* 50 (2016), 01LT01. DOI: 10.1088/1361-6455/50/1/01lt01. arXiv: 1606.09404 [cond-mat.quant-gas].

[204] R. Jannin, P. Cladé, and S. Guellati-Khélifa. "Phase shift due to atom-atom interactions in a light-pulse atom interferometer". In: *Phys. Rev. A* 92 (2015), p. 013616. DOI: 10.1103/PhysRevA.92.013616.

[205] M. Fattori et al. "Atom Interferometry with a Weakly Interacting Bose-Einstein Condensate". In: *Phys. Rev. Lett.* 100 (2008), p. 080405. DOI: 10.1103/PhysRevLett.100.080405. arXiv: 0710.5131 [cond-mat.other].

[206] N. Gross and L. Khaykovich. "All-optical production of ^{7}Li Bose-Einstein condensation using Feshbach resonances". In: *Phys. Rev. A* 77 (2008), p. 023604. DOI: 10.1103/PhysRevA.77.023604. arXiv: 0712.0717 [physics.atom-ph].

[207] T. L. Nicholson et al. "Optical Feshbach resonances: Field-dressed theory and comparison with experiments". In: *Phys. Rev. A* 92 (2015), p. 022709. DOI: 10.1103/PhysRevA.92.022709. arXiv: 1502.00026 [physics.atom-ph].

[208] J. H. T. Burke et al. "Confinement effects in a guided-wave atom interferometer with millimeter-scale arm separation". In: *Phys. Rev. A* 78 (2008), p. 023619. DOI: 10.1103/PhysRevA.78.023619. arXiv: 0710.1081 [physics.atom-ph].

[209] S. R. Segal et al. "Revealing buried information: Statistical processing techniques for ultracold-gas image analysis". In: *Phys. Rev. A* 81 (2010), p. 053601. DOI: 10.1103/PhysRevA.81.053601. arXiv: 0905.1979 [cond-mat.quant-gas].

[210] R. P. Kafle, D. Z. Anderson, and A. A. Zozulya. "Analysis of a free oscillation atom interferometer". In: *Phys. Rev. A* 84 (2011), p. 033639. DOI: 10.1103/PhysRevA.84.033639. arXiv: 1012.4380 [physics.atom-ph].

[211] M. Horikoshi and K. Nakagawa. "Suppression of Dephasing due to a Trapping Potential and Atom-Atom Interactions in a Trapped-Condensate Interferometer". In: *Phys. Rev. Lett.* 99 (2007), p. 180401. DOI: 10.1103/PhysRevLett.99.180401. arXiv: 1801.05658 [physics.atom-ph].

[212] P. A. Altin et al. "Optically trapped atom interferometry using the clock transition of large ^{87}Rb Bose-Einstein condensates". In: *New J. Phys.* 13 (2011), p. 065020. DOI: 10.1088/1367-2630/13/6/065020. arXiv: 1011.4713 [quant-ph].

[213] G. Kleine Büning et al. "Extended Coherence Time on the Clock Transition of Optically Trapped Rubidium". In: *Phys. Rev. Lett.* 106 (2011), p. 240801. DOI: 10.1103/PhysRevLett.106.240801. arXiv: 1103.2283 [quant-ph].

[214] N. Lundblad, M. Schlosser, and J. V. Porto. "Experimental observation of magic-wavelength behavior of ^{87}Rb atoms in an optical lattice". In: *Phys. Rev. A* 81 (2010), 031611(R). DOI: 10.1103/PhysRevA.81.031611. arXiv: 0912.1528 [cond-mat.quant-gas].

[215] G. Afek et al. "Revival of Raman Coherence of Trapped Atoms". In: *Phys. Rev. A* 96 (2017), p. 043831. DOI: 10.1103/PhysRevA.96.043831. arXiv: 1708.02129 [physics.atom-ph].

[216] H. Mueller. "Quantum mechanics, matter waves and moving clocks". In: (2013). arXiv: 1312.6449 [quant-ph].

[217] A. West. "Systematic effects in 2D trapped matter-wave interferometers". In: (2019). arXiv: 1904.12707 [physics.atom-ph].

[218] A. C. Vutha et al. "Displacement operators: the classical face of their quantum phase". In: *Eur. J. Phys.* 39 (2018), p. 025405. DOI: 10.1088/1361-6404/aa9ca5. arXiv: 1702.01833 [quant-ph].

[219] Travis L. Nicholson. "A new record in atomic clock performance". PhD thesis. University of Colorado, Boulder, 2018.

[220] R. H. Leonard and C. A. Sackett. "Effect of trap anharmonicity on a free-oscillation atom interferometer". In: *Phys. Rev. A* 86 (2012), p. 043613. DOI: 10.1103/PhysRevA.86.043613. arXiv: 1209.4127 [physics.atom-ph].

[221] Sydney Schreppler. "Quantum measurement with atomic cavity optomechanics". PhD thesis. University of California, Berkeley, 2016.

[222] P. Storey and C. Cohen-Tannoudji. "The Feynman Path Integral Approach to Atom Interferometry: A tutorial". In: *J. Phys II France* 4 (1994), p. 1999. DOI: 10.1051/jp2:1994103.

[223] P. W. Graham et al. "Dark matter direct detection with accelerometers". In: *Phys. Rev. D* 93 (2016), p. 075029. DOI: 10.1103/PhysRevD.93.075029. arXiv: 1512.06165 [hep-ph].